

UNCLASSIFIED

AD NUMBER

ADB000286

LIMITATION CHANGES

TO:

Approved for public release; distribution is unlimited.

FROM:

Distribution authorized to U.S. Gov't. agencies only; Administrative/Operational Use; JUN 1974. Other requests shall be referred to Federal Aviation Administration, Supersonic Transport Office, 800 Independence Avenue, SW, Washington, DC 20590.

AUTHORITY

faa ltr, 26 apr 1977

THIS PAGE IS UNCLASSIFIED

THIS REPORT HAS BEEN DELIMITED
AND CLEARED FOR PUBLIC RELEASE
UNDER DOD DIRECTIVE 5200.20 AND
NO RESTRICTIONS ARE IMPOSED UPON
ITS USE AND DISCLOSURE.

DISTRIBUTION STATEMENT A

APPROVED FOR PUBLIC RELEASE;
DISTRIBUTION UNLIMITED.

Report No. FAA-SS-73-18

(1)

FG

SST Technology Follow-On Program-Phase II

A LOW SPEED MODEL ANALYSIS AND DEMONSTRATION OF ACTIVE CONTROL SYSTEMS FOR RIGID-BODY AND FLEXIBLE MODE STABILITY

R. A. Gregory, A. D. Ryneveld, R. S. Imes

Boeing Commercial Airplane Company

P.O. Box 3707

Seattle, Washington 98124

AD B 000286



D6-60295

June 1974

FINAL REPORT

Task 5

DDC
RECEIVED
DEC 5 1974
E

AD No. _____
DDC FILE COPY

Approved for U.S. Government only. This document is exempted from public availability because of restrictions imposed by the Export Control Act. Transmittal of this document outside the U.S. Government must have prior approval of the Supersonic Transport Office

Prepared for
FEDERAL AVIATION ADMINISTRATION

Supersonic Transport Office

800 Independence Avenue, S.W.

Washington, D.C. 20590

6 -

ACCESSION NO.	
RTS	Wallo Swifox <input type="checkbox"/>
POC	But Swifox <input checked="" type="checkbox"/>
MANAGEMENT	
JUSTIFICATION	
BY	DISTRIBUTION CENTER
DATE	YEAR
13	

<p>1. Report No. FAA-SS 73-18 ✓</p>	<p>2. Government Accession No.</p>	<p>3. Recipient's Catalog No.</p>
<p>4. Title and Subtitle SST TECHNOLOGY FOLLOW-ON PROGRAM PHASE II: A Low Speed Model Analysis and Demonstration of Active Control Systems for Rigid-Body and Flexible Mode Stability.</p>	<p>5. Report Date June 74 ✓</p>	<p>6. Performing Organization Code</p>
<p>7. Author(s) R. A. Gregory, A. D. Ryneveld F. S. /Imes</p>	<p>8. Performing Organization Report No. D6-60295 ✓</p>	<p>10. Work Unit No.</p>
<p>9. Performing Organization Name and Address Boeing Commercial Airplane Company P.O. Box 3707 Seattle, Washington 98124 ✓</p>	<p>11. Contract or Grant No. DOT-FA-72-WA-2893 ✓</p>	<p>13. Type of Report and Period Covered Final Report. Phase 2 May 72 - June 74 or</p>
<p>12. Sponsoring Agency Name and Address Federal Aviation Administration Supersonic Transport Office 800 Independence Avenue S.W.. Washington, D.C. 20590 ✓</p>	<p>14. Sponsoring Agency Code Phase 2, Task 5</p>	<p>15. Supplementary Notes (See P. xi)</p>
<p>16. Abstract An existing low-speed SST flutter model was modified to include two hydraulic aileron control systems and a horizontal stabilizer system. Wing mode flutter suppression systems were analyzed and wind tunnel tested, using wing strain gages and the aileron systems in the active control feedback loops. Rigid-body stability systems were theoretically analyzed and experimentally synthesized using body-mounted sensors. Variable rigid-body stability was achieved through a remote-transfer water ballast system. The results of parallel analysis and wind tunnel tests, the methods of approach, the problems encountered, and a list of recommendations for the advancement of the active controls technology are reported in this document.</p> <p>21 Report on SST Technology Follow-On Program. See also AD-913/365L, AD-B444/285L.</p>		
<p>17. Key Words Closed loop Active control systems Nyquist Feedback Flutter suppression Automatic flight control system</p>	<p>18. Distribution Statement Approved for U.S. Government only. This document is exempted from public availability because of restrictions imposed by the Export Control Act. Transmittal of this document outside the U.S. Government must have prior approval of the Supersonic Transport Office.</p>	
<p>19. Security Classif. (of this report) Unclassified</p>	<p>20. Security Classif. (of this page) Unclassified</p>	<p>21. No. of Pages 196</p>
<p>22. Price</p>		

-a' 390 145 ✓

mt

CONTENTS

	Page
1.0 SUMMARY	1
2.0 INTRODUCTION	2
2.1 Program Goals	2
2.2 Control System Design Considerations	3
2.3 Configuration Selection	4
2.4 Analytical Simulation	4
3.0 MODEL DESCRIPTION	5
3.1 Design of Original Model	5
3.2 Modification	6
3.2.1 Component Installation	6
3.2.2 Hydraulics	7
3.3 Model Suspension	8
4.0 LABORATORY TESTING	9
4.1 Wing Box Vibration Test	9
4.2 Model Support Frequency Check	10
4.3 Control Surface Actuator Bench Tests	10
4.3.1 Internal Loop Compensation	10
4.3.2 Actuator Stiffness Calibration	11
4.3.3 Actuator Frequency Response	11
4.4 Complete Model Vibration Tests	12
4.5 Preflight Preparation	12
5.0 BASIC ANALYSES	15
5.1 Structural Analysis	15
5.2 Vibration Analysis	16
5.3 Residual Flexibility	17
5.4 Unsteady Aerodynamics	17
5.5 Sensors	19
5.6 Model Stability	19
5.7 Flutter Analysis	20
6.0 FLUTTER STABILITY AUGMENTATION SYSTEM STUDIES	21
6.1 FSAS Analysis	21
6.2 FSAS Wind Tunnel Test Procedures and Results	22
6.3 FSAS Analytical-Experimental Correlation	26
7.0 AUTOMATIC FLIGHT CONTROL SYSTEM STUDIES	27
7.1 AFCS Analysis	27
7.2 AFCS Wind Tunnel Test Procedures and Results	28
8.0 CONCLUDING REMARKS	33

CONTENTS (Concluded)

	Page
APPENDIX A—Design Details of the TX1129D Model	141
APPENDIX B—Auxiliary Test Equipment	147
APPENDIX C—Instrumentation and Electronic Equipment	155
APPENDIX D—Analytical Details	167
APPENDIX E—Problem Areas	189
REFERENCES	195

FIGURES

No.	Page
1 TX1129D Flutter SAS Results	35
2 Comparison of Test and Analysis in the FSAS.	36
3 AFCS Test Results at 100 Knots and 60.6% CR	37
4 Wing Fuel Management Study	38
5 Internal Structure of the Model	39
6 General Configuration of the Model	40
7 Hydraulic Tubing and Internal Structure of Ailerons	41
8 Exploded View of Aileron Actuator	42
9 Majority Voting Single Redundancy Block Diagram	43
10 Horizontal Stabilizer Servo Valve/Position Transducer System	44
11 Model Mounted in Test Section	45
12 Comparison of Modes of Vibration for Right-hand Wing Without Nacelles	46
13 Comparison of Modes of Vibration for Left-hand Wing Without Nacelles	47
14 Comparison of Modes of Vibration for Right-hand Wing With Nacelles	48
15 Comparison of Modes of Vibration for Left-hand Wing With Nacelles	49
16 Inertia Model on Cable System	50
17 Effect of Cable Tension on Inertia Model Rigid Modes	51
18 Bench Test of Aileron Actuator	52
19 Open Loop Stabilizer Response Characteristics	53
20 Closed Loop Stabilizer Response Characteristics	54
21 Bench Test of Stabilizer Servo System	55
22 Structural Idealization and Substructures	56
23 Model Structure Analytical Idealization	57
24 Comparison of Load/Deflection Curves—Load Point 23	58
25 Comparison of Load/Deflection Curves—Load Point 27	59
26 Comparison of Load/Deflection Curves—Load Point 34	60
27 Comparison of Load/Deflection Curves—Load Point 36	61
28 Comparison of Load/Deflection Curves—Load Point 41	62
29 Comparison of Load/Deflection Curves—Load Point 42	63
30 Symmetric Vibration Mode 1	64
31 Symmetric Vibration Mode 2	65
32 Symmetric Vibration Mode 3	66
33 Symmetric Vibration Mode 4	67
34 Symmetric Vibration Mode 5	68
35 Symmetric Vibration Mode 6	69
36 Symmetric Vibration Mode 7	70
37 Symmetric Vibration Mode 8	71
38 Symmetric Vibration Mode 9	72
39 Symmetric Vibration Mode 10	73
40 Symmetric Vibration Mode 11	74
41 Antisymmetric Vibration Mode 1	75
42 Antisymmetric Vibration Mode 2	76
43 Antisymmetric Vibration Mode 3	77
44 Antisymmetric Vibration Mode 4	78

FIGURES (Continued)

No.	Page
45 Antisymmetric Vibration Mode 5	79
46 Antisymmetric Vibration Mode 6	80
47 Antisymmetric Vibration Mode 7	81
48 Antisymmetric Vibration Mode 8	82
49 Antisymmetric Vibration Mode 9	83
50 Antisymmetric Vibration Mode 10	84
51 Aerodynamic Grids	85
52 Perspective View of an Analytical Mode Shape	86
53 Stability Analysis—Symmetric—51% C_R	87
54 Stability Analysis—Antisymmetric—51% C_R	88
55 Stability Analysis—Symmetric—58% C_R	89
56 Stability Analysis—Symmetric Flexible Model	90
57 Effect of CG on Symmetric Flutter Speed	91
58 Antisymmetric Flutter—48% C_R	92
59 Effect of Feedback Gain on Wing Flutter Mode Suppressed With Inboard Aileron	93
60 Wing Flutter Suppressed With Inboard Aileron	94
61 Wing Flutter Suppressed With Outboard Aileron	95
62 Effect of Phase Shift on Inboard Aileron System at 150 Kn	96
63 Effect of Phase Shift on Outboard Aileron System at 150 Kn	97
64 Unaugmented Flutter Cycle—140 Kn	98
65 Flutter Cycle With Inboard Aileron Active—150 Kn	100
66 Flutter Cycle With Outboard Aileron Active—150 Kn	102
67 Modal Accelerations at 15.9 Hz 130 KTAS Convair Low Speed Tunnel	104
68 Strain Gage Locations	105
69 Strain Gage 33 Response to Inboard Aileron Excitation	106
70 Frequency Response of Single Pole Compensation Filter— Inboard Aileron System	107
71 Open-Loop Transfer Function of Inboard Aileron System—130 Kn	108
72 Effect of Active Inboard Aileron on Frequency Response at Strain Gage 33	109
73 10 Hz Notch Filter Frequency Response	110
74 Compensation Network Transfer Function	111
75 Wing Flutter Suppressed With Inboard Aileron	112
76 Effect of Active Inboard Aileron on 15 Hz Mode at 130 Kn	113
77 Strain Gage 30 Response to Outboard Aileron Excitation—130 Kn	114
78 12.8 Hz Notch Filter Transfer Function	115
79 Closed Loop Frequency Response of Outboard Aileron System— Gain of 500 at 130 Kn	116
80 Effect of Active Outboard Aileron on 15 Hz Mode at 130 Kn	117
81 Open-Loop Transfer Function of Stabilizer/Elevator System—130 Kn	118
82 Closed Loop Transfer Function of Stabilizer/Elevator System—130 Kn	119
83 Comparison of Results of Inboard Aileron on Wing Flutter	120
84 Comparison of Results of Outboard Aileron on Wing Flutter	121
85 Pitch Feedback Control of Low Frequency Modes	122

FIGURES (Concluded)

No.	Page
86 Pitch Rate Control of Low Frequency Modes	123
87 Acceleration Feedback Control of Low Frequency Modes	124
88 Velocity Feedback Control of Low Frequency Modes	125
89 Combined Pitch and Velocity Feedback Control of Low Frequency Modes	126
90 Effect of Tunnel Velocity on Combined Pitch and Velocity Control	127
91 Variation of Pitch Rate Transfer Function With Tunnel Speed	128
92 Variation of Acceleration Transfer Function With Wind Tunnel Speed	129
93 Pitch Rate Open Loop Transfer Function for Pitch Mode	130
94 Acceleration Open Loop Transfer Function for Pitch Mode	131
95 Pitch Rate Open Loop Transfer Function for Plunge Mode	132
96 Acceleration Open Loop Transfer Function for Plunge Mode	133
97 Effect of CG Position on Rigid Stability	134
98 Compensation Filter Calibration for Plunge Mode	135
99 Effect of Tunnel Velocity on Plunge Mode	136
100 Effect of Active Horizontal Stabilizer With Pitch Rate Feedback on Plunge Mode	137
101 Effect of Active Horizontal Stabilizer With Vertical Velocity Feedback on Plunge Mode—Sensor at 36% of Body Length	138
102 Effect of Active Horizontal Stabilizer With Vertical Velocity Feedback on Plunge Mode—Sensor at 90% Body Length	139
103 Effect of Active Inboard Ailerons With Vertical Velocity Feedback on Plunge Mode Sensor at 36% of Body Length	140
A1 Stabilizer Actuator Position Sensors	143
A2 Stabilizer Hydraulic Lines Installation	144
A3 Aileron Attachment	145
B1 Cable Support System—Plan and Side Views	149
B2 Cable Snubber System	150
B3 Hydraulic Power Supply System Schematic	151
B4 Dynamic Pressure Reducer	152
B5 Water Ballast Control Schematic	153
C1 Control System Block Diagram	159
C2 Test Electronics—Data Acquisition Racks	160
C3 Test Electronics—System Control Racks	161
C4 Model Instrumentation	162
C5 Compensation Card	163
C6 Summation and q Division Card	164
C7 Data Acquisition System Block Diagram	165
D1 Stabilizer Actuator Stiffness	185
D2 Stabilizer Actuator Response	186
D3 Aileron Actuator Stiffness	187
D4 Aileron Actuator Response	188
E1 Stabilizer Actuator System Failure	194

TABLES

No.		Page
1	Dynamic Scaling of the 1129D Model	6
2	Static Failure Characteristics of the Horizontal Stabilizer Majority Voting Servoactuator System	8
3	Comparison of Vibration Frequencies of the Wing Box	9
4	Displacements of the Rigid Modes of the Inertia Model	10
5	Comparison of Vibration Modes	18
6	Strain Gage Response to Inboard Aileron Excitation	24

ABBREVIATIONS AND SYMBOLS

a	Aerodynamic coefficient
A	Airplane
A_A	Area, airplane $\sim \text{in.}^2$
AFCS	Automatic flight control system
A_M	Area, model $\sim \text{in.}^2$
AMAS	Aeroelastic modal analysis system
b_0	Reference chord length, in.
c	Damping coefficient, lb-sec/in.
cg	Center of gravity, % C_R
CIC	Computer Instrument Corporation
C_R	Root reference chord, in.
DRAS	Dynamic response actuated switch
E	Modulus of elasticity, lb/in. ²
f	Frequency, Hz
F_A	Actuator force, lb
FSAS	Flutter stability augmentation system
g	Structure damping coefficient = 2ξ
G, H	Transfer function defined by experimental test
IRIG	Inter-Range Instrumentation Group
k	Stiffness, lb/in.
kn	Knots
K	Gain factor
KTAS	Knots true air speed

L	Length, in.
m	Inertia, lb-sec ² /in.
Q	Generalized external force
q	Dynamic pressure, lb/in. ² , generalized displacement
s	Laplace transform variable
S	Span, in.
sec	Second
t	Skin thickness, in.
v	volt
V	Air speed, kn
z	Vertical displacement
α	Angle of attack, deg
δ_A	Actuator displacement, in.
ϵ	Input signal, volts
ω	Frequency in radian per second
ω_n	Natural circular frequency, rad/sec
ϕ	Generalized mode shape
ρ	Air density, lb-sec ² /in. ⁴
θ	Pitch angle, deg
ξ	Damping ratio

PREFACE

Theoretical analyses and wind tunnel tests of a low-speed aeroelastic model of the SST were conducted by the Boeing Commercial Airplane Company under contract DOT-FA-72-WA-2893 of the SST Technology Follow-on, phase II. This report covers the modification of the model to provide active control system capability, test of the model in the performance of flutter suppression and rigid-body stabilization tasks in the General Dynamics low speed tunnel in San Diego, California, and the analyses conducted in support of the above tasks.

The contract work contained herein was performed during the period from May 1972 through June 1974. The low-speed flutter model from which the active control model evolved was built and tested in 1969 during the supersonic transport program. The modification of the model to the active control configuration was designed by P. C. Foster in coordination with J. Hill, who determined the weight distribution. The design of electronic circuits, the performance of laboratory testing, and the operation of electronic equipment during all phases of testing were the responsibility of H. E. Anderson, assisted by N. L. Olsen and H. W. Buse of Dynamic Test. The theoretical analyses of the model were directed by A. D. Ryneveld, assisted by R. S. Imes. The technical direction of the experimental and analytical efforts was the responsibility of R. A. Gregory. J. B. Bartley was the program manager.

A color and sound documentary motion picture was produced by The Boeing Company to summarize the experimental portion of the program. The film, titled "Active Controls Development," number 3740.11, is the property of the Department of Transportation.

The cooperation and assistance of the General Dynamics/Convair low-speed tunnel engineering staff headed by J. C. Struthers were greatly appreciated in the conduct of the experimental portion of the contract. The authors are indebted to his staff for many of the photographs and sketches included in the text.

The encouragement and suggestions received during this program from C. R. Ritter and C. C. Troha of the Department of Transportation are gratefully acknowledged.

1.0 SUMMARY

The work reported in this document deals with the development and demonstration of a flutter stability augmentation system (FSAS) and an automatic flight control system (AFCS) on a full-span, subsonic SST flutter model. The FSAS was designed to improve the flutter speed of the model and to demonstrate the feasibility of such a system for full-scale aircraft application. The purpose of the AFCS was to stabilize a flutter model which was statically unstable for aft cg conditions. Both systems were tested at the Convair low speed wind tunnel.

The full-span flutter model used in this program was a 1/20 scale low-speed model of the Boeing 2707-300 airplane which was designed and built as part of the U.S. Supersonic Transport Program. The original model was dynamically scaled and complete except for control surfaces, sensors, and feedback networks. The latter were added to the model under the SST Technology Follow-On Program.

The development of the FSAS and AFCS involved analyses as well as wind tunnel test work. The analyses employed methods used during the U.S. SST program which were extended to provide for control system simulation. The wind tunnel test procedures differed significantly from those used during the U.S. SST program. Development of the control systems required investigation of the frequency response of the model in a specific configuration whereas the primary objective in previous testing was to obtain flutter speeds for as many configurations as possible.

Most of the work accomplished during this program was directed toward the FSAS development, since FSAS was believed to have more general application to aircraft design. The AFCS study applied primarily to full-span flutter model testing. Also, the AFCS system involved substantially greater risk to the model, since the instability that the AFCS was designed to suppress could involve large excursions of the model in the tunnel. Thus, AFCS testing was deferred until the later stages of the program.

The FSAS was successfully demonstrated, and a summary of flutter speed improvement is presented in figure 1. A comparison of analysis versus test results is given in figure 2 for the inboard aileron and outboard aileron systems. While the inboard aileron system exhibited good test/analysis agreement, the outboard aileron system did not show similar correlation. Further study is required to explore possible reasons for the poor correlation of the outboard aileron test and analysis results. The test demonstrated that a significant increase in flutter speed was possible using a FSAS on a full-span configuration. The amount of increase achieved was not limited by feedback gain but by the aerodynamic energy available from the active control surface within a reasonable oscillation amplitude in the mode of suppression dictated by the control law selected.

Results of the AFCS study were not as conclusive as those for the FSAS study. The nature of the instability achieved during testing was not the same as that for which the system had been designed. Testing was initiated to employ active controls to stabilize the plunge instability that did occur, figure 3; however, the model was damaged before that testing was completed.

2.0 INTRODUCTION

The U.S. Supersonic Transport configuration required a substantial increment of structural weight over strength design material in order to achieve adequate flutter speed margins. Two constraints of the airplane made a flutter-free design unusually difficult: (1) the relatively low payload/total weight ratio made additional structural weight or mass balance particularly distasteful, and (2) any rearrangement of lifting surface planforms, thickness, or major mass relocation (e.g., nacelles) degraded the delicate cruise economy or cg balance. Because of this flutter dilemma, a vigorous program of flutter analysis and verification with flexible models was undertaken on the SST, as reported in references 1 and 2. At the time of contract termination, the dynamic simulation of the airplane subsonic configuration was complete except for simulation of control systems.

The DOT/SST Technology Follow-On Program provided an opportunity to complete the dynamic simulation of the airplane. An automatic flight control system was developed to improve pitch stability of the model. Previously, the marginal pitch stability was improved by ballasting the model to a forward cg condition. The disadvantage of this approach was that for some configurations the flutter mode was changed from a wing mode to a body mode (see fig. 4). Thus, the development of an AFCS for the subsonic flutter model was a significant improvement in test technology.

In addition to the AFCS, a stability augmentation system was designed that operated in the frequency range of the wing flutter modes to increase flutter speeds. A system of this type is one method of improving flutter speed without adding substantial weight.

2.1 PROGRAM GOALS

The primary program objectives as stated in section 3.6.1 of reference 3 were:

- a) To develop an automatic flight control system (AFCS) to regulate the operation of an SST subsonic flutter model with statically unstable weight conditions representative of the SST configuration.
- b) To develop a stability augmentation system that operates in the frequency range of the wing flutter modes to improve flutter speeds of the SST airplane (FSAS).
- c) To demonstrate the system on an SST subsonic flutter model in a low-speed wind tunnel.

Several guidelines were established for the design, analysis, model test, and evaluation of the program. Briefly, they were:

- a) To employ existing analytical and experimental techniques to determine and demonstrate the stated objectives.
- b) Wherever possible, to use the simplest processes to achieve the objectives.

- c) To design into the test vehicle ample flexibility of function and alternatives in operation and testing.
- d) To provide a capability for evaluating the performance of an experimental active control system.

2.2 CONTROL SYSTEM DESIGN CONSIDERATIONS

Keeping the above goals in mind, the philosophy of the present program was to demonstrate closed-loop system testing on a selected SST flutter model configuration and to demonstrate the ability to analyze the processes by digital computer programs. There were no attempts to develop new principles in automatic control theory, such as in references 4 and 5, nor to develop new hardware design techniques. The analysis programs were adapted from flutter solution programs or quasi-steady state computer programs. Although the aileron actuators were designed specifically for the flutter suppression application, all other system components were off-the-shelf items or had been tested previously on the low-speed model.

The purpose of the automatic flight control system (AFCS) was to employ a closed-loop control system in place of cg control through mass balance, thus eliminating the instability of the 4-Hz mode caused by the mass balance, and at the same time, maintaining airplane weight and inertia simulation. This system required the active control of the hydraulically powered horizontal stabilizer with its geared elevator, capable of variable angular amplitude and frequency, and incorporating angular position feedback. The hydraulic actuator system and stabilizer-elevator surfaces were salvaged from a partially completed 1/17-scale transonic model and, therefore, were disproportionately large for the 1/20-scale model.

The flutter stability augmentation system (FSAS) consisted primarily of active control surfaces on the wing trailing edge, functioning as inboard and outboard ailerons. Each aileron was activated by a hydraulically powered actuator capable of variable angular amplitude and frequency and incorporating angular position feedback.

It was considered desirable to provide capability to suppress unstable modes of arbitrary characteristics. Thus, while the stabilizer control system was designed primarily for rigid-body control, it did perform flexible mode control also. The aileron control systems were designed to control relatively high frequency (10- to 50-Hz) modes, but the ailerons controlled the very low frequency (1-Hz) modes as well. Symmetric, antisymmetric, and unsymmetric modes were controlled simultaneously since each wing panel feedback loop was independent of the other. On the basis of preliminary analytical studies, the ailerons were located to provide excitation, and thus potential suppression, for a large number of wing flexible modes.

Since the control model provided a full-time power trim and symmetric maneuvering capability, the problem of reliability had to be considered. The design was based on an evaluation of catastrophic failure modes. The horizontal stabilizer had to be protected against the most probable failures since a loss of power or pitch control signal would almost certainly be catastrophic at any tunnel speed, regardless of inherent model stability. Details

of the stabilizer control system redundancy are discussed in section 3.2.2. The aileron systems threatened no such calamity except when they were operated in the FSAS mode. The anticipated time to be spent above the normal flutter speed and the consequences of aileron control system failure appeared insufficient to warrant the developmental time, expense, and complication of a redundant aileron control system. This assessment is by no means a general one, but it was temporized to the set of test conditions and tunnel operating conditions. If the system were being tested, for instance, in a supersonic tunnel, redundancy would undoubtedly have been considered in a different light.

2.3 CONFIGURATION SELECTION

The selection of the particular configuration upon which to demonstrate flutter suppression was based on the following: (1) the requirement of a low flutter speed of the basic model in order to allow comfortable margin for increase in flutter speed due to operation of the closed-loop system and (2) the selection of a configuration including significant body weight so that control system hydraulics, restraint system equipment, and servoinstrumentation could be used to replace payload and fuel weight of a configuration that had been previously tested.

These conditions were all satisfied in the configuration selected: empty wing, full body fuel and payload, rigid nacelles. The flutter speed was 125.5 kn. The additional weight of the hydraulic control system in the wing was compensated by removal of the static weights in the model for airplane controls and equipment in the rear spar area.

2.4 ANALYTICAL SIMULATION

The analytical simulation of the experimental model began during the SST development contract with a finite element analysis of the original model structure. Revisions to the analysis were made when the model wing trailing edge was modified to accommodate the aileron hydraulic systems. The unsteady aerodynamics computer program by Rowe, reference 6, was used in the flutter analysis of the model when FSAS was involved. Experience during the SST development period, and verified in reference 2, indicated that finite element structural analysis and lifting surface unsteady aerodynamics were required to adequately define the flutter characteristics of the SST wing. Details on the analysis are covered in appendix D.

3.0 MODEL DESCRIPTION

3.1 DESIGN OF ORIGINAL MODEL

The SA1129D-1 model used for this investigation was a 1/20-scale low-speed flutter model of the Boeing 2707-300 airplane. The wing was a stressed skin design. The body was of conventional spar and section design, except through the wing root area, where caps on the wing root rib provided scaled body longitudinal stiffness, and sectioned fairings above and below the wing carrythrough structure provided fuselage shape. The wing panels were designed so that they could be tunnel-tested as half-span surfaces cantilevered from the body centerline, if so desired. The non-flow-through nacelles were scaled in shape and mass. They were mounted to the wing through metal springs that could be varied in stiffness to change nacelle support frequency. The rigid tail surfaces were scaled for mass and geometry and were of conventional construction. The horizontal stabilizer, which was driven by a remotely controlled geared electric motor located in the body, provided pitch trim. Fuel and payloads were simulated in the body by lumped masses. Wing fuel was simulated by steel plates attached to the lower surface of the wing by 62 posts (per side) attached internally to the webs of the wing spars.

The model scaling parameters are listed in table 1. Body design stiffness requirement data were obtained in conventional EI/GJ form, but the wing design data were provided in terms of skin gage, spar web thickness, spar cap areas, and corresponding wing ordinates. The wing was made of very thin fiberglass-foam sandwich subassemblies. Details of the wing internal structure are illustrated in figure 5.

Model skin thickness and areas were found by use of the following equations:

$$t_M = \frac{E_A}{E_M} \left(\frac{L_A}{L_M} \right)^3 t_A$$
$$A_M = \frac{E_A}{E_M} \left(\frac{L_A}{L_M} \right)^2 A_A$$

where

- t = Skin thickness
- E = Modulus of elasticity
- M = Model
- A = Airplane
- L = Length
- A_A = Area airplane
- A_M = Area model

TABLE 1.—DYNAMIC SCALING OF THE 1129D MODEL

Linear dimensions	$D = \frac{\ell_M}{\ell_A}$.05
Reduced frequency	$K = \frac{\omega_M \ell_M v_A}{v_M \omega_A \ell_A}$	1
Mass ratio	$M = \frac{m_M \rho_A \ell_A^2}{m_A \rho_M \ell_M^2}$	1
Froude number	$F = \frac{V_M^2 g_A \ell_A}{V_A^2 g_M \ell_M}$	1
Gravitational acceleration	$G = \frac{g_M}{g_A}$	1
Frequency	$f = K \left(\frac{FG}{D} \right)^{1/2}$	4.472
Density	$P = \frac{\rho_M}{\rho_A}$	1.823
Mass distribution	$m = MPD^2$	2.279×10^{-4}
Mass moment of inertia	$i = MPD^4$	5.697×10^{-7}
Dynamic pressure	$q = FPGD$.091
Velocity	$v = (FGD)^{1/2}$.224
Stiffness	$k = FPGD^5$	5.697×10^{-7}

M = model
A = airplane

Instrumentation consisted of strain gage bridges on the wing for measurement of spanwise, chordwise, and torsional strain levels at 16 locations per semispan.

3.2 MODIFICATION

The 1129D model was modified to incorporate hydraulically operated inboard and outboard ailerons, horizontal stabilizer with geared elevator, and wingtip aerodynamic vanes. Each aileron was powered by a rotary hydraulic actuator and incorporated angular position feedback. The stabilizer was driven by a linear hydraulic actuator and also incorporated angular position feedback. The wingtip vanes were powered by rotary hydraulic actuators and were used for the investigation of transient excitation techniques for flutter testing (ref. 7). The general configuration of the model without the wingtip vanes is shown in figure 6.

3.2.1 Component Installation

Prior to installation of the wing trailing edge control system components, the model structure aft of the wing rear spar was completely removed. The hydraulic supply tubing and actuators were installed, and the trailing edge structure was rebuilt. The ailerons were attached to their respective actuators to complete the wing modification. The modified

horizontal stabilizer/elevator with the hydraulic actuator was installed together with a new aft body section. Ballast tanks were installed in the forebody.

The wingtip vanes could be removed when desired. Hydraulic pressure was supplied to the tip vane actuators through the same hydraulic tubing which supplied the outboard ailerons. This was done to limit the tubing runs along the wing rear spar. Therefore, either the outboard ailerons or the tip vanes could be used at one time.

Additional details of the model components and their design are presented in appendix A.

3.2.2 Hydraulics

Hydraulic power and its control by electronics through the use of servovalves was chosen over mechanical or electrical actuation because of the high ratio of power to installed weight. The wide range of amplitudes and frequencies demanded and the precision of control necessary were achievable only by high resolution hydraulic circuits for the weight allowance available. Further, the high pressure possible in the hydraulic system permitted design of very small and powerful actuators that were aerodynamically acceptable when installed in the model.

One initial uncertainty concerned the size of the supply tubing to the actuators in the wing and the effect on local stiffness of the wing. Stainless steel annealed tubing having 0.022-in. wall thickness and 0.18-in. dia was selected for the fluid supply. This tubing was used because (1) it fit the allowable space, (2) it was easily bent, (3) it could be brazed, (4) its thin wall allowed maximum flow, (5) it had a high burst pressure, and (6) it had good fatigue properties. Some breadboard tests on the tube sizing were performed and the stiffening effect was found to be small. The tubing was oriented for minimum effect on structural stiffness as shown in figure 7.

Two separate supply systems were desired for safe operation of the model. Pumps were external to the model with two supply lines and one return line to a distribution manifold mounted in the model. The hydraulic circuit assured that the stabilizer would be operational despite loss of either supply pump; i.e., one pump supplied the stabilizer exclusively and the second pump supplied the stabilizer, ailerons, and snubber.

An operating pressure of 1000 psi was adequate, although both aileron and stabilizer actuators were designed and checked at 3000 psi. The volume of fluid required was not a problem. The volume of flow required was controlled mostly by the combined leakage rate of all actuators and servovalves and any inadvertent small leak rates in the supply lines. Flowmeter measurement in the single return line showed that less than one-half gallon per minute was being used with all actuators active. Once the model was completely operational, there were no hydraulic leaks in the model systems.

Each of the ailerons was controlled by a single servovalve. Each aileron actuator had a feedback torsion blade supported on one end by a slot in the actuator shaft and on the outboard end by a cantilever beam rigidly attached to the actuator housing; figure 8 illustrates the relationship. The blade was steel 0.01 in. thick and 0.15 in. wide in the working length. At 15° of twist, the blade was stressed to 30,000 psi under the gages.

Since the stabilizer was a primary flight control surface, special redundancy was provided in the hydraulic circuit, figure 9. Three servovalves were manifolded together with a dual supply and a common return to operate concurrently in controlling the single stabilizer actuator. Three linear position transducers, one for each servovalve, moved simultaneously to signal stabilizer position. If one servovalve or position transducer failed, the second valve/position transducer system balanced unwanted signals while the third servo-valve/position transducer system maintained control of the stabilizer. Static failure characteristics of this majority voting system are shown in table 2. This installation is shown in figure 10.

TABLE 2.—STATIC FAILURE CHARACTERISTICS OF THE HORIZONTAL STABILIZER MAJORITY VOTING SERVOACTUATOR SYSTEM

Failure in one branch	Effect on actuator (output) position	Change in system sensitivity (input/output) in a small range about null position	Overall change in system sensitivity (input/output)	
Loss of input signal	None	2/3 Normal	None	
Loss of feedback signal	None	4/3 Normal	None	
Large input signal	Small positive shift of null position	None	None	
Large feedback signal	Small negative shift of null position	None	None	

3.3 MODEL SUSPENSION

The model was suspended in the General Dynamics low speed tunnel by a system of 1/8-in.-dia braided aircraft-type cables, shown in figure 11. The locations of cable pulleys in the model, cable length and orientation, cable angles, and several other support system parameters were determined from a rigid-body stability analysis of the model and support system, adapted from W. H. Reed's work, reference 8.

The tension in the cables was applied to one end of the rear cable by a manually controlled hydraulic jack operating through a 20-lb/in. coiled spring. The support system geometry and a simulated model were set up in the laboratory for preliminary assessment of dynamic characteristics, as discussed in section 4.

Since the cable system allowed model excursions in both lateral and vertical directions, a restraint (snubber) system was devised consisting of three cables attached to the body structure in a "Y" orientation at a forward cg location. The cables were attached through a system of springs and dampers to a hydraulic actuator, which applied spring tension to the model to restrain it or which could be set to restrict the model to a circle of freedom in the test section.

Schematics of the model suspension and snubber system are included in the discussion of test equipment, appendix B.

4.0 LABORATORY TESTING

The laboratory tests conducted prior to the wind tunnel tests were oriented toward (1) component design verification and (2) generation of basic and correlation data for the theoretical analyses. Since the basic test vehicle and most of the actuators existed at the outset of the follow-on contract, a decision was made to use experimental data to support the analysis as often as possible. The instrumentation and electronics used for the laboratory and wind tunnel testing are discussed in appendix C.

4.1 WING BOX VIBRATION TEST

The wing trailing edge of the original experimental model was built of light structure consisting of a plastic film stretched over balsa wood chordwise ribs. Prior to the aileron installation, the complete wing trailing edge was removed. A vibration test of each wing panel, cantilevered from the body centerline, was conducted to provide data with which the analytical wing structural representation was correlated. Vibration modes were obtained with and without nacelles since the analytical modeling of the wing-nacelle support beam structural attachment was particularly difficult and represented an area of sensitivity in the dynamic representation of the flutter mechanics of the model/airplane.

Node line plots comparing analysis and test results, mode frequency, and damping are shown in figures 12 through 15. The vibration test results are summarized in table 3. The only significant difference between left- and right-wing panel frequencies occurred with the nacelles attached. Small changes in mode frequency have been traced to nacelle attachment bolt torque. The modes were excited with an electromagnetic shaker at a single location. The response of a surface-mounted accelerometer was analyzed using an aeroelastic modal analysis system (see app. C) by comparing its output with the exciter coil current. A Kennedy-Pancu plot, reference 9, indicated the modal frequency and damping.

TABLE 3.—COMPARISON OF VIBRATION FREQUENCIES OF THE WING BOX

	Mode	Test				Analysis	
		Right-hand wing		Left-hand wing		Frequency (Hz)	Damping (g)
		Frequency (Hz)	Damping (g)	Frequency (Hz)	Damping (g)		
No nacelles	1	13.04	.0125	12.93	.0117	13.91	0
	2	32.76	.0099	32.18	.0112	34.47	↕
	3	48.28	.0089	48.10	.0102	54.28	↕
	4	81.3	.0127	80.3	.0141	65.91	↕
	5	86.95	.0116	86.2	.0155	92.25	0
Nacelles with rigid attachments	1	9.68	.0097	9.75	.0096	9.68	0
	2	16.60	.0100	16.57	.0106	14.62	↕
	3	21.00	.0090	21.63	.0081	17.00	↕
	4	32.22	.0101	30.90	.0114	33.20	↕
	5	49.8	.0105	50.95	.0101	47.20	↕
	6	57.2	.0122	54.35	.0277	60.62	0

4.2 MODEL SUPPORT FREQUENCY CHECK

The frequencies and rigid-body modes of the model on the cable support were determined in the laboratory with a cable system simulation of the wind tunnel configuration. A model of the inertial properties, shown in figure 16, was instrumented with accelerometers to indicate displacements in the six component directions. All wind tunnel support system geometry was duplicated in the laboratory. Electrical cables and pressurized hydraulic lines completed the simulation.

Rigid mode frequencies and component axes displacements were obtained with an electromagnetic shaker excitation. The variations of frequency with cable tension are shown in figure 17. The results of this test were used in the stability analysis of the rigid-body modes. The displacements in the component directions of each mode are shown in table 4.

TABLE 4.—DISPLACEMENTS OF THE RIGID MODES OF THE INERTIA MODEL

Mode	Frequency (Hz)	Acceleration					
		(In./sec ²)			(Rad/sec ²)		
		Longitudinal	Lateral	Vertical	Pitch	Roll	Yaw
Symmetric	1.22	2.93	0	2.04	.167	0	0
	2.15	-.27	0	5.42	.008	0	0
	9.55	5.71	0	.49	.019	0	0
Antisymmetric	1.04	0	3.43	0	0	.038	-.160
	1.33	0	.38	0	0	.037	-.012
	1.92	0	2.35	0	0	-.019	-.042

4.3 CONTROL SURFACE ACTUATOR BENCH TESTS

Bench testing in the laboratory was used extensively in the early phases of the program to develop the wing and stabilizer servosystems, to define instrumentation requirements, and to establish many of the test procedures used to support wind tunnel testing.

A typical test setup is shown in figure 18. The rotary actuator was block mounted with the aileron inertia simulated by an aluminum weight. The length and diameter of the tubing between the actuator and the servovalve simulated the proposed model installation. These tests were instrumental in minimizing the tubing diameter and finalizing the actuator configuration. Excessive heating occurred if the tubing diameter was too small. The internal leakage in the initial actuator configurations accentuated this problem and modifications were made to reduce the leakage to acceptable limits.

4.3.1 Internal Loop Compensation

The internal loop with position feedback was designed to give each control surface servosystem adequate frequency response, static stiffness, and damping. The design and laboratory tests were oriented to assure gain and phase margins large enough to prevent instability when operated in conjunction with the external loop. An uncompensated

frequency response plot of the stabilizer and actuator, figure 19, indicates the high response of the system before compensation. The response shown in figure 20 has been compensated (or de-rated) for rigid-body and low-frequency flexible mode stability work.

The control surface stiffness level could not be firmly established from analytical data before the first wind tunnel test. Therefore, the internal loop gain was increased and compensation was applied to prevent instability until the control surfaces had an acceptable stiffness based on engineering experience. The internal leakage of the rotary actuators on the wing caused a comparatively soft, but acceptable, system because of the flow gain of the servovalve. The stabilizer linear actuator had essentially zero leakage, and the pressure gain of the servovalve caused a definite change in stiffness with valve displacement. A lower spring constant existed at ± 0.005 in. actuator travel with stabilizer centered at the null position. A constant stiffness existed beyond these limits with 1000 psi pressure on the actuator. These observed stiffness characteristics had no detectable influence on the operation of the control system during wind tunnel testing. The hysteresis was difficult to measure because of the small magnitudes. It was in the range of ± 0.00015 in. of stabilizer actuator travel.

Conducting-film, linear potentiometer feedback transducers were evaluated for use on the stabilizer system. A flexure mount was developed to prevent excessive loading of the wiper by the possible mechanical misalignment of the installation. The linear transducers provided a satisfactory electrical signal and service life.

4.3.2 Actuator Stiffness Calibration

The dynamic stiffness of the stabilizer servosystem was determined with the test setup shown in figure 21. The combined mechanical and hydraulic stiffness of the actuator and compensation circuit was calibrated primarily for analytical simulation of the system. The electrodynamic shaker applied a sinusoidal force to the actuator at a selected frequency. The actuator displacement was monitored with the calibrated feedback signal. The force was monitored with the differential hydraulic pressure transducer connected to each side of the piston and was computed from this differential pressure and the known piston area. An oscillograph provided a signal record. The resulting dynamic stiffness curve was used to develop actuator equations. (See app. D.)

4.3.3 Actuator Frequency Response

The actuator frequency response was determined with the aeroelastic modal analysis system, AMAS, discussed in appendix C. Servosystem transfer functions were produced in polar form with this equipment. These plots were used to optimize each servosystem using standard Nyquist procedures. Electrical feedback compensation was introduced as required to modify the frequency response and static stiffness of the original servosystem configurations. This procedure made possible the location of the servovalves some distance from the actuators and the optimization of the servosystem response to meet test requirements. The frequency responses for the final servosystem configurations used to support wind tunnel testing are included in the development of actuator equations in appendix D.

4.4 COMPLETE MODEL VIBRATION TESTS

Two vibration tests of the completed control systems model were conducted. One test was conducted to determine, essentially, the free-free mode frequencies of the model in order to provide a correlation with the free-free mode calculations of the theoretical analysis. The free-free condition was simulated in the laboratory by a single elastic support located at the model cg which produced a very low frequency in vertical translation of approximately 0.5 Hz. The procedure was similar to that of the wing box vibration test except that symmetrically located electrodynamic shakers were employed in phase to shake the symmetric modes; out-of-phase excitation was used to define the antisymmetric modes. The data from this test are discussed in conjunction with vibration analysis in section 5.

Another still-air test of the full-span model was conducted in the wind tunnel test section. This test was similar to the "free-free" test except that the cable support system was used to provide the rigid-body boundary conditions. Excitation of the model was accomplished by a random noise input to electromagnetic shakers. The random response of the model was analyzed by a Fourier analyzer to determine frequencies, damping, and mode shapes. The latter were obtained by analyzing the response of each accelerometer on the wing surface.

4.5 PREFLIGHT PREPARATION

The preparation of the model electronics for test occupied approximately 3 days. The complete circuits of the two data systems and one servosensor system were checked from sensor to recorder including phasing, balancing, and setting of amplifier gain levels. Because of the multiplicity of the required data channels, they were grouped by type of testing to be performed so that only a relatively small number of data groups were recorded at any one time.

A similar functional electronic check was made of the servosystem consisting of the sensors, inner and outer feedback loops, the amplifiers, compensation networks, the servocontrollers, signal generators, the servovalves, and finally, the control surfaces themselves. A thorough calibration of each control system was performed to verify that the inner-loop compensation was identical to that obtained in the laboratory.

The hydraulic system also required a thorough preflight check. Prior to connecting the hydraulic supply to the model, the fluid was pumped through line filters for several hours. The filter elements were then changed prior to connection to the model. The model system was bled to eliminate trapped air in the lines. Opening of the system during the test was avoided, but in the event that it was necessary, the lines were re-bled. The rationale was that the valve and actuator passages were so small that any foreign material or entrapped air could cause a serious malfunction.

Prior to each day of testing, each data channel to be recorded was given a functional check. The performance of each active control system was checked at several frequencies. A systematic check procedure held the preflight checks and the troubleshooting to approximately 3 hours per day.

As in any active control system, the gain of the outer loop affects the gain (and stability) of the inner loop. Before operation of any servocontrol system combination in the closed-loop mode, the maximum system gain was determined by the following procedure with the tunnel off. The servosystem was excited with a square wave input while the outer-loop gain limit was increased. Maximum gain was achieved when the square wave shape, as viewed on an oscilloscope, indicated low damping in the control surface loop. The outer gain setting was recorded as an upper limit for use during flight.

5.0 BASIC ANALYSES

The analyses performed for the automatic flight control system and the flutter stability augmentation system development used the same data base whenever possible. The model structural and vibration analyses and the open-loop flutter analysis were identical. This section describes those analytical results. However, some specific analytical segments applied to either the AFCS or to the FSAS analysis exclusively. To avoid confusion, those analyses results are described separately in their respective sections.

Except for the structural analysis which required long flow times and for which only limited experimental data were available, all segments of the analysis were revised as more test data became available. The net effect was that a higher level of confidence was achieved in both the test and the analytical results.

Analytical requirements and other details pertaining to the method of analysis are treated in appendix D.

5.1 STRUCTURAL ANALYSIS

Structural analysis work was time consuming because large volumes of data had to be prepared and checked in the finite element structural analysis. Fortunately, large sections of the 1129D model were not altered and the original drawings were available to start on the creation of a mathematical model of the structure. The model structure was divided into fourteen substructures, figure 22, to take advantage of the economics of smaller problem size and to ease data handling. Substructuring permitted the starting of an analysis of those model sections that had been completed while other parts were being designed and built. The assumption of symmetry about the body centerline necessitated only one-half of the model to be analyzed. The application of appropriate boundary conditions enabled either symmetric or antisymmetric problems to be analyzed.

A typical model wing cross section and its idealization are illustrated in figure 23. Throughout the analysis, the hetrafoam filler in the skin sandwich was neglected as a structural material. Skins were idealized as orthotropic membrane plates. Beam spar caps were represented by truss (axial force) members. Beam shear webs were treated as quadrilateral membrane plates.

A model feature that was carefully simulated in the structural analysis was the horizontal stabilizer/elevator gearing. The geometry of the linkage that attached the elevator to the stabilizer and the body was retained to maintain the 1.91 to 1.0 elevator-stabilizer gearing ratio. The stiffness of the linkage was determined from the cross sectional area. Both geometry and stiffness were unchanged throughout the analysis.

Free-free stiffness matrices were generated for each substructure. These substructures were then merged into a complete structure representing either the symmetric or the antisymmetric case by the appropriate application of boundary conditions. Finally, the cable support stiffness was merged with the model stiffness matrix to represent the cable restrained system. The symmetric structural mathematical model was represented by 174 degrees of freedom and the antisymmetric by 214 degrees.

The quality of a structural analysis can be evaluated in two ways: (1) comparison of analytical and experimental influence coefficients and (2) vibration analysis results. The dependence of the first method on the availability of experimental data often precludes its use, but for the 1129D model, a limited amount of measured influence coefficient data was available. During the SST program, the original 1129D wing had been stiffness-calibrated. A half wing panel had been cantilevered at the centerline and subjected to repeated loading to measure deflections at a number of points. These data were used to check the quality of the wing box structural analysis. For the comparison, fixed boundary conditions were applied to the degrees of freedom representing the body centerline, and the resulting wing box stiffness matrix inverted to obtain a flexibility matrix. For loads applied at selected points, the deflection shape of the wing box at various chords was calculated and compared with experimental results.

Figures 24 through 29 show the comparison of load/deflection curves for loads applied on the front and rear spars. The comparison is good, especially inboard. One factor to be considered is that the experimental data apply to a total wing complete with trailing edge structure, whereas the analysis represents strictly the wing box. This difference was not as severe as it might have been since the original model trailing edge aft of the rear spar was essentially nonstructural, acting only as a support for aerodynamic fairing. The model had been built and tested before the SST trailing edge structure had been defined. Recognizing these dissimilarities, the wing box mathematical simulation was accepted.

No other experimental static deflection data were available for evaluation of the other segments of the structural analysis (body, trailing edge, empennage, etc.). The substructures were merged with the wing box and checked by the second method, the vibration analysis.

5.2 VIBRATION ANALYSIS

The basic components of the model vibration analysis were a stiffness matrix and a mass matrix. The matrices were combined to form a dynamic matrix that was rooted for natural frequencies (eigenvalues). Mode shapes (eigenvectors) were also calculated.

Basic mass data were generated by weighing and/or calculating the weight of the large number of components that were used to construct the model. This information, as reported in reference 10, was used to calculate the mass matrix used in the vibration analysis. The panel weights were redistributed to the location of the structural degrees of freedom. The model overall static balance was carefully maintained (total weight and cg were held constant). Concentrated masses such as the actuators and gyros were lumped at single points or at a minimum number of locations on the load path. Nacelle mass properties were treated to maintain total weight, static balance, and pitch inertia of the components moving with the nacelle support beam. Allowance was made for the weight of those components in the cable support and umbilicals which were assumed to move with the model, but pitch inertia was not maintained. The mass at the ballast tank location was varied to represent the model with a cg range from 48% to 60.6% of the root reference chord, C_R .

The calculation of natural modes and frequencies assumed zero damping. Fifty modes were calculated for both symmetric and antisymmetric boundary conditions. Eigenvectors or mode shapes were normalized to the greatest deflection, and the computer output was plotted automatically in any desired perspective view. Node lines were obtained by interpretation of the mode shape plots.

Vibration analyses were compared with experimental results obtained with the model supported by a bungee cable. When agreement was judged satisfactory, based on agreement of node lines (mode shapes) and within 10% on natural frequency, the vibration analyses were repeated for the model restrained by the cable system. Experience had shown the above criteria to be sufficient to obtain reasonable analysis/test correlation on flutter speed.

Correlation of analytical and experimental modes and frequencies of vibration for the model on cables are shown in figures 30 through 50. Selected symmetric modes are compared in figures 30 through 40; antisymmetric modes in figures 41 through 50. Table 5 compares experimental and analytical frequencies. The matching is governed by similar mode shapes. Some analytical modes were not measured experimentally.

5.3 RESIDUAL FLEXIBILITY

During the SST program it became apparent that truncation of elastic modes had significant effect on SST frequency response (ref. 11). Truncation neglects the "residual flexibility" of modes of vibration greater than some given frequency on the assumption that the truncated elastic modes do not contribute significantly to the flutter characteristics of the configuration. Corrections for residual flexibility have become accepted as an essential requirement for those dynamic analyses dealing with handling qualities, stability and control, stability augmentation systems, and dynamic loads for flexible aircraft.

Residual flexibility effects were considered to a limited extent in the subject analyses. The basic flutter equations were modified to isolate control surface motion. It was assumed that the actuator equation provided the total structural hinge moment for a control surface deflection; therefore, the stiffness matrix was altered to reflect this assumption. Specific details are included in appendix D.

5.4 UNSTEADY AERODYNAMICS

The reduced-frequency-dependent unsteady aerodynamics chosen for this analysis were based on a kernel function formulation. A computer program, reference 6, was used to calculate three-dimensional compressible generalized airforces for the wing planform with partial span trailing edge control surfaces and for the horizontal tail/elevator as a planform with a full span trailing edge control surface. For the antisymmetric case, unsteady aerodynamics were also calculated for the vertical tail. To take into account the lack of a mirror image surface for the vertical tail, unsymmetric generalized airforces were calculated. By adding unsteady aerodynamics for both the symmetric and the antisymmetric cases, and multiplying the result by 0.5, the aerodynamics representing a surface on only one side of a centerline was obtained. All aerodynamic forces were calculated at $M = 0.2$.

The aerodynamic grids for the surfaces are shown in figure 51. These grids, based on geometric spanwise and streamwise collocation point distributions, resulted in 54 downwash

TABLE 5.—COMPARISON OF VIBRATION MODES

Mode	Test		Analysis		Test		Analysis	
	Frequency (Hz)	Damping c/c _c						
Antisymmetric 48% CR								
1			0	0			0	0
2			0	0			0	0
3			0	0			0	0
4	5.42	—	5.15	.004	6.02	.004	6.04	.004
5	10.39	—	9.04	.005	9.12	.005	9.51	.005
6	14.18	—	12.45	—	—	—	12.45	—
7	14.80	.013	14.38	.008	14.95	.008	14.39	.008
8	—	—	16.06	—	—	—	16.51	—
9	18.59	—	17.07	—	—	—	17.11	—
10	19.70	.009	19.35	.007	21.52	.007	19.36	.007
Symmetric 48% CR								
1	.64	.208	.712	0			.903	0
2	2.04	.100	1.98	0			1.98	0
3	5.39	.014	4.66	0	5.75	.004	5.38	.004
4	8.29	.081	8.29	0	8.51	.010	8.56	.010
5	12.12	.012	12.30	0	12.70	.007	12.47	.007
6	16.34	.009	15.08	0	16.67	.005	15.32	.005
7	—	—	18.03	0	—	—	18.34	—
8	20.55	.012	19.58	0	21.92	.006	19.58	.006
9	21.20	.010	22.99	0	—	—	23.56	—
10	24.20	.010	23.93	0	—	—	23.95	—
11	25.95	.014	25.16	0	25.40	.008	25.18	.008
Symmetric 58% CR								

points for the wing, 54 downwash points for the horizontal tail/elevator, and 42 downwash points for the vertical tail.

Since the structural analysis grid was not identical to the aerodynamic grid, a computer program was used to obtain interpolated deflections and slopes at the aerodynamic collocation points. The interpolation was based on the assumption of a plate-type surface for which plate deflection and slope equations were solved.

5.5 SENSORS

Once the symmetric modes of vibration had been calculated for the configurations with cg at 48%, 54%, and 58% C_R , the location of body-mounted sensors could be established. The specific parameters of interest were the displacement and slope at any location on the body for all the vibration modes of interest. A computer program was used which converted the displacement at the limited number of body locations available from the vibration analysis to displacement and slope at any position on the body. This information was presented in both tabular and graphic form. Figure 52 shows a typical program output plot. Inspection of the plots facilitated the choice at candidate locations.

5.6 MODEL STABILITY

One segment of the analysis which was relatively independent from other analytical work was the determination of the stability of the model as a rigid body on a flexible cable system in a steady state airflow. Except for total model weight and inertia, the location of the pulleys, and the cable suspension geometry, all data were available at the program start. Aerodynamic coefficients were obtained by adjustment of SST airplane data to reflect different cg configurations. Other data became available upon completion of the inertia model and its test.

The stability of the model as a rigid body on a flexible cable system in a steady state air flow was investigated as a function of cg location, cable tension, and airspeed. Figure 53 shows the effect of airspeed and cable tension for a symmetric 51% C_R configuration. As shown, the pitch mode becomes more stable with airspeed as well as with increased cable tension. All other modes remain stable. The antisymmetric stability for the configuration is shown in figure 54; all modes are stable. For the aft cg configuration (58% C_R), the same conclusions were reached, based on figure 55, which shows the results for the symmetric case.

When the results of this investigation did not agree with previous experience, this segment of the analysis was stored and another approach was tried. The second step in the model stability analysis was to consider a flexible model on a flexible cable system subjected to unsteady aerodynamic forces. The mathematical model had to await the completion of both the 1129D model as well as the structural analysis. The cable system was also modeled by finite elements guided by the stiffness values calculated with the previously referred to rigid-body/cable stability analysis, the inertia model test, and vibration data obtained in the tunnel.

The model stiffness and cable stiffness matrices were merged and used as input to a still-air vibration analysis. The results were compared with the cable mode frequencies measured on the inertia model in the laboratory. Tuning the cable support system stiffness to improve agreement with test frequencies followed. After restraining the model in the fore/aft mode, the symmetric boundary condition modes for the 48% C_R cg containing the vertical translation and pitch cable modes were used to generate reduced-frequency-dependent unsteady aerodynamics. The low frequency stability for airspeeds from 100 to 160 kn was then investigated using a computer program which is described in the discussion of flutter analysis. Other cg configurations (58% and 60.6% C_R) were studied with the same procedure.

The results of the analysis, which considered the flexible model on the flexible cable system subjected to unsteady aerodynamic forces, are shown in figure 56. The effect of cg location and airspeed can be evaluated. Consistent with expectation, the stability of the model varies inversely with cg location and increases with increased velocity. The frequency and the mode component vector for this coupled mode clearly showed it to be a vertical translation (plunge) mode. The pitch mode at a lower frequency was critically damped for all cg configurations and airspeeds that were analyzed.

5.7 FLUTTER ANALYSIS

The flutter analyses performed for the open loop AFCS and FSAS systems were identical to the previously described model stability analysis except for the emphasis on the frequency range. The model rigid-body stability system was designed to control the cable modes (1 Hz for pitch and 2 Hz for vertical translation) and the lowest flexible body bending frequency mode (5 Hz). The expected wing flutter mode occurred at about 16 Hz.

For the symmetric case, the flutter analysis included equations 1 through 29 as listed in appendix D. That is, 20 flexible modes and the complete control system (horizontal stabilizer/elevator, inboard, and outboard ailerons) were included with closed inner loop but open outer (feedback) loops. The equations were solved for increased velocity up to the critical flutter speed. To assure that the model would not encounter an unexpected flutter mode, the antisymmetric flutter boundary was also investigated.

The flutter analyses indicated the maximum speed to which the model could be flown with the open-loop configurations. Figure 57 shows the flutter boundary for the symmetric case represented by the 48% and 58% C_R configurations. The antisymmetric case flutter boundary for the 48% C_R configuration is shown in figure 58. Both flutter modes are the result of wing bending-wing torsion-nacelle coupling but contain components of up to six still air modes. The effect of cg configuration was very small; the flutter speed for the 48% C_R configuration was found to be 142 kn; for the 58% C_R configuration, it was 143 kn.

6.0 FLUTTER STABILITY AUGMENTATION SYSTEM STUDIES

Flutter stability augmentation system (FSAS) development represented the major part of the subject task. This section discusses the analyses performed, the wind tunnel test procedures used, and the analytical/experimental correlation of the results obtained.

6.1 FSAS ANALYSIS

To preclude a model rigid-body stability problem, the flutter stability augmentation design was performed with the forward cg configuration (48% C_R). The still air vibration modes were calculated for this configuration with the model suspended on the cable support system. Twenty flexible modes were used in the control system design. These modes, equations 1 through 20 in appendix D, represented the model with ailerons and the stabilizer/elevator for the symmetric boundary case. Also included in the analysis were equations 21 through 33 which represented the control circuit loops of the inboard and outboard ailerons as well as the stabilizer/elevator.

Inner loop gains were determined during laboratory testing, section 4.3.1, and held constant for all subsequent analyses. The outer open-loop response at five locations on the wing was used to determine the most promising location(s) of the feedback loop sensors. Following a decision to initially concentrate on single sensor/single control surface, the model response to acceleration feedback control of the inboard aileron was investigated for increasing levels of feedback gain at constant airspeed (150 kn), figure 59, using a compensation network similar to that developed during wind tunnel testing; see section 6.2 and appendix D. The effect of gain and increasing airspeed was then investigated as shown in figure 60. As expected, too high a gain level leads to instability as does increasing velocity. The same procedure was followed for the outboard aileron controlled by feedback from the same sensors as used for the inboard aileron, figure 61.

The sensitivity of the FSAS design to phase shift is shown in figures 62 and 63, which apply to the inboard and outboard aileron control systems, respectively. At constant speed, both systems exhibit nearly classical results, typical of a narrow band system. The figures also show the potential of the two control surfaces for frequency alteration in the 15-Hz mode. An analysis of these effects is essential for a mode-separation type of suppression system.

The facility to "freeze" the problem at a specific moment is especially useful in the investigation of the mechanism responsible for system behavior. This technique was used to evaluate the flutter stability augmentation system analysis. By calculating the eigenvectors for the reduced frequency and velocity at flutter, it was possible to display the shape of the wing at any point in the flutter cycle.

The unaugmented flutter mode is illustrated in figure 64. Shown are the real and imaginary parts of the flutter cycle at 140 kn. While the inner control loop was active, the outer feedback loop was open so that the control surfaces were constrained by their static stiffness effects only. Consequently, these surfaces moved along with the rest of the wing.

The effect of an active inboard aileron system is shown in figure 65. Comparison of the real parts in figures 64 and 65 shows the change in phasing due to the active control system. The equivalent plots of the imaginary part show that the wing torsion node line has been shifted further aft, especially near the wing tip. The result is an increase in the flutter speed to 150 kn.

Figure 66 applies to the closed-loop outboard aileron flutter suppression system. Comparison with figure 64 clearly shows the influence of this system on the flutter mode. Although the flutter speed also has been raised to 150 kn, the larger displacements required of the outboard aileron as compared to the inboard aileron are graphically illustrated.

6.2 FSAS WIND TUNNEL TEST PROCEDURES AND RESULTS

The first task undertaken in FSAS testing was to determine the flutter speed. This was done by increasing tunnel speed until the model exhibited oscillations of increasing amplitude. Flutter oscillations of the model were quickly dissipated in the General Dynamics low speed tunnel through the use of a q-reducer (app. B).

The critical flutter mode of the model modified for hydraulic control systems exhibited the same displacement characteristics as the original model. Minor stiffening of the wing near the rear spar was inevitable because of the stainless steel tubing that was laid along the spar for actuator fluid supply. The in-flight mode was a coupled mode of two wing-nacelle modes and the fundamental wing mode. The displacement in this mode was characterized by relatively large pitch oscillations of the outboard nacelle and vertical translation of the wing in the general area of the nacelle support beam attachment to the wing. The frequency at flutter of the unstable mode was increased from 15.4 Hz to 15.7 Hz after modification. The tunnel speed at flutter was increased from 127 kn to 136 kn. The presence of the closed inner control system loops, section 4.3.1, may have contributed to the difference in flutter speed.

The next step in the program was to determine the frequency response of the model. The response of each accelerometer and strain gage to oscillation of each control surface used in a feedback loop was determined at each flexible mode resonance. Both the phasing and magnitude of response of each transducer in a given mode were likely to be different for each control surface because of the difference in aerodynamic force patterns generated on the lifting surface. The data were taken at a speed close to the flutter speed so that the mode shape closely resembled that at onset of flutter. The difference in recorded critical mode shapes on the wing by inboard and outboard aileron excitation is shown in figure 67. The data were reduced on the AMAS analyzer (app. C) by referencing each sensor signal to the aileron input signal and resolving the response ratio into real and imaginary components. Modal damping and the phase relationship of that transducer-control surface combination were determined in the process. The response amplitude and phase of all model transducers were determined off-line by recording all responses and control surface input signals on magnetic tape and reducing the data through AMAS on a nonoperating shift.

At this point the theoretical analysis was referenced to determine the degree of complication required to achieve a successful suppression system. Prudence dictated initially using a single sensor, single control surface per side system. Analysis showed that the

inboard aileron was more effective than the outboard. Either accelerometers or strain gages could have been used for feedback in the closed loop. The desirability of maintaining a link with the theoretical analysis dictated the use of accelerometers, since the analytical variables are in orders of displacement. To produce an analytical strain distribution on a model wing surface in a given mode would have been very difficult; however, strain gages yielded a cleaner signal in the frequencies of interest. Details are covered in appendix E under sensing.

A simple active system including the inboard aileron and a single strain gage per side, locations 33 and 45 in figure 68, was selected. The wing strain response at the above gage locations was large because of the influence of the outboard nacelle. The symmetry of the mode was unimportant since each wing panel had its own sensing and suppression control system; however, as the analysis indicated, the mode was symmetric. Strain gage response in the principal flexible modes to sinusoidal excitations of the inboard and outboard ailerons is shown in table 6.

An open-loop transfer function of the inboard aileron/strain gage system was obtained with a random noise input from the HP5451 Fourier analyzer and shown in figure 69. From these data a manual Nyquist plot was made to determine the compensation necessary. A single pole filter, as shown in figure 70, was inserted into the feedback circuit of either wing panel. The spectrum was re-plotted with the compensation loop added. Figure 71 indicates that the single critical mode is properly compensated to achieve maximum damping in that mode.

Optimization of the closed-loop system was conducted at a speed just below the critical flutter speed in order to minimize the phase and gain variation as the test speed was increased to the supercritical speed range. The technique at supercritical speeds was the same as that followed subcritically. One of the active inboard ailerons was driven at discrete frequencies by an oscillator signal in the flexible modes of interest. The response of the model, as indicated by the feedback transducer, was monitored for phase and amplitude ratio. If the phase compensation remained satisfactory at a supercritical speed, the feedback gain was sometimes optimized by observing the response of the feedback transducer on a strip chart recorder to a control surface pulse or to tunnel turbulence at each successive gain setting. The damping read from the chart indicated whether the gain had been optimized at that speed. The augmented flutter speed was finally reached when neither increase nor decrease in gain could be implemented without sustained flutter oscillations.

The loop was closed at 130 KTAS with only the phase correction filter in the feedback loop. The necessity of a high-pass filter was quickly recognized when the closed-loop system responded to small changes in static wing loading (maneuvering). A filter was selected such that the phase shift in the 16-Hz mode was minimal. As the feedback gain was increased, fast sine sweeps were made on the active ailerons, one at a time, to determine the phase and response amplitude ratio in the flexible modes that could be excited by the inboard ailerons. Figure 72 shows plots of the spectrum at feedback gain settings of 0, 250, and 450. The significant characteristic is the mode at 10.4 Hz. Referring to the open-loop plot, figure 71, the response in that mode is very low and the damping is high. However, the phase orientation is adverse, indicating a potential instability caused by the closed loop. When the closed-loop feedback gain reached 450, the damping had dropped to approximately the still-air value, indicating that the aerodynamic damping had vanished.

TABLE 6.-STRAIN GAGE RESPONSE TO INBOARD AILERON EXCITATION

Forcing frequency, Hz Strain gage No.	10.2		15.8		22.5		40.3	
	Amplitude	Phase	Amplitude	Phase	Amplitude	Phase	Amplitude	Phase
25	.827	96.6	6.325	-90.0	.377	-19.2	2.550	-150.3
26	.269	45.0	1.789	-45.0	.113	-18.6	0.982	-165.1
27	.583	77.5	5.831	-77.5	.287	7.2	1.087	-125.5
28	.202	128.6	4.604	-105.9	.213	0.0	1.976	-140.2
29	1.360	90.0	11.401	-86.8	.780	-24.2	1.147	65.6
30	.126	90.0	8.130	-103.5	.225	18.4	1.620	-128.7
31	.032	0.0	0.000	0.0	1.389	140.2	.443	90.0
32	.926	-82.2	7.752	78.2	0.000	0.0	.597	32.0
33	4.785	-82.4	19.350	78.7	1.036	149.1	2.851	-109.4

Data taken at 130 KTAS
Strain gage response referenced to aileron servo input signal

TABLE 6.-STRAIN GAGE RESPONSE TO OUTBOARD AILERON EXCITATION (CONCLUDED)

Forcing frequency, Hz Strain gage No.	10.3		2.7		15.7		22.5		40.5		53.4	
	Amplitude	Phase	Amplitude	Phase	Amplitude	Phase	Amplitude	Phase	Amplitude	Phase	Amplitude	Phase
25	1.642	51.9	2.220	35.8	12.668	-86.9	1.321	-106.7	7.286	-133.3	3.048	-142.5
26	.225	90.0	.361	56.3	3.420	-56.3	.318	-95.8	2.720	-126.0	3.029	-158.2
27	1.158	61.0	1.628	47.5	10.743	-42.6	.340	-68.3	3.302	-125.1	1.794	138.8
28	1.462	22.6	3.202	14.5	12.490	-70.8	.811	-110.6	4.880	-135.8	1.336	-157.8
29	2.591	62.9	3.493	66.4	24.698	-50.2	1.727	-81.6	3.280	37.6	1.642	-52.0
30	1.108	24.0	4.243	45.0	17.029	-68.2	.553	-103.2	4.061	-142.0	1.463	87.8
31	.982	13.2	2.088	16.7	3.963	-118.6	1.581	-126.9	1.077	21.8	1.001	-51.8
32	1.489	-79.1	2.452	-78.2	16.322	125.5	.202	51.4	2.385	33.0	2.402	-57.4
33	8.347	-104.0	11.444	-95.0	77.003	132.3	4.817	93.8	12.468	174.0	8.501	117.6

Data taken at 130 KTAS
Strain gage response referenced to aileron servo input signal

The proximity of the 10-Hz mode to the 15-Hz mode plus the orientation of the 15-Hz mode open loop prevented addition of a simple roll-off filter to reorient the 10-Hz mode to a more favorable position. A notch filter shown in figure 73 was designed and inserted into the system. The 15-Hz mode was recompensated for the phase angle introduced by the notch filter. The combined compensation, including the inboard aileron transfer function, is shown in figure 74.

The remainder of the aileron closed-loop testing was conducted using the technique of discrete frequency excitation; the response analysis was made on the AMAS equipment. A summary of the inboard aileron closed-loop data is presented in figures 75 and 76. The modal damping data are presented at constant feedback gain and at constant airspeed. The data available at supercritical speeds are obviously rather sparse, because under optimum conditions of moderate modal damping, the analysis of the many modes in an active control system is very time consuming. When the damping is low, the scatter in the data requires several times longer to obtain comparable data quality. The data shown at constant gain setting of 250 indicate a near-constant increment of damping above the unaugmented values. This result might be expected since at constant amplitude (gain), the aileron represented a constant damping force. The data also indicated that a gain of 250 was less than the optimum gain at all of the speeds below the maximum speed shown (perhaps including that speed also) since the damping does not show a decline. However, the amplitude of aileron oscillation was approaching practical limits.

The outboard aileron closed-loop systems were synthesized in the same manner as the inboard pair with the same strain gages for feedback. However, the force excitation from the outboard aileron was more generally applied to the modal spectrum. The flexible modes were excited to higher amplitudes and more of the higher frequency modes were included. The open-loop modal response shown in figure 77 illustrates most of the modes excited by the outboard ailerons with the single strain gage feedback. As indicated, considerable phase compensation was necessary for the 15-Hz mode. However, before the loop was closed, a 12.8-Hz notch filter, shown in figure 78, was installed in each aileron loop, allowing the 15-Hz mode to be compensated by a single pole, high-pass filter. As seen in figure 78, the attenuation of the 15-Hz mode was compromised somewhat by the notch filter. The mode spectrum at 130 kn, plotted from AMAS equipment, is shown in figure 79. The response at 60% of the maximum feedback gain shows a 54-Hz mode oriented at a phase angle where it would be forced by the system. A notch filter was subsequently installed in the feedback system to bypass this mode also.

The data in figure 80 summarize the results of the outboard aileron closed loop. The inboard aileron data are shown for comparison. The difference between the left- and right-wing panel possibly reflects a difference in the flow characteristics across the tunnel test section. The flutter speed of the outboard aileron system was increased from 135.9 kn to 140.3 KTAS.

An active control system consisting of a single strain gage sensor and two ailerons per wing panel was synthesized by holding the closed-loop inboard aileron system feedback constant and optimizing the outboard aileron. Open-loop response of the model to a discrete frequency oscillation of the outboard aileron was obtained, one side at a time, with the inboard aileron loop closed and fixed. However, for this system, the open-loop response

was obtained at a speed in excess of the unaugmented flutter speed. The phase compensation for the outboard ailerons was centered at a slightly different frequency from the inboard aileron systems in an attempt to limit the phase shift of the critical mode response. The gain of the outboard aileron system was optimized as in the inboard single surface system. This system increased flutter speed by 11%.

The horizontal stabilizer with a feedback signal from a servoaccelerometer located in the aft body at 86% of body length was used to further stabilize a potentially unstable mode of predominately fundamental body mode displacement at approximately 4.75 Hz. Checkout of the stabilizer closed-loop system was performed subcritically at 130 kn since the wing flutter speed was 135.9 kn. The damping in the mode was increased by a factor of 8. Damping in the short period mode was slightly degraded, but it remained well-damped.

The polar plot of the compensated open-loop response of the model in the body mode suppression configuration is shown in figure 81. Phase compensation consisted of a single pole filter described by the transfer function:

$$\frac{s}{s + 55.92}$$

The Nyquist plot of the 3-5-Hz body mode and the short period (pitch) mode is shown in figure 82.

6.3 FSAS ANALYTICAL-EXPERIMENTAL CORRELATION

The inboard and outboard aileron control systems were successfully used to increase the flutter speed. Test and analysis results for the inboard aileron system correlated well, as shown in figure 83. The outboard aileron system test and analysis results, figure 84, did not agree. Possible reasons for these discrepancies include: (1) the analytical results were valid strictly for acceleration feedback while the model test data were taken with strain gage feedback as strain gages gave a cleaner signal and (2) the analytical description of the model, model support, unsteady aerodynamics, control system, and compensation networks assumed linear theory to be valid. Further analytical and testing effort is necessary to isolate the cause. No comparison of analysis and test data for the combined inboard and outboard configuration was made because of the poor agreement of the outboard system alone.

7.0 AUTOMATIC FLIGHT CONTROL SYSTEM STUDIES

The automatic flight control system (AFCS) was designed to stabilize the model for statically unstable cg conditions. The system used a hydraulically powered horizontal stabilizer with a geared elevator. Instabilities were sensed using miniature gyros and servoaccelerometers mounted in the body of the model. Compensation in the feedback network was provided by an analog system.

7.1 AFCS ANALYSIS

The AFCS analysis was performed entirely in the frequency domain using the equations developed in appendix D. The advantages of this type of analysis were considered to outweigh the difficulty of predicting power requirements. In fact, the horizontal stabilizer/elevator was 20% larger than scaled size in comparison to the rest of the model, and the actuator driving the surface had ample power reserve.

The initial AFCS analysis used a stiffness matrix representing the SST 2707-300 airplane. The stiffness matrix was altered to include the model support system based on the model rigid-body stability analysis and the inertia model test data. Care was taken to assure a pitch instability in the 58% C_R configuration, as previous testing experience indicated that such an instability existed.

The next phase of the analysis involved the generation of suitable control system loops to investigate what sensor location and type was effective for the AFCS. For the 58% C_R configuration, the effect of using pitch, pitch rate, acceleration and velocity sensors alone and in combination, with and without compensation, was investigated. The location of the pitch and pitch rate sensor was held constant at station 127.5 (corresponding to the location of the gyros in the model), but velocity and acceleration sensors were tried at a number of body locations. All studies were for 130 kn ($M = 0.2$).

The most promising systems were then checked for two other cg configurations (48% and 54% C_R) and at two other tunnel speeds ($M = 0.10, 0.25$). These results yielded a variety of potential solutions to the AFCS problem which could be applied in the experimental work. Results presented in figures 85 through 89 show the ability of the AFCS to affect the pitch (0.5 Hz), plunge (1 Hz), and first body bending (4-Hz) modes of the model. The effect of using pitch feedback, figure 85, was to stabilize the pitch mode while destabilizing the plunge mode. Figure 86 indicates that a pitch rate signal would stabilize the pitch mode at the cost of driving the first body bending mode unstable. Acceleration feedback, figure 87, was shown to be of little value. The effect of velocity feedback on the pitch and plunge modes was similar to pitch feedback, as shown in figure 88. Pitch and velocity signals were combined to improve damping in the pitch mode without altering damping of the plunge mode, figure 89. The effects of changing Mach number or velocity at sea level are shown in figure 90 for a combined pitch and velocity feedback system. Increasing Mach number was stabilizing on pitch and plunge modes and destabilizing on the first body bending mode.

Upon completion of the initial analysis, the emphasis of the analysis was shifted to the FSAS design. The result was that AFCS data were extracted from the FSAS results as required. Because the analysis showed the pitch and vertical translation modes to be stable for the configuration investigated, the AFCS analysis was deemphasized and the decision was made to rely on experimental results. Only where analytical trends appeared to match tunnel experience were the results consulted and used as a guide to potential physical solutions.

7.2 AFCS WIND TUNNEL TEST PROCEDURES AND RESULTS

The experimental development of the AFCS was different from the flutter suppression development since maximum speed attainment was not necessarily the ultimate goal. Analysis indicated that the pitch mode and the plunge mode were least stable at low speed, while initial testing indicated that the plunge mode was less stable at high speeds. The test speed of the model was limited to a range of speeds between 80 KTAS (minimum flight speed) and 135 KTAS (approaching flutter). Two test speeds were selected to evaluate the rigid-body stability characteristics: 100 kn and 130 kn.

Early in the test program, the feasibility of using the horizontal stabilizer with feedback from the pitch rate gyros or servoaccelerometers was investigated. The open-loop responses of the model to excitation by the horizontal stabilizer with a random noise signal from the HP5451 Fourier analyzer was obtained for the pitch rate gyros and servoaccelerometers. The data shown in figures 91 and 92 were obtained from tests of a configuration with the cg at 48% C_R at 100 KTAS and 130 KTAS. The data were available at the test site in Bode plot and Nyquist plot form to determine the compensation necessary to optimize the feedback loop for any mode. From these plots and an indication from preliminary analyses that the pitch mode at approximately 0.5 Hz was the critical mode, phase compensation in the pitch mode was determined for each sensor. The resulting compensated open-loop responses were replotted in figures 93 and 94. A review of these plots indicated that at the forward cg (48% C_R), the attitude gyro with the compensation filter indicated in figure 93 offered the better potential for a closed-loop system. The low frequency mode was oriented to provide maximum damping increment. The vector plot in figure 94 indicated that the aft body accelerometer signal loop could be closed without phase compensation to stabilize the pitch mode but that the fundamental body mode at approximately 4.7 Hz would become a problem as the loop gain was increased. Conversely, the pitch rate signal in figure 93 required a large phase (lag) adjustment, allowing a two-pole, low pass filter to roll off all but the pitch mode and a trace of the plunge mode. There was no indication that the plunge mode would be critical within the cg range of interest, 48% to 58% C_R . Compensated feedback plots of the two body-mounted transducers are shown in figures 95 and 96.

A preliminary closed-loop evaluation of the acceleration and pitch rate systems was conducted on a configuration with its cg at 48% C_R . The results using servoaccelerometer feedback indicated that, although the system added damping to the pitch mode, the improvement was very limited because of the negative damping it produced on the fundamental flexible body mode. The pitch rate system appeared to be very effective with only approximate phase compensation. At each gain, system damping was evaluated from a decay record of the modes excited by a stabilizer pulse. The plunge mode was not effectively excited by stabilizer pulse because of the high modal damping.

In the next series of tests on the AFCS a marginally stable configuration was sought; hopefully, one that would be stable at the lower speed and unstable at the higher so that retreat from an unstable condition could be effected by decreasing tunnel speed. This combination would avoid transferring water ballast out of the body tank once the closed-loop system was established and replacing the ballast once optimization was reached. The condition of starting and stopping the tunnel with an unstable model configuration was to be avoided, at least in the early stages of AFCS development. The possibility existed that active control surface effectiveness would be lost before flying speed was lost, or flying speed would be established before control effectiveness.

The wind tunnel synthesis of the rigid-body stability system began by determining the rigid-mode characteristics produced by a change in longitudinal cg. Initially, the stability of the model was determined at 130 kn with the cg at 58% C_R (ballast tank empty). The model was fully restrained on the hydraulic snubber until the tunnel speed reached the 130 kn test condition. When the snubber was released a small amount so that the model was flyable in a small circle of freedom, it immediately diverged in a rigid-body mode, indicating that the cg had exceeded a marginally stable configuration. However, on reviewing the data records it was determined that the frequency of oscillation was not one that could be related to the rigid-body modes of the model (less than 1.8 Hz), but that it was an instability (at 5.7 Hz) created by the snubber. The conclusions reached were: (1) the snubber could not be relied upon to restrain the model with cg at 58% C_R or more, and (2) there was no quick method of determining relative rigid-body stability except to start at forward cg and plot the model responses as measured with the pitch rate gyro, or a similar sensor, as the cg was moved aft.

Open-loop rigid-mode stability of the model was evaluated for various cg conditions at increments of 2% of wing root chord. Two methods were employed: first, frequency and damping were assessed by applying a square wave signal to a control system servo, usually the horizontal stabilizer. The rigid-body modes and the fundamental flexible body mode responded to pulses the periods of which corresponded approximately to their own. Data from a sensor on the body were recorded on a strip chart recorder at the two evaluation speeds (100 kn and 130 kn) at each successive cg.

Also at each test condition a discrete frequency analysis was made of each mode. Voltages at each selected frequency were delivered to a control surface servocontroller. In the case of the stabilizer, the signal was imposed on all three controllers. The response of the potential feedback transducers was referenced to the input signal, analyzed by the AMAS (app. C) equipment, and plotted in real and imaginary components on a polar plot. The first flexible mode was monitored to determine if that mode would interface with a rigid-body mode during closed-loop testing, thereby requiring a compensation filter. One transducer at a time could be plotted on line. All other potential feedback transducer responses were stored on magnetic FM tape where they were available for plotting off-line at any time.

The change in open-loop damping of the two rigid-body modes varied rapidly with cg as shown in figure 97. No data were obtained for the plunge mode at 1.4 Hz at forward cg, but the damping was significantly greater than in the pitch mode as indicated by the model responses to stabilizer pulse at each cg configuration. The open-loop phase relationship between the pitch angle and the stabilizer excitation signal is shown in the upper plot; the

phase indicated that the unintegrated rate signal would provide near-optimum compensation for the closed-loop system. The figure also illustrates the reason for seeking a marginally stable configuration before attempting to synthesize a closed-loop system since the damping and phase characteristics vary with cg. The variation was enough so that the critical mode changed characteristics completely from forward to aft cg.

When a low-damped condition in a rigid-body mode was reached, the phases of the response of the rate gyros and accelerometers were plotted for each mode that could be excited by the force-producing control surface. The servotransducer with the better potential for suppression was selected based on (1) desirable phase and output in the desired mode, (2) lack of response in other modes, and (3) phase orientation in other modes that, upon compensation of the selected mode, did not degrade damping.

The compensation of the critical rigid-body mode, the 1-Hz plunge mode, was designed to provide maximum damping in a single mode. The phase of the feedback signal was rotated to the positive real axis for maximum suppression. Before the compensation filter was installed in the model circuit, a frequency calibration response was performed, similar to that shown in figure 98. The calibration was accomplished with AMAS in the same manner as for the forced model response.

With the outer loop closed, a determination was made of the maximum feedback gain permissible with air off. This exercise was conducted to determine the effects of outer-loop gain on inner-loop (control system) stability. Usually, the static or air-off condition is more critical than the air-on case because of the absence of aerodynamic damping. This criterion is not altogether rigorous, but it does serve the purpose of evaluating the magnitude of full-scale outer-loop gain.

The outer loop was closed prior to the start of the tunnel test, and the attenuator in the feedback circuit was set to 0. No circuits were made or broken anywhere in the feedback loop while the model was flying, nor were amplifiers or relays switched. Small voltage changes caused by changes in electrical power loads were considered to be a potential problem. As testing progressed, the precautions were extended to the elimination of intermittent-contact electronic indicator lights. This decision was made after disturbances in the model were traced to indicator lights on a signal control panel.

With the test speed held constant, the outer-loop gain was increased incrementally. At each outer-loop setting, the model was excited through the inner loop by square waves of varying frequency. The existence of low-damped modes could be observed visually or recorded on a strip chart. At some gain settings a complete complex plane plot of response was generated. Phase angles, amplitude ratios, and damping in each mode were tracked as a function of outer-loop gain at constant speed. When a significant damping increase was achieved with a phase angle of $0 \pm 35^\circ$ and a linear feedback gain of 0.3 to 0.8, the speed of open-loop instability could be approached. Generalized procedural criteria cannot be established because each mode and/or active control surface exhibit different dynamics.

It was concluded that the overscaled, geared stabilizer-elevator exerted a powerful stabilizing influence on the rigid-body modes of the model. The difficulty encountered was the very small stabilizer deflection necessary to maneuver the model symmetrically. This

extreme force sensitivity made the synthesis of a rigid-body, closed-loop system very difficult and also very hazardous.

It became apparent during the testing at 58% C_R that the yaw stability was deteriorating. A ventral fin, which had been designed in anticipation of the yaw problem, was installed on the empennage after yaw instability was encountered at a cg of 60.6% C_R at a lift-off speed of 80 kn.

The open-loop response of the model to the stabilizer excitation is shown in figure 99 for the body-mounted servoaccelerometers and the pitch rate gyros. The model response to the inboard ailerons, operating symmetrically, as measured by the servoaccelerometers is also indicated. The inboard ailerons appeared to provide a desirable solution to the pitch sensitivity problem. The plunge mode damping decrement with speed, indicated in figure 99, allowed initial optimization of the feedback loop of each active system prior to reaching critical or supercritical speeds without the necessity of transferring ballast in flight.

The initial closed-loop optimization was conducted at 100 kn with the phase information obtained during the open-loop testing. The results of the pitch rate/stabilizer closed-loop testing is shown in figure 100 at 100 kn and at 130 kn. The effect of airspeed on the feedback gain is shown by the amplitude ratio data. Although the feedback gain voltage was considerably lower at 130 kn than at 100 kn, the total loop gain was more than double at the higher speed, reflecting the decrease in damping at the higher speed. At the higher gain and 130 kn, the modal damping is significantly higher than at the lower gain, indicating that the optimum gain has not been reached. This effect may be compared with the damping and amplitude ratio at 100 kn where the damping has already begun to decrease at a relatively low amplitude ratio. The phase relationship between model response and the stabilizer excitation signal indicated near-optimum loop compensation at 130 kn.

Although the modal damping at 130 kn was high, the model became uncontrollable when it began to translate randomly about the test section. Apparently, the model was excited by either random turbulence in the tunnel or by minute stabilizer displacements within its hysteresis band. A review of the instrumentation record following tunnel shutdown revealed that the stabilizer motion in the closed plunge mode loop at the highest gain setting at 130 kn was approximately $\pm 0.03^\circ$, indicating the extreme sensitivity of model response.

Plunge mode feedback systems for the 60.6% C_R configuration were also synthesized with servoaccelerometers located at 36% and at 90% of body length. The acceleration signal, in either system, was integrated to achieve the desired phase compensation. The phase, amplitude ratio, and modal damping of the two systems may be compared in figures 101 and 102. The forward body vertical velocity appeared to be the more sensitive with respect to amplitude ratio for a given feedback gain, but the vertical velocity at the aft-body position was more effective in increasing the modal damping. The limit airspeed for the fore-body system was 120 kn; 125 kn for the aft-body system. However, unlike the pitch rate system, the speed limitation for the linear velocity systems was occasioned by deterioration of the plunge mode damping. The relative value of the pitch rate gyro, the integrated pitch rate gyros, and the integrated accelerometers was difficult to predict since the pitch attitude change in the plunge mode was very small. Thus, pitch rate was the better feedback signal for both the pitch mode at forward cg and the plunge mode at aft cg.

The apparent answer to the model pitch sensitivity at 60.6% C_R was found when the inboard ailerons were operated symmetrically in the closed loop. The initial feedback sensor was the forebody accelerometer. In the optimization of the feedback system, the model was excited in the plunge mode with approximately 2° of aileron rotation. Preliminary results shown in figure 103 indicate that the amplitude ratio was still very small.

The test was terminated when the model was damaged as a result of an uncontrolled pitch oscillation. Post-test investigation of the model revealed that an electrical cable separated from one of the three stabilizer inner loop feedback position transducers. The open circuit in the one loop caused a finite offset of the surface, pitching the delicately balanced model violently. With the remaining two stabilizer circuits functioning normally, the stabilizer was repositioned to the trim position but not before the model had assumed an attitude from which recovery was impossible.

8.0 CONCLUDING REMARKS

The goals of this program, listed in section 2.1, were met or exceeded. An active control system, capable of controlling rigid and flexible modes, was developed for a low-speed, full-span SST flutter model. The system used hydraulically powered inboard ailerons, outboard ailerons, and horizontal tail with geared elevator for control. Instabilities were sensed using subminiature gyros, accelerometers, and strain gages. Compensations in the feedback loops were provided by an analog network. The flutter model used was a structurally detailed model of the SST 2707-300 airplane, and thus it was an excellent dynamic simulation of a possible airplane configuration. The active control system proved to be versatile with considerable capability to explore a variety of feedback combinations.

Feedback systems were demonstrated that increased damping of the rigid pitch mode, the rigid plunge mode, the first flexible body mode, and the wing flutter mode. Damping was increased in the rigid pitch mode at forward cg by using the horizontal tail and pitch rate gyros. The rigid plunge mode at aft cg was the only symmetric rigid-body mode to exhibit instability. It was stabilized by the horizontal tail or the inboard ailerons using either the pitch rate gyros or accelerometers for sensing. This control of a rigid mode demonstrated the ability of the system to act as an automatic flight control system (AFCS). The horizontal tail with feedback from accelerometers was used to increase damping in the first flexible body mode by a factor of 8. The flutter stability augmentation system (FSAS) achieved an increase in flutter speed of up to 11.3% through use of the inboard aileron alone and the inboard and outboard ailerons together. Onset of the flutter mode was sensed using a single strain gage on each wing panel.

Near the end of the planned testing, the model was damaged as the result of an electrical system failure. The failure occurred in a redundant voting circuit and would not have caused damage to the model during tests of a statically stable configuration. However, to demonstrate the AFCS, it was necessary to fly the model in an extreme aft cg configuration ($60.6\% C_R$) because of the larger tail. The snubber and model support systems were designed for a configuration with a smaller tail and forward neutral point and were not able to provide adequate restraint when the failure occurred. The result was severe pitching with attendant structural damage.

This program of active controls study pointed out the importance of accuracy in structural and aerodynamic representations of the model. Sensor response is indicative of motion of a point on the model and thus requires a higher order of accuracy than is required to determine flutter speed. During this program, analytical techniques were checked against experimental results at several stages of development. The techniques used were able to accurately determine flutter speed, but sensor response was not always correct. Further refinement of analytical techniques is necessary to accurately define sensor response. Problem areas are discussed in appendix E.

The most important aspect of this program was the development of a tool by which active control technology as applied to airplanes can be assessed. In order to realize the full potential of this tool, the model developed in this program must be repaired. The repaired model will provide a means to evaluate analytical techniques and a test bed for developing

scaled hardware. A variety of feedback systems can be simulated by using the three sets of control surfaces singly or in various combinations with one or more sensors providing the feedback signal. Compared to full-scale airplane testing, the model provides an inexpensive tool for developing active control technology with little risk to hardware or personnel.

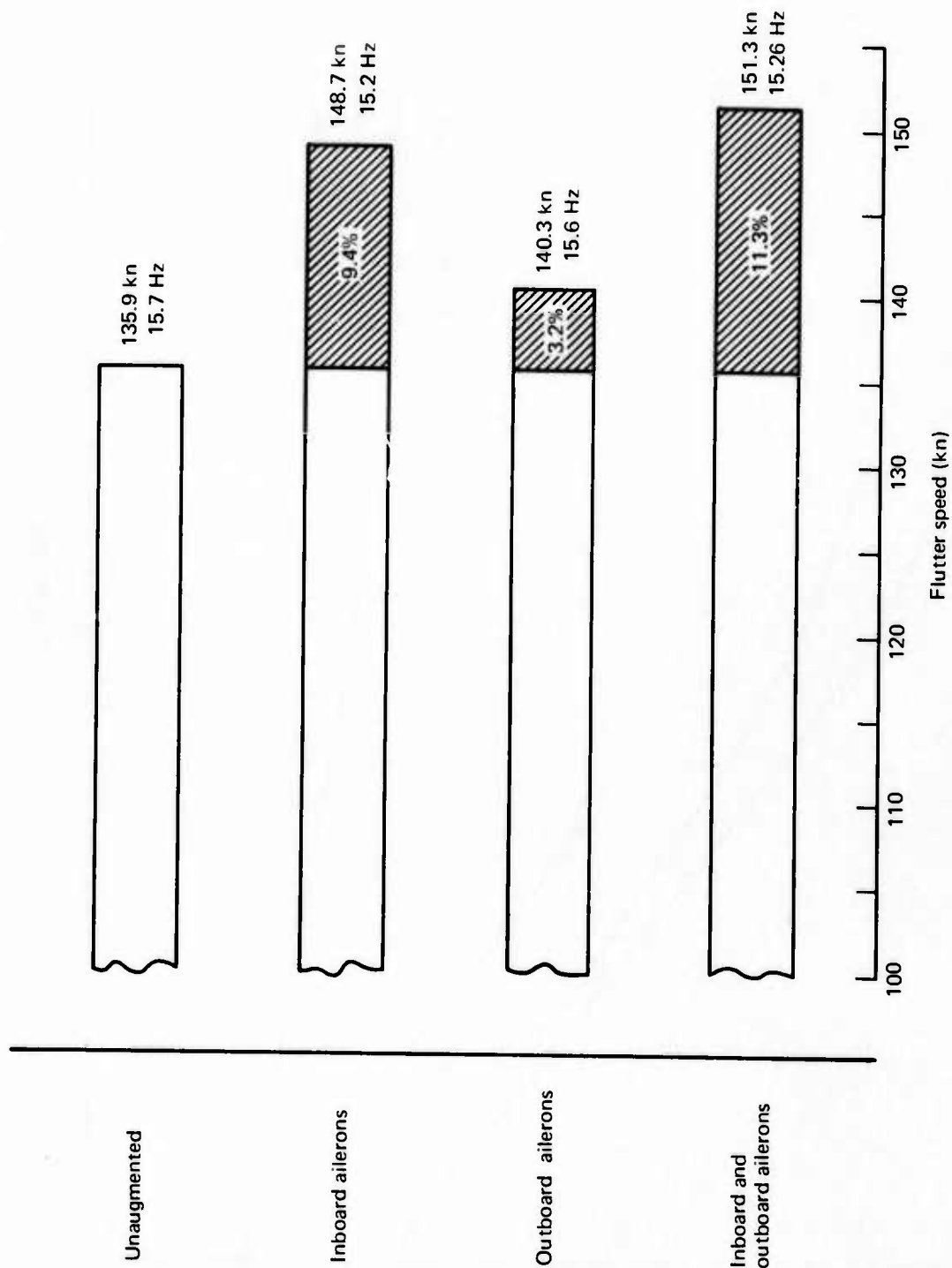


FIGURE 1.—TX1129D FLUTTER SAS RESULTS

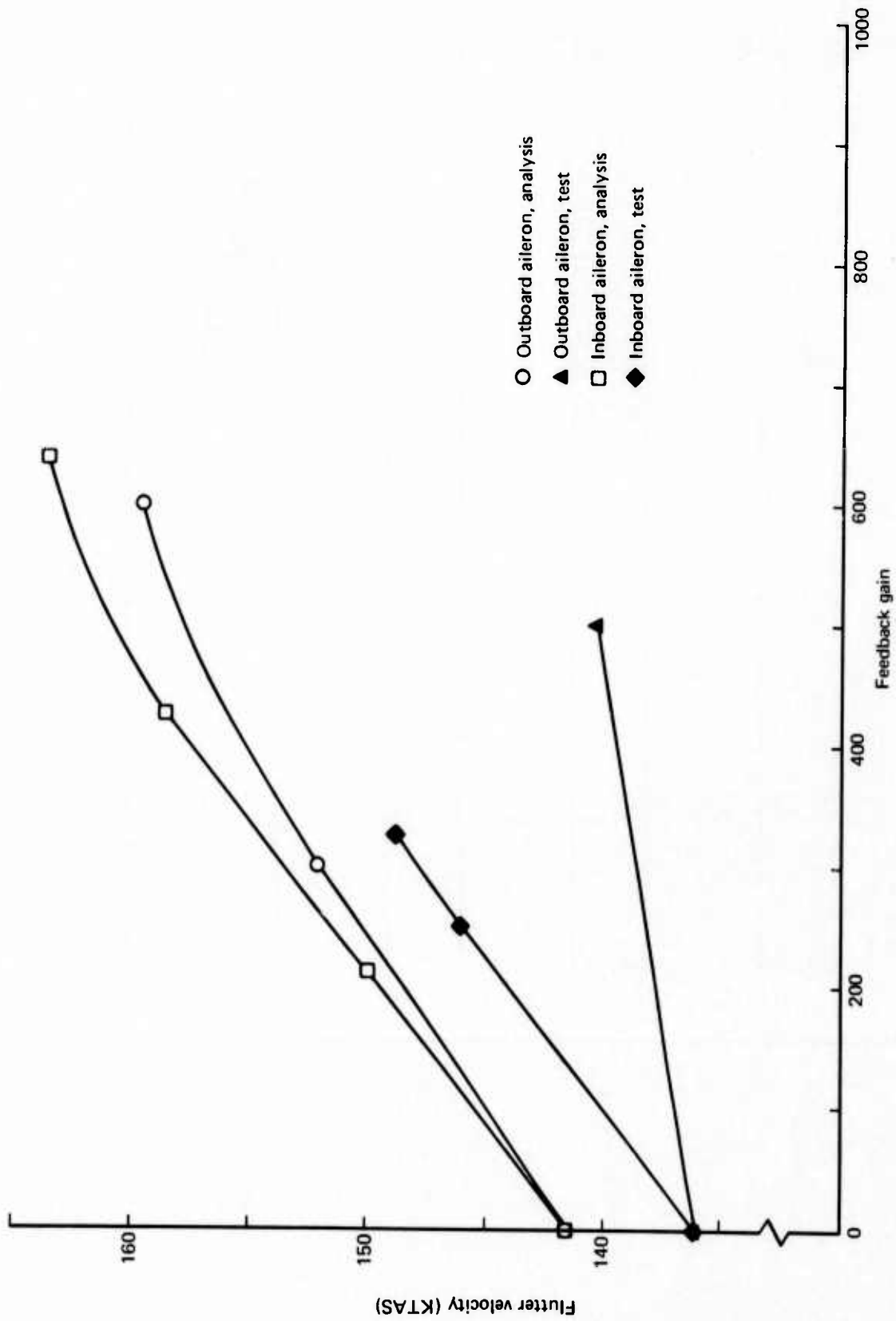


FIGURE 2.—COMPARISON OF TEST AND ANALYSIS IN THE FSAS

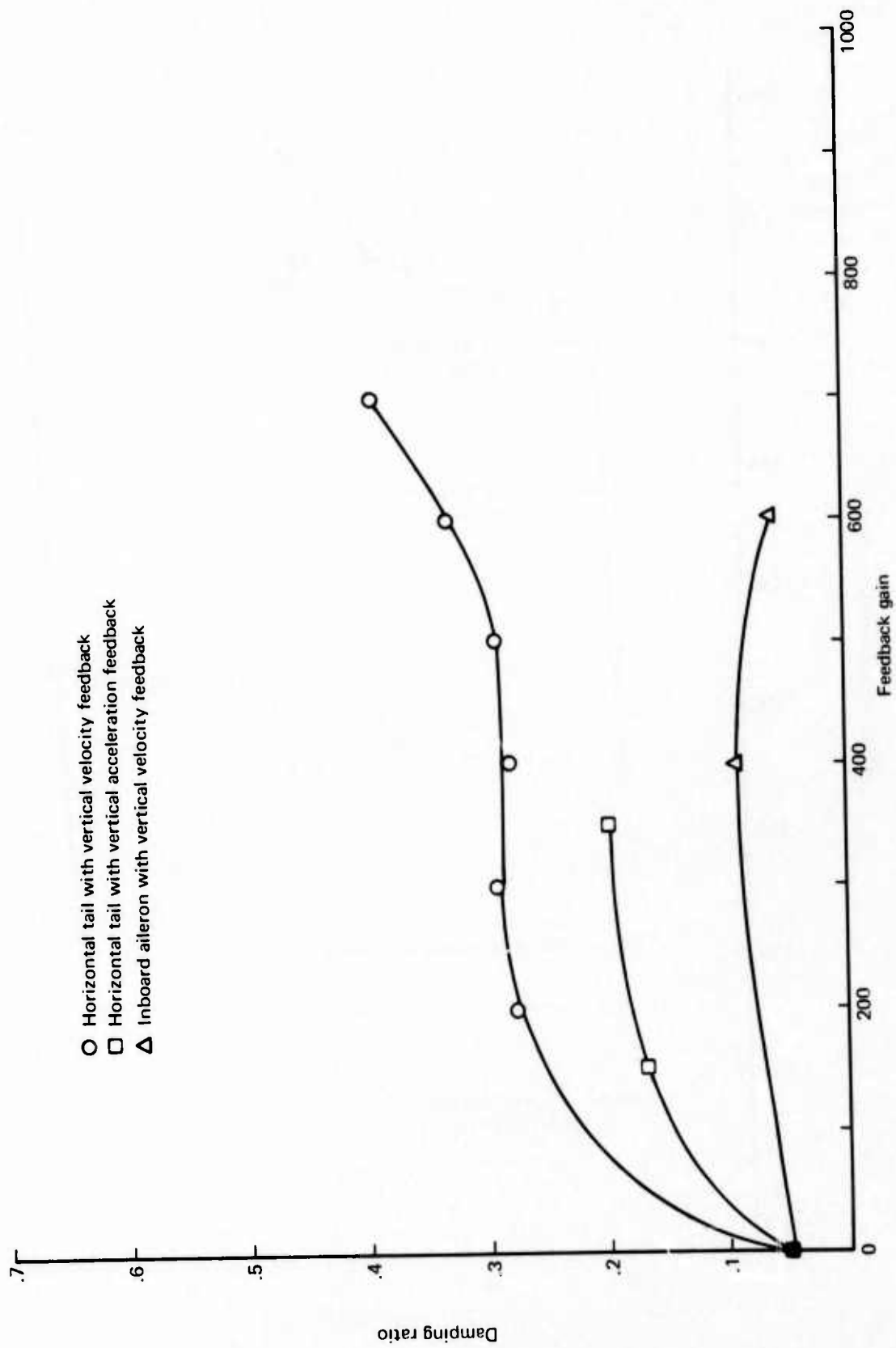


FIGURE 3.—AFCS TEST RESULTS AT 100 KNOTS AND 60.6% CR

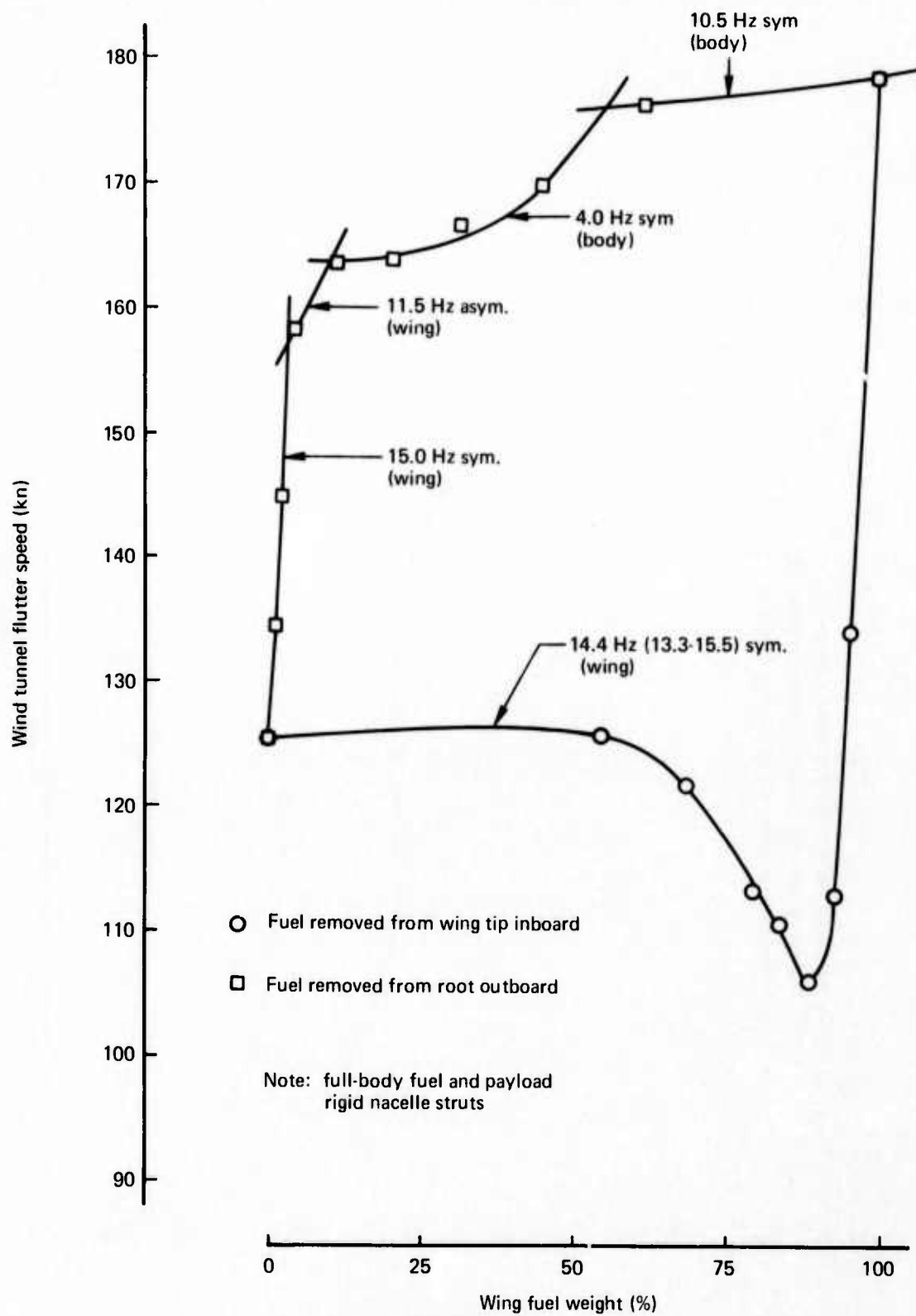


FIGURE 4.—WING FUEL MANAGEMENT STUDY

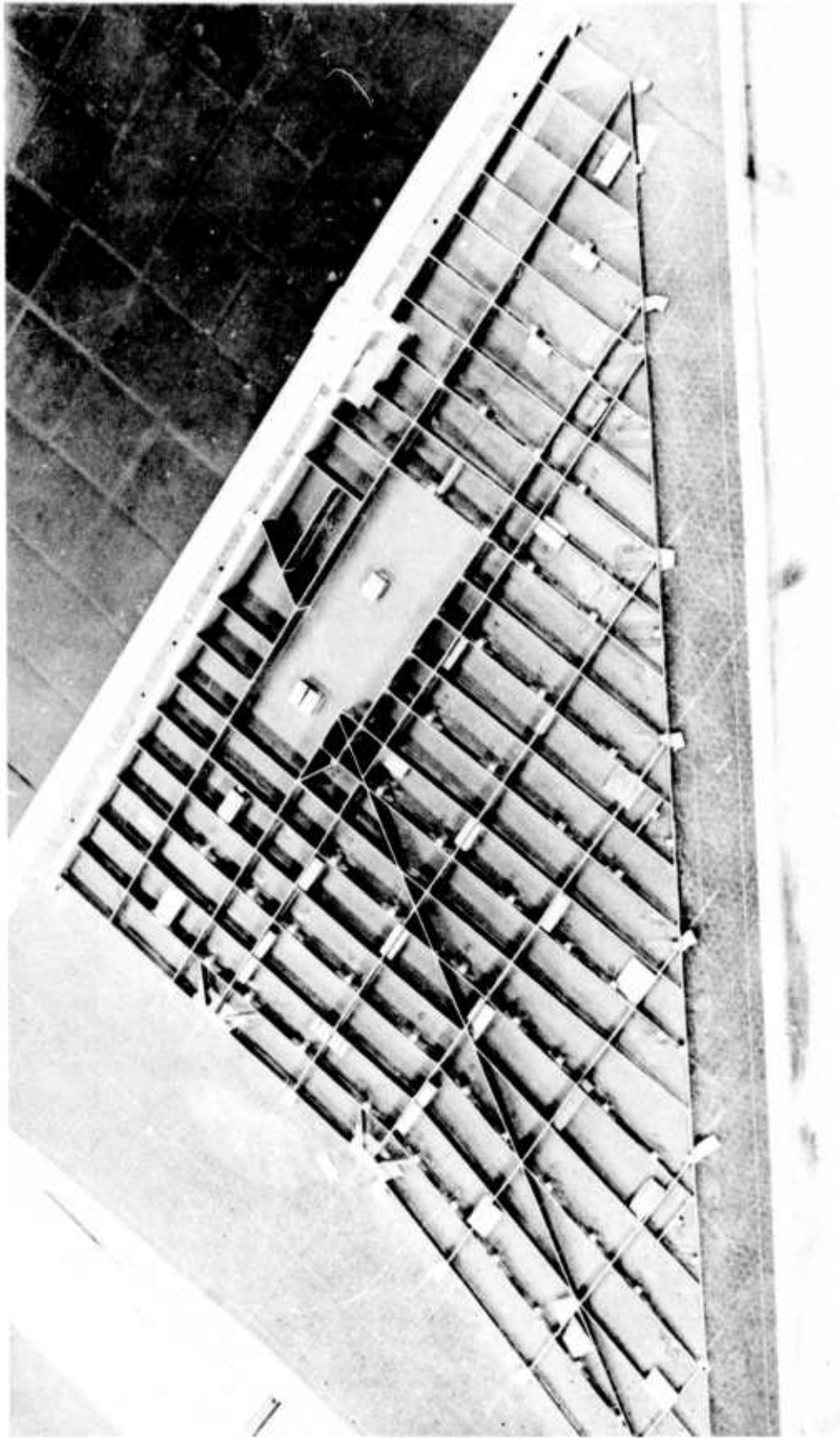


FIGURE 5.—INTERNAL STRUCTURE OF THE MODEL

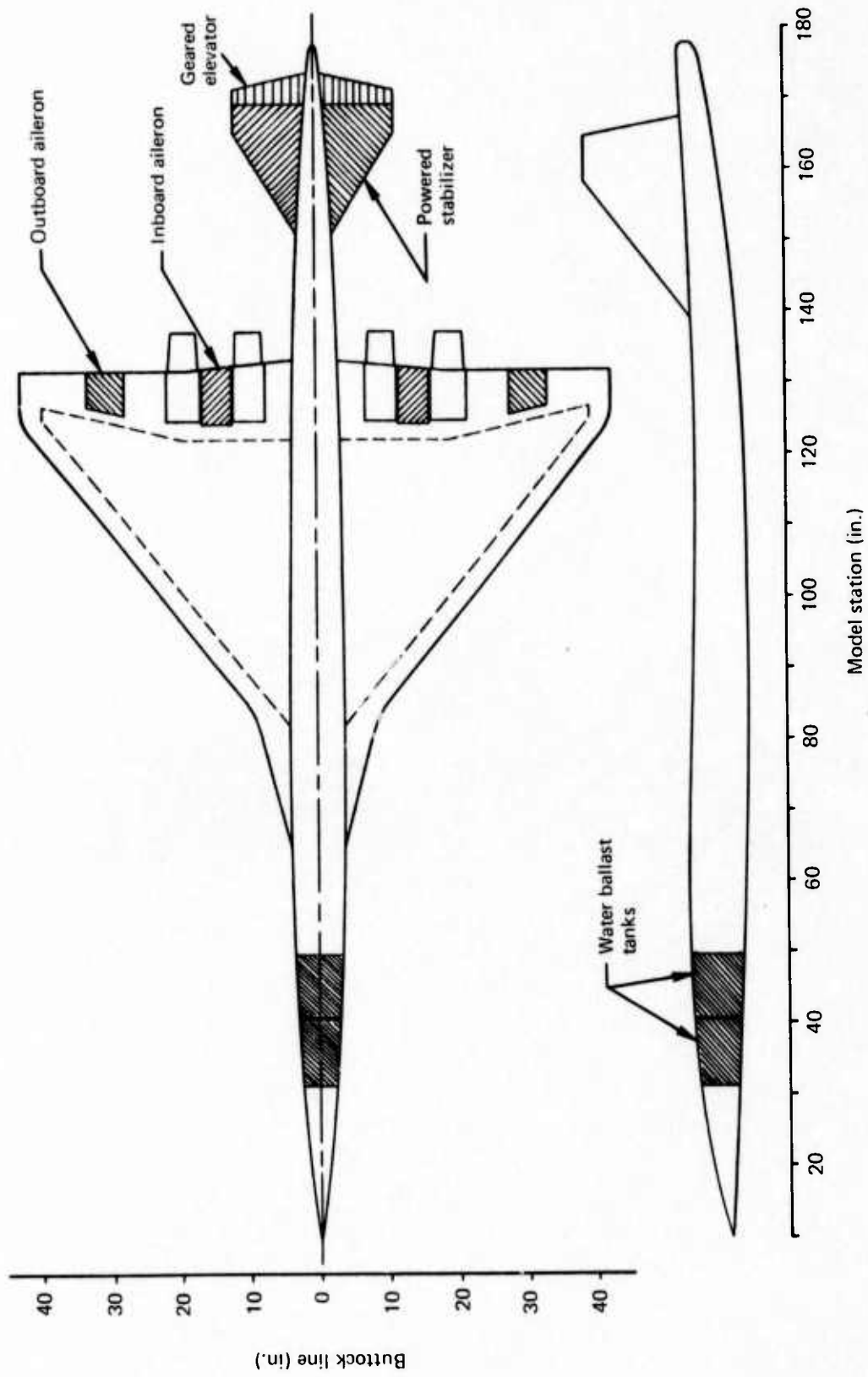


FIGURE 6.—GENERAL CONFIGURATION OF THE MODEL

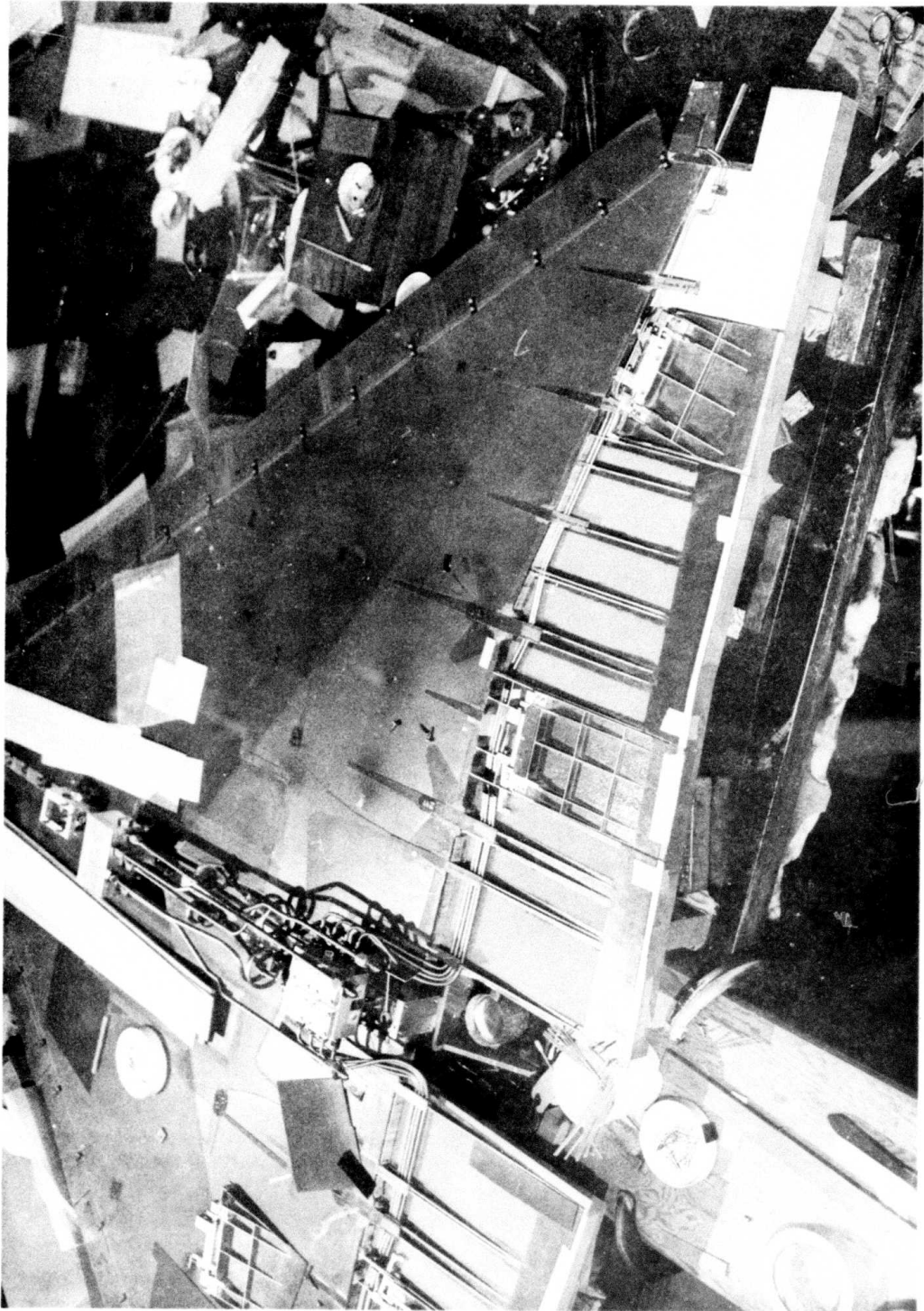


FIGURE 7.—HYDRAULIC TUBING AND INTERNAL STRUCTURE OF AILERONS

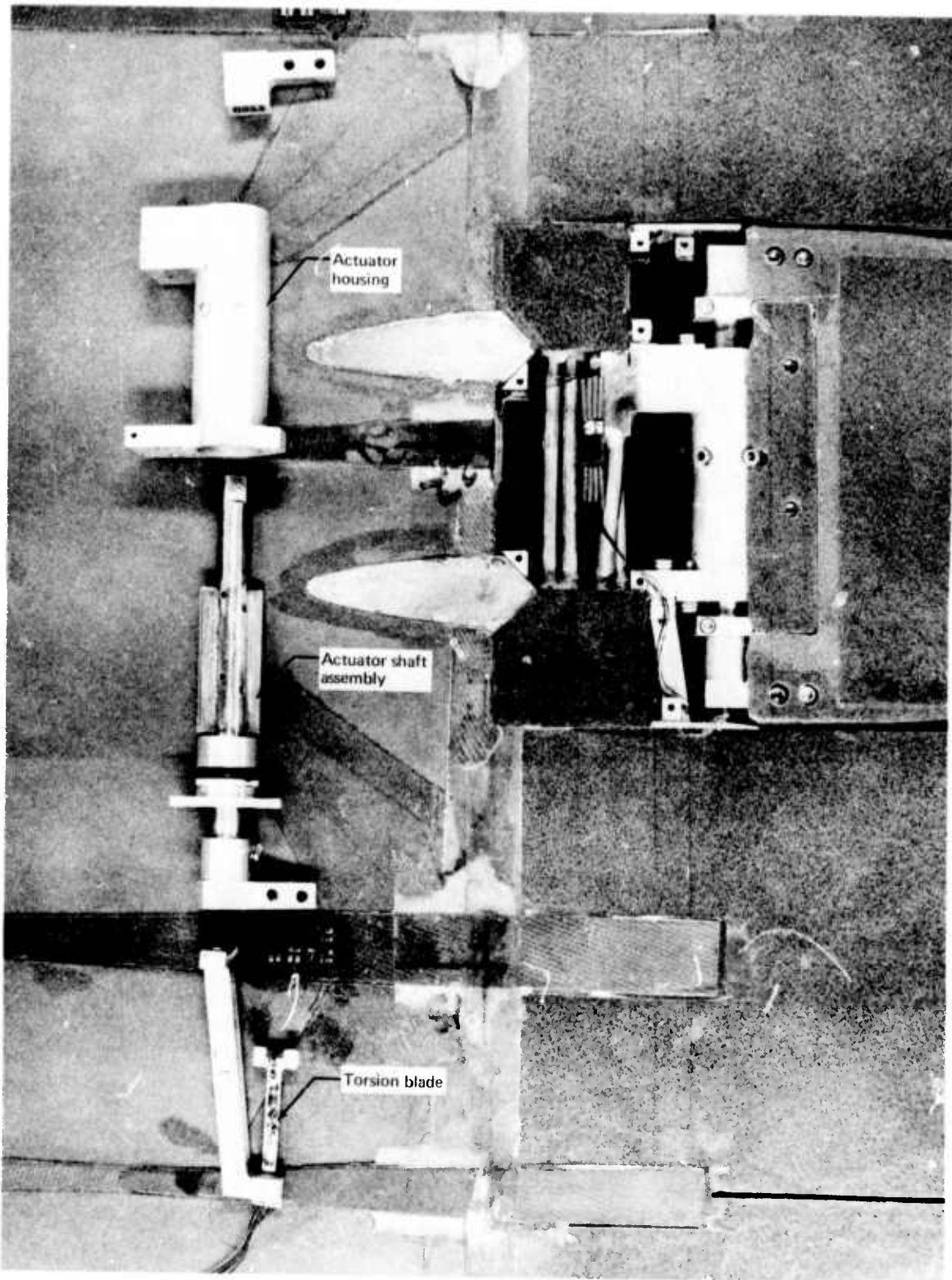


FIGURE 8.—EXPLODED VIEW OF AILERON ACTUATOR

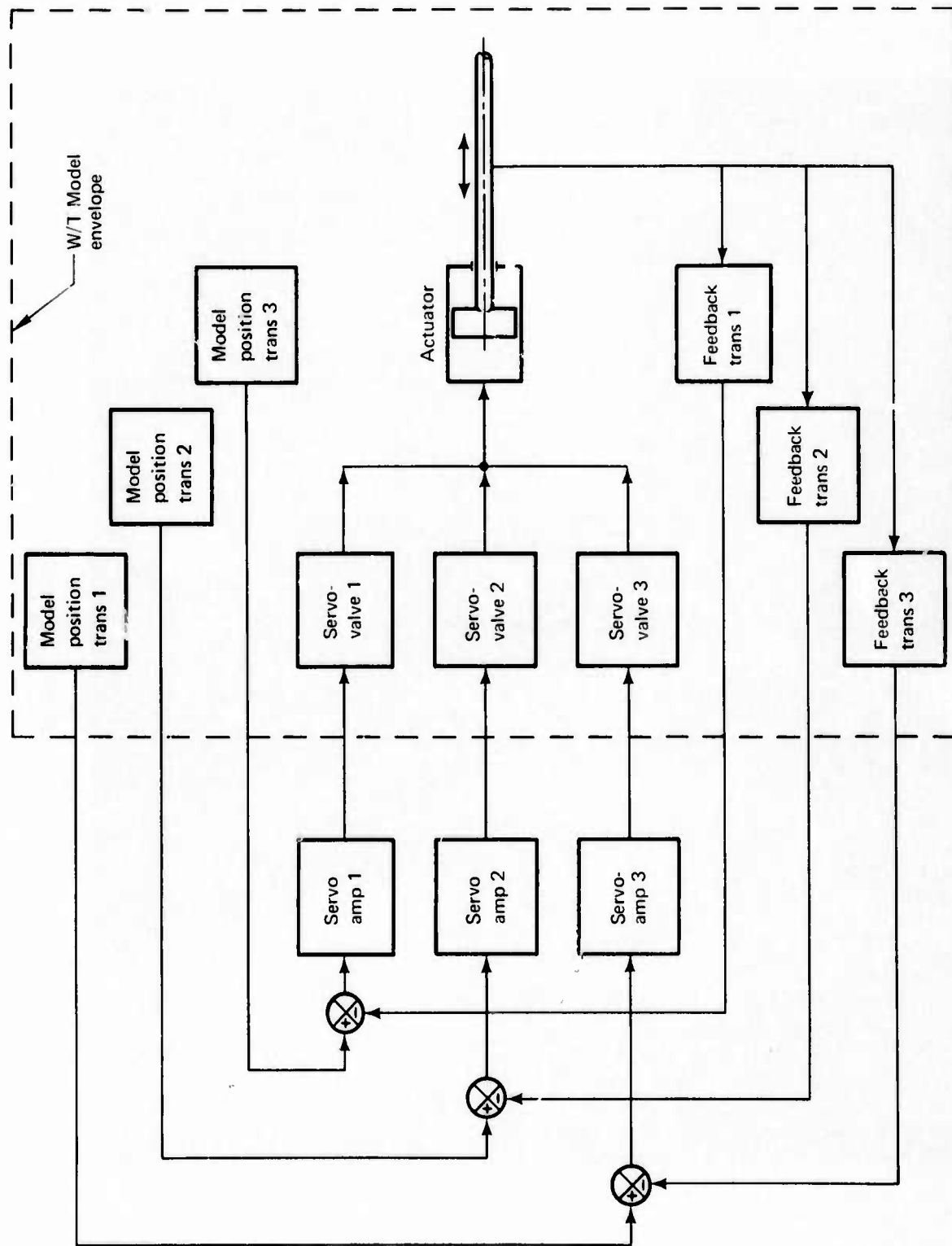


FIGURE 9.—MAJORITY VOTING SINGLE REDUNDANCY BLOCK DIAGRAM

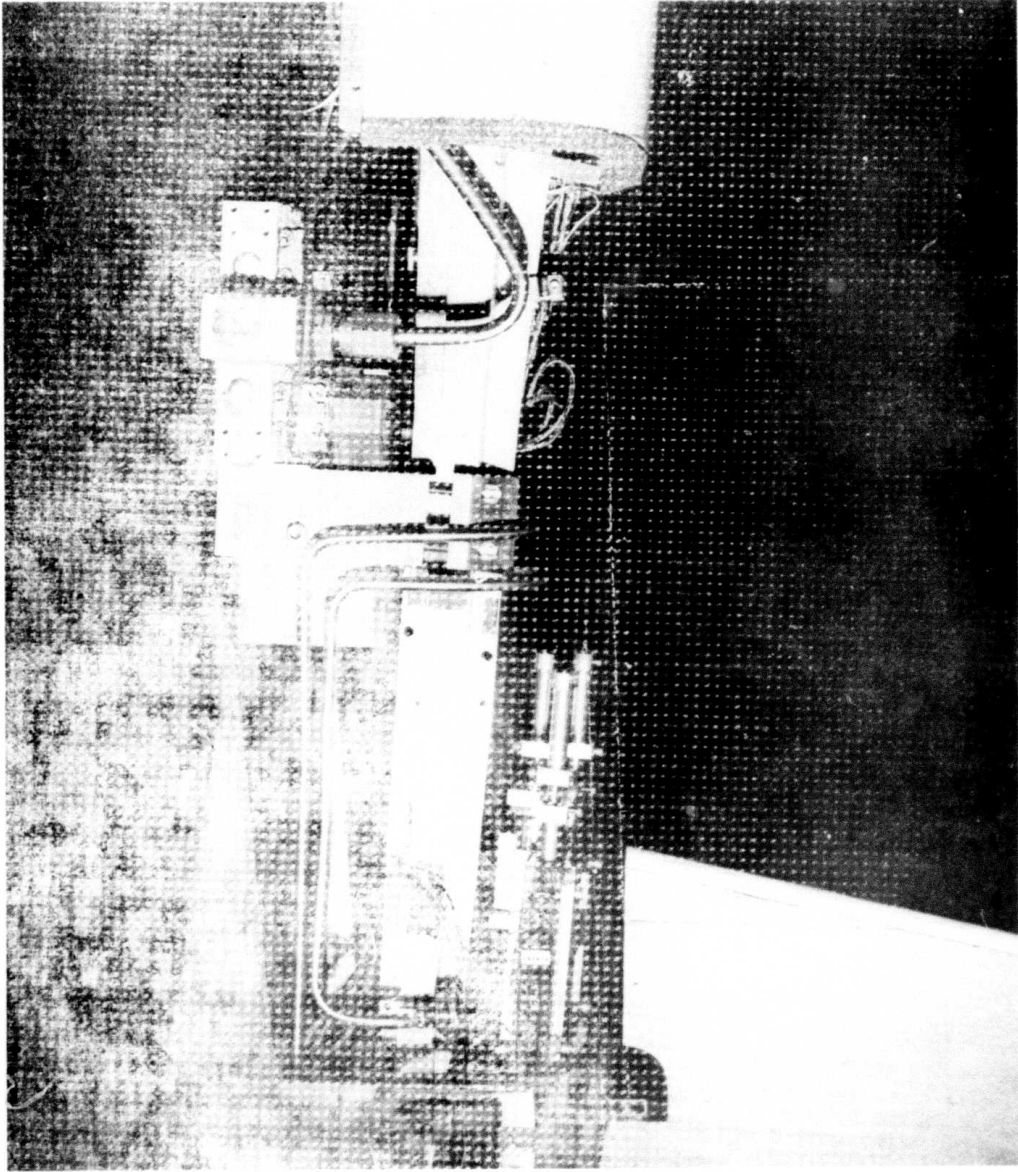


FIGURE 10.—HORIZONTAL STABILIZER SERVO VALVE/POSITION TRANSDUCER SYSTEM

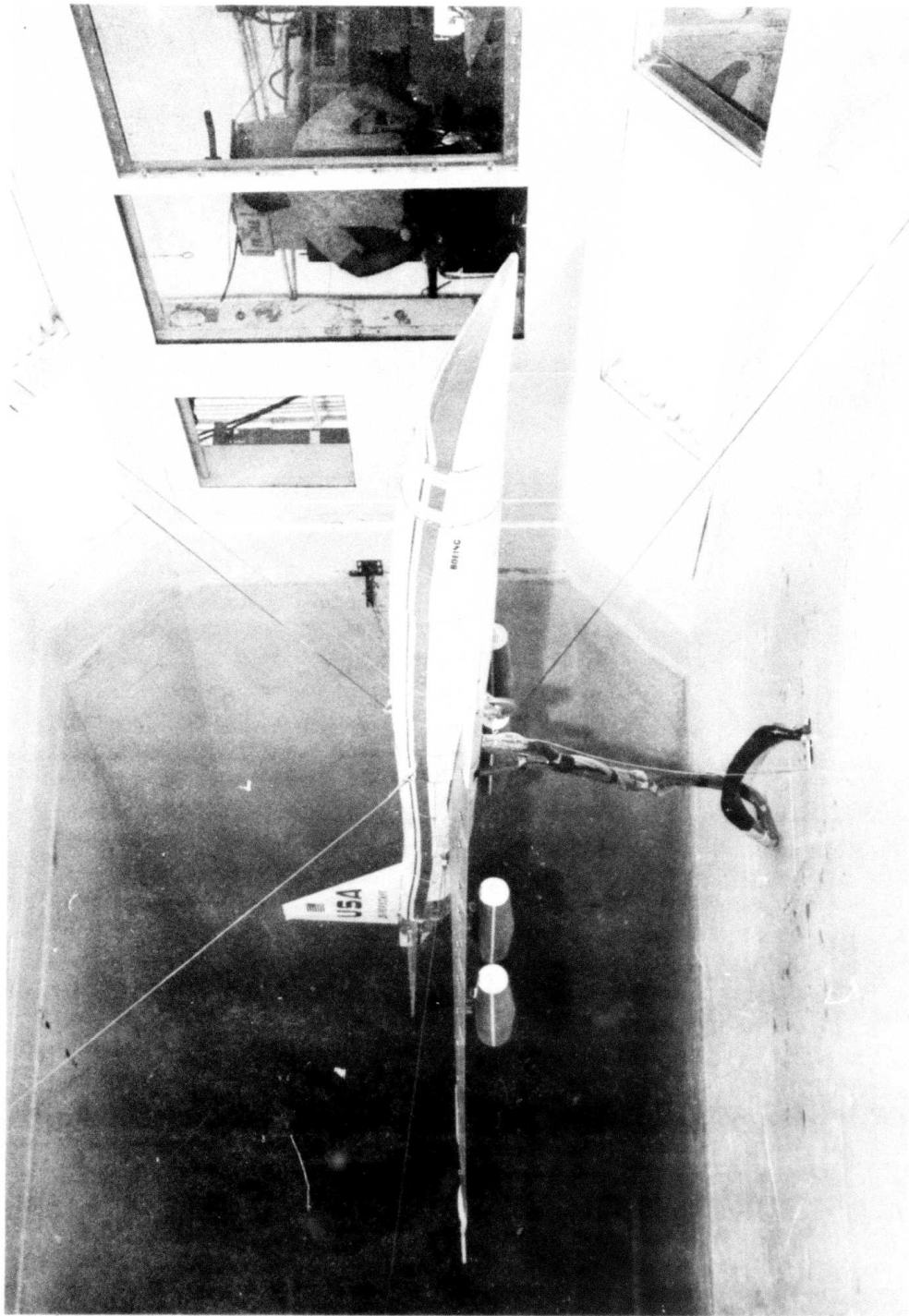


FIGURE 11.—MODEL MOUNTED IN TEST SECTION

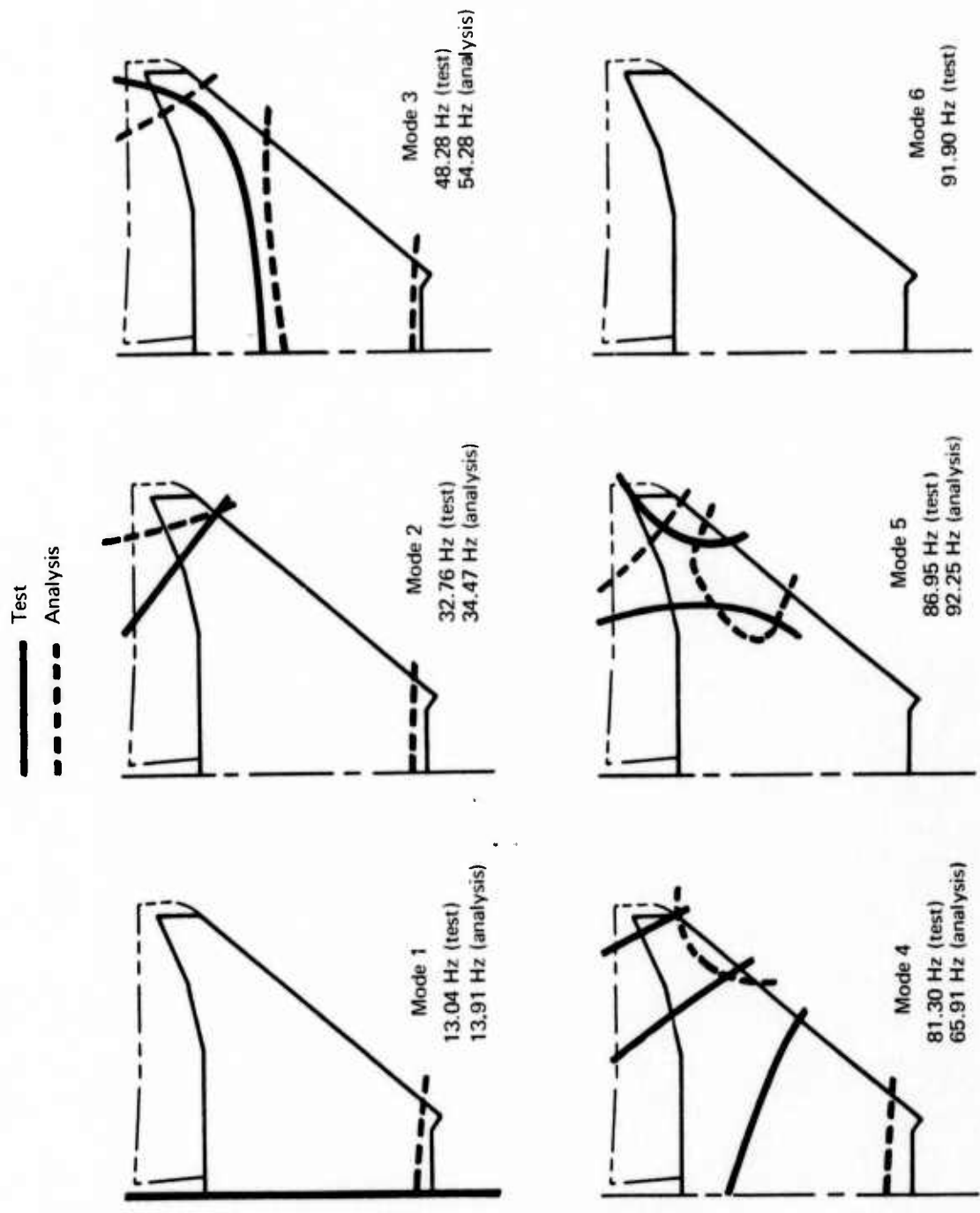


FIGURE 12.—COMPARISON OF MODES OF VIBRATION FOR RIGHT-HAND WING WITHOUT NACELLES

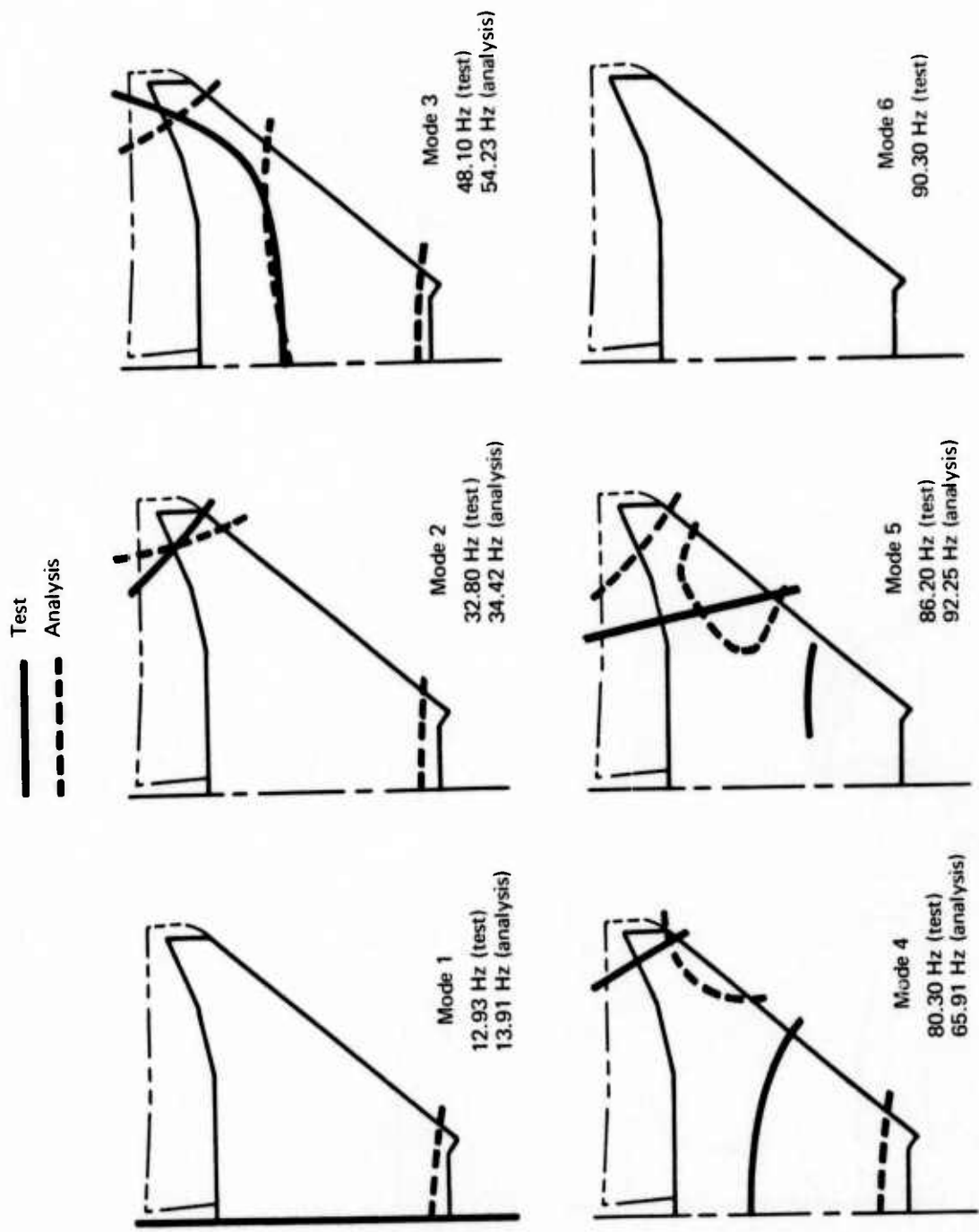


FIGURE 13.—COMPARISON OF MODES OF VIBRATION FOR LEFT-HAND WING WITHOUT NACELLES

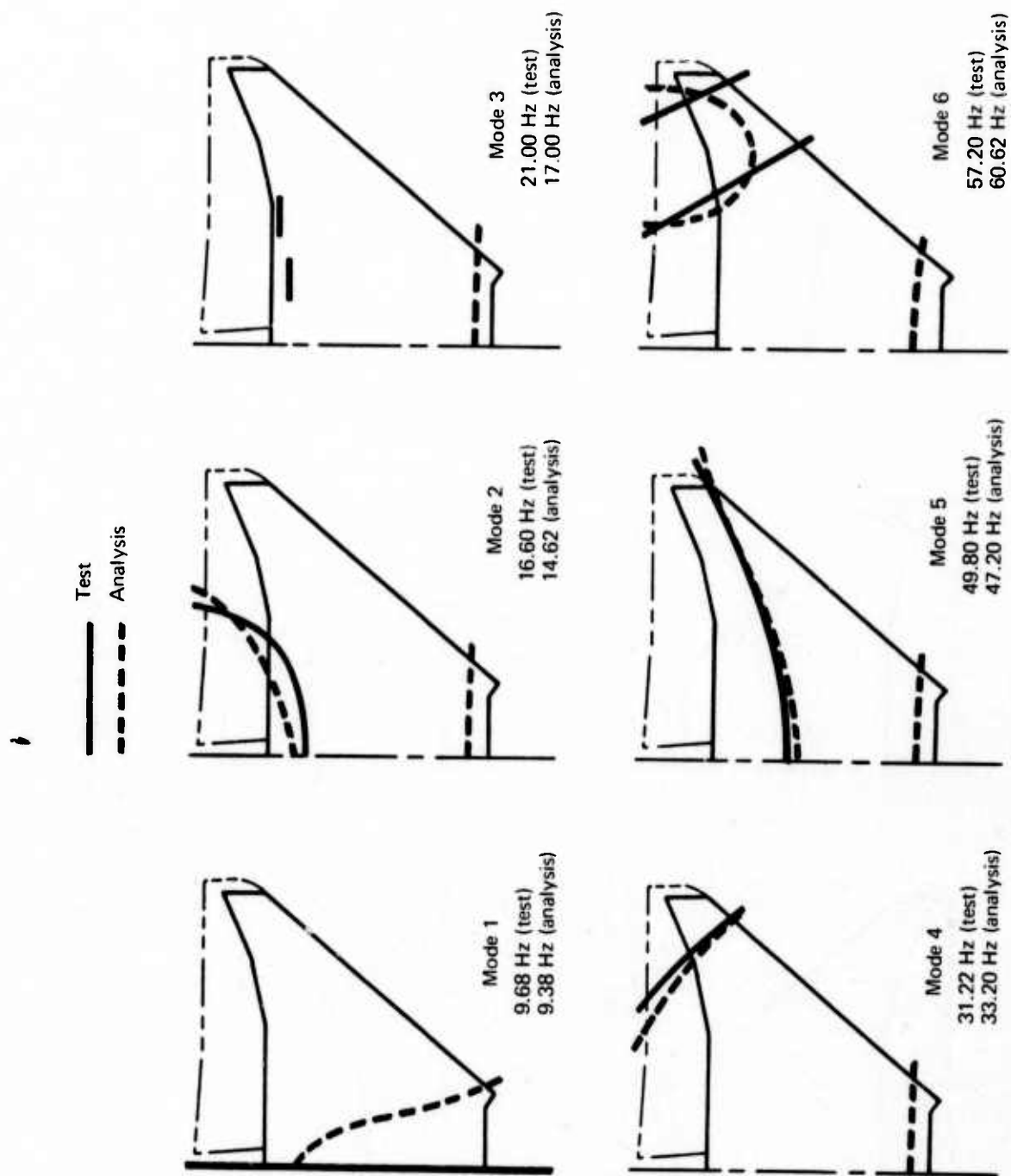


FIGURE 14.—COMPARISON OF MODES OF VIBRATION FOR RIGHT-HAND WING WITH NACELLES

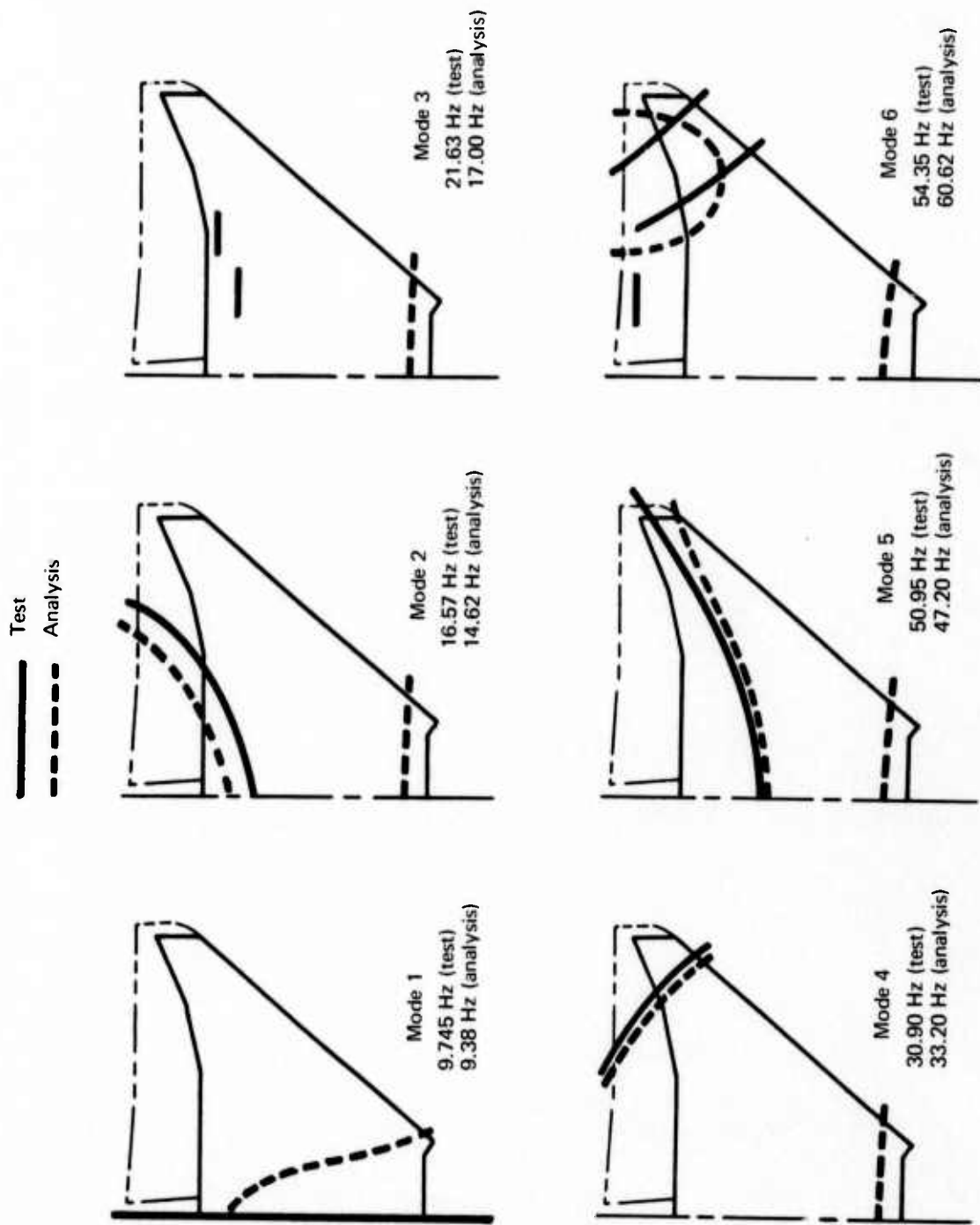


FIGURE 15.—COMPARISON OF MODES OF VIBRATION FOR LEFT-HAND WING WITH NACELLES

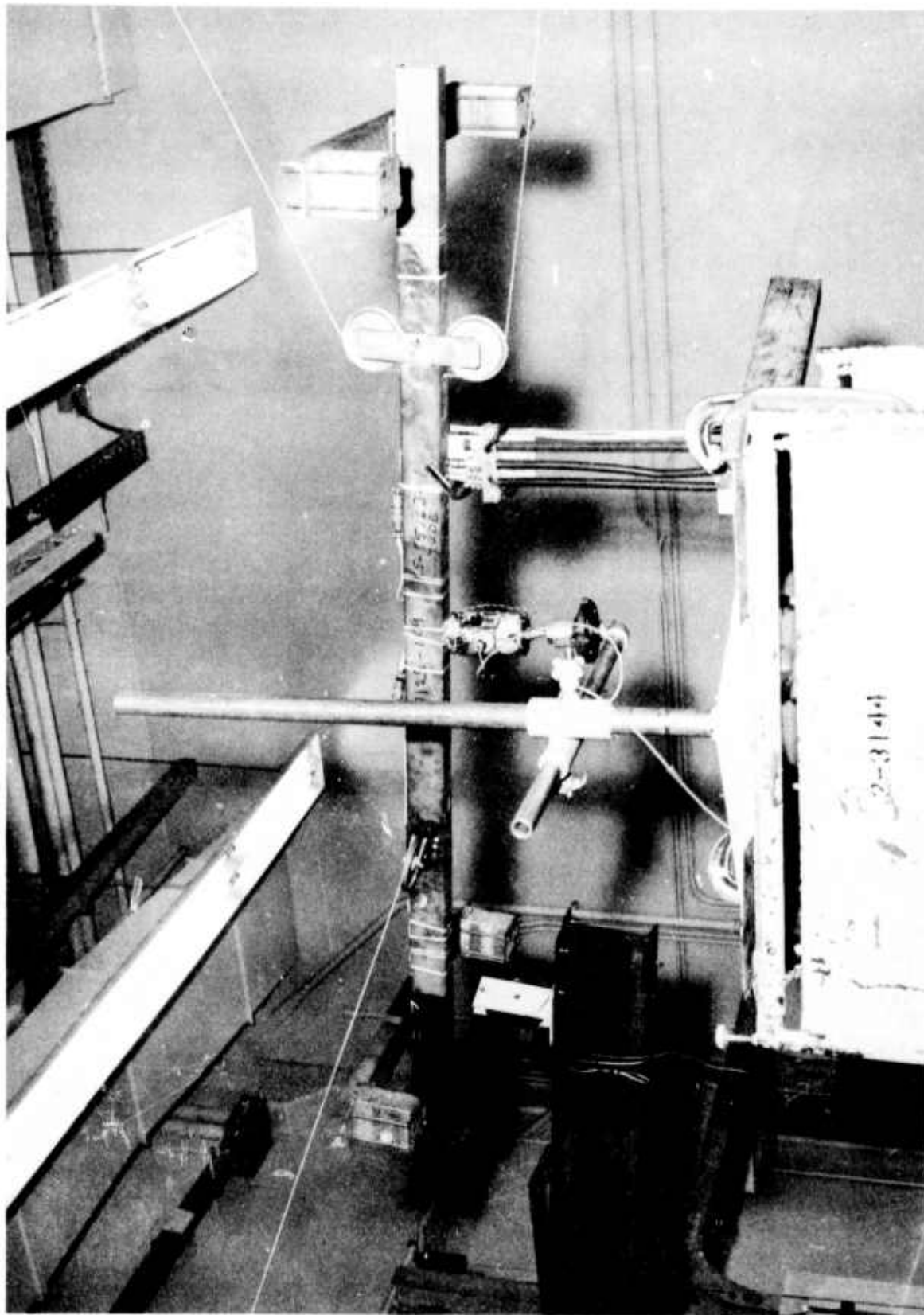


FIGURE 16.—INERTIA MODEL ON CABLE SYSTEM

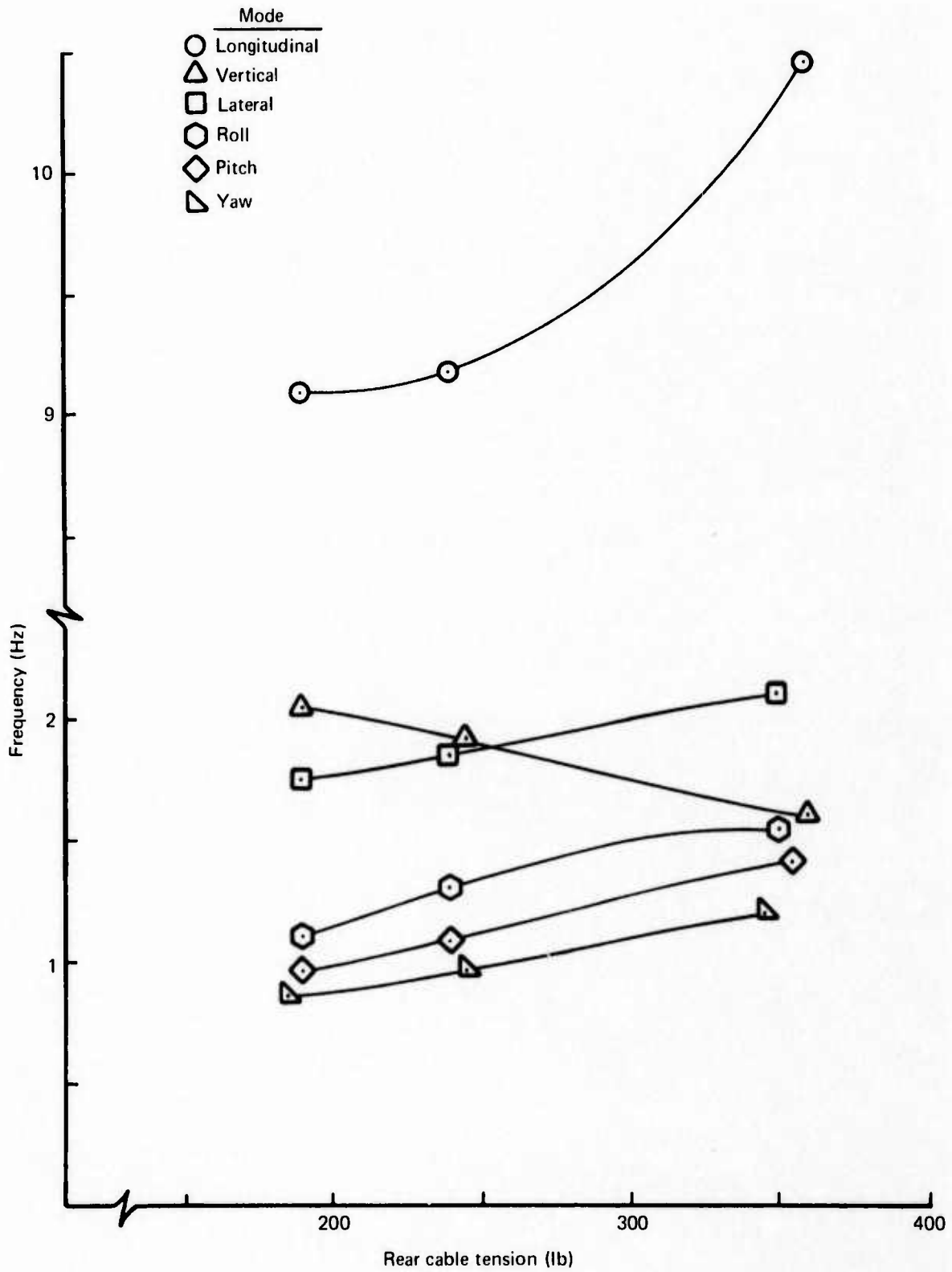


FIGURE 17.—EFFECT OF CABLE TENSION ON INERTIA MODEL RIGID MODES

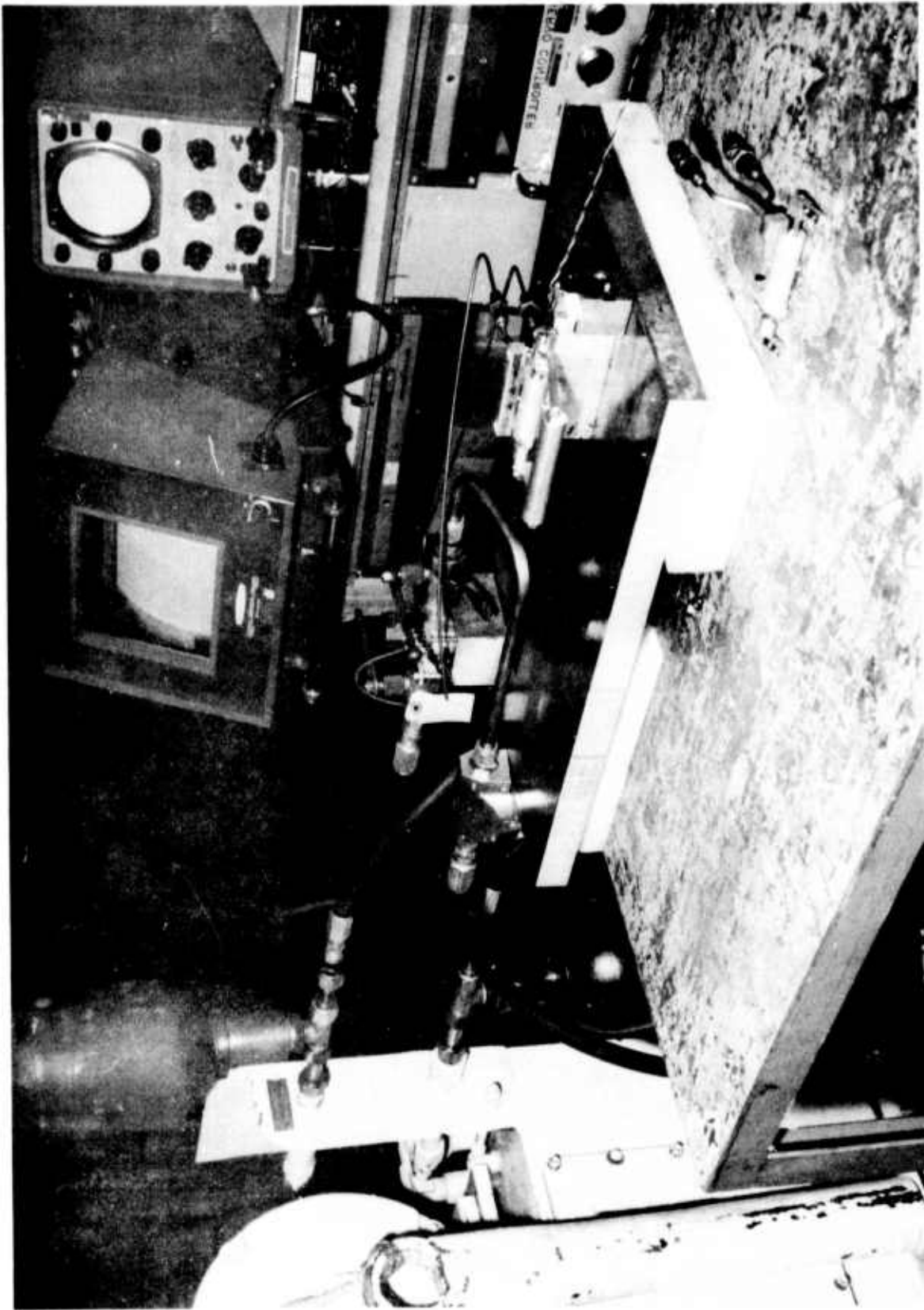


FIGURE 18.—BENCH TEST OF AILERON ACTUATOR

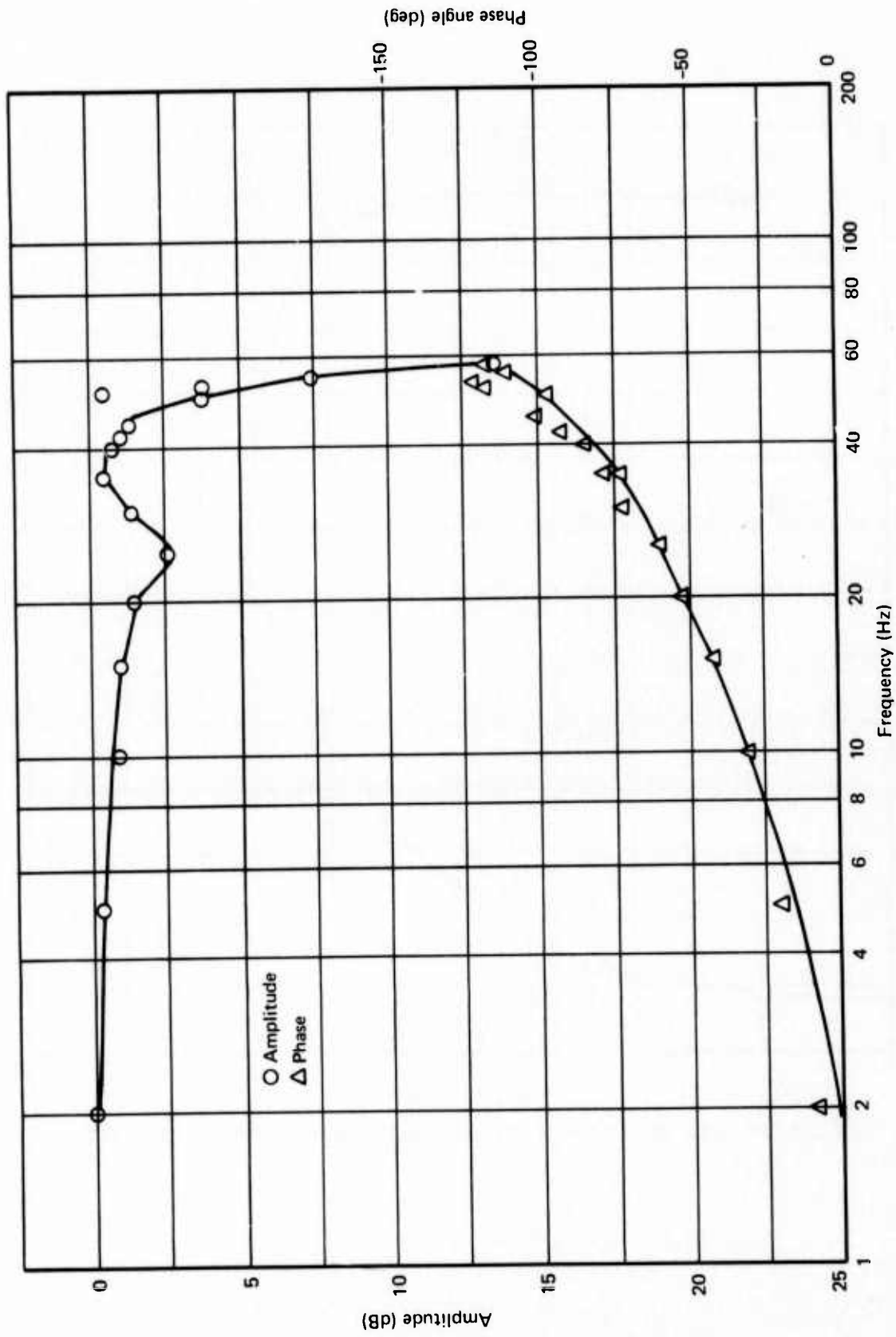


FIGURE 19. — OPEN LOOP STABILIZER RESPONSE CHARACTERISTICS

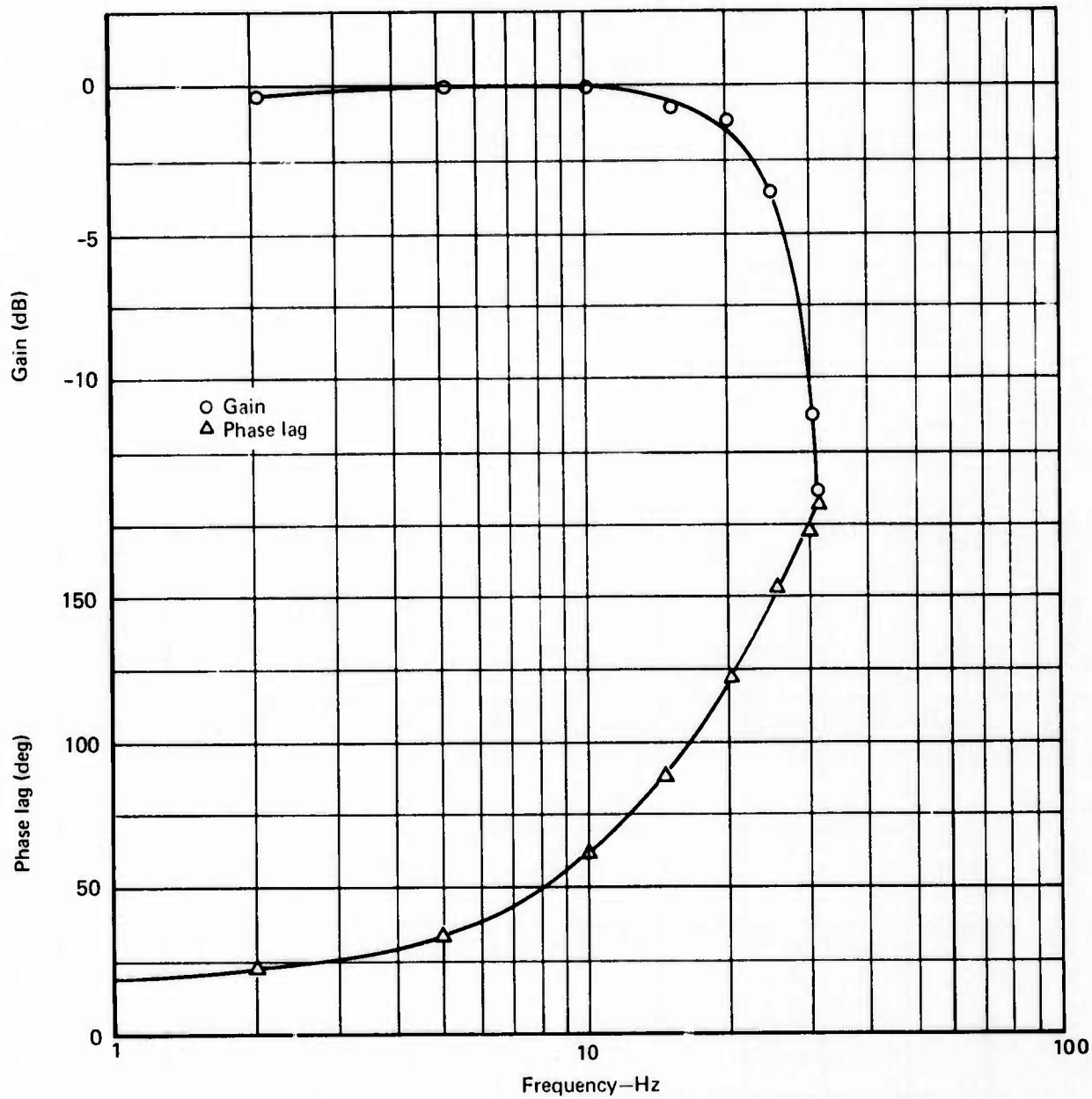


FIGURE 20.—CLOSED LOOP STABILIZER RESPONSE CHARACTERISTICS

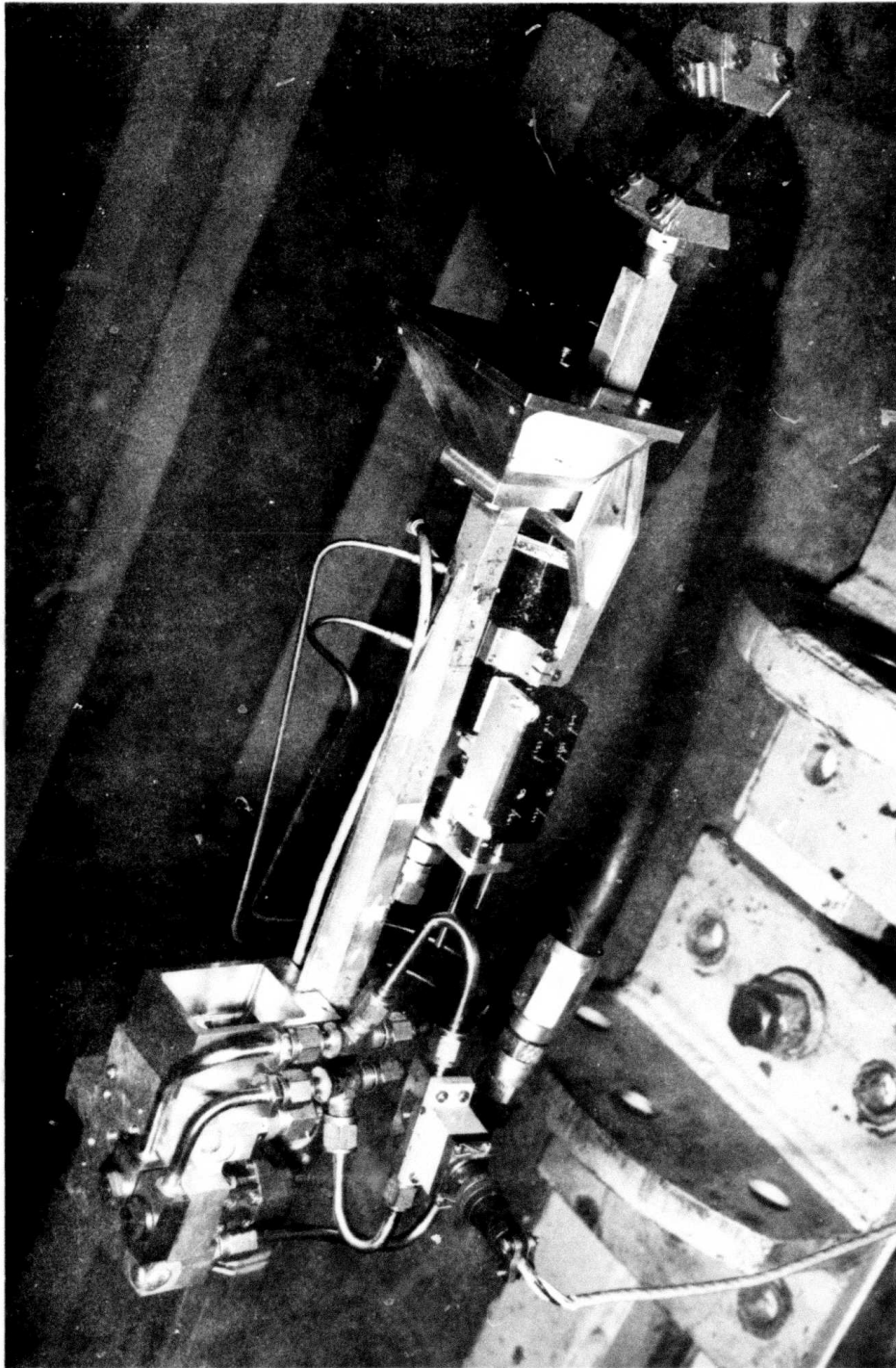


FIGURE 21.—BENCH TEST OF STABILIZER SERVO SYSTEM

Substructure no.	Description	Nodes	Beams	Plates
1	Wing	530	799	1250
2	Half body	172	151	202
3	Empennage support	11	9	0
4	Horizontal tail	19	2	14
5	Elevator	18	2	12
6	Horizontal tail linkage	2	1	0
7	Vertical tail	15	2	15
8	Trailing edge	247	366	385
9	Hydraulic tubing	38	37	0
10	Ailerons	84	180	155
11	Vane	9	4	4
12	Actuator springs	10	5	0
13	Nacelles	8	6	0
14	Cable support	5	2	0
Totals		1168	1566	2037

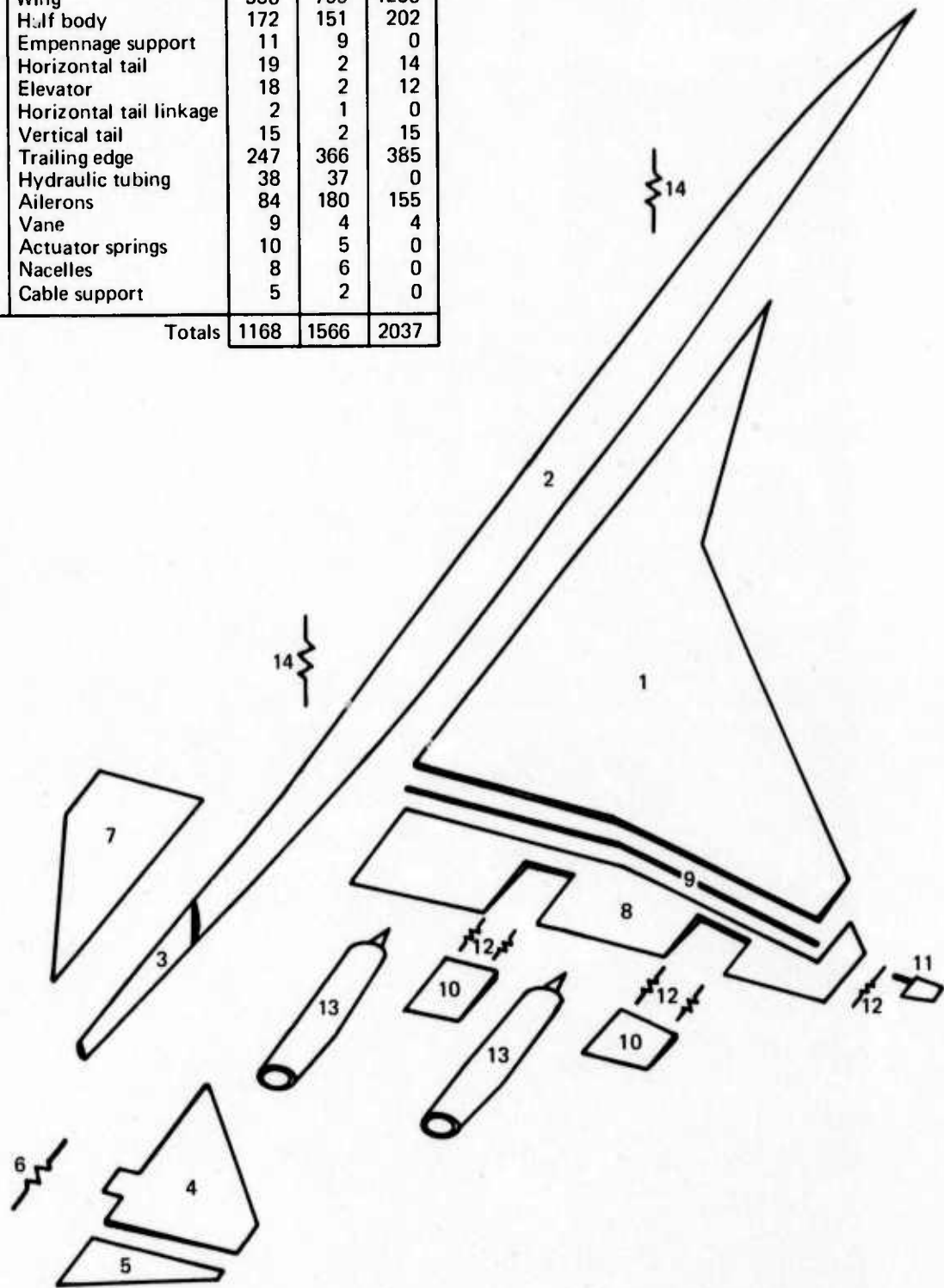
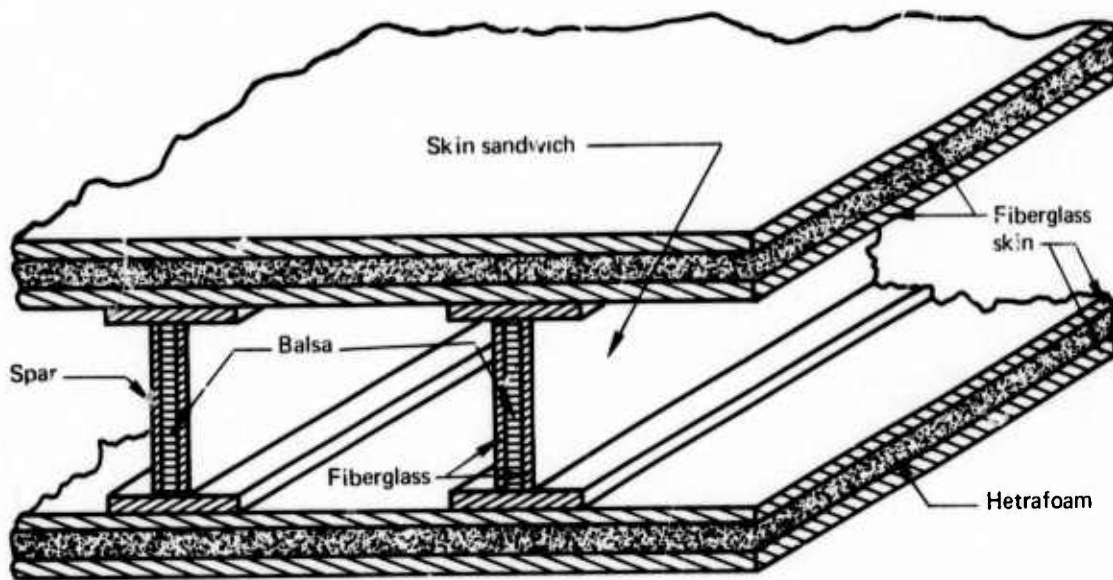
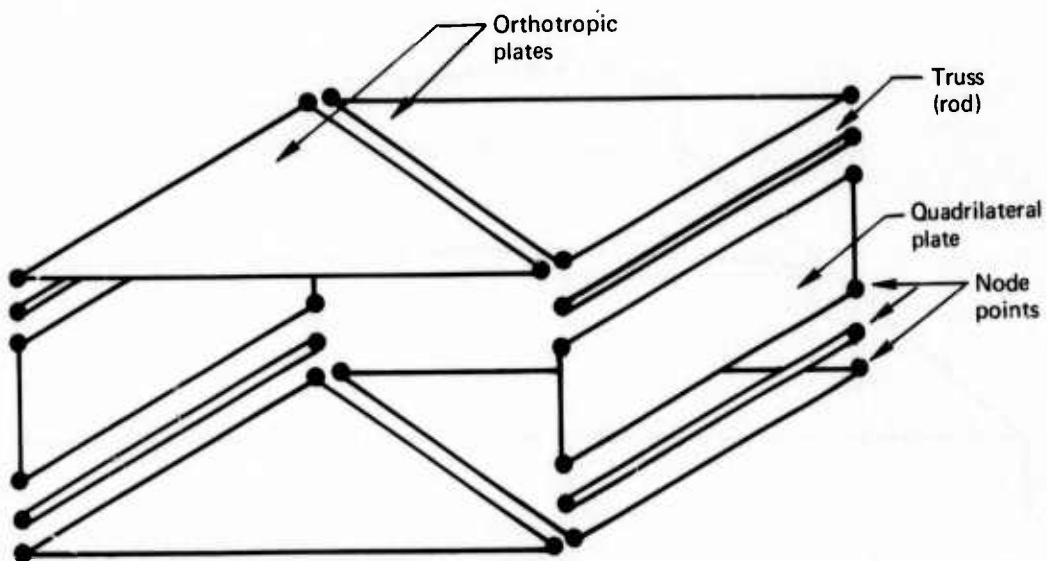


FIGURE 22.—STRUCTURAL IDEALIZATION AND SUBSTRUCTURES



Typical Cross Section



Idealization

FIGURE 23.—MODEL STRUCTURE ANALYTICAL IDEALIZATION

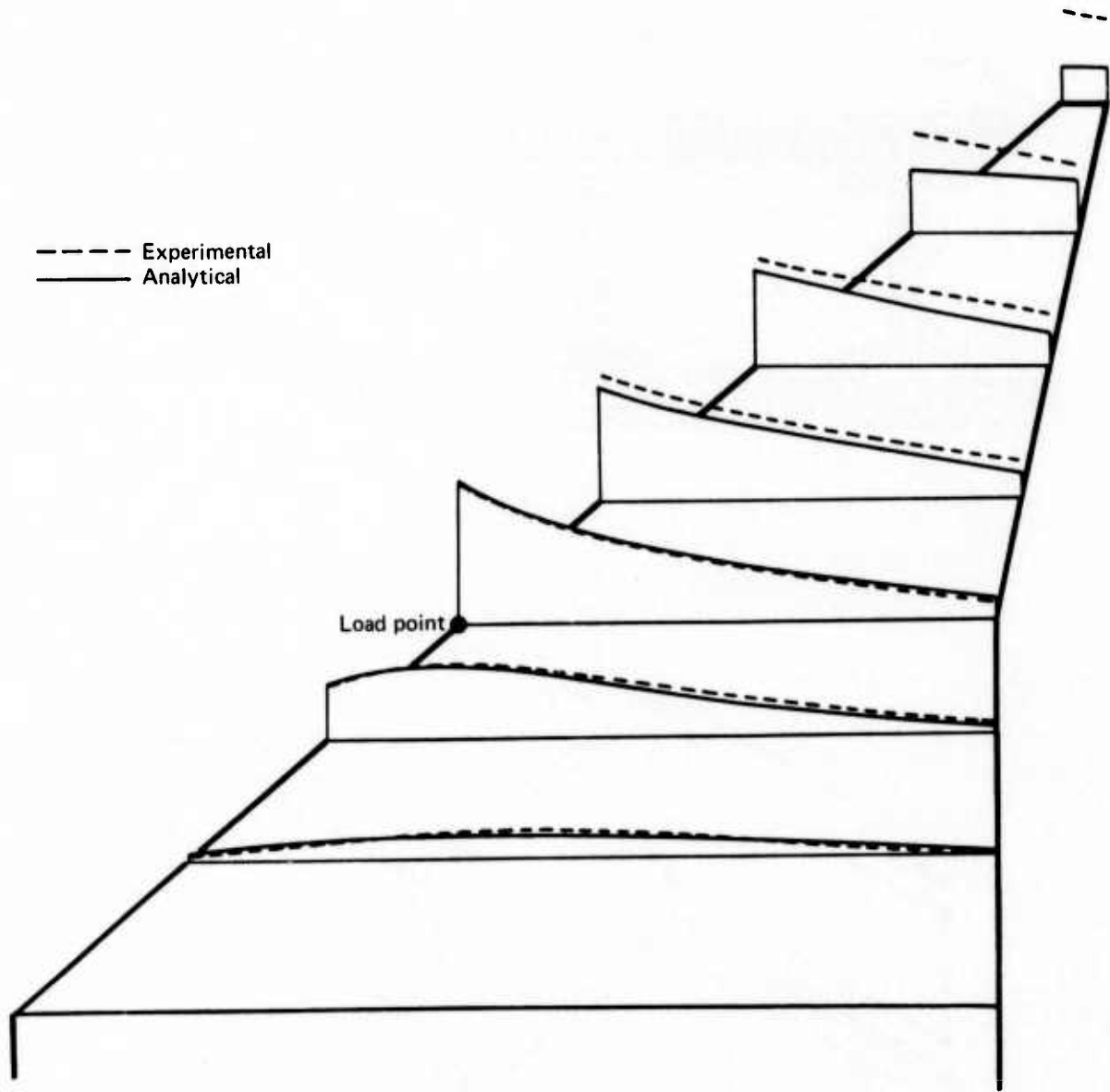


FIGURE 24.—COMPARISON OF LOAD/DEFLECTION CURVES—LOAD POINT 23

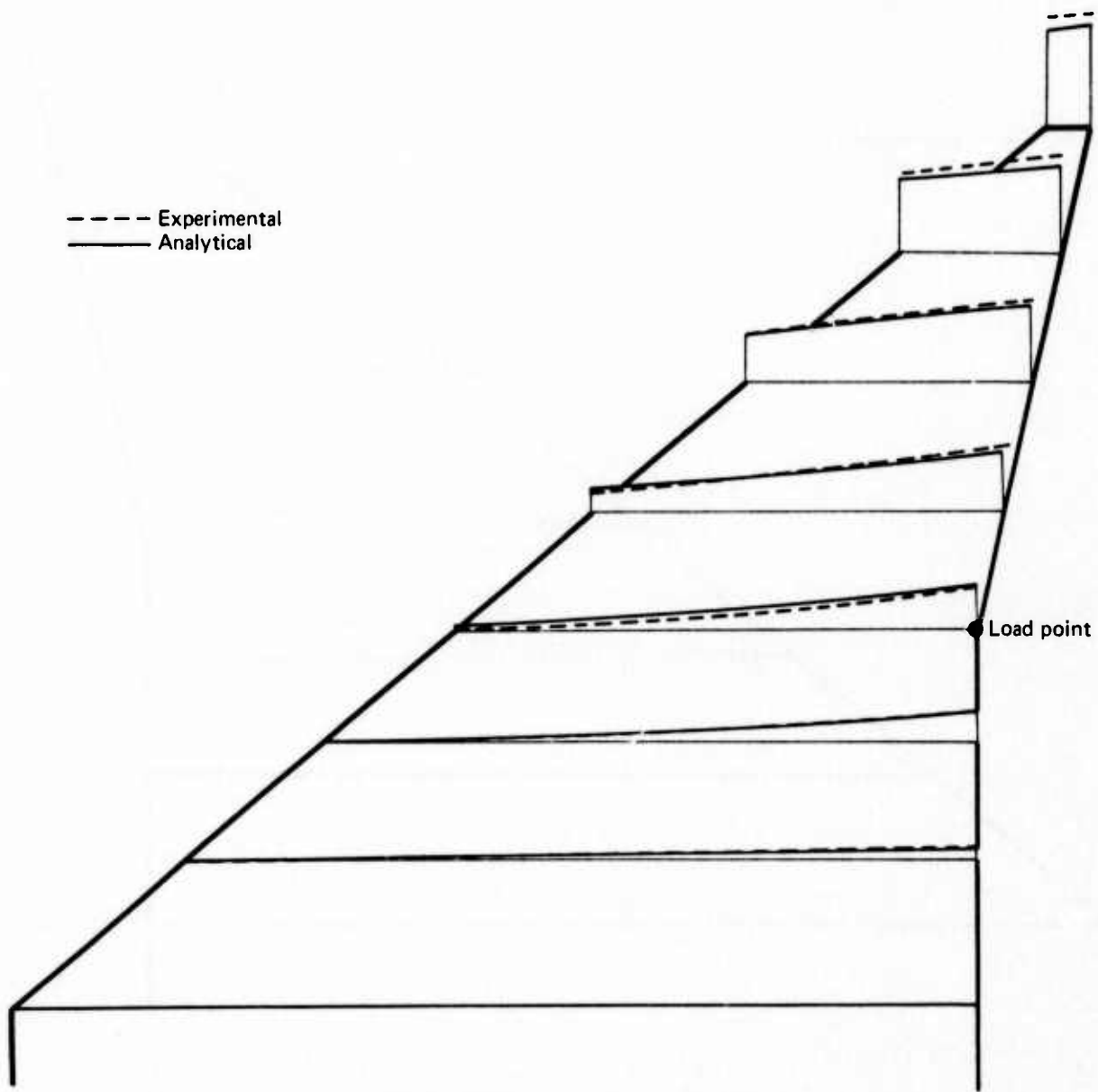


FIGURE 25.—COMPARISON OF LOAD/DEFLECTION CURVES—LOAD POINT 27

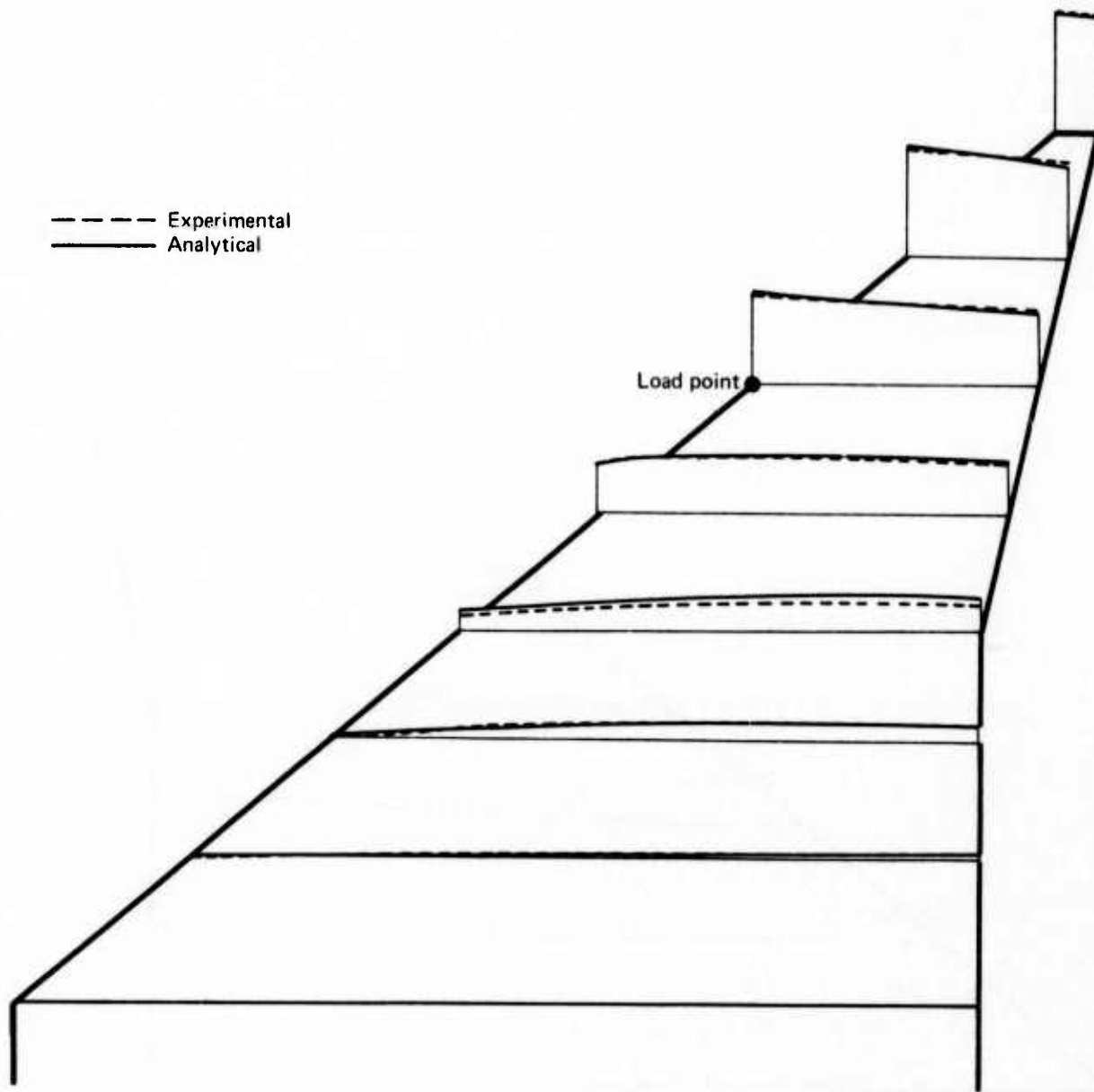


FIGURE 26.—COMPARISON OF LOAD/DEFLECTION CURVES—LOAD POINT 34

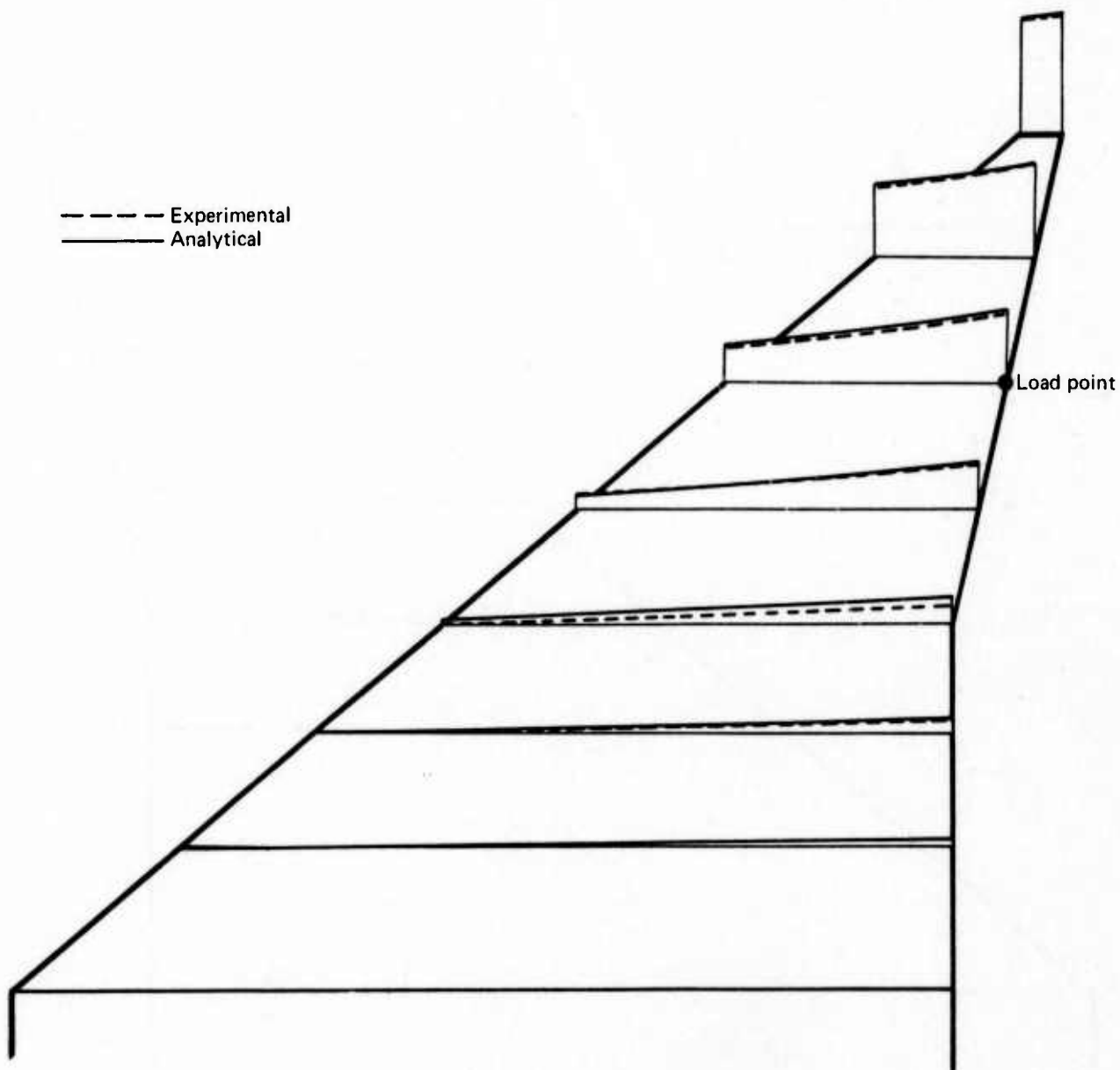


FIGURE 27.—COMPARISON OF LOAD/DEFLECTION CURVES—LOAD POINT 36

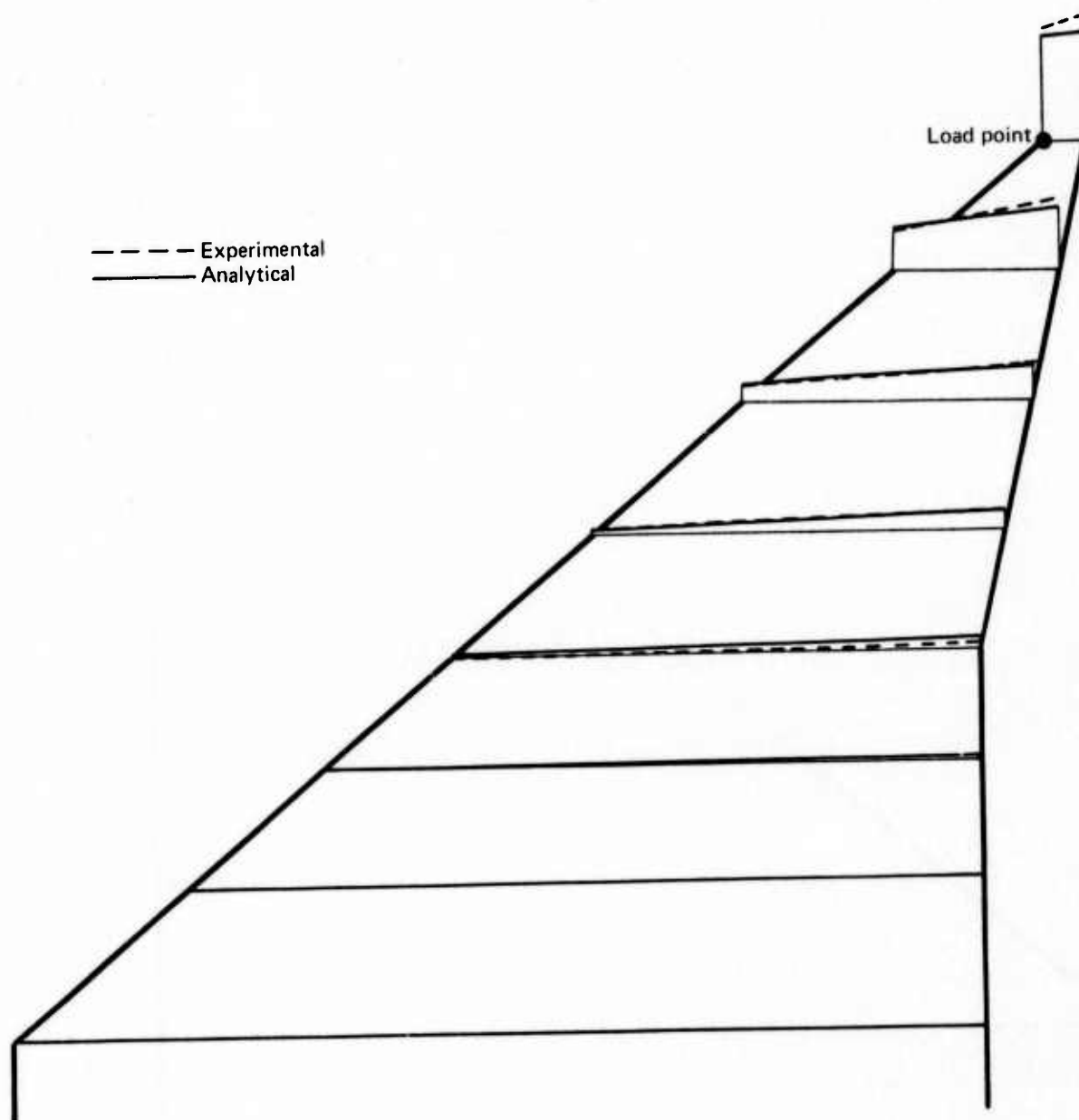


FIGURE 28.—COMPARISON OF LOAD/DEFLECTION CURVES—LOAD POINT 41

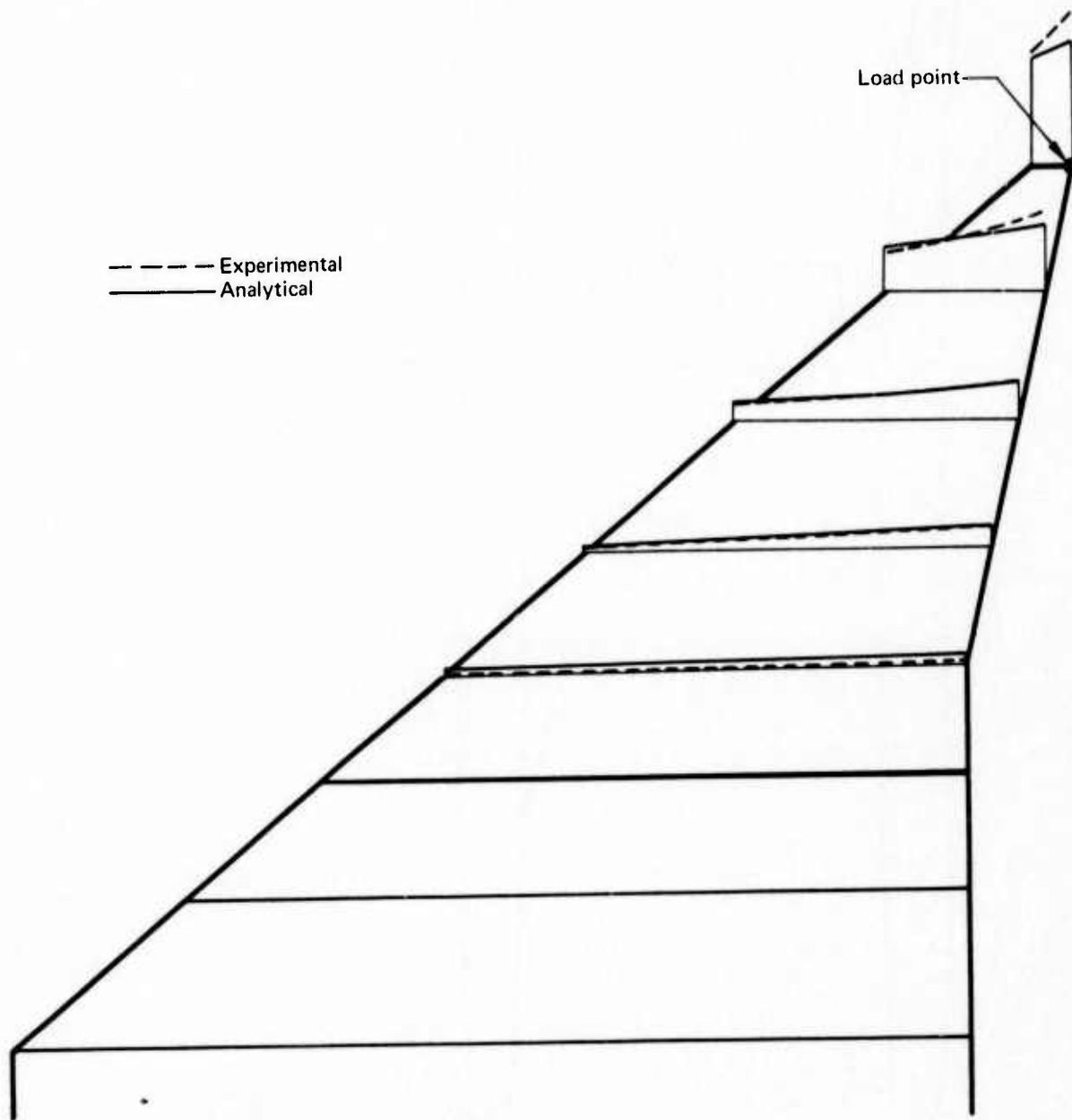
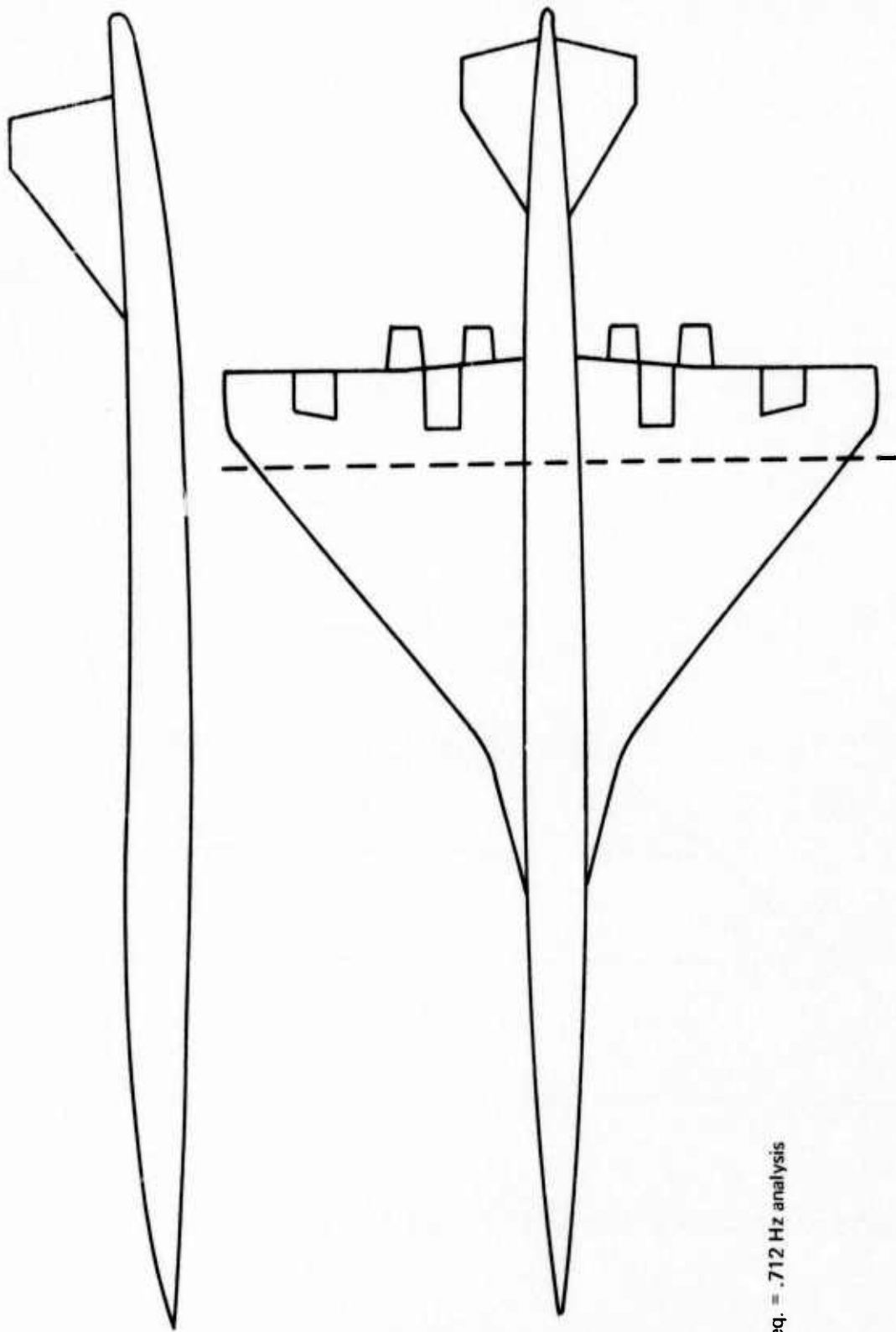
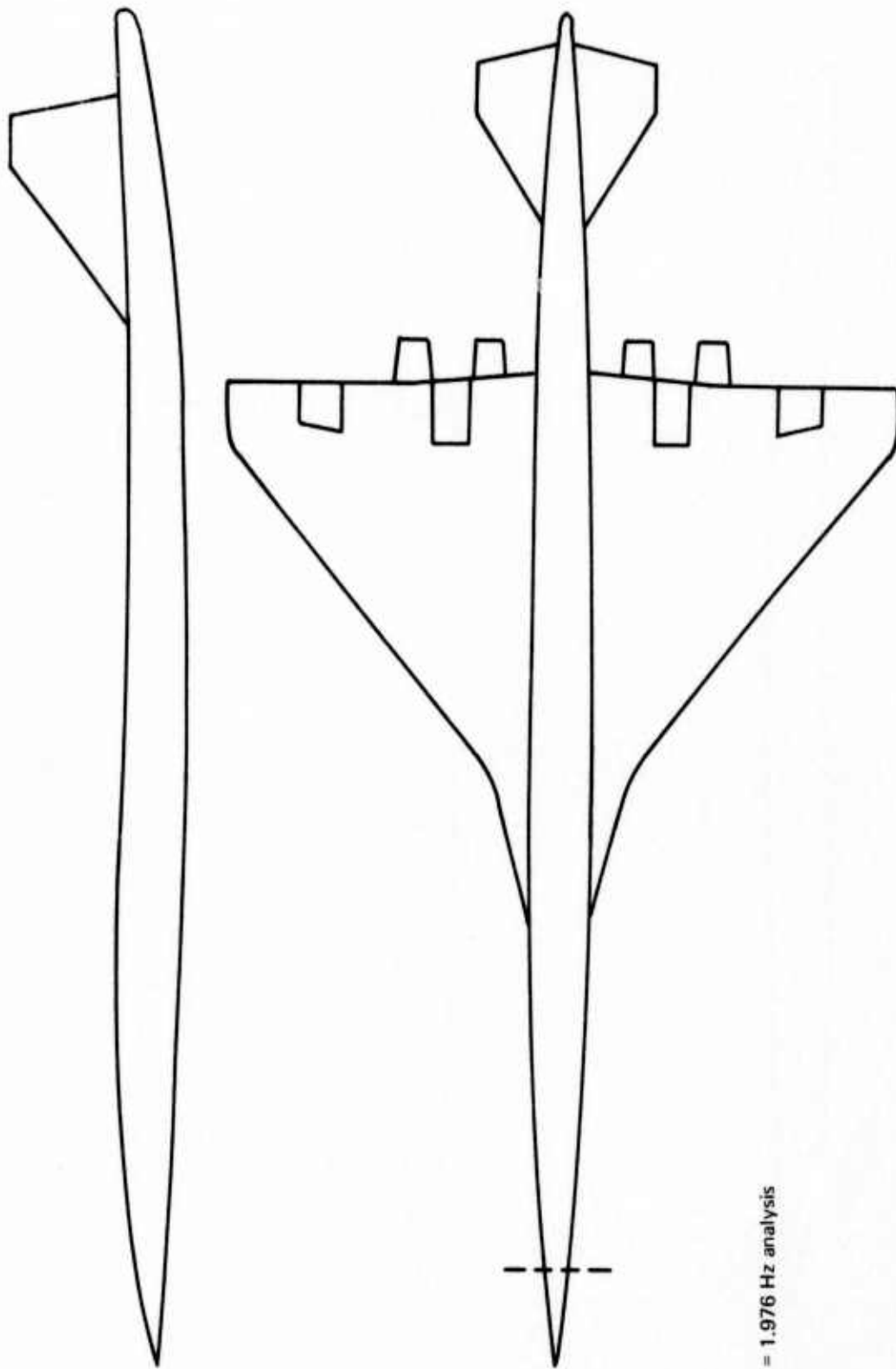


FIGURE 29.—COMPARISON OF LOAD/DEFLECTION CURVES—LOAD POINT 42



Freq. = .712 Hz analysis

FIGURE 30.—SYMMETRIC VIBRATION MODE 1



Freq. = 1.976 Hz analysis

FIGURE 31.—SYMMETRIC VIBRATION MODE 2

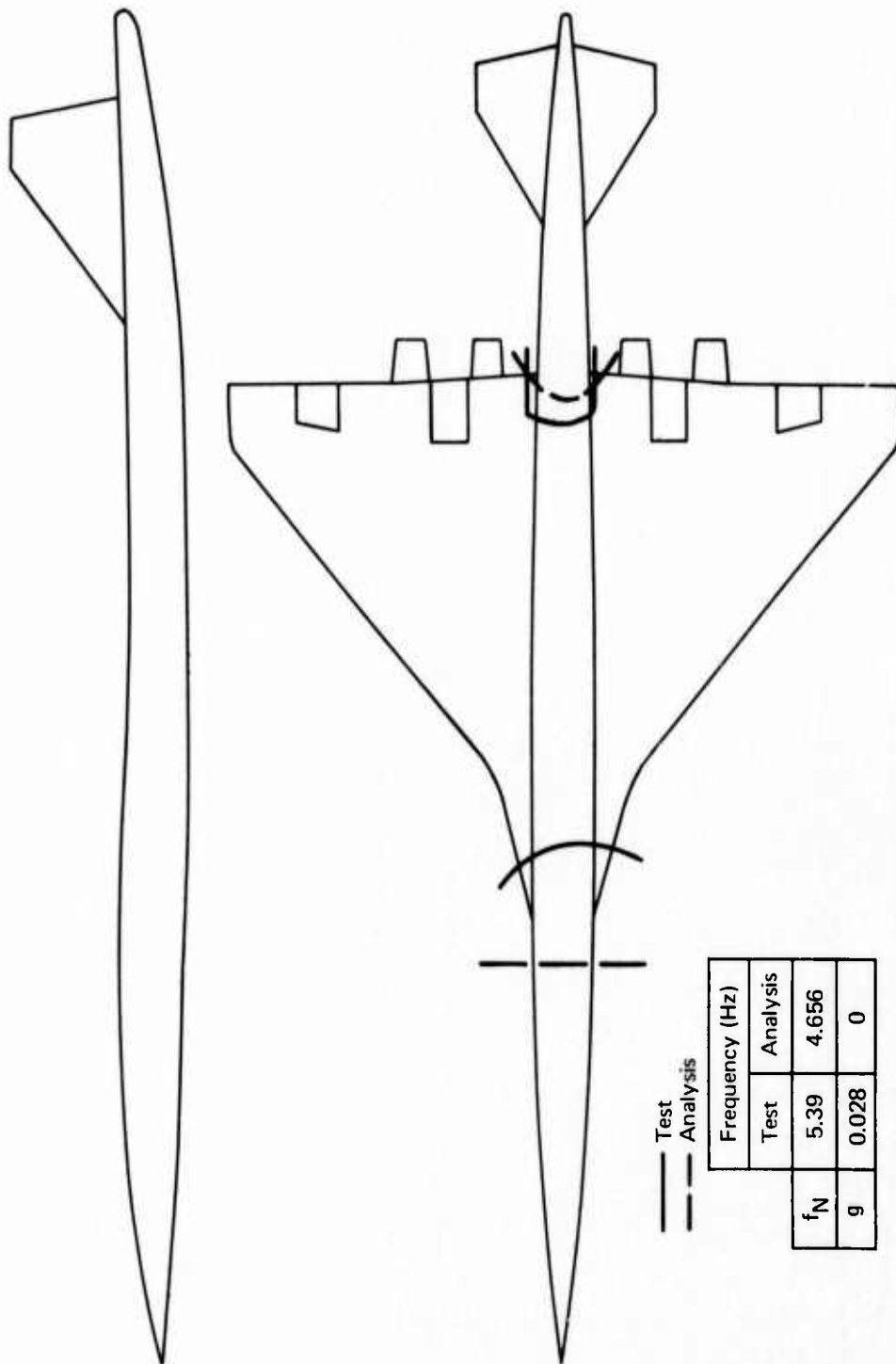


FIGURE 32.—SYMMETRIC VIBRATION MODE 3

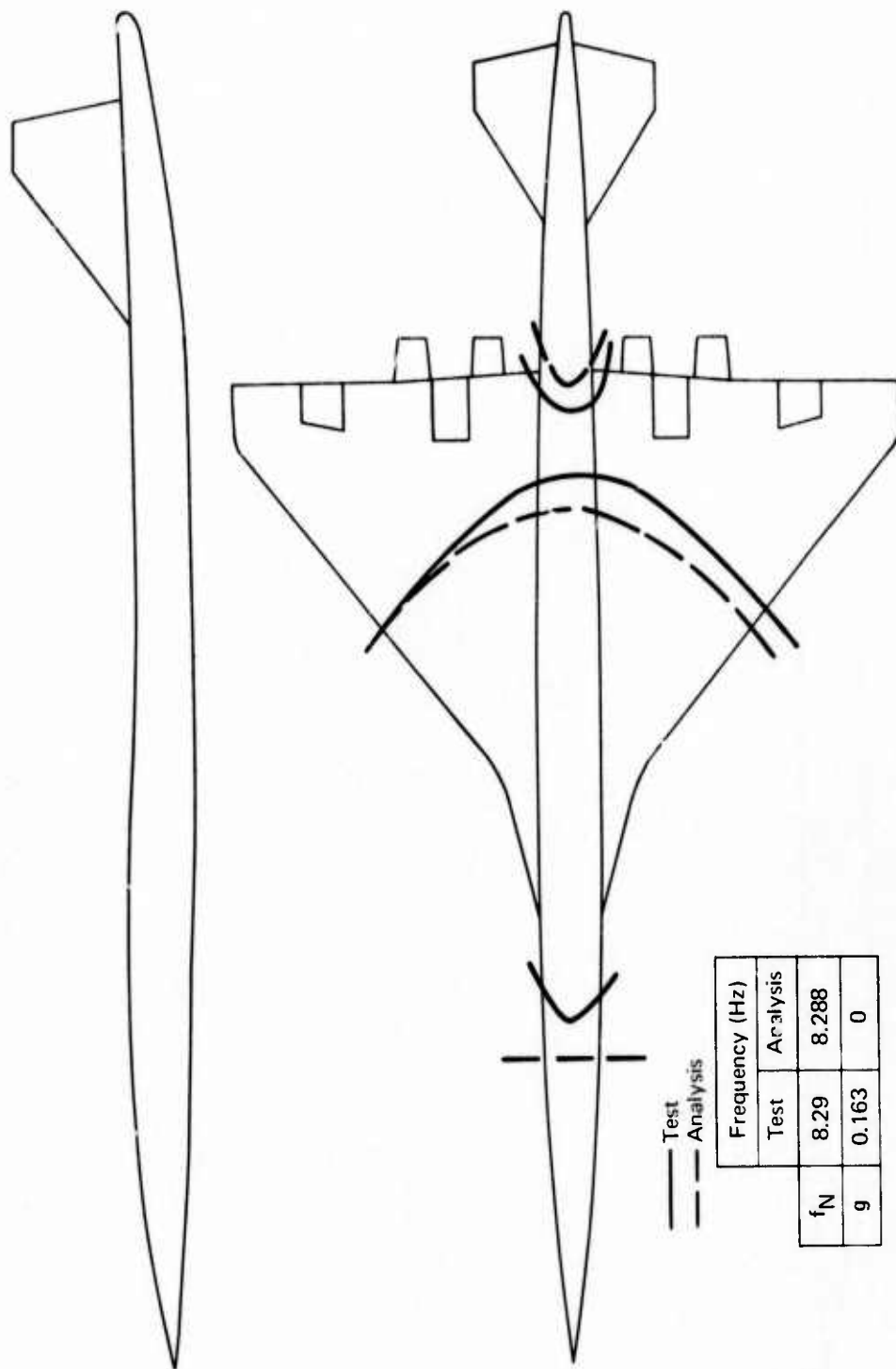


FIGURE 33.—SYMMETRIC VIBRATION MODE 4

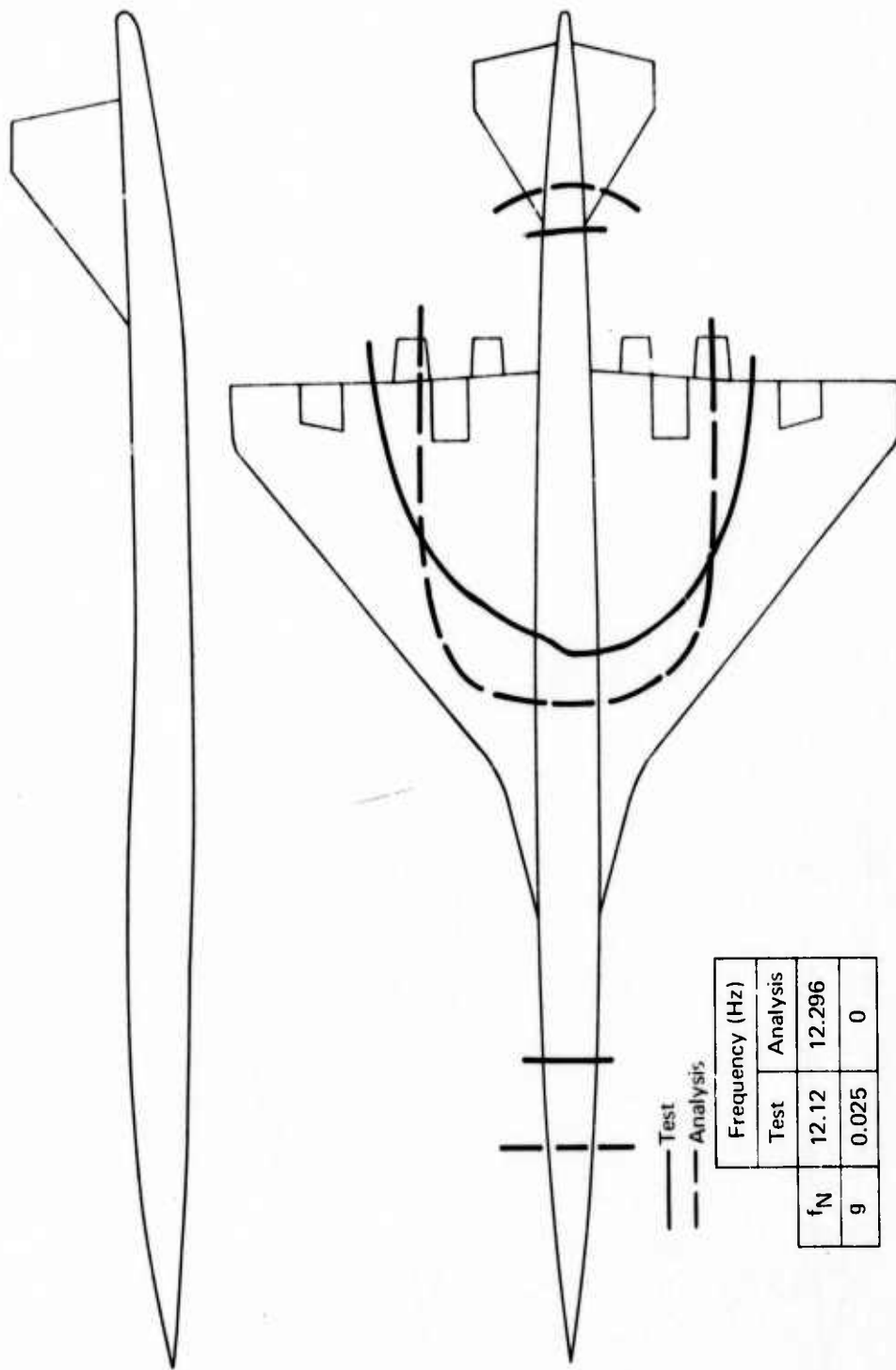
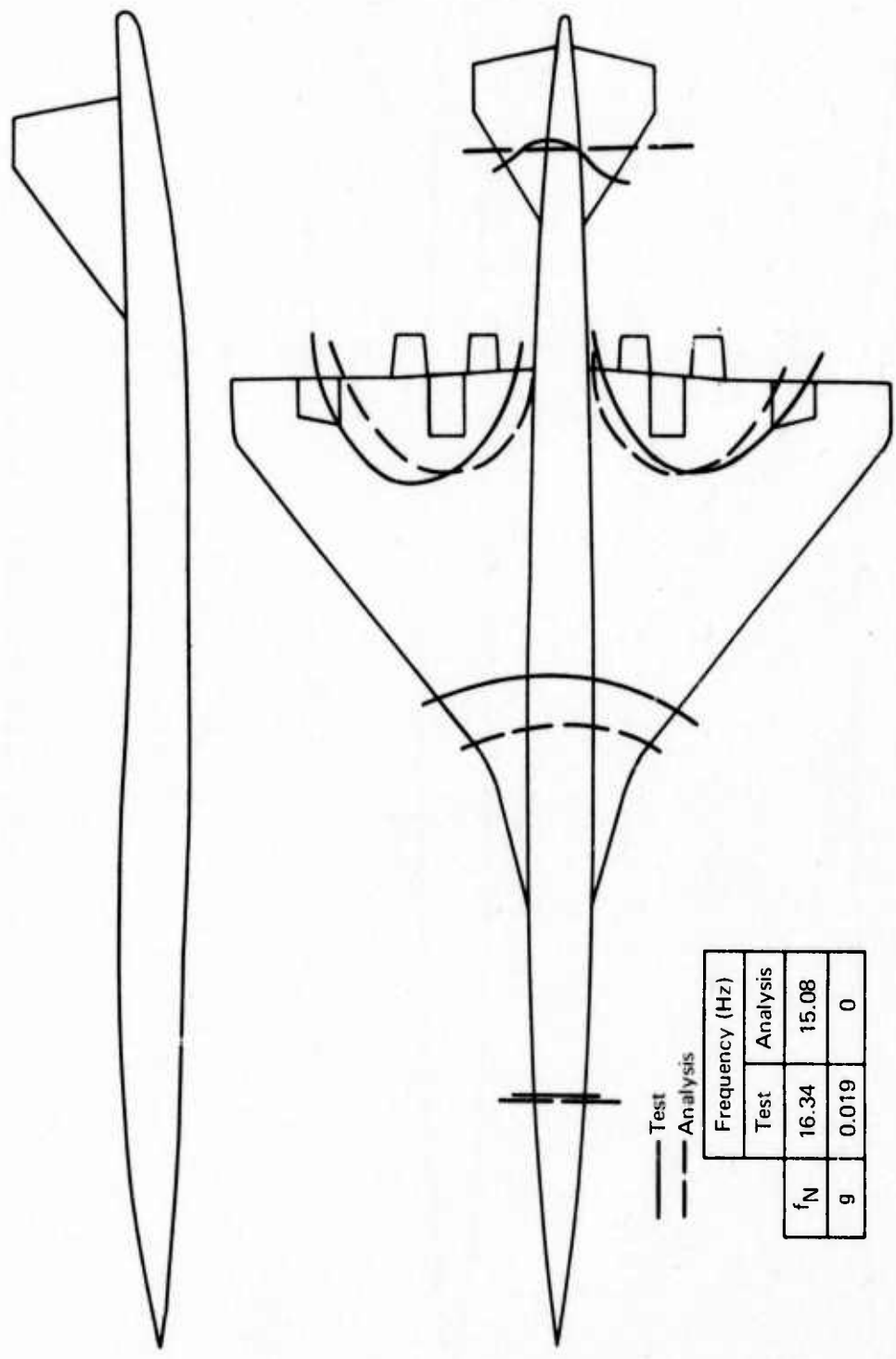
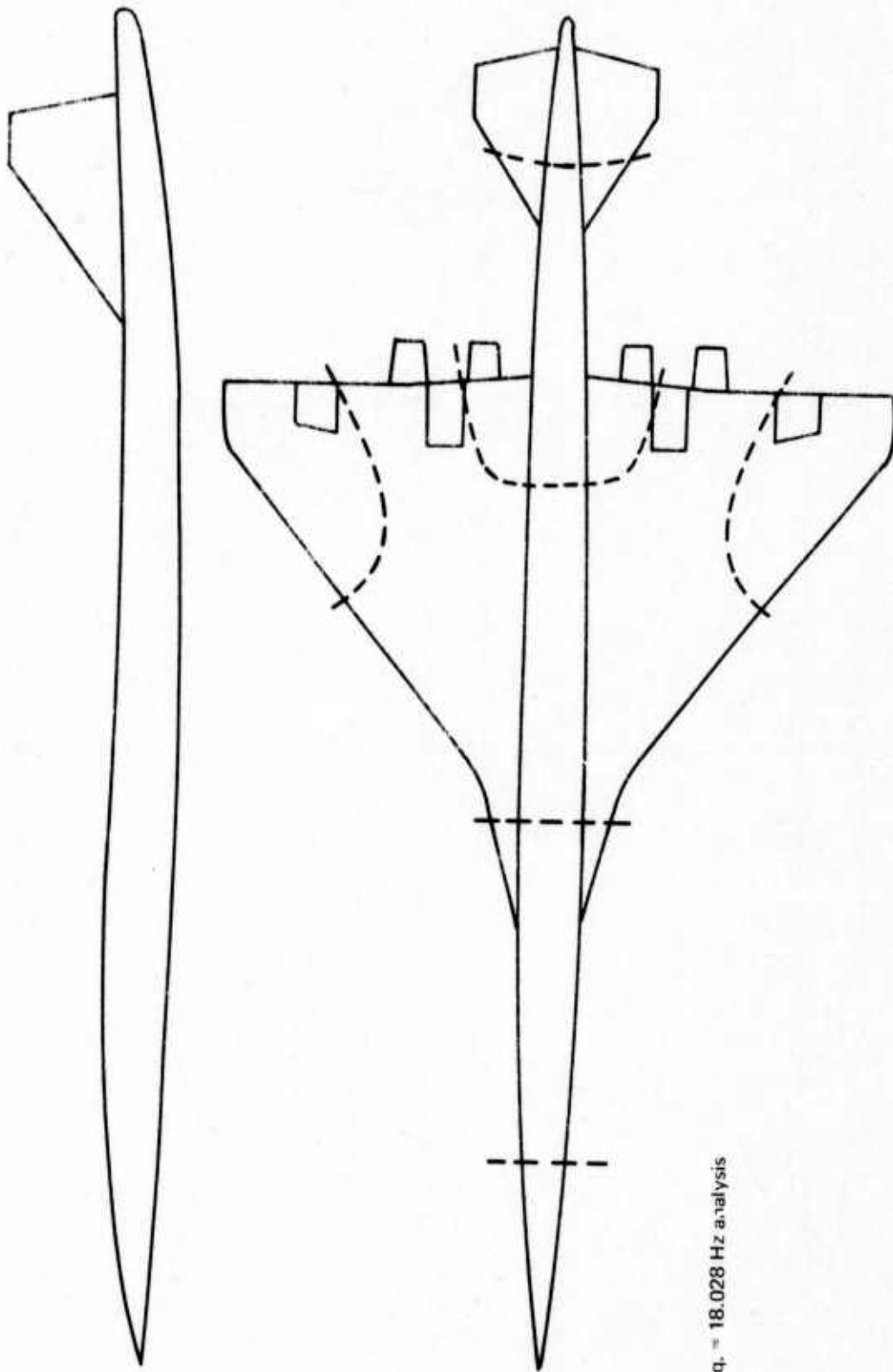


FIGURE 34.—SYMMETRIC VIBRATION MODE 5



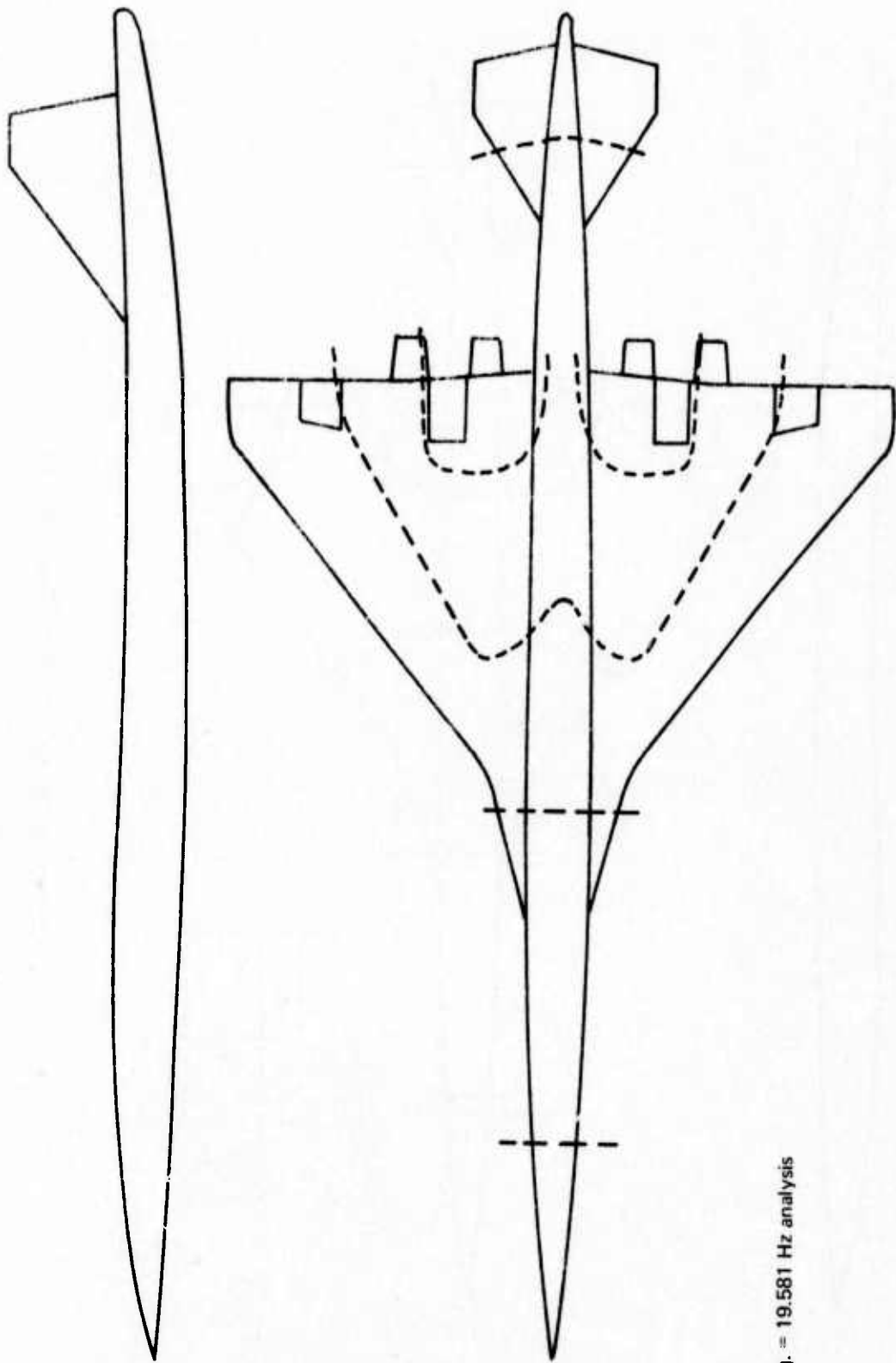
		Frequency (Hz)	
		Test	Analysis
f_N	9	16.34	15.08
		0.019	0

FIGURE 35.—SYMMETRIC VIBRATION MODE 6



Freq. = 18.028 Hz analysis

FIGURE 36.—SYMMETRIC VIBRATION MODE 7



Freq. = 19.581 Hz analysis

FIGURE 37.—SYMMETRIC VIBRATION MODE 8

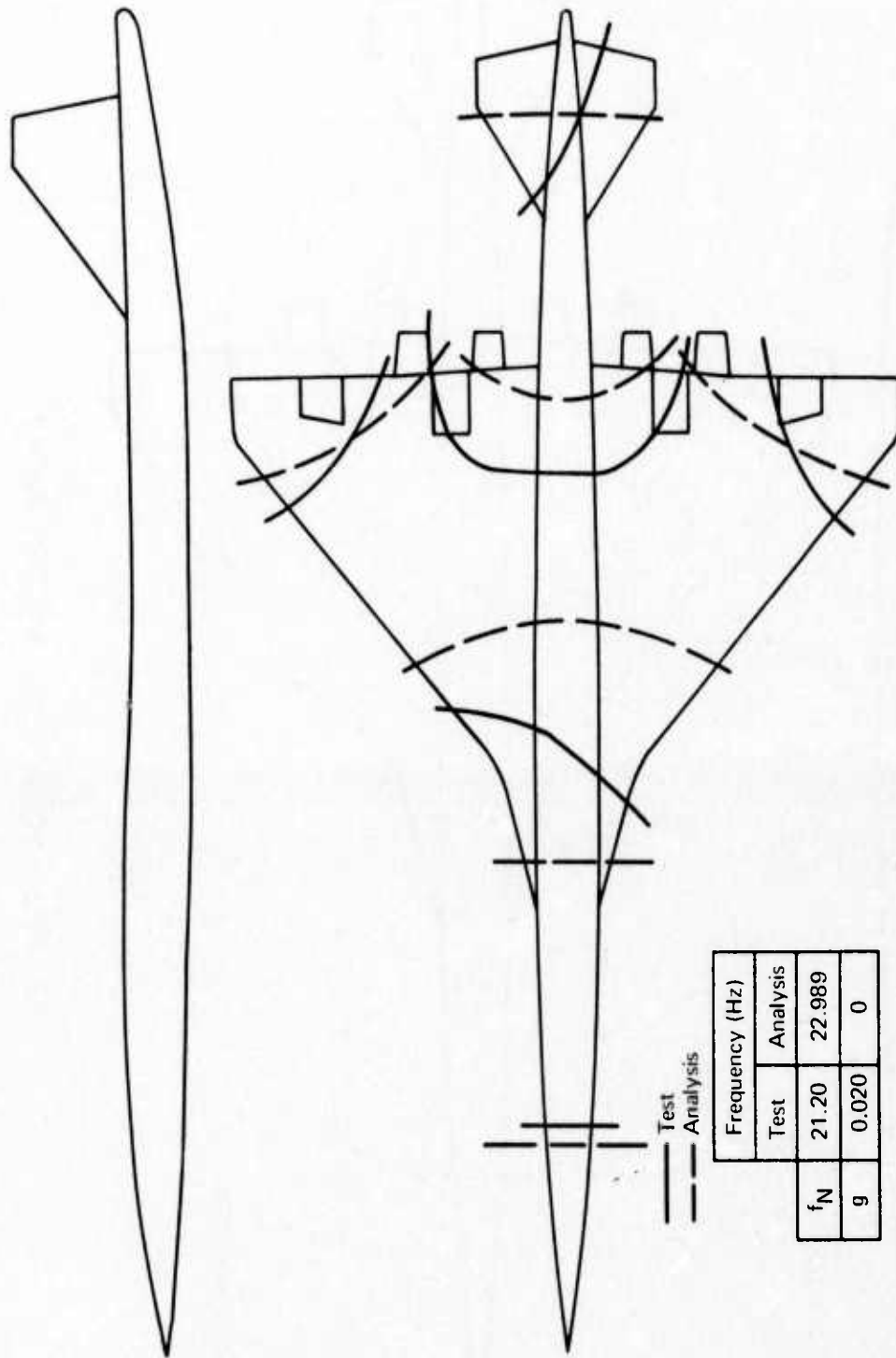
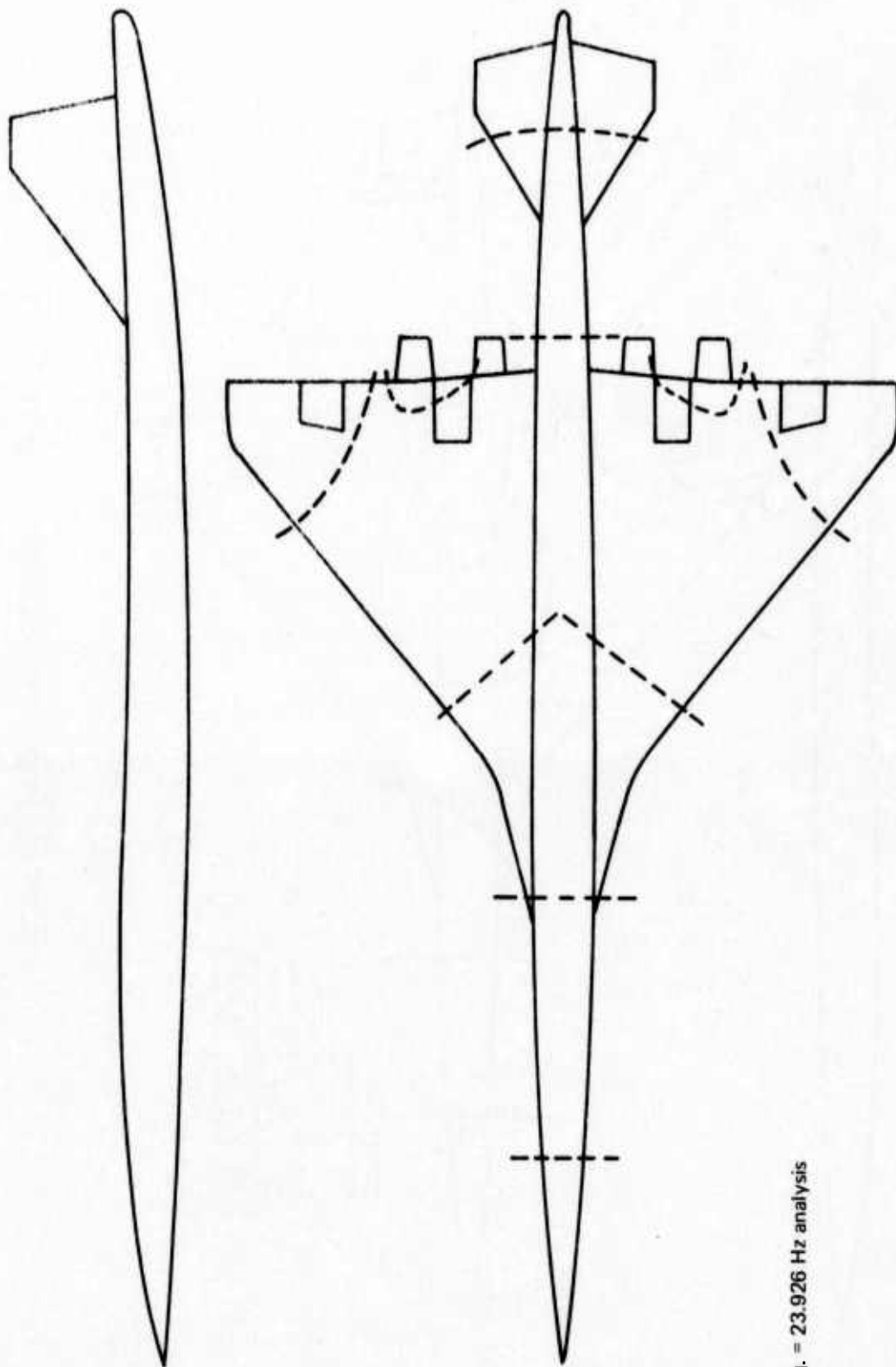


FIGURE 38.—SYMMETRIC VIBRATION MODE 9



Freq. = 23.926 Hz analysis

FIGURE 39.--SYMMETRIC VIBRATION MODE 10

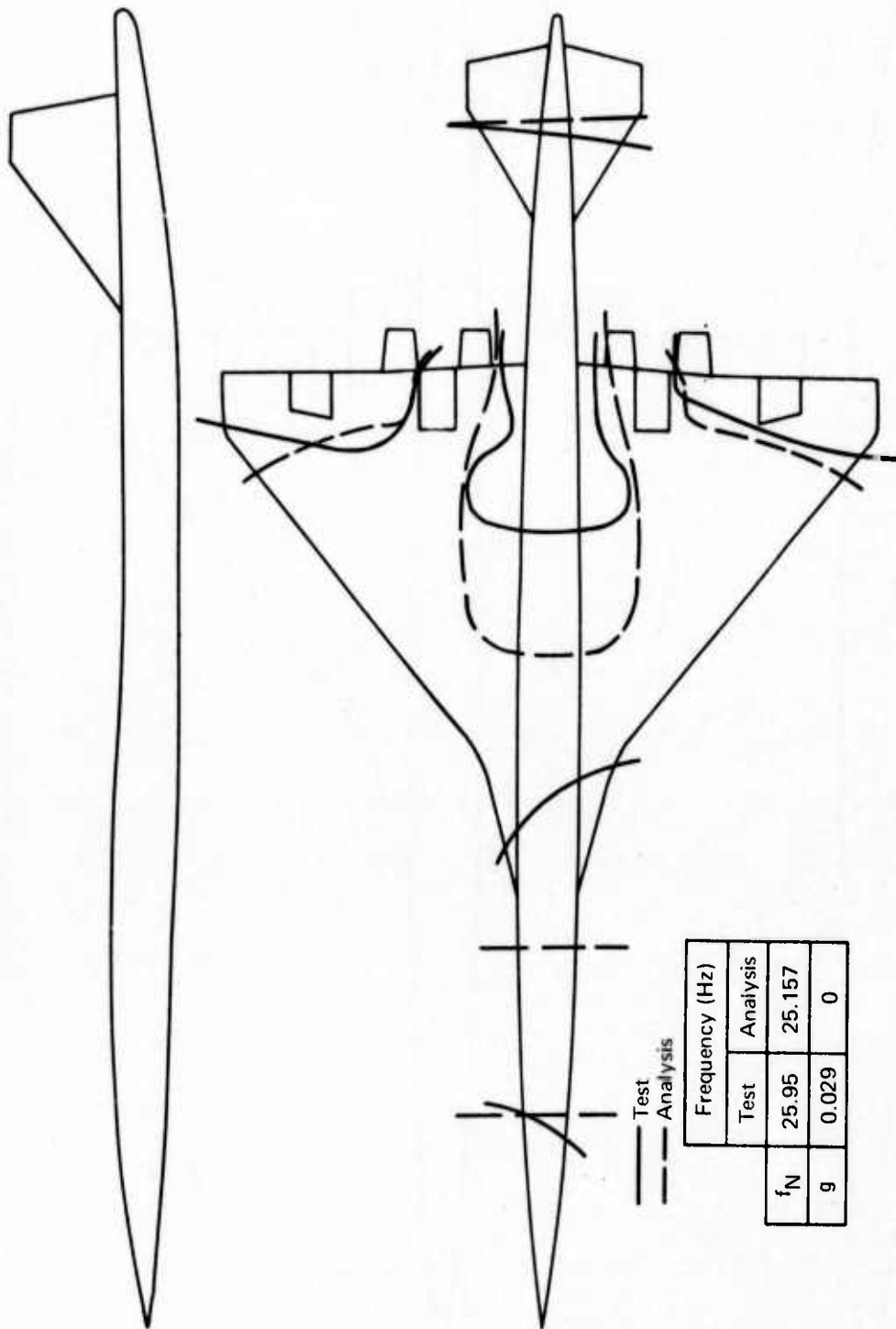
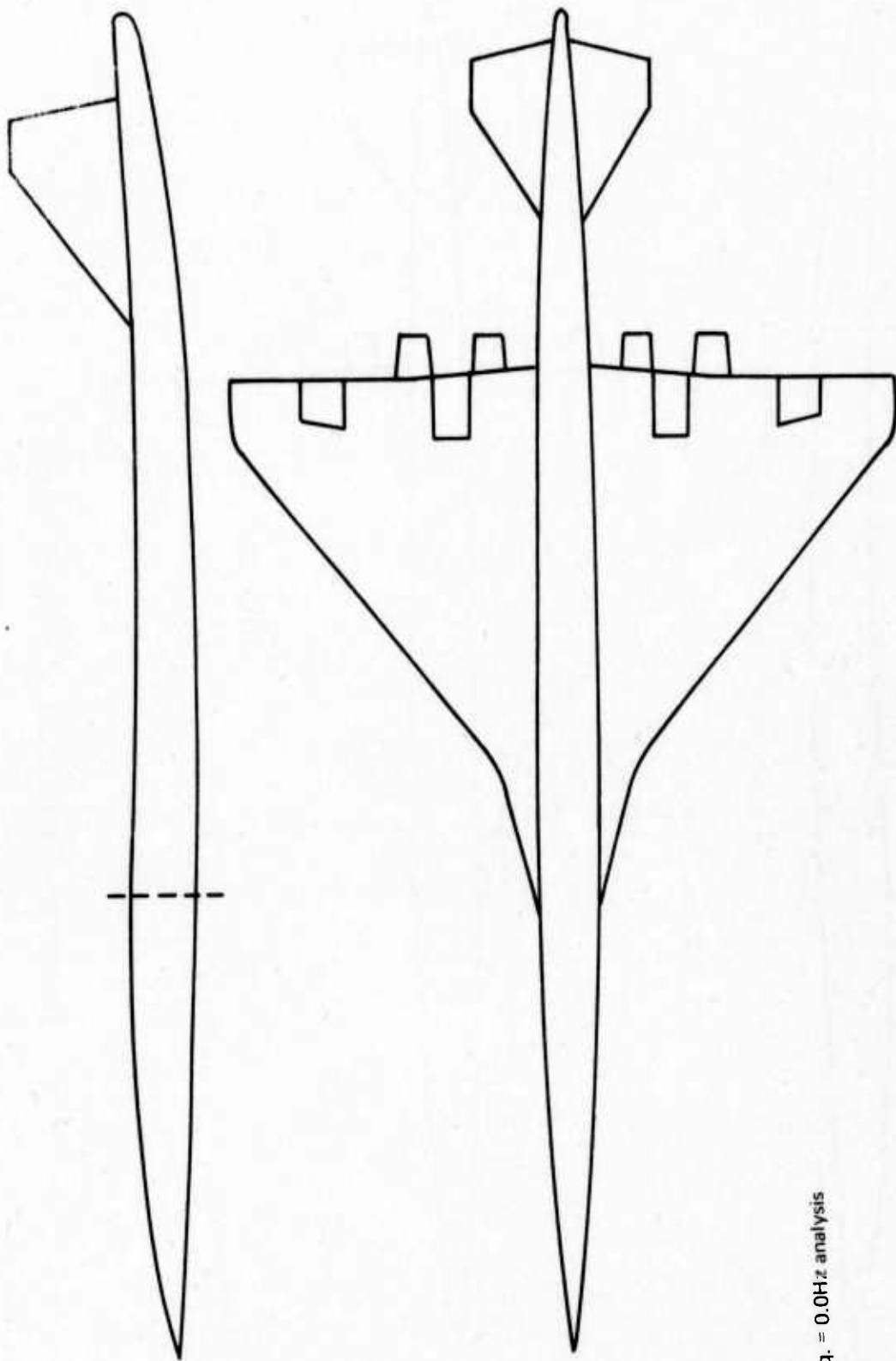
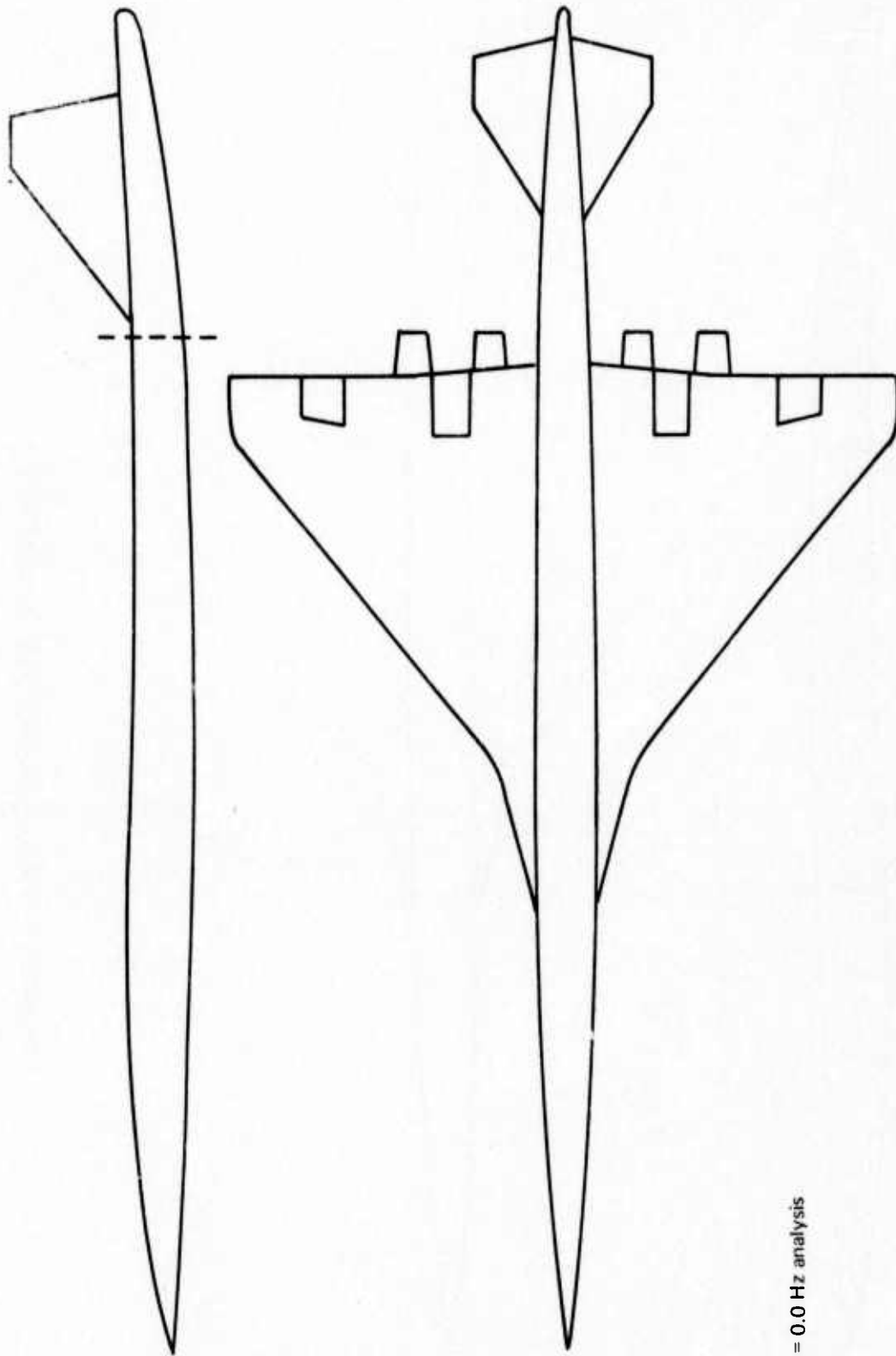


FIGURE 40.—SYMMETRIC VIBRATION MODE 11



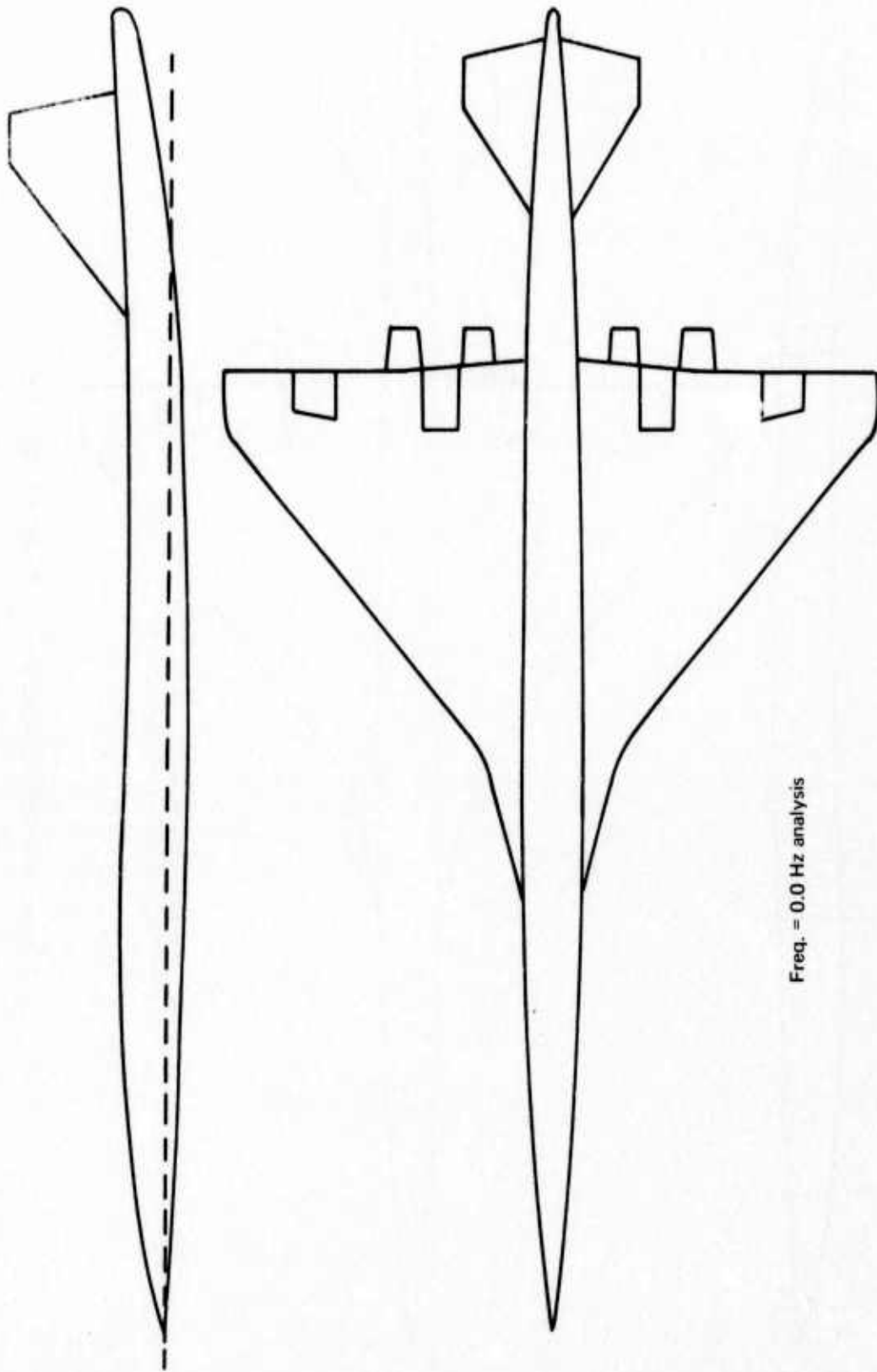
Freq. = 0.0Hz analysis

FIGURE 41.--ANTISYMMETRIC VIBRATION MODE 1



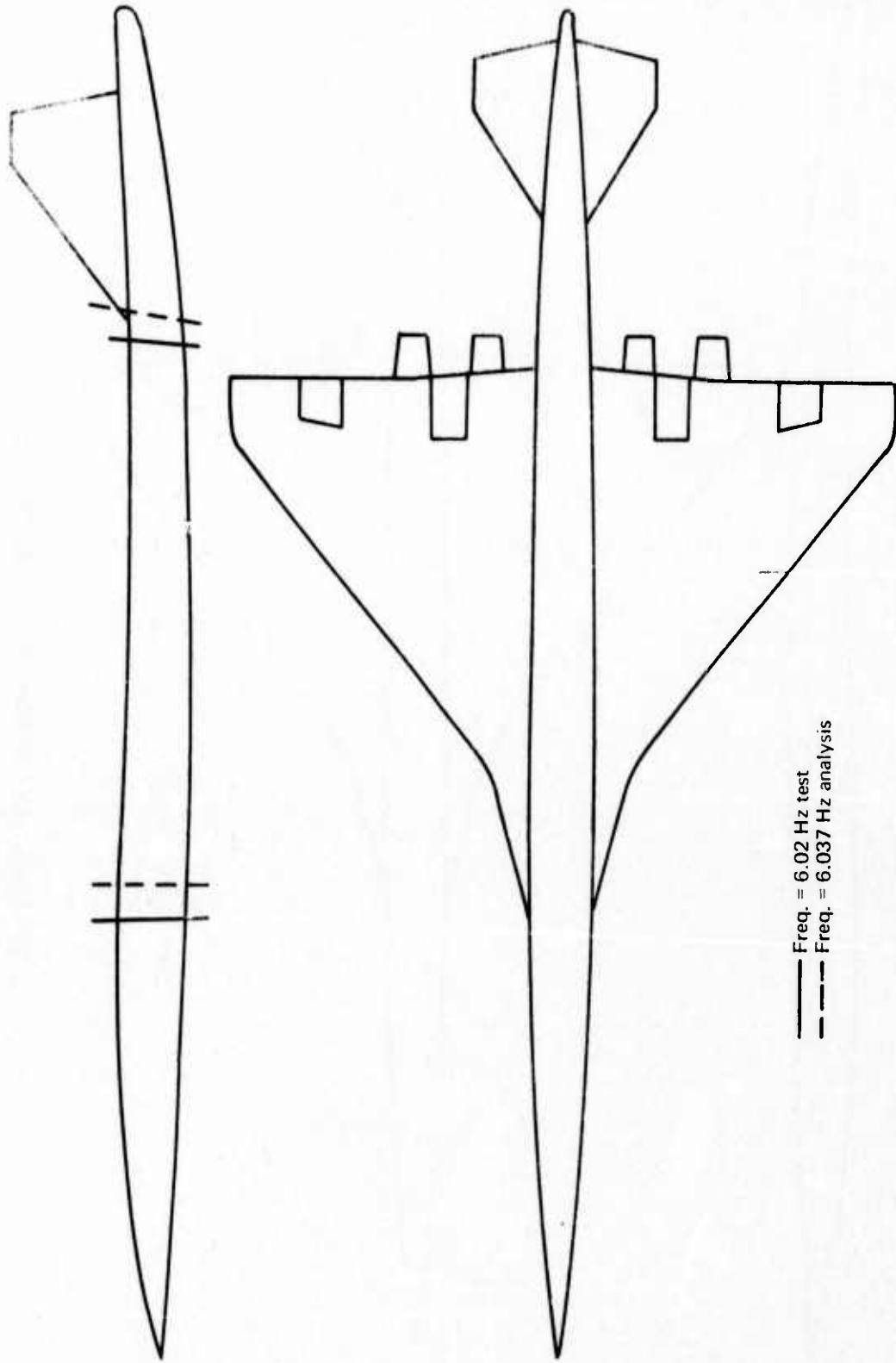
Freq. = 0.0 Hz analysis

FIGURE 42.—ANTISYMMETRIC VIBRATION MODE 2



Freq. = 0.0 Hz analysis

FIGURE 43.—ANTISYMMETRIC VIBRATION MODE 3



— Freq. = 6.02 Hz test
- - - Freq. = 6.037 Hz analysis

FIGURE 44.—ANTISYMMETRIC VIBRATION MODE 4

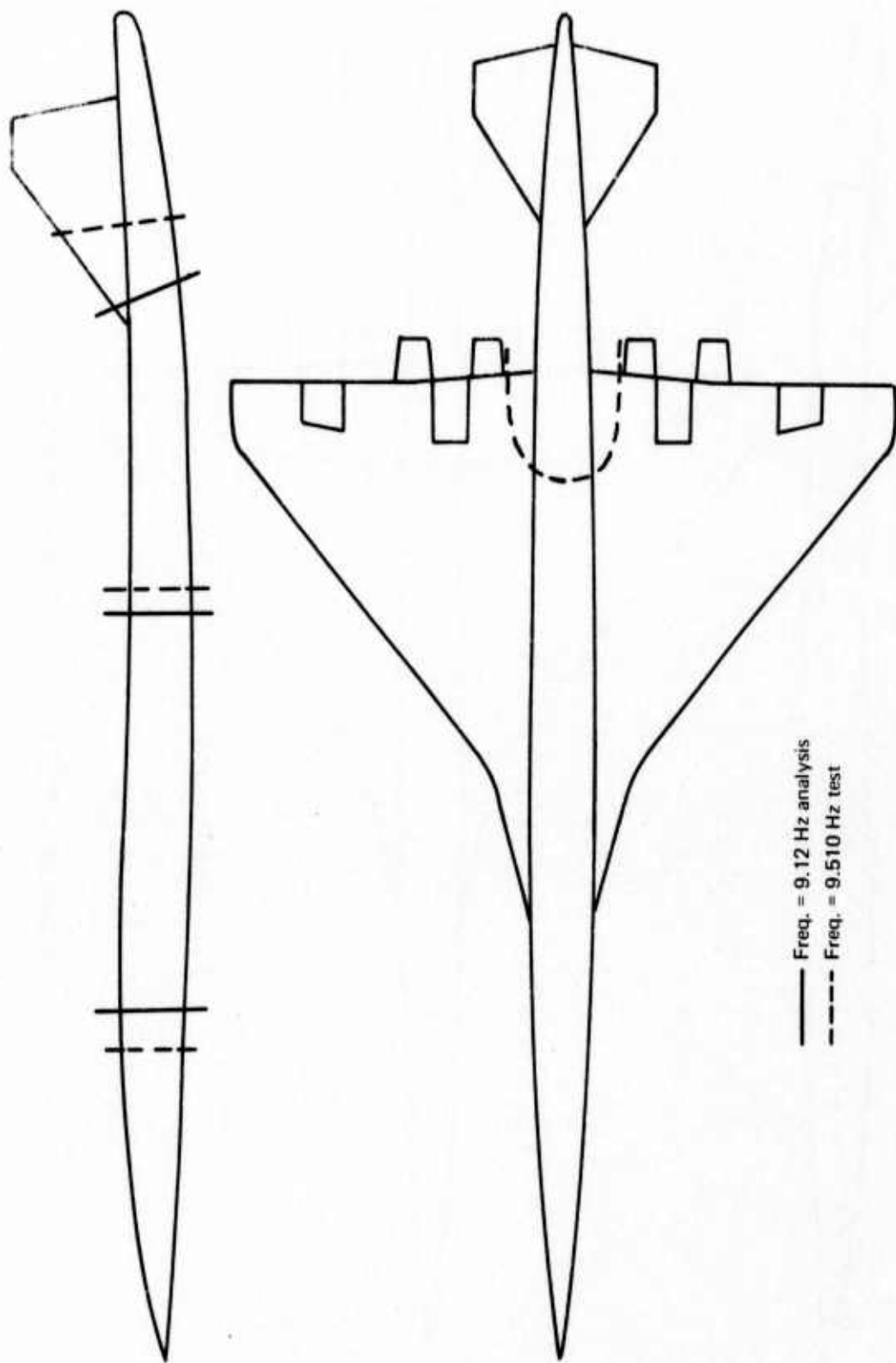
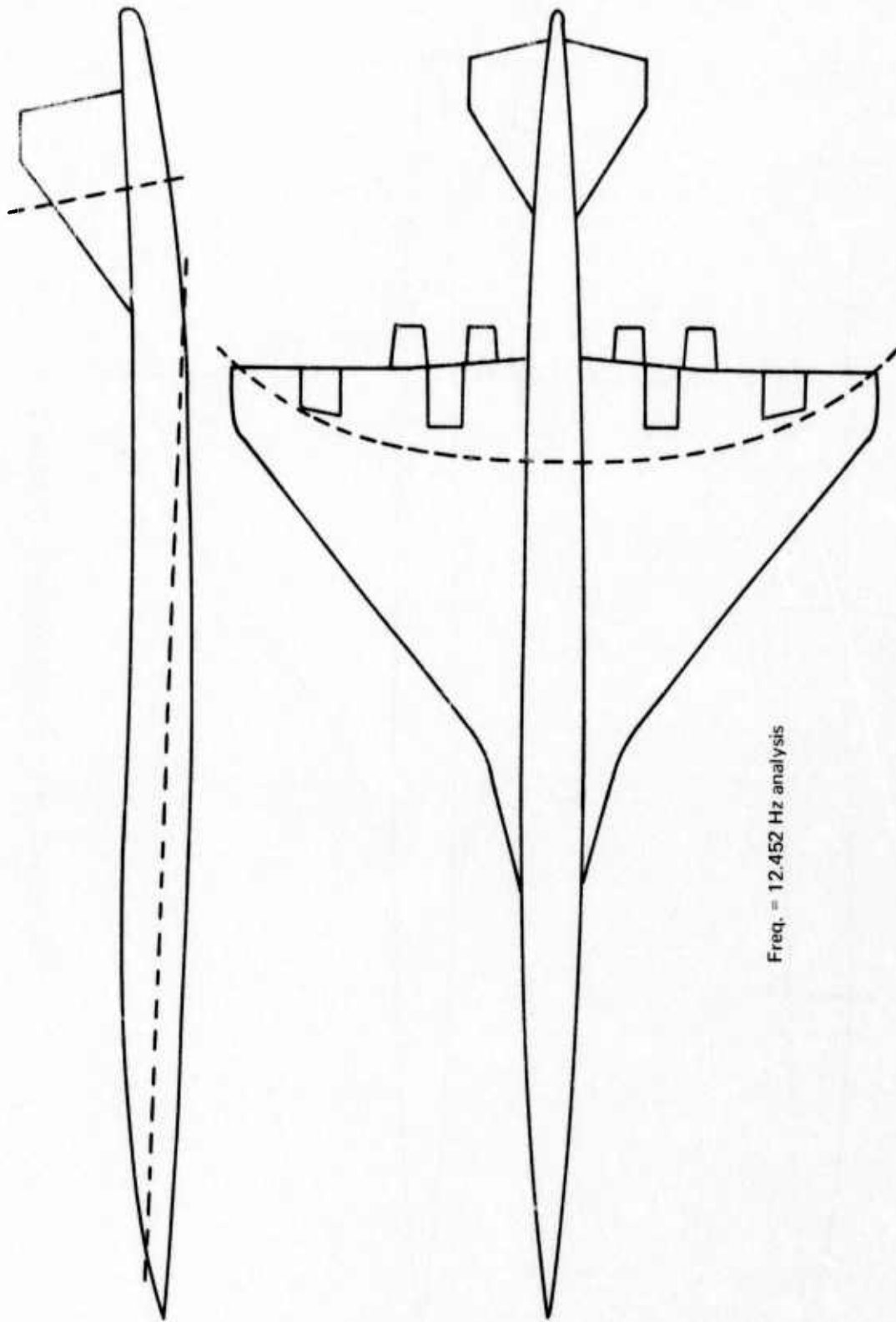


FIGURE 45.—ANTISYMMETRIC VIBRATION MODE 5



Freq. = 12.452 Hz analysis

FIGURE 46.—ANTISYMMETRIC VIBRATION MODE 6

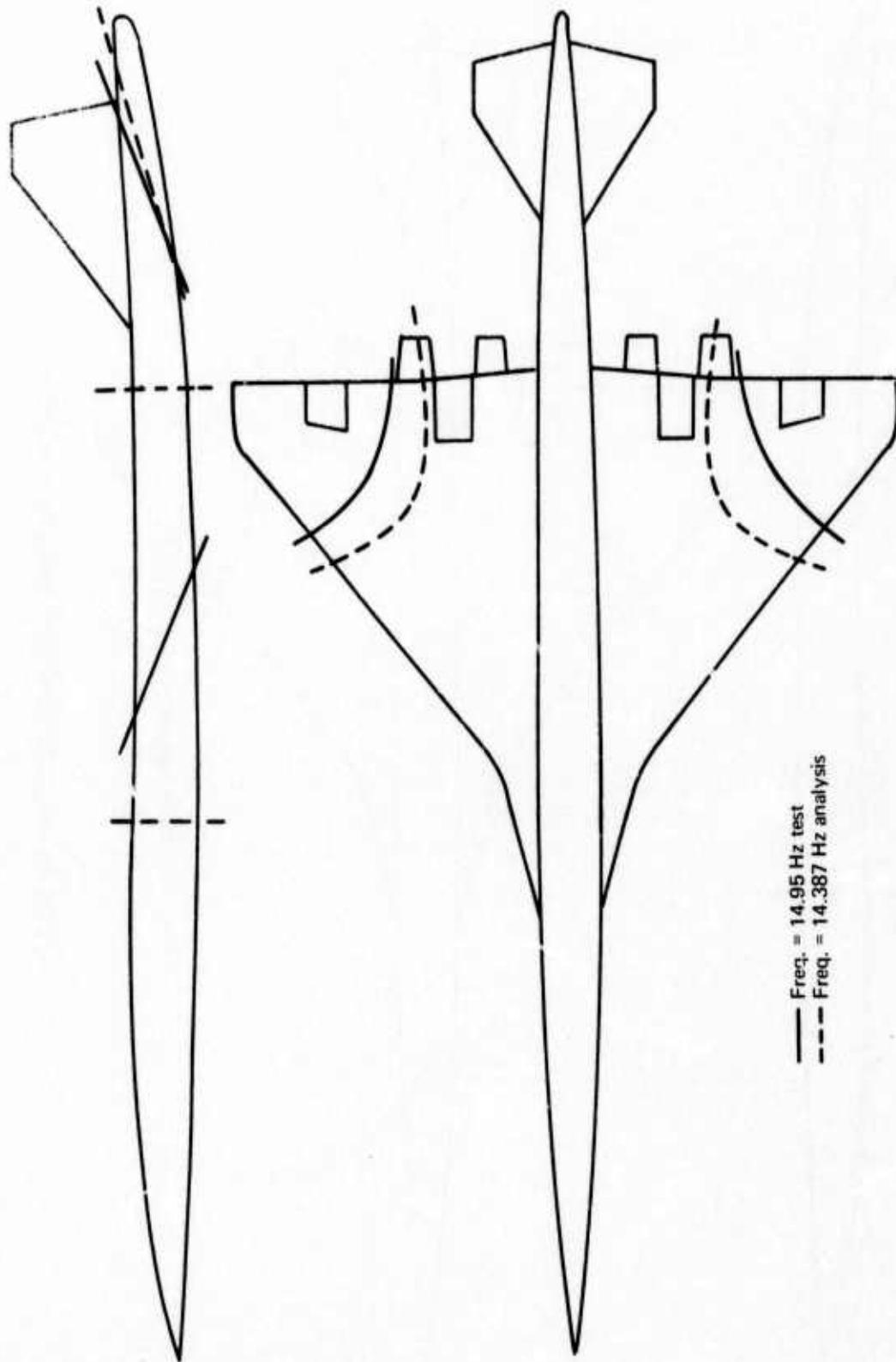
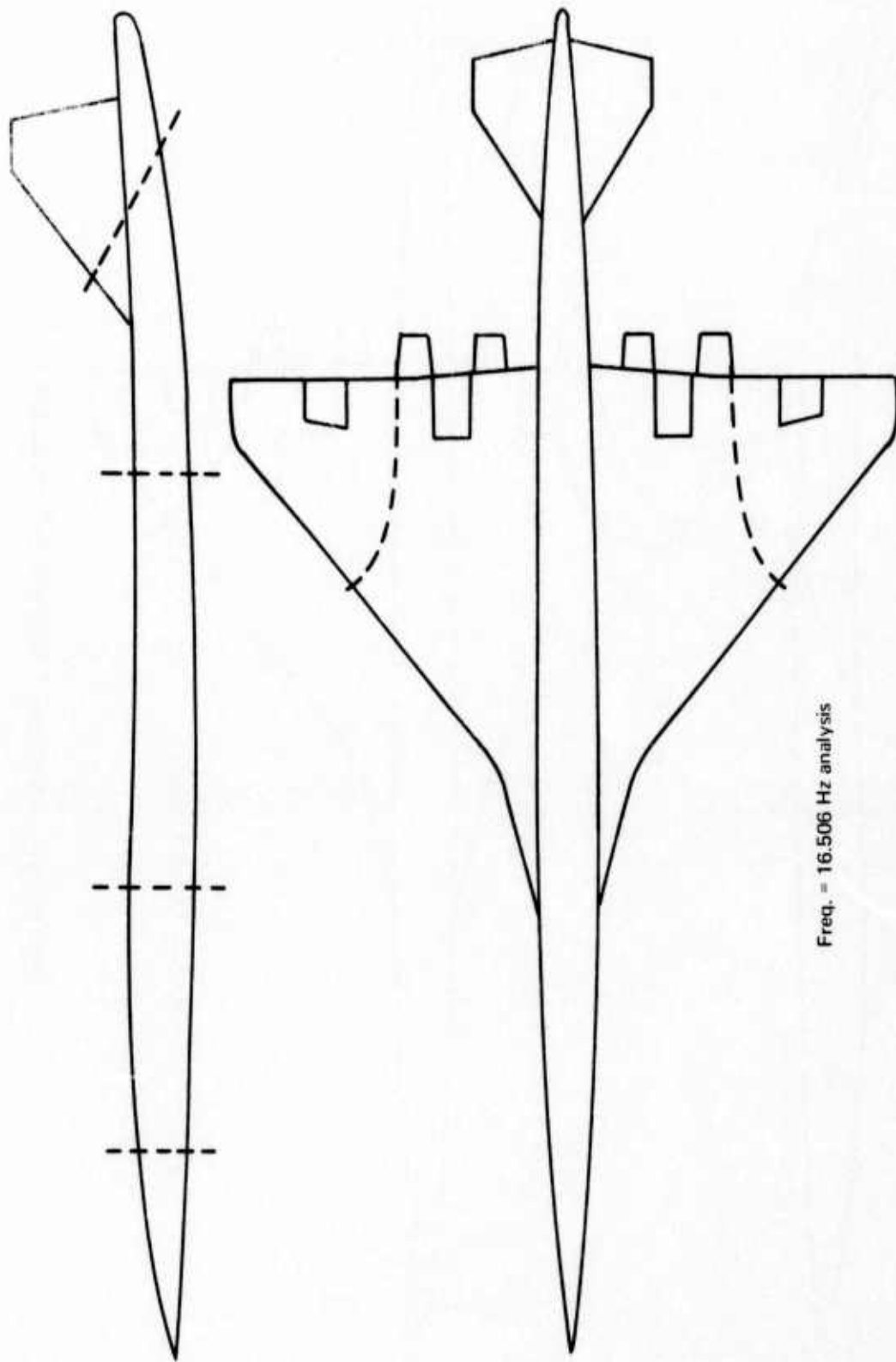
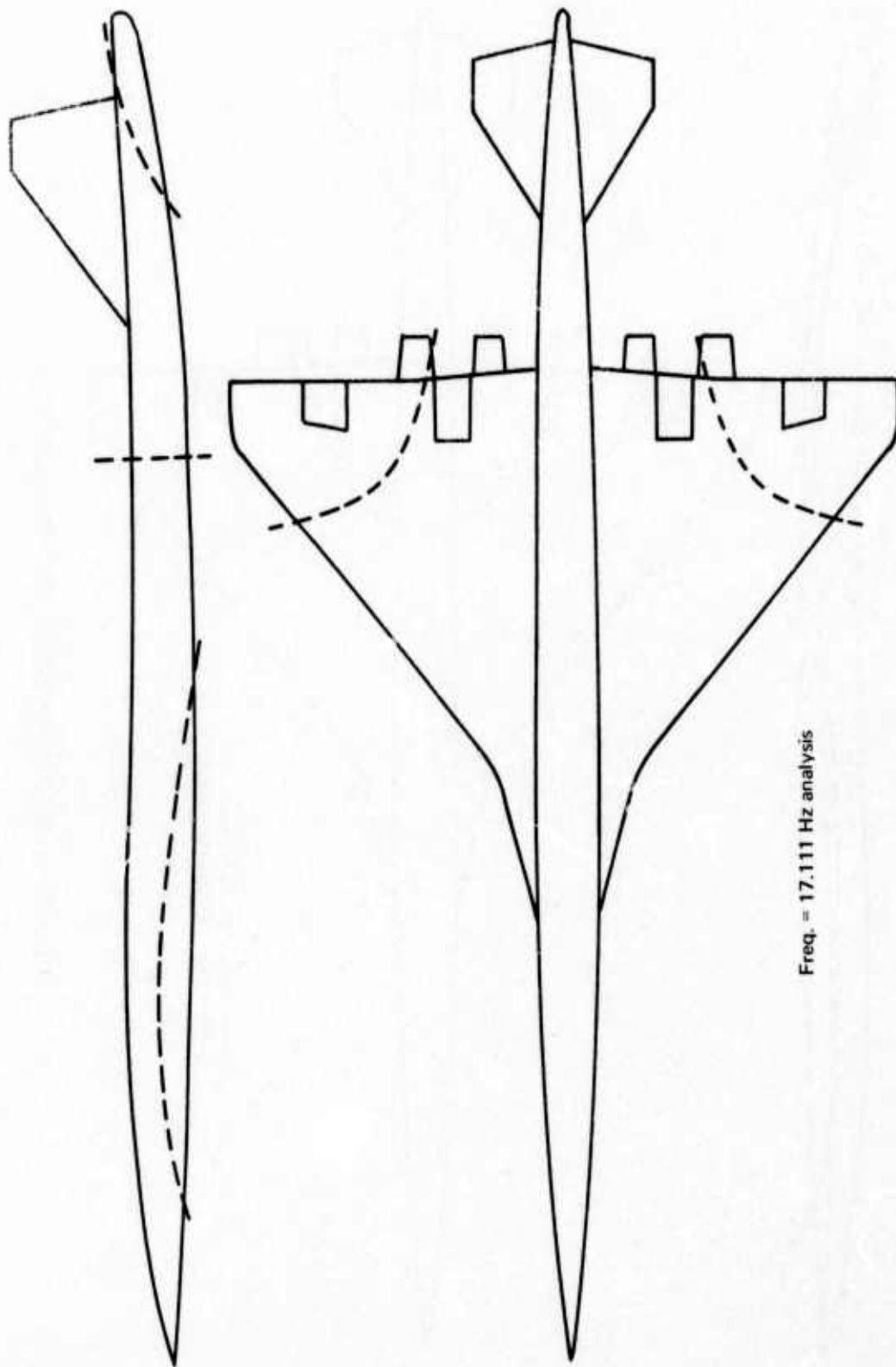


FIGURE 47.—ANTISYMMETRIC VIBRATION MODE 7



Freq. = 16.506 Hz analysis

FIGURE 48.—ANTISYMMETRIC VIBRATION MODE 8



Freq. = 17.111 Hz analysis

FIGURE 49.—ANTISYMMETRIC VIBRATION MODE 9

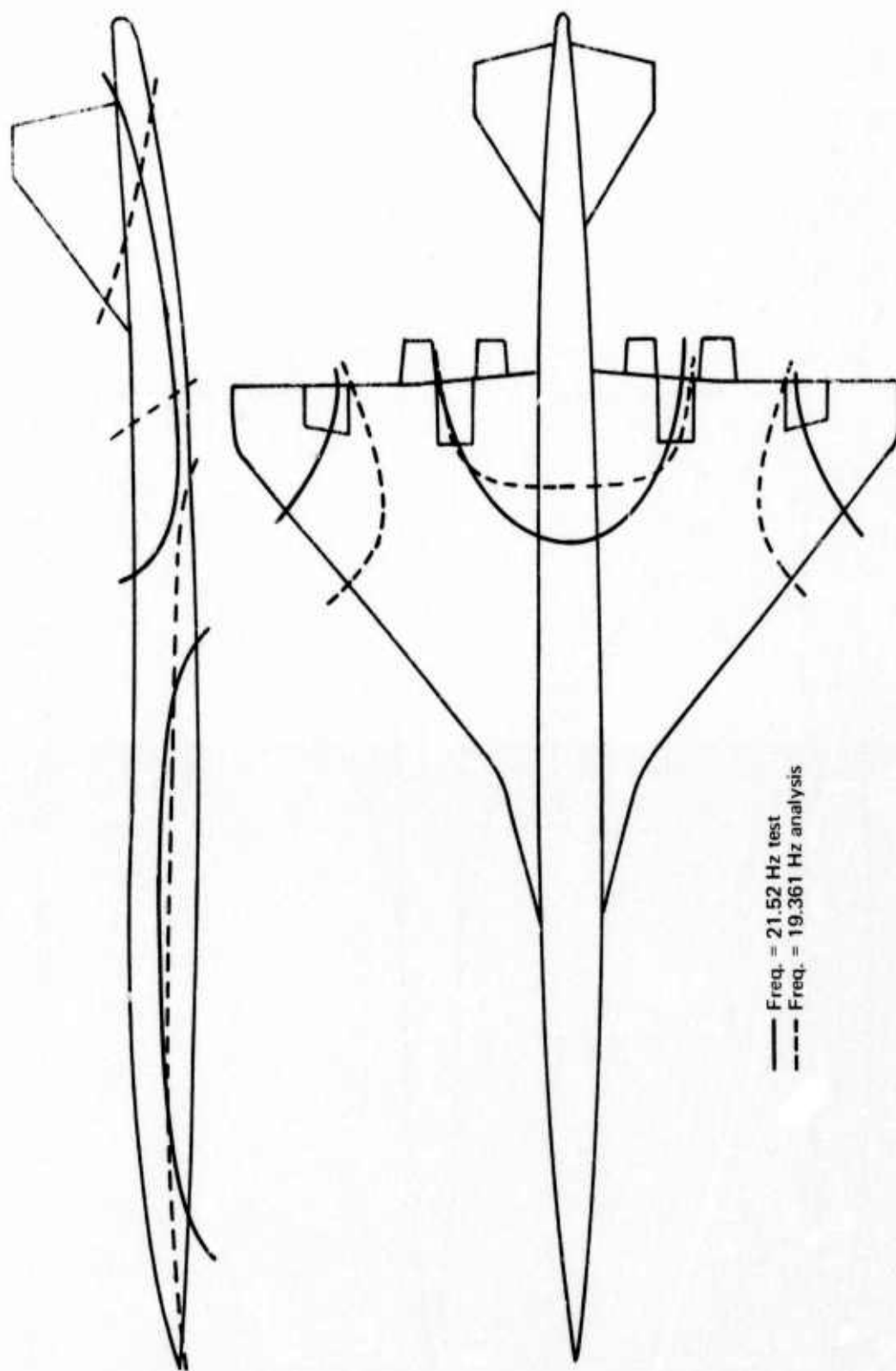
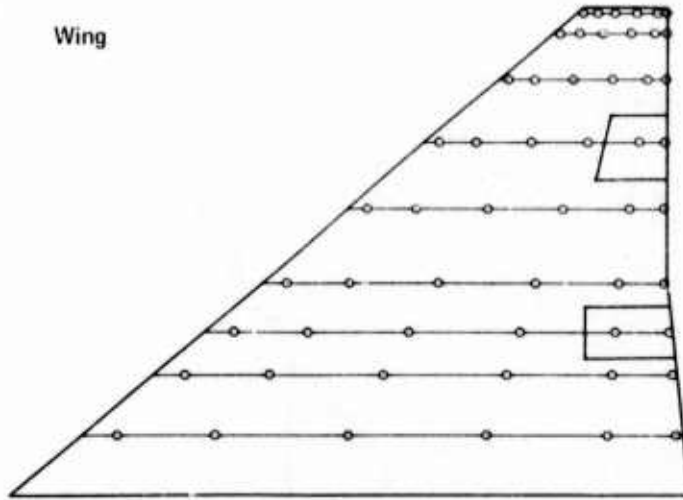
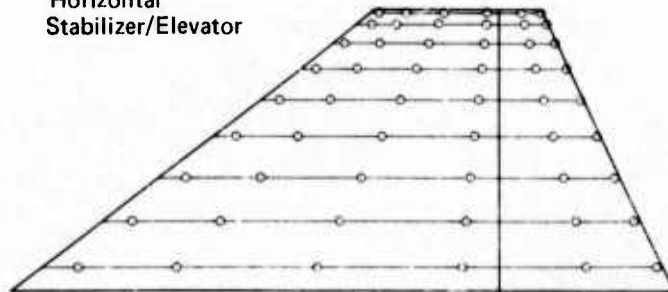


FIGURE 50.—ANTISYMMETRIC VIBRATION MODE 10

Wing



Horizontal Stabilizer/Elevator



Vertical Stabilizer

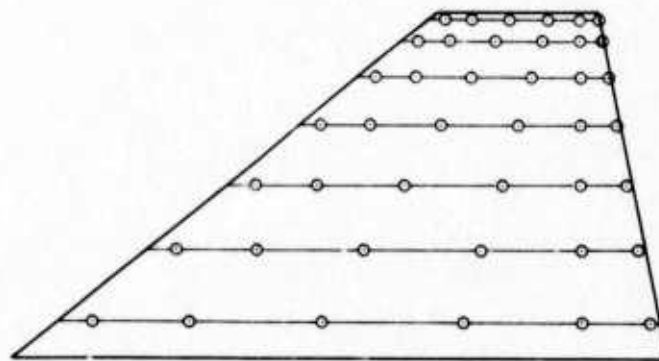


FIGURE 51.—AERODYNAMIC GRIDS

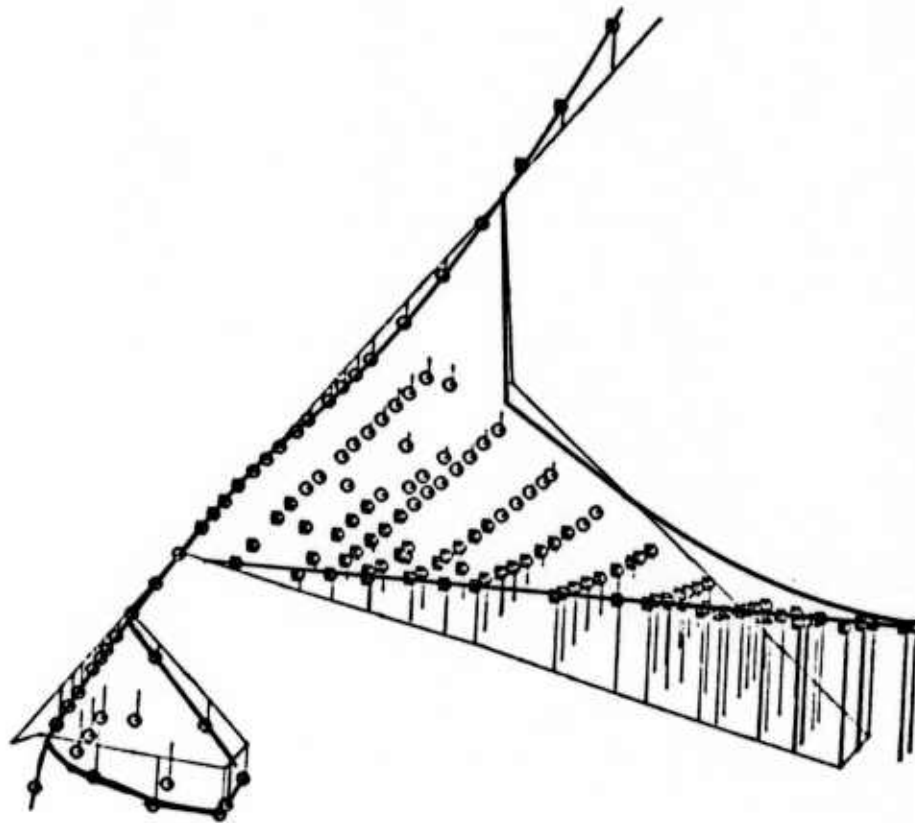


FIGURE 52.—PERSPECTIVE VIEW OF AN ANALYTICAL MODE SHAPE

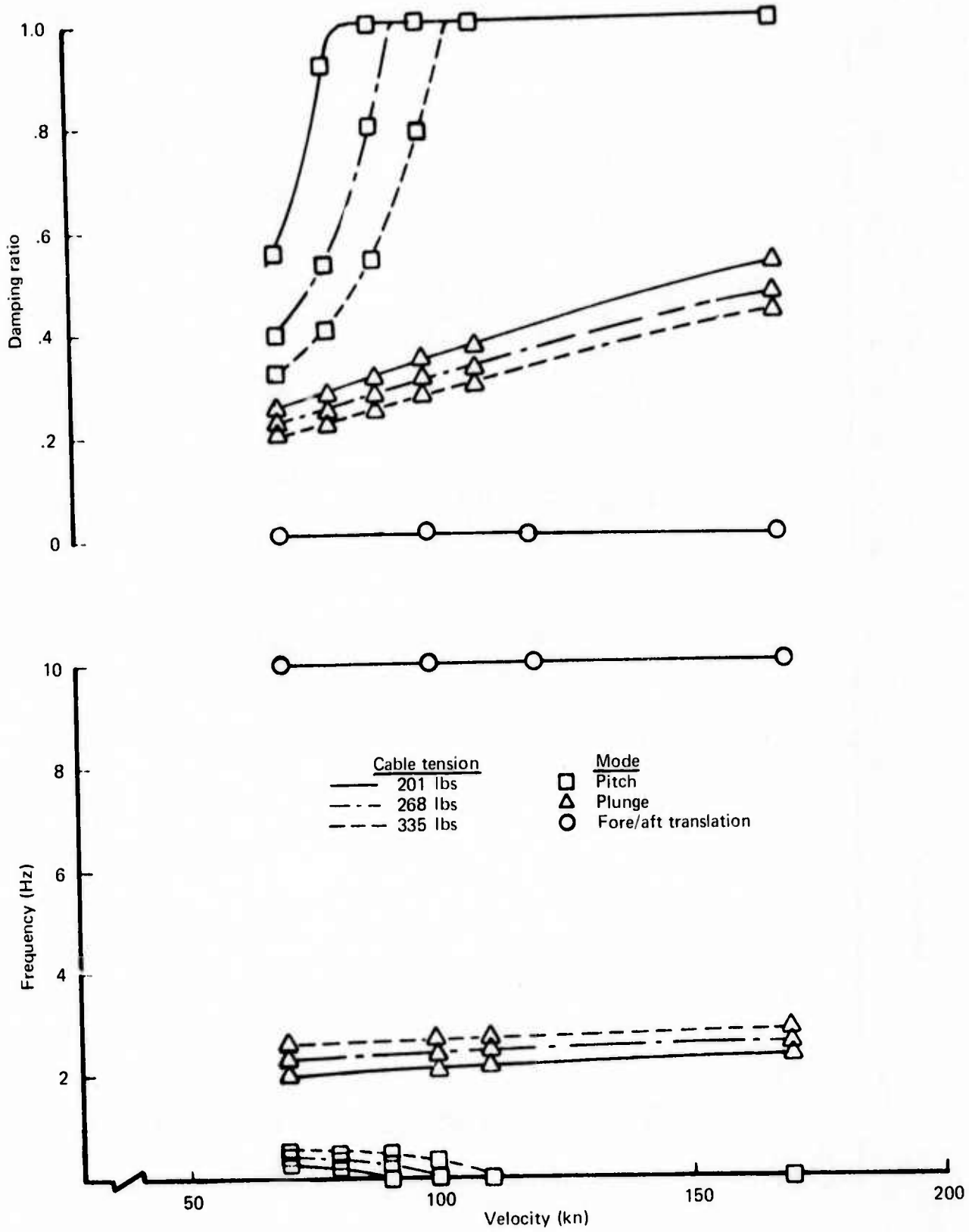


FIGURE 53.—STABILITY ANALYSIS—SYMMETRIC—51% C_R

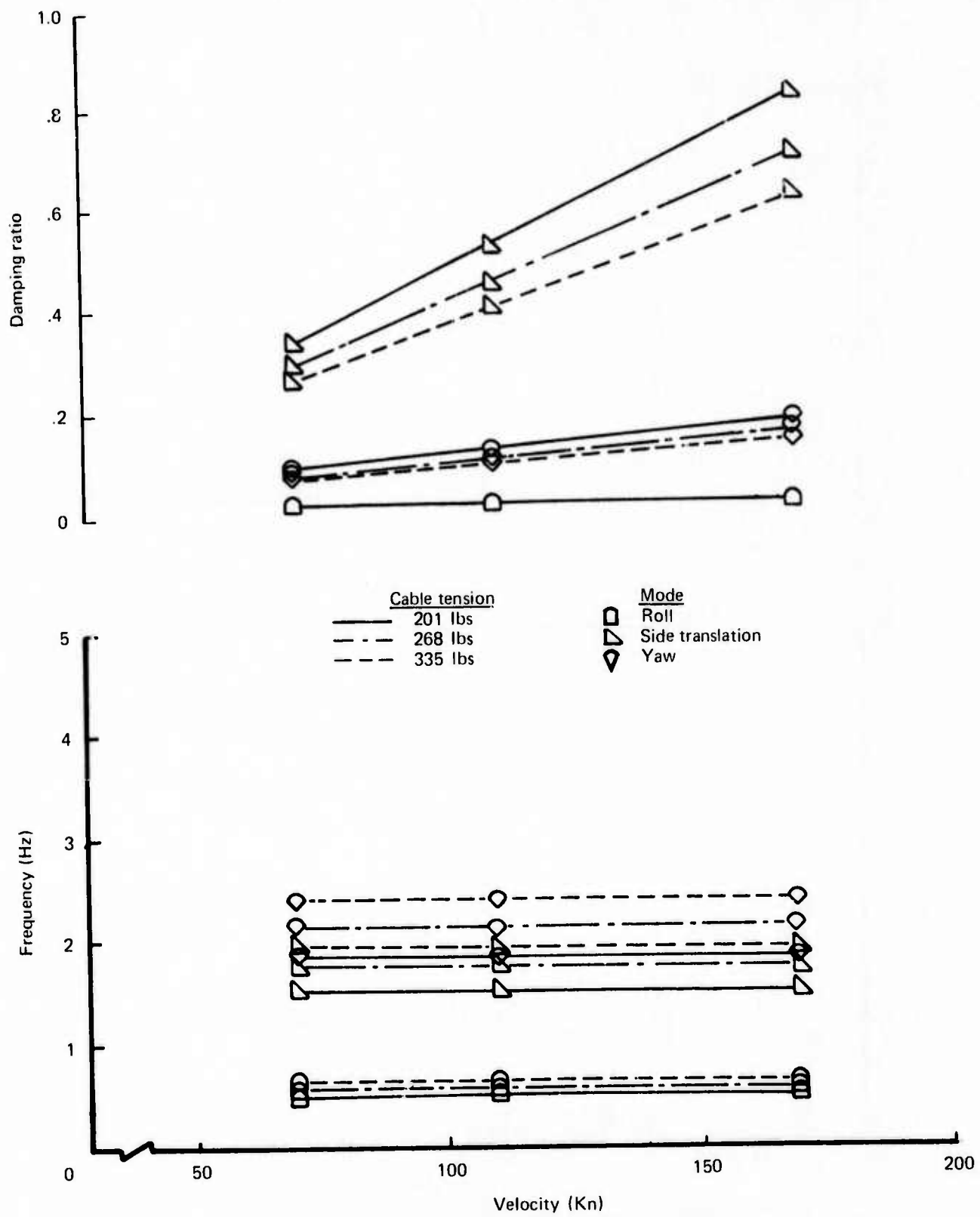


FIGURE 54.—STABILITY ANALYSIS—ANTISYMMETRIC—51% C_R

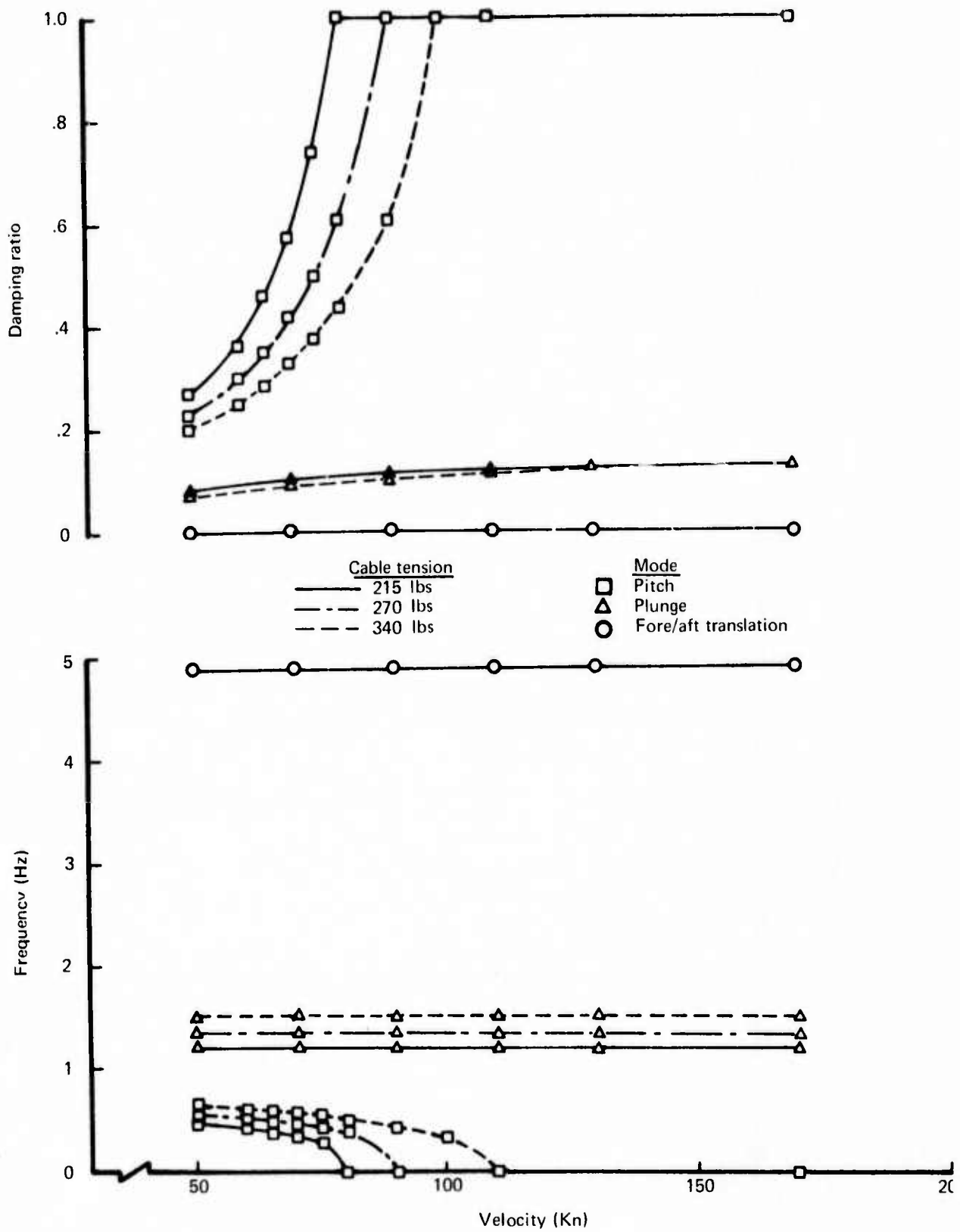


FIGURE 55.—STABILITY ANALYSIS—SYMMETRIC—58% C_R

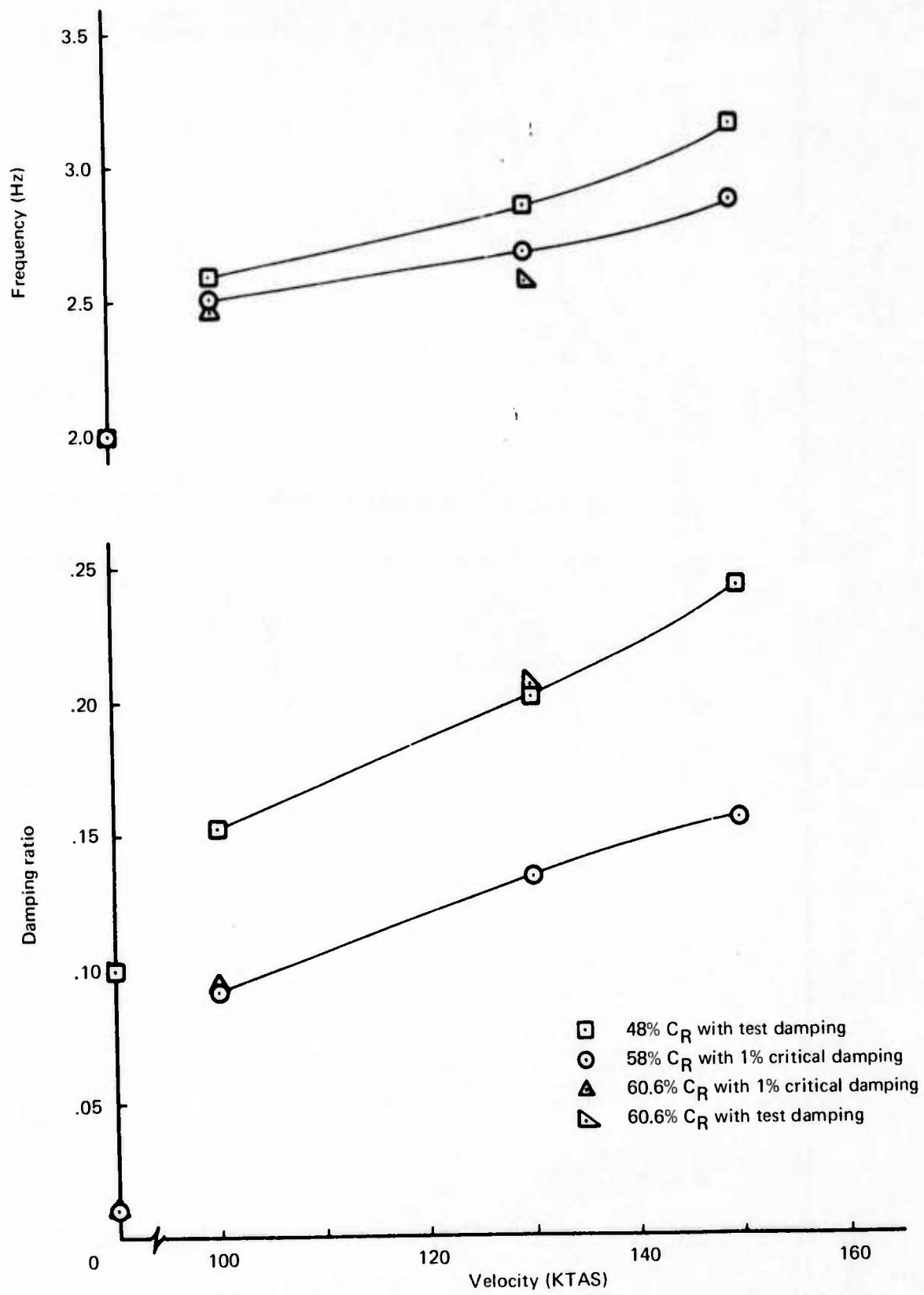


FIGURE 56.—STABILITY ANALYSIS—SYMMETRIC FLEXIBLE MODEL

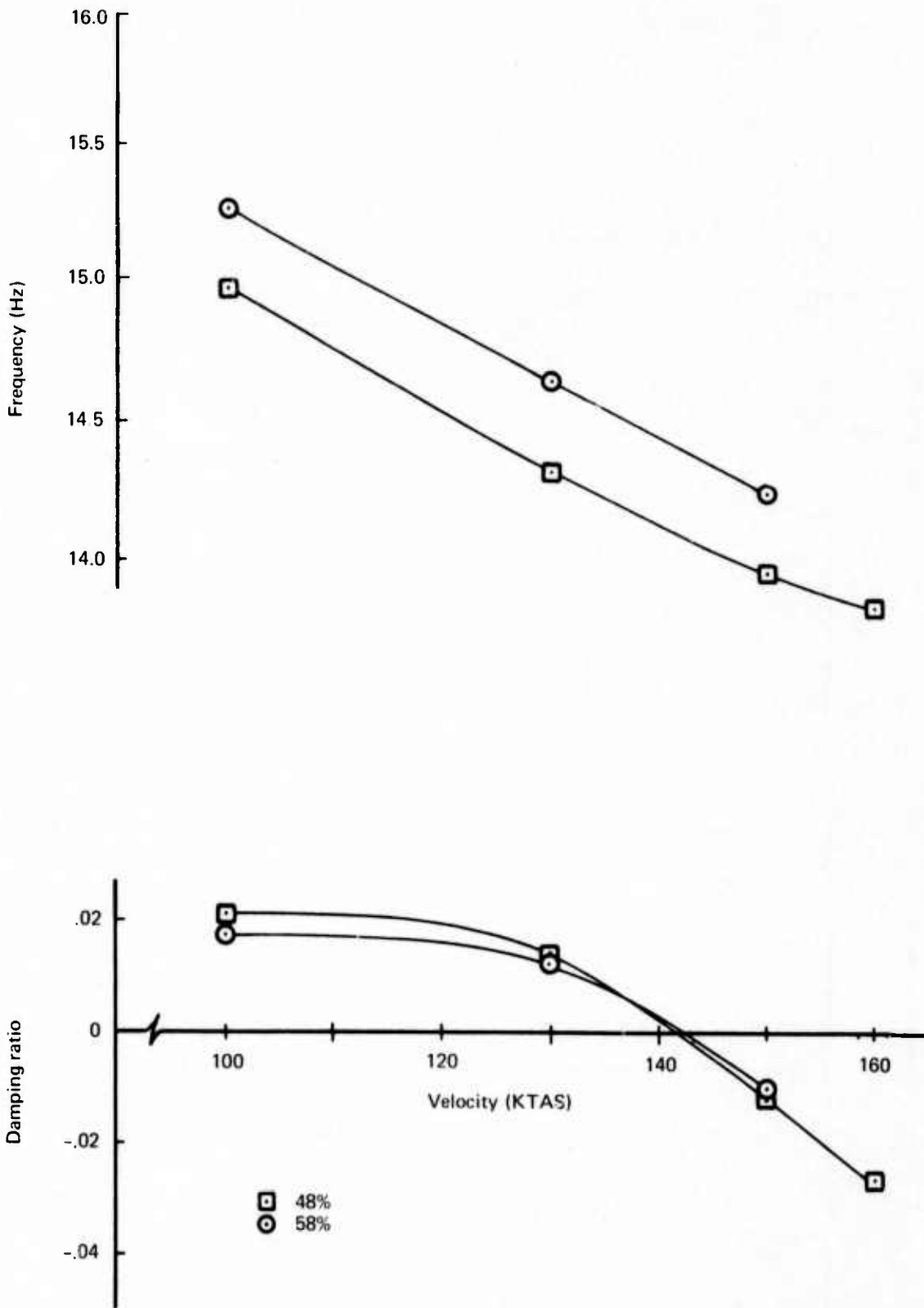


FIGURE 57.—EFFECT OF CG ON SYMMETRIC FLUTTER SPEED

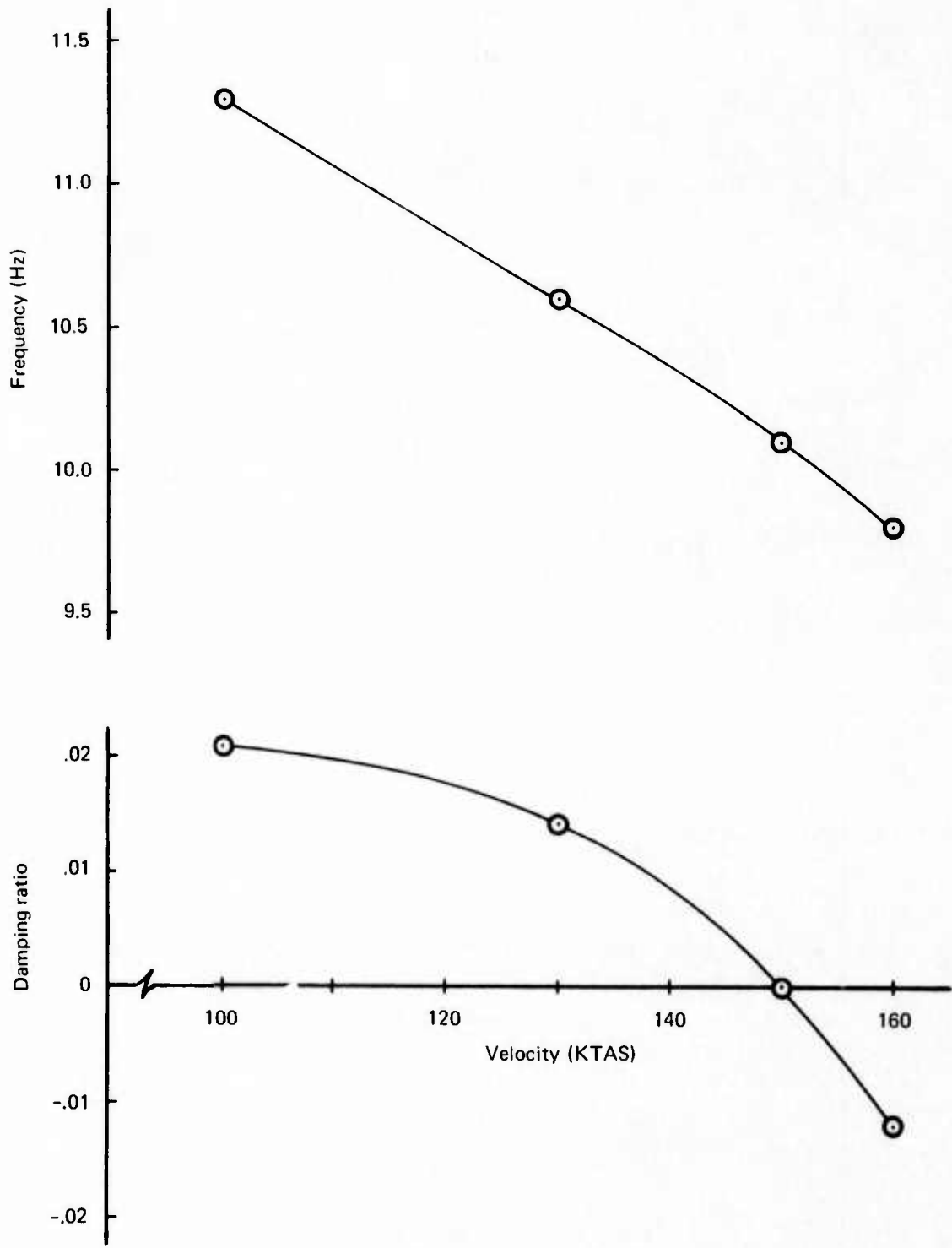


FIGURE 58.—ANTISYMMETRIC FLUTTER—48% C_R

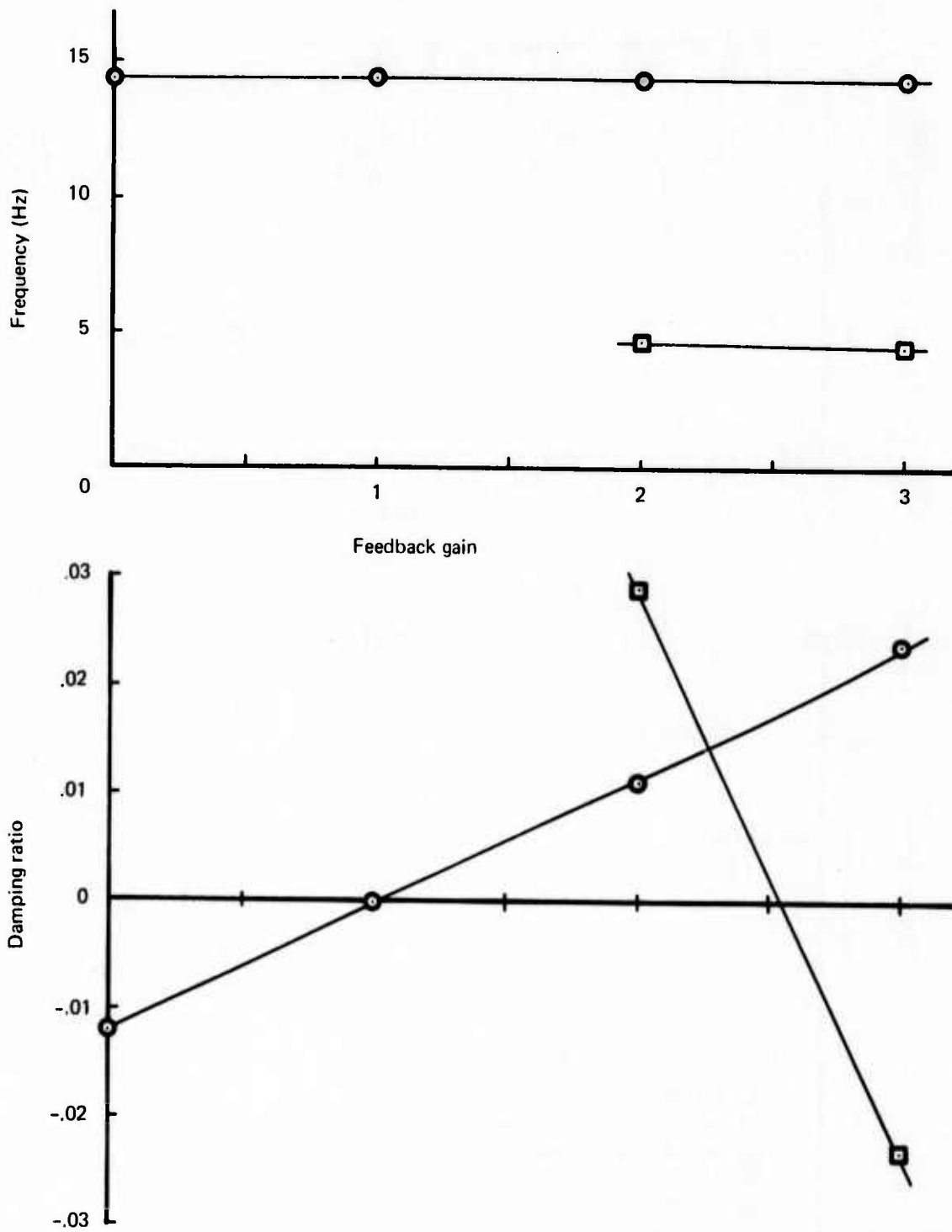


FIGURE 59.—EFFECT OF FEEDBACK GAIN ON WING FLUTTER MODE SUPPRESSED WITH INBOARD AILERON

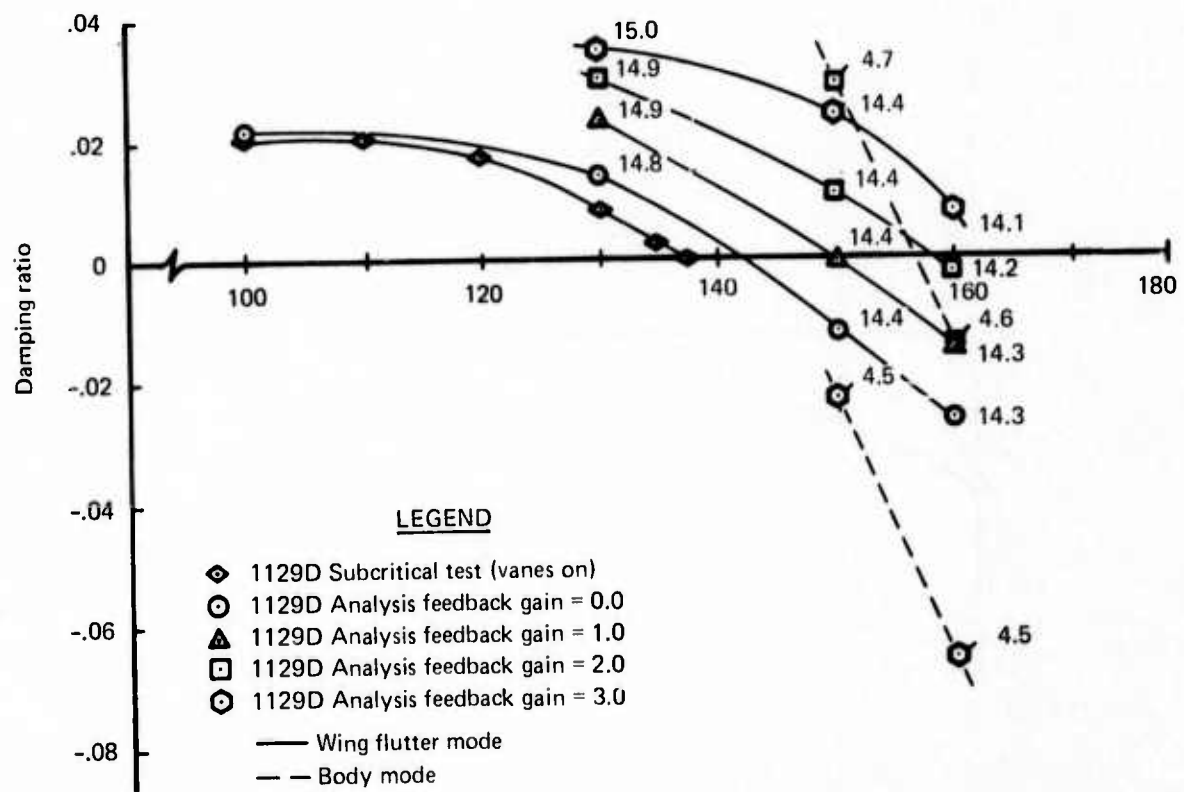
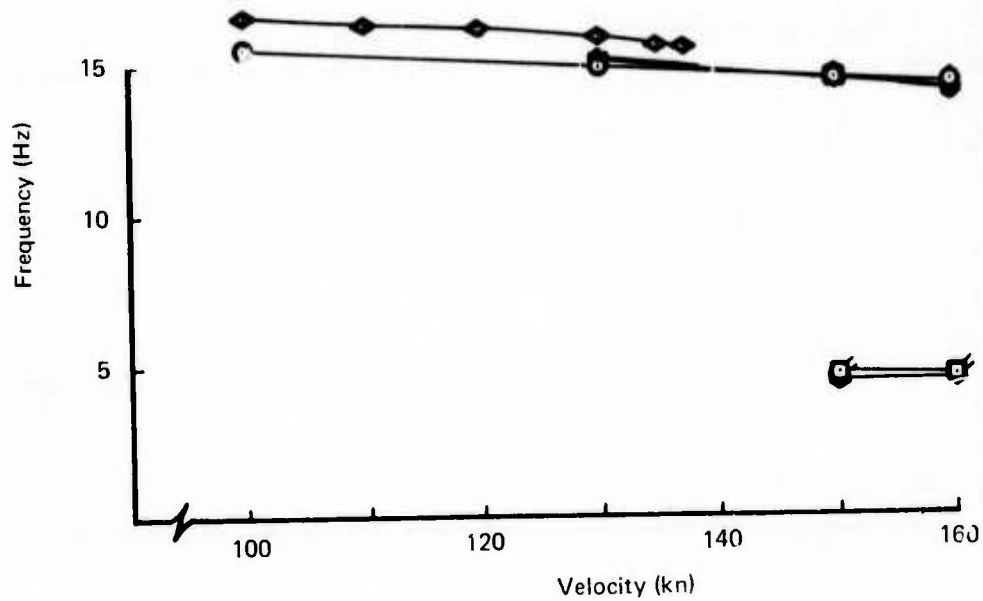


FIGURE 60. -WING FLUTTER SUPPRESSED WITH INBOARD AILERON

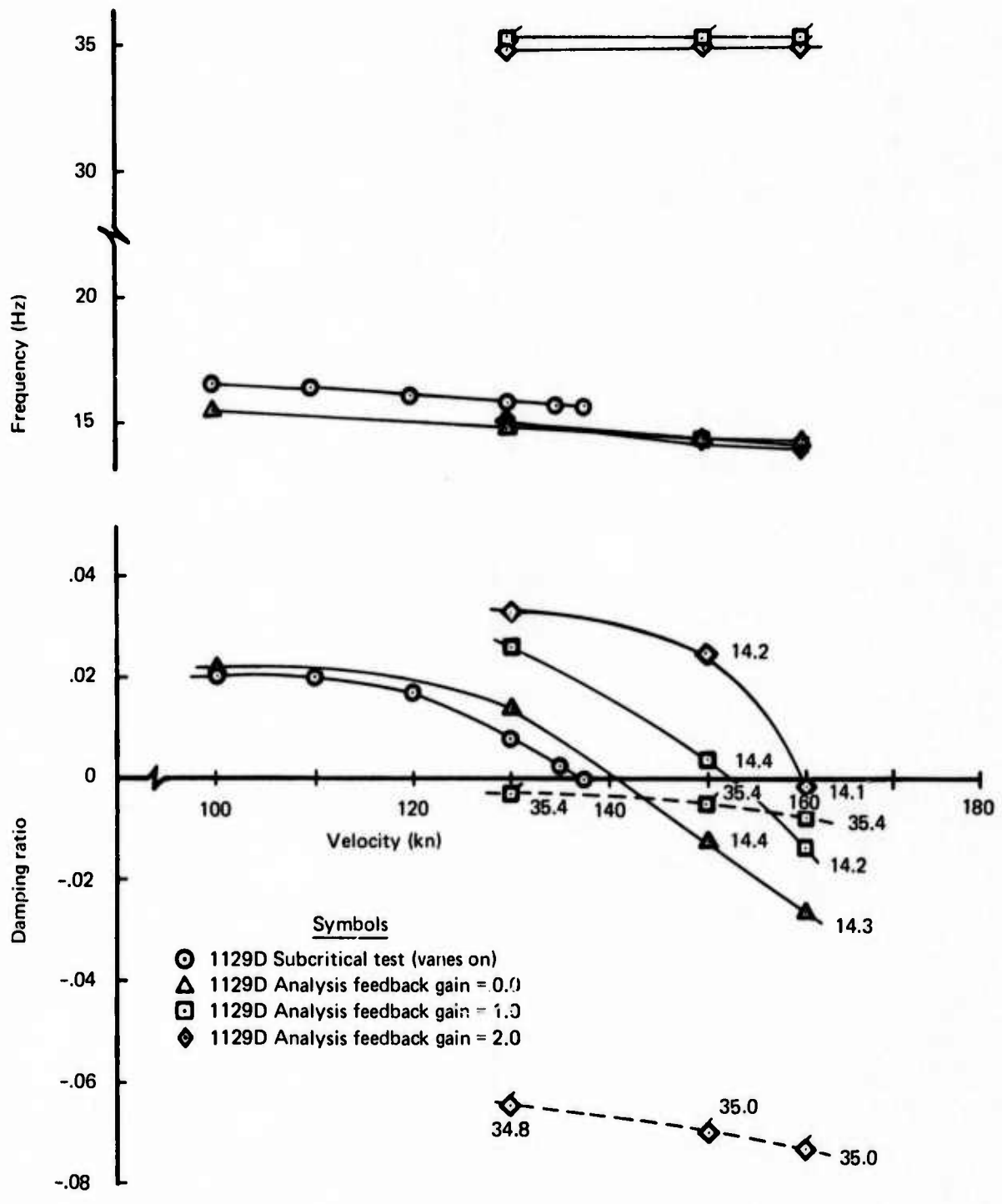


FIGURE 61.—WING FLUTTER SUPPRESSED WITH OUTBOARD AILERON

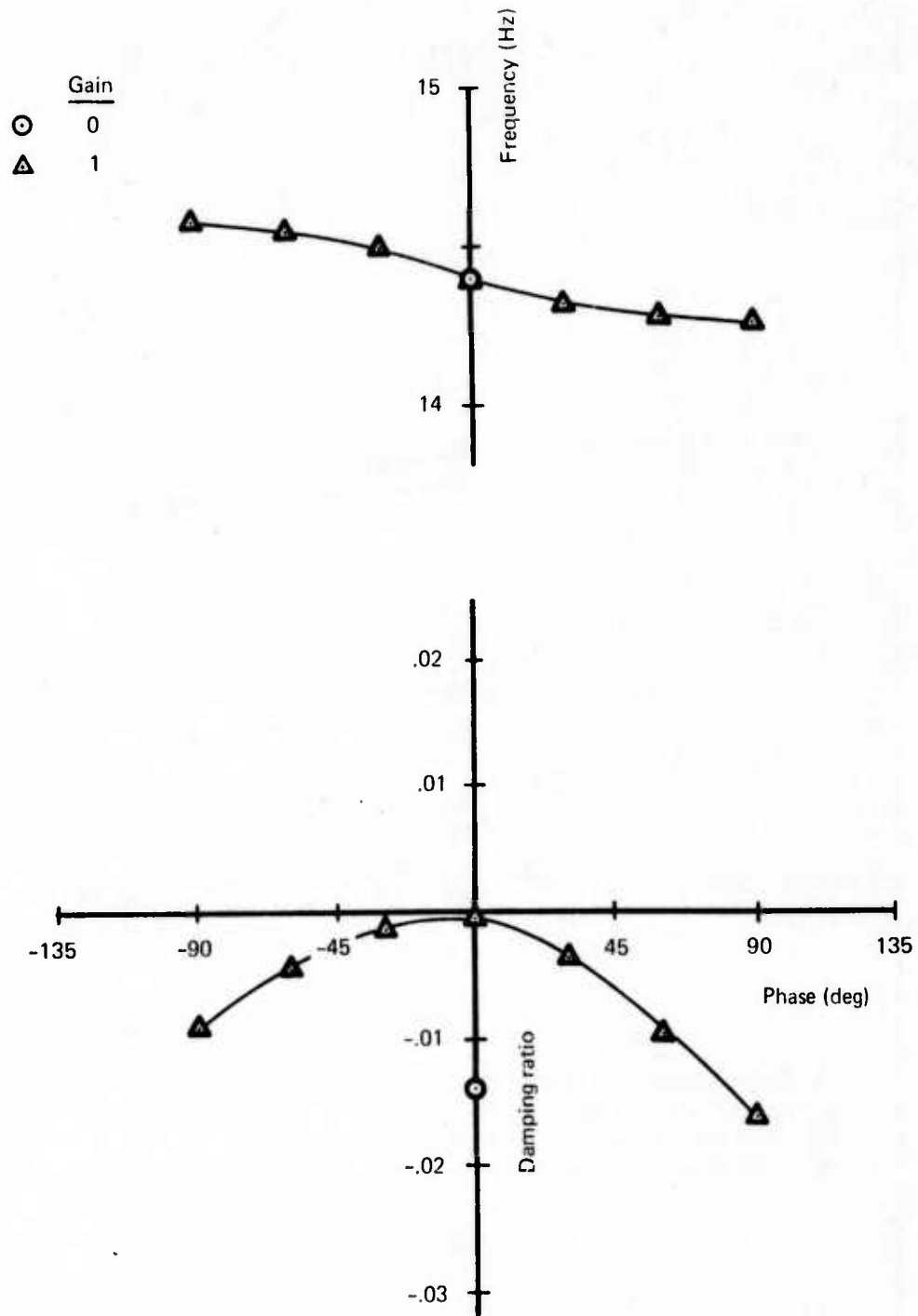


FIGURE 62.—EFFECT OF PHASE SHIFT ON INBOARD AILERON SYSTEM AT 150 KN

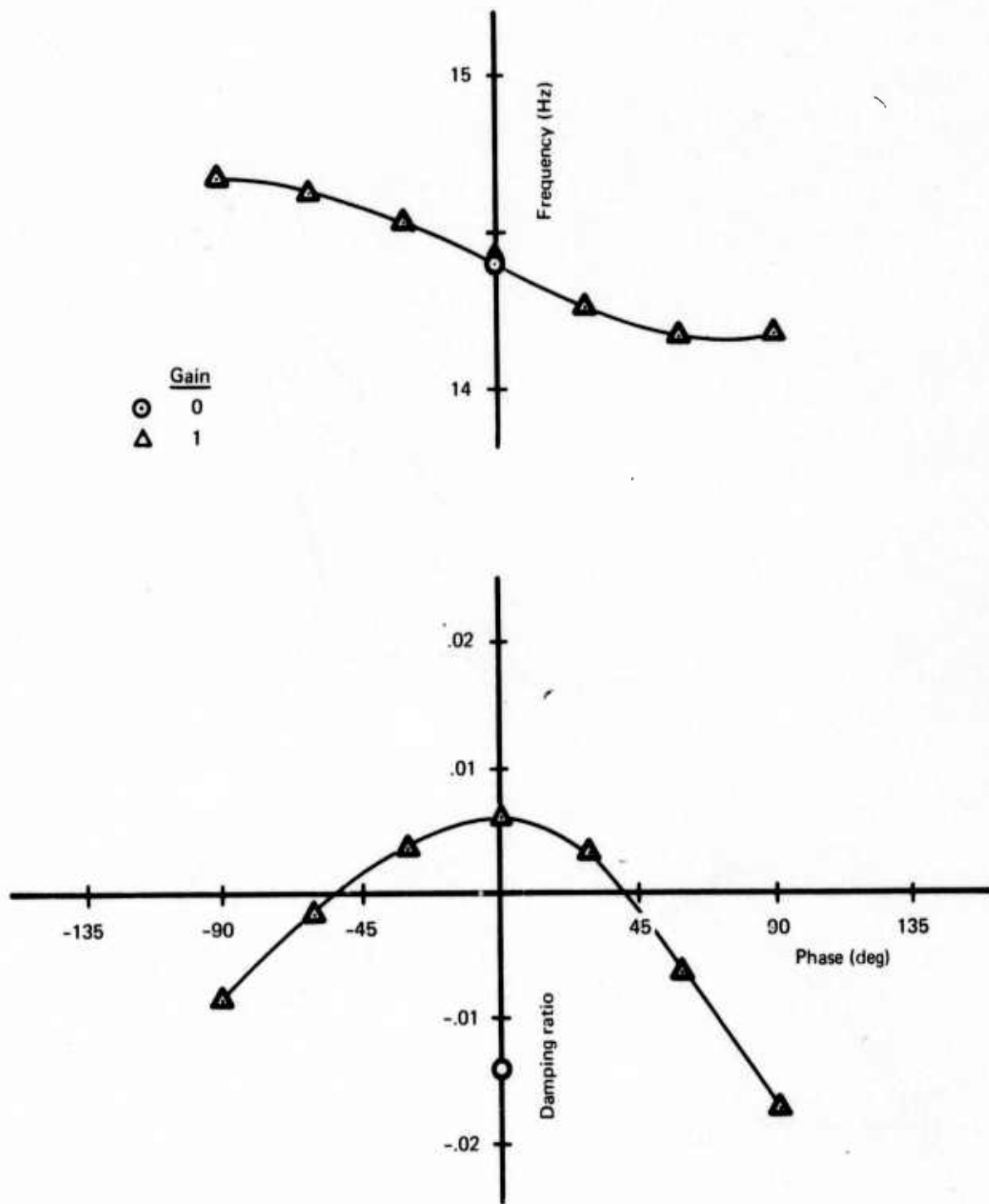


FIGURE 63.—EFFECT OF PHASE SHIFT ON OUTBOARD AILERON SYSTEM AT 150 KN

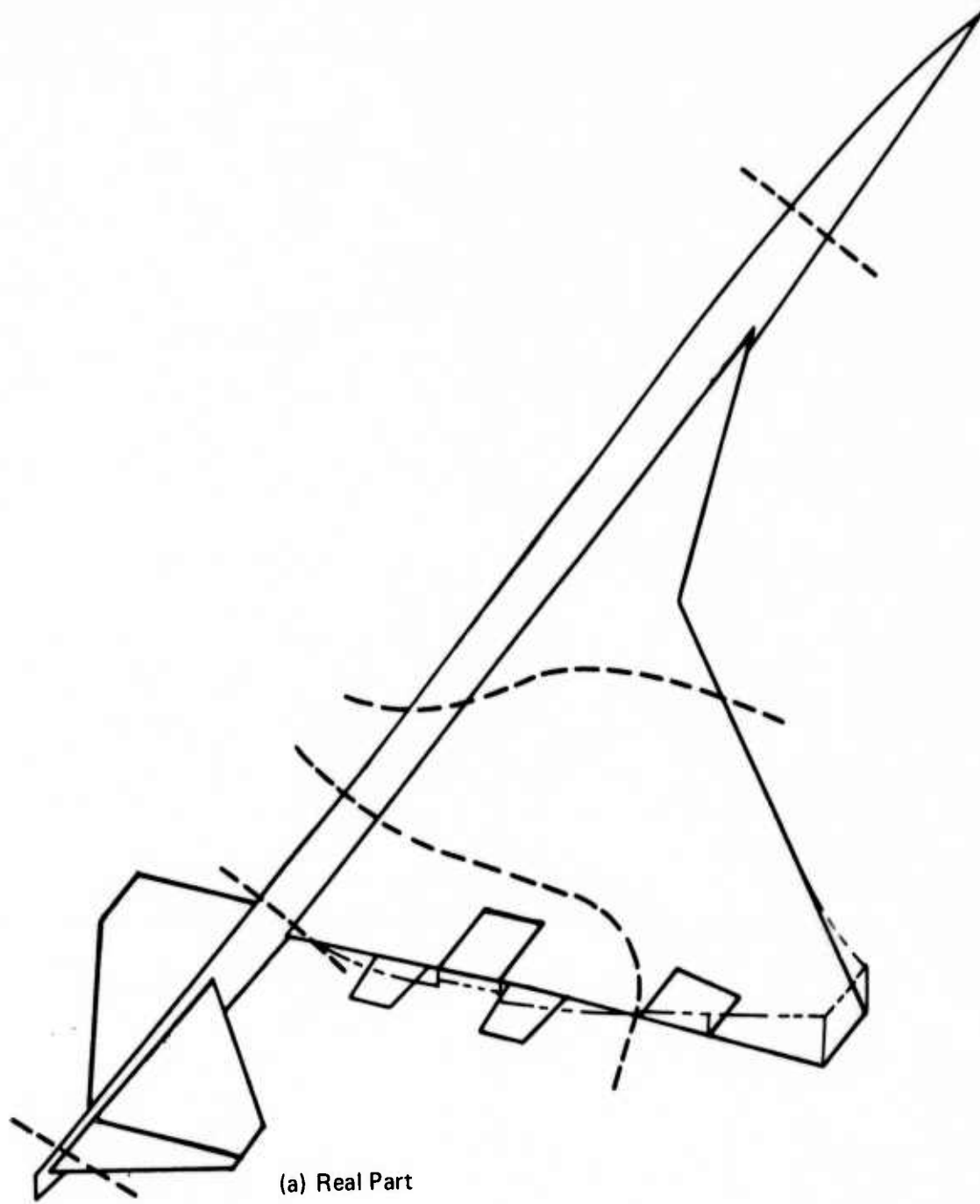
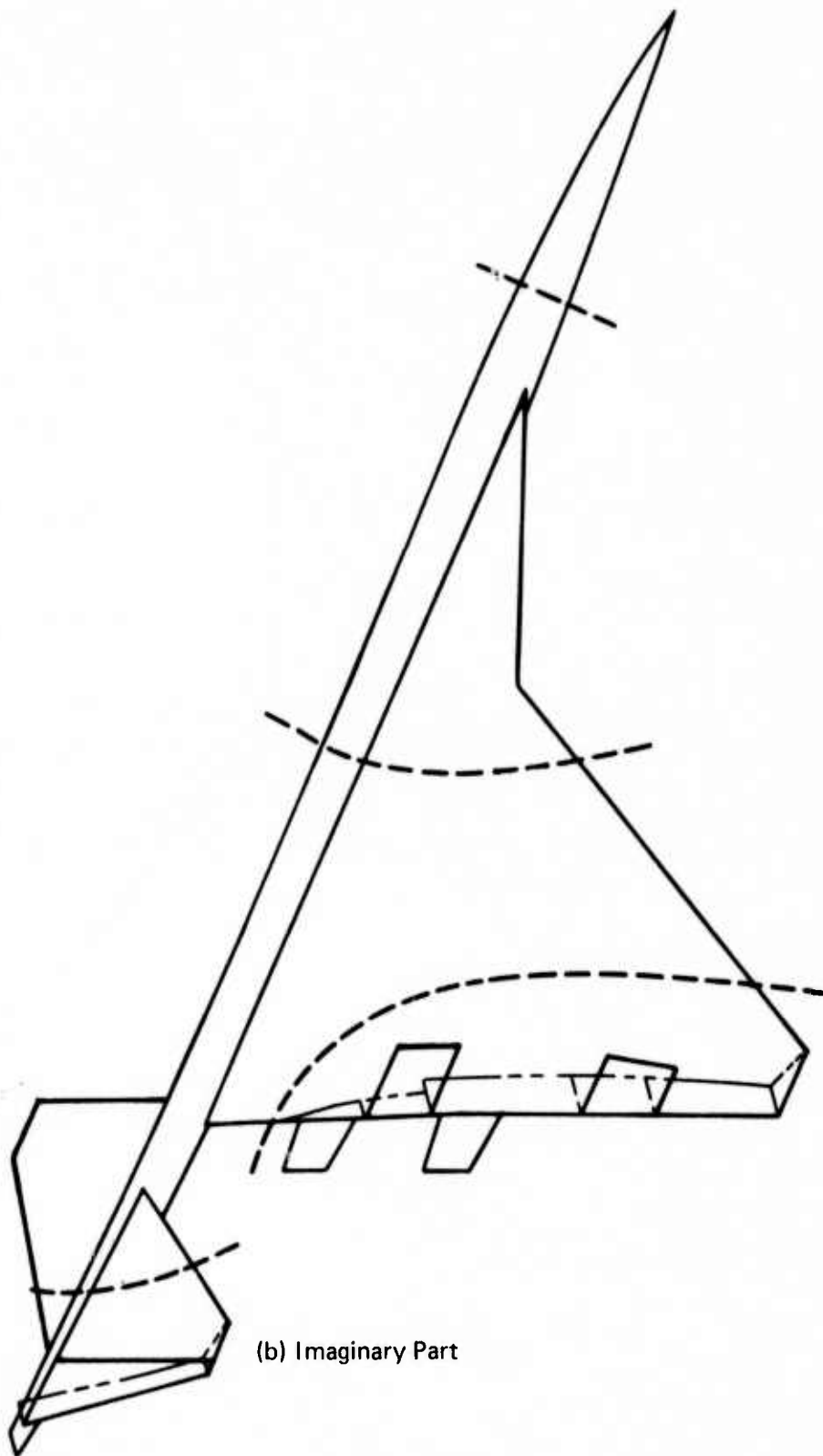


FIGURE 64.—UNAugmented FLUTTER CYCLE—140 KN



(b) Imaginary Part

FIGURE 64.—CONCLUDED

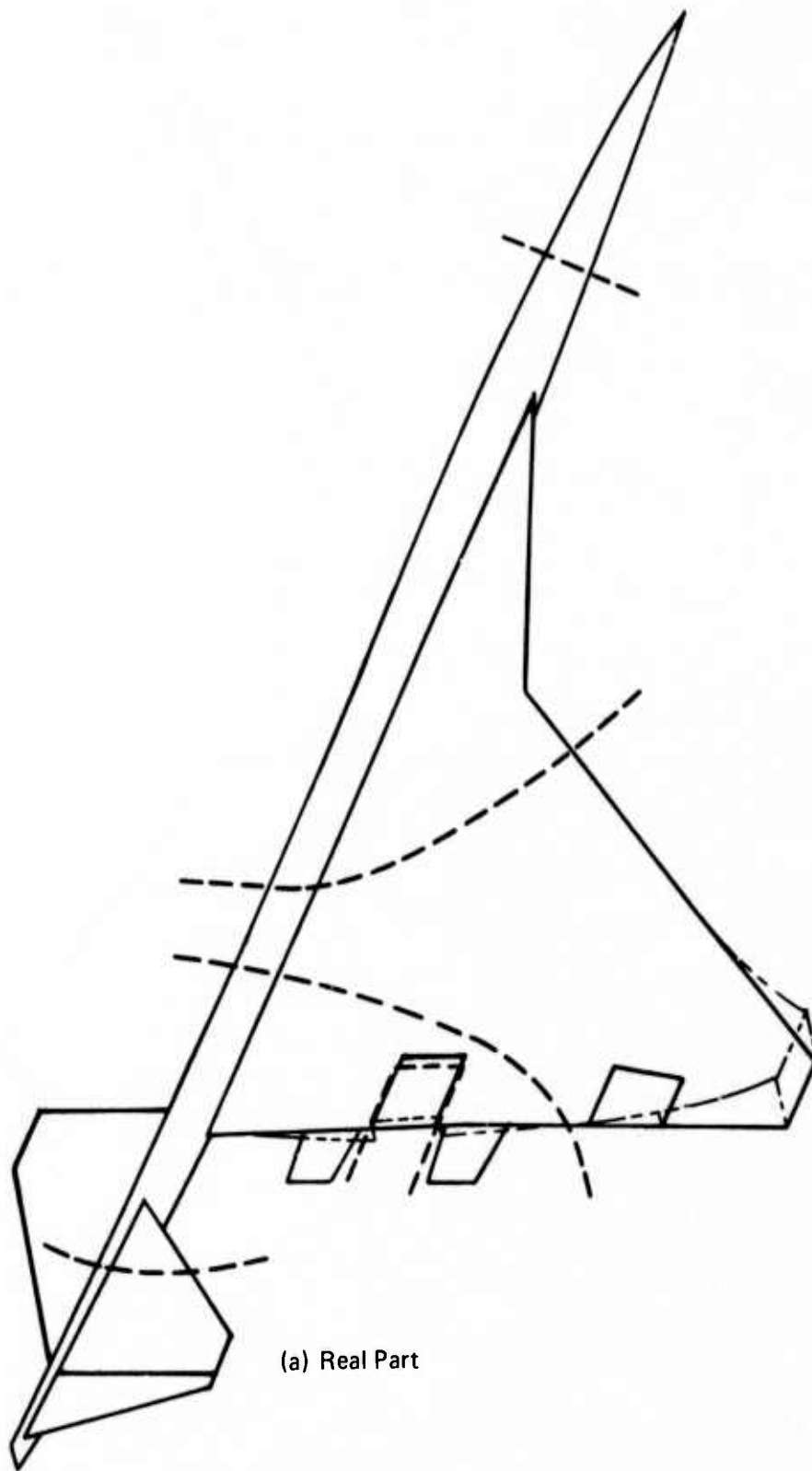
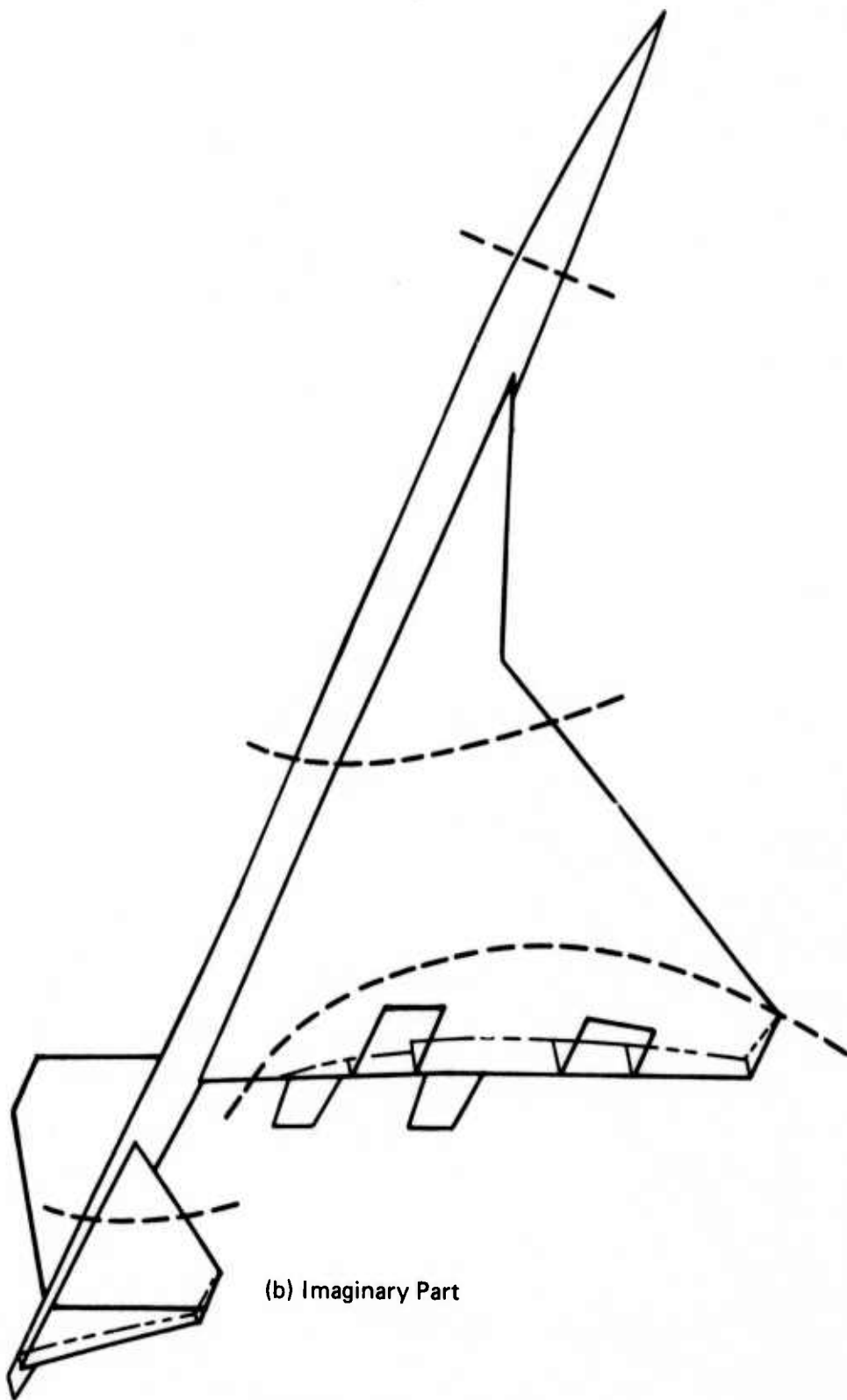


FIGURE 65.—FLUTTER CYCLE WITH INBOARD AILERON ACTIVE—150 KN



(b) Imaginary Part

FIGURE 65.—CONCLUDED

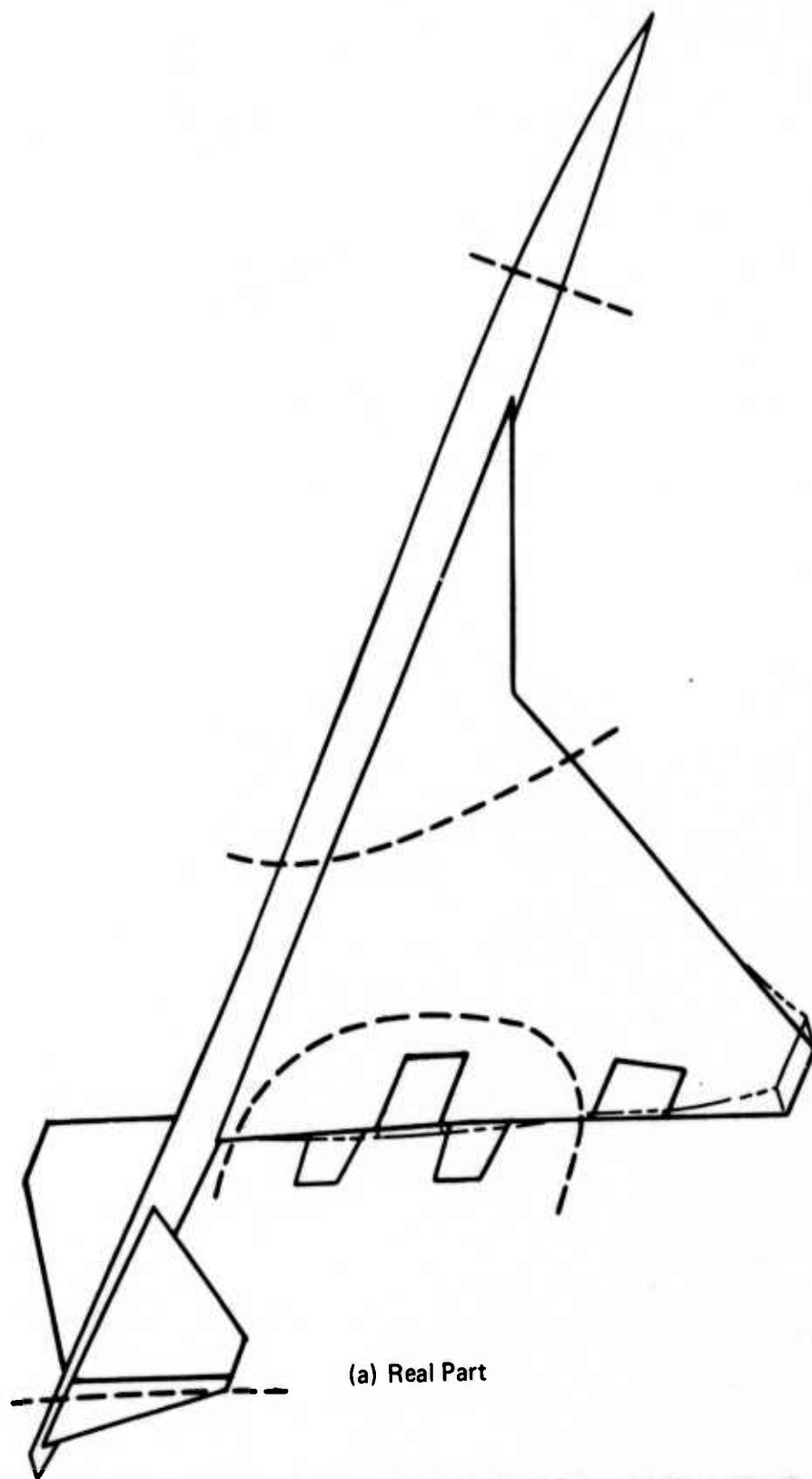
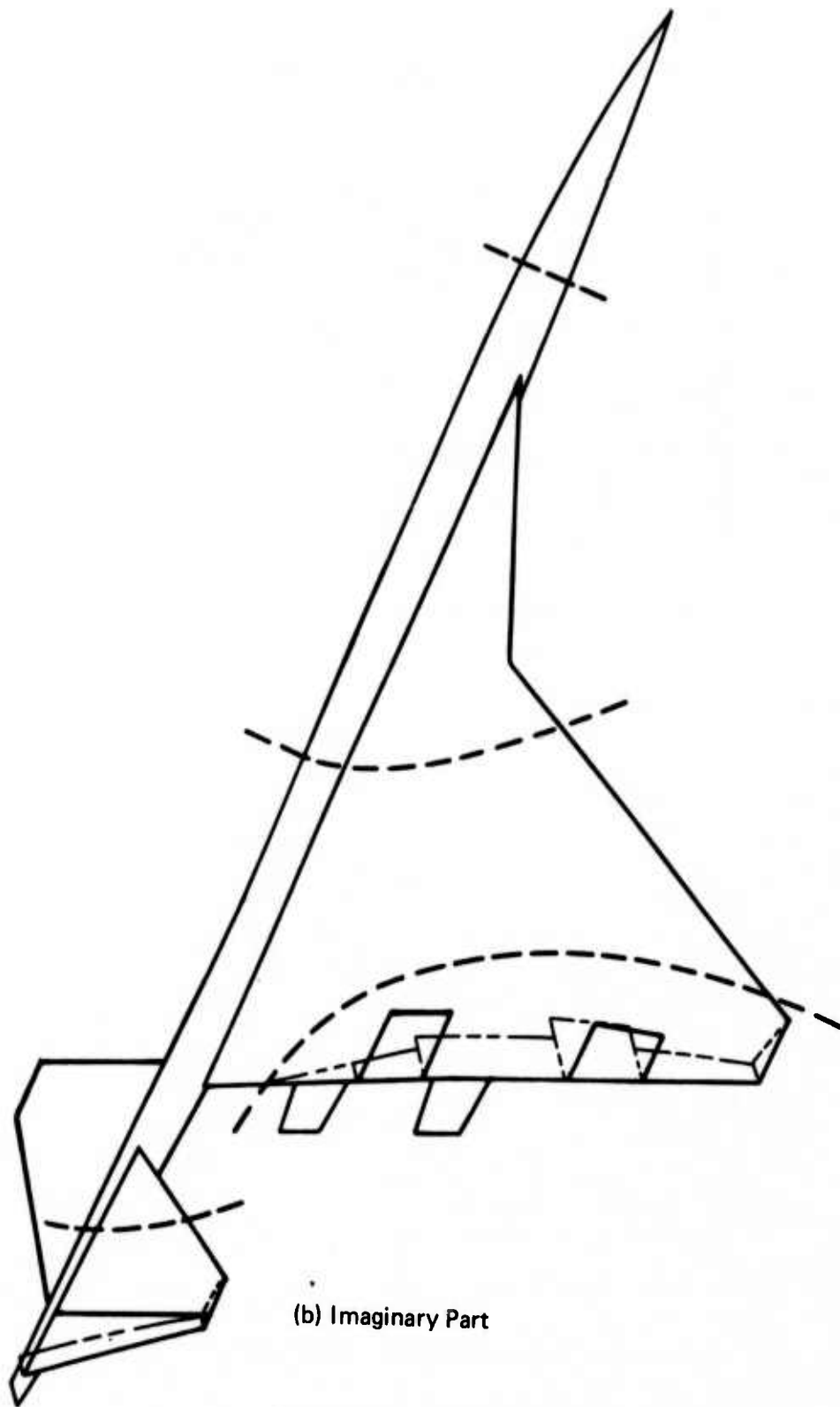


FIGURE 66.—FLUTTER CYCLE WITH OUTBOARD AILERON ACTIVE—150 KN



(b) Imaginary Part

FIGURE 66.—CONCLUDED

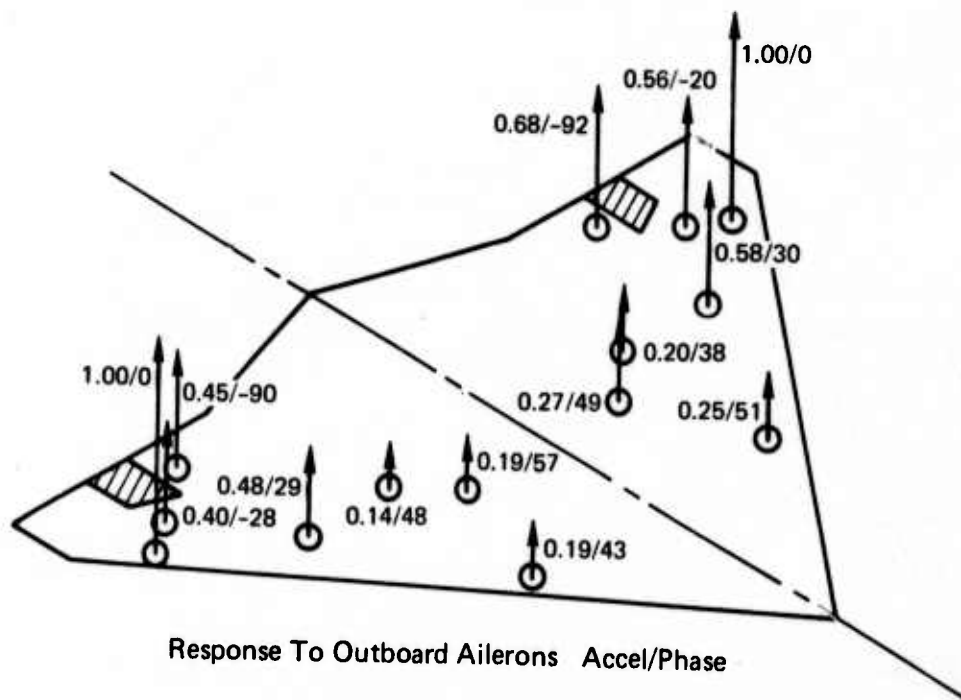
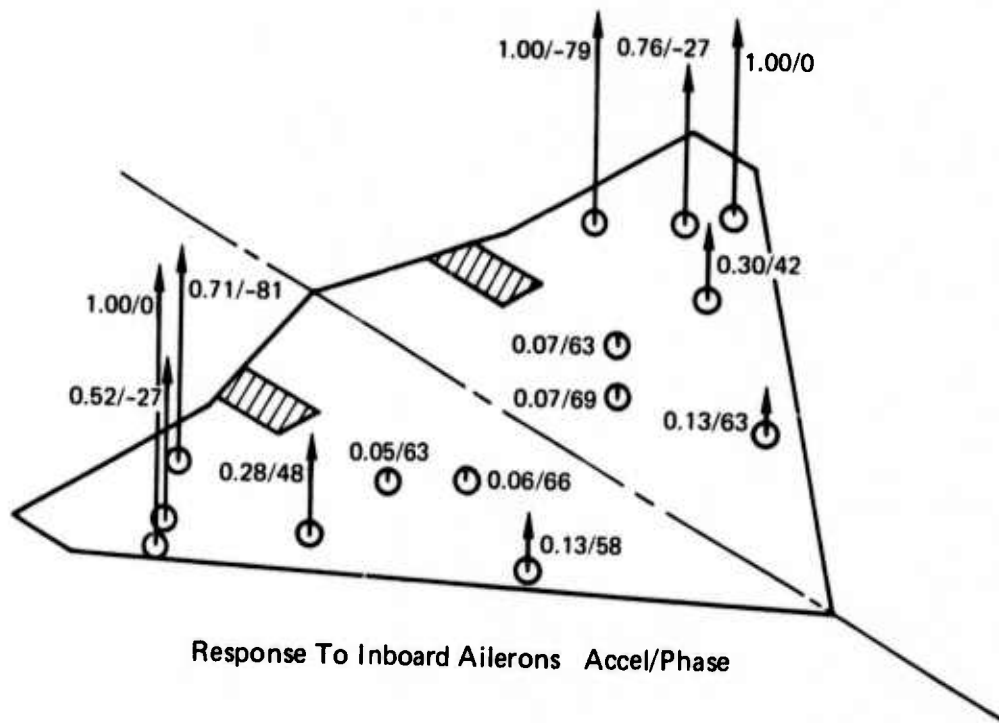


FIGURE 67.—MODAL ACCELERATIONS AT 15.9 Hz 130 KTAS CONVAIR LOW SPEED TUNNEL

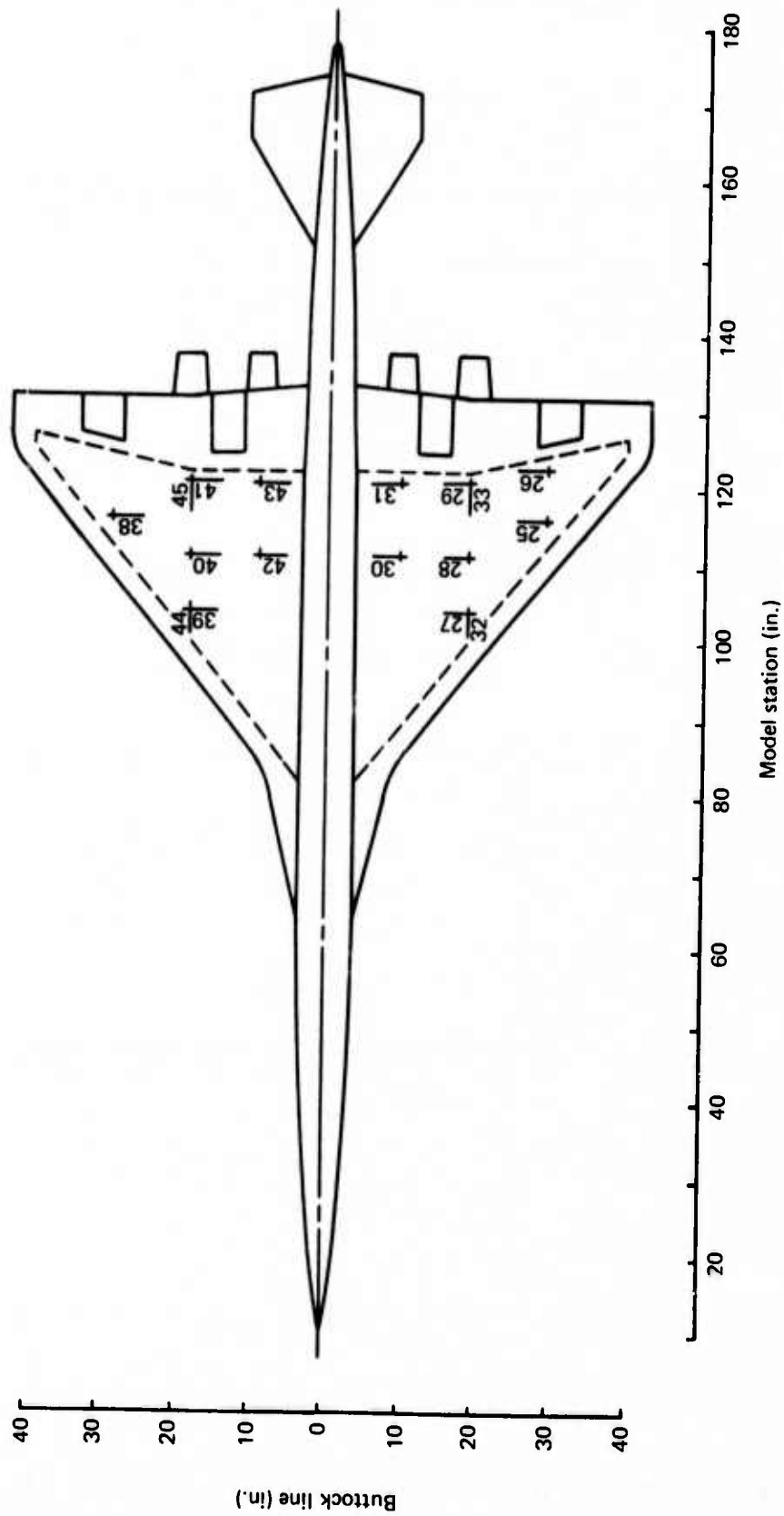
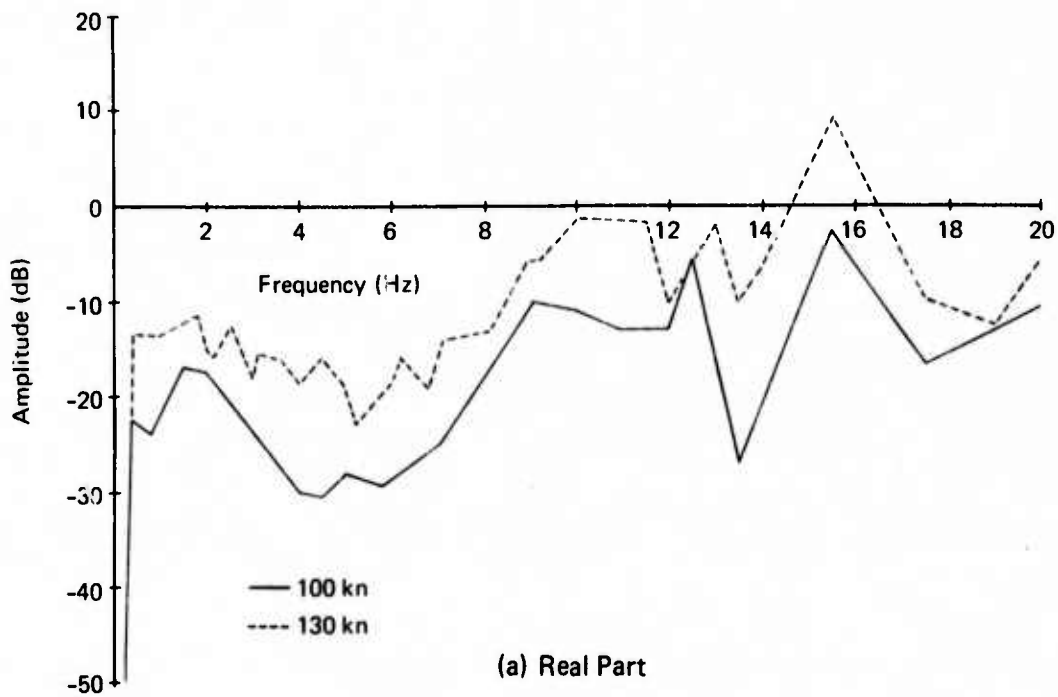
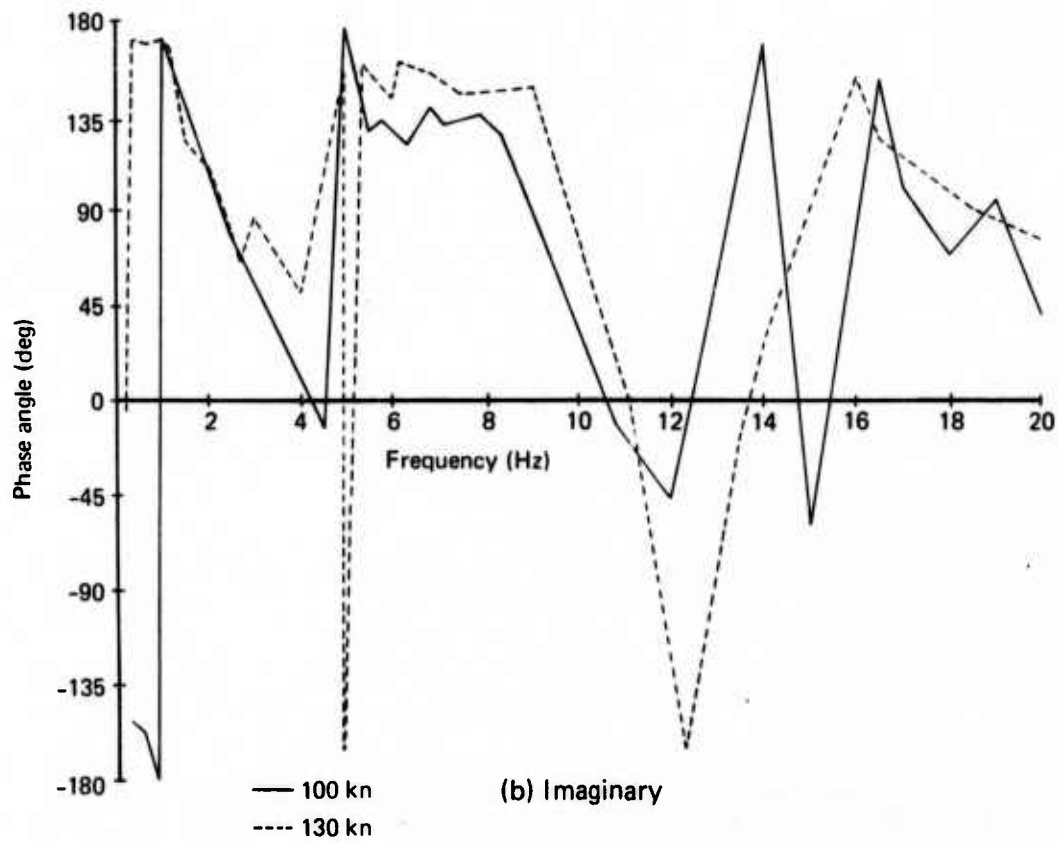


FIGURE 68.—STRAIN GAGE LOCATIONS



(a) Real Part



(b) Imaginary

FIGURE 69.—STRAIN GAGE 33 RESPONSE TO INBOARD AILERON EXCITATION

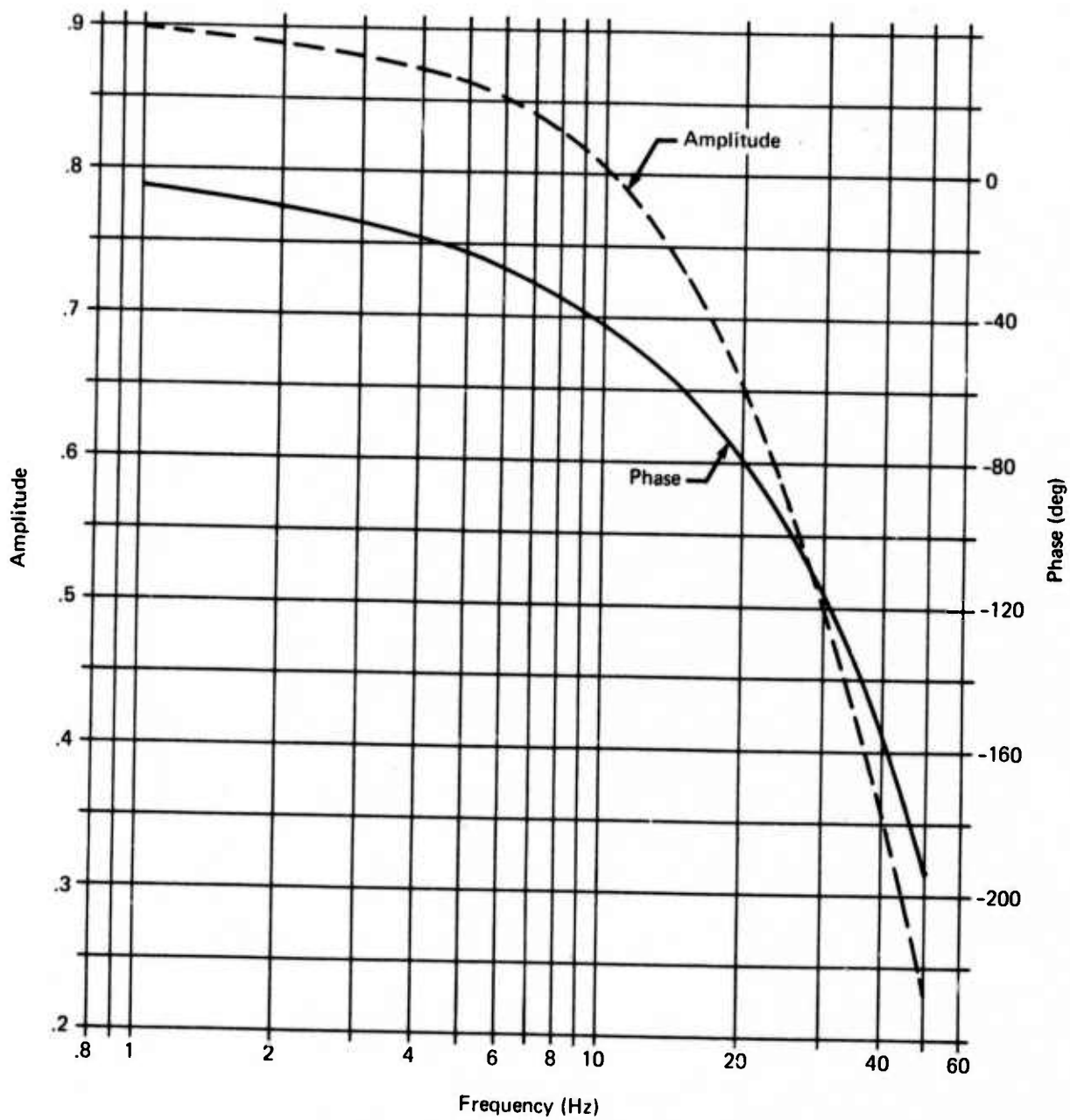


FIGURE 70.—FREQUENCY RESPONSE OF SINGLE POLE COMPENSATION FILTER—INBOARD AILERON SYSTEM

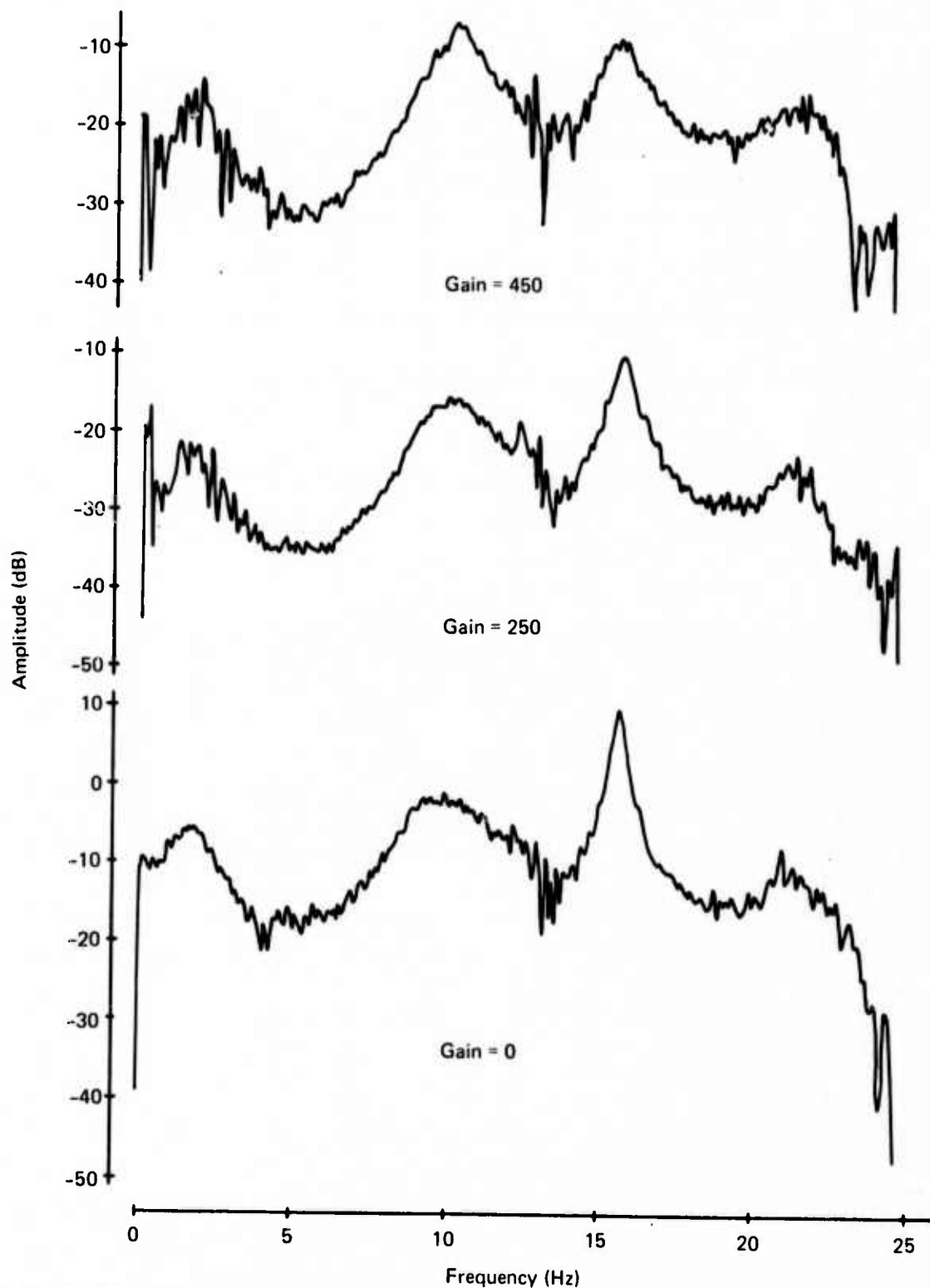


FIGURE 72.—EFFECT OF ACTIVE INBOARD AILERON ON FREQUENCY RESPONSE AT STRAIN GAGE 33

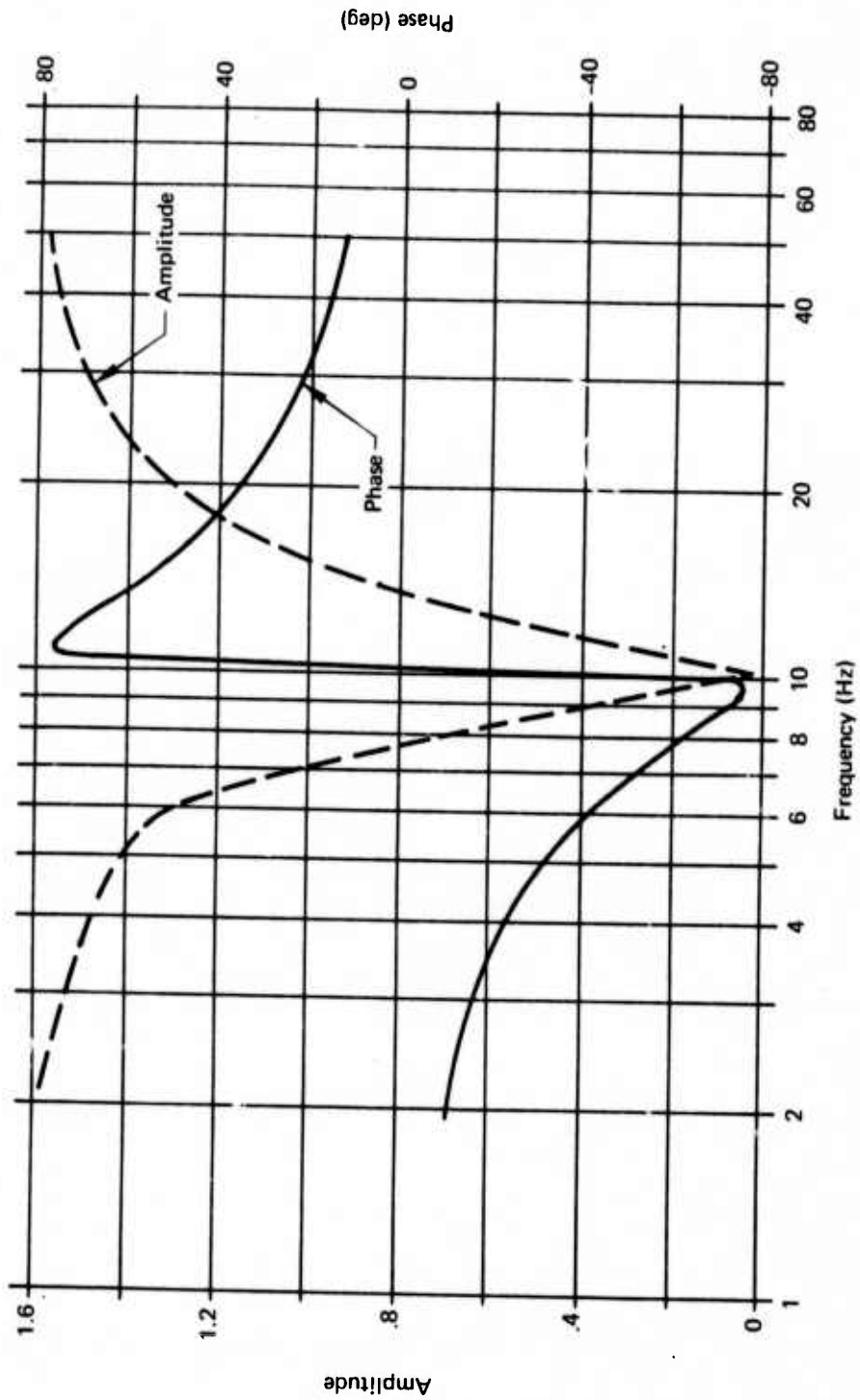


FIGURE 73. — 10 Hz NOTCH FILTER FREQUENCY RESPONSE

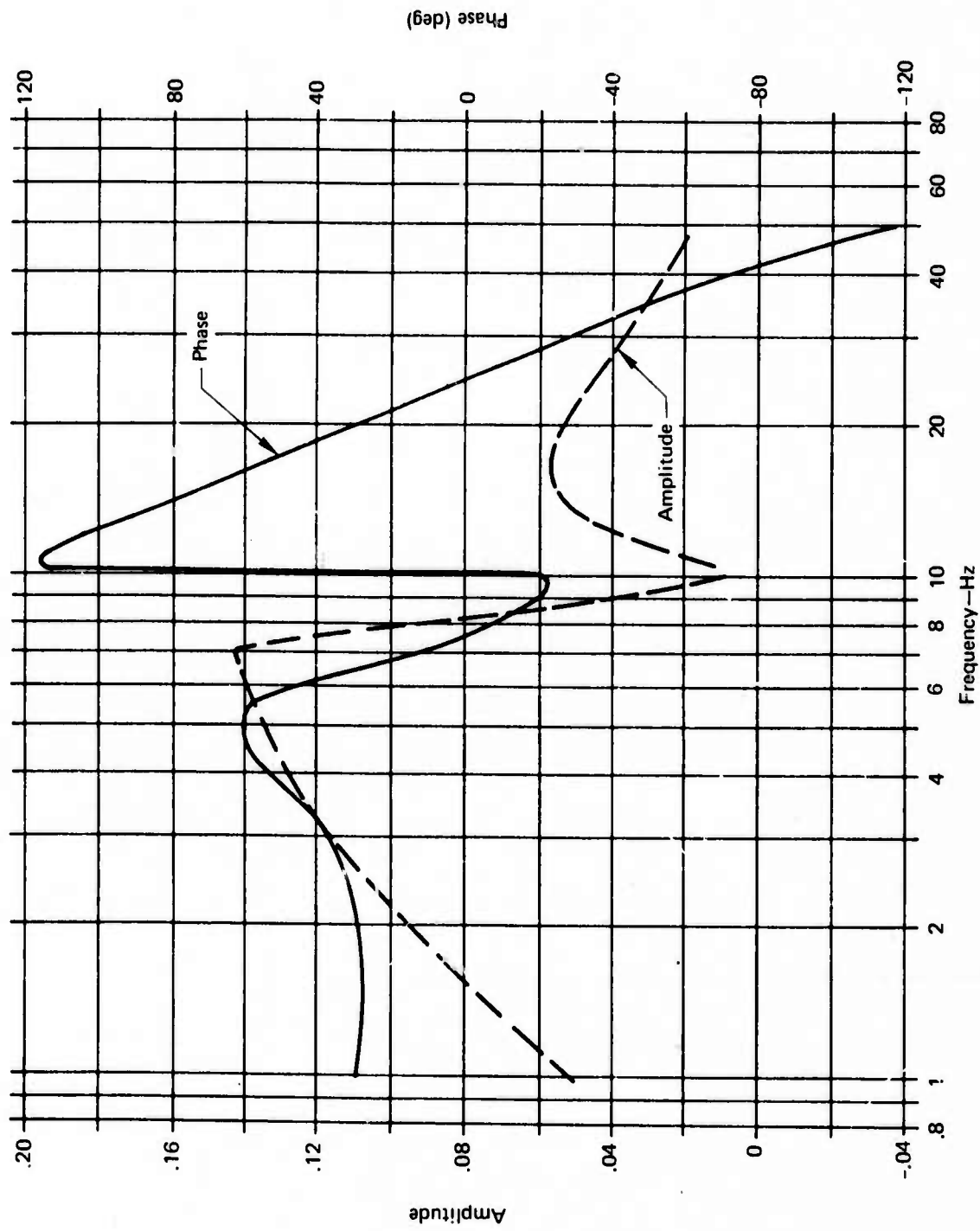


FIGURE 74.—COMPENSATION NETWORK TRANSFER FUNCTION

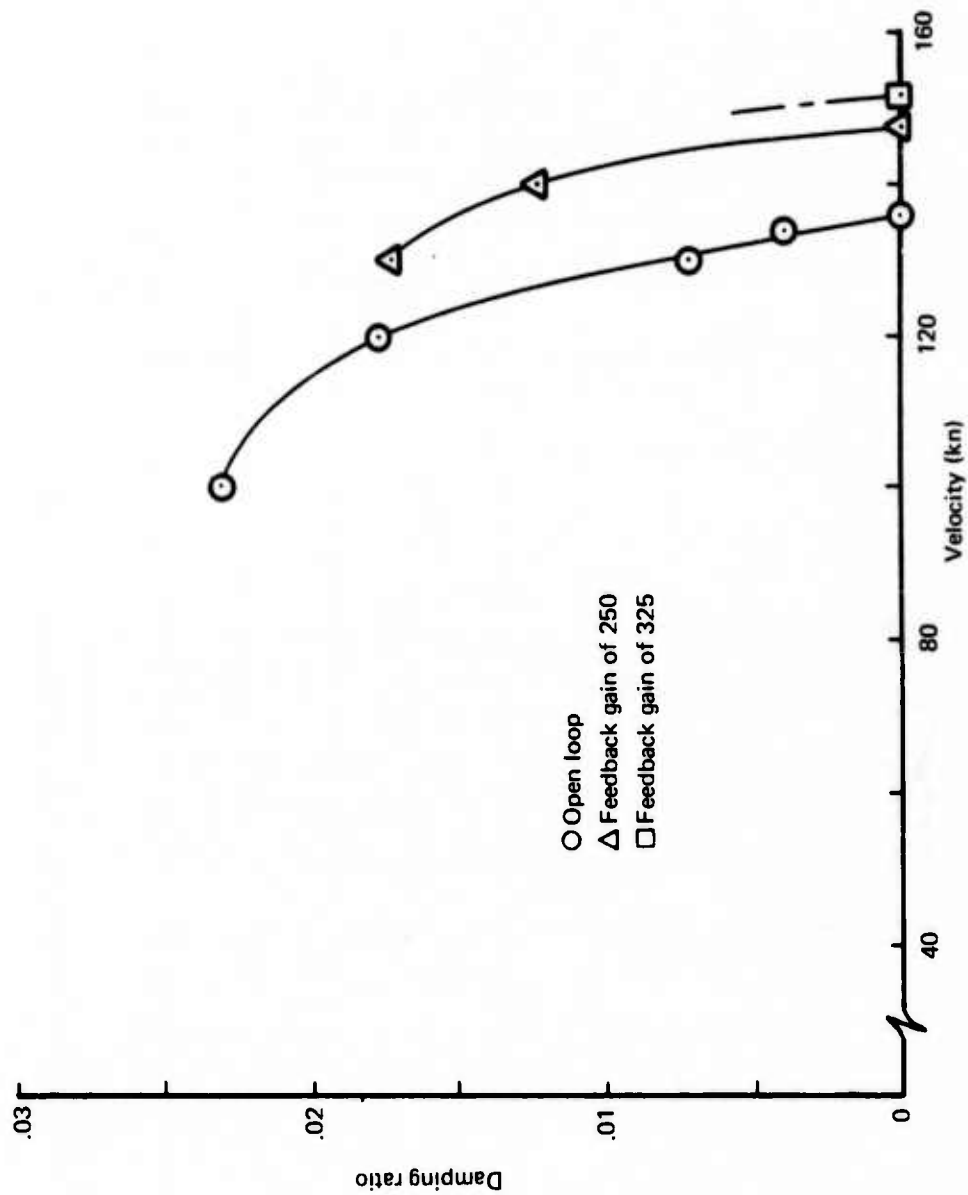


FIGURE 75.—WING FLUTTER SUPPRESSED WITH INBOARD AILERON

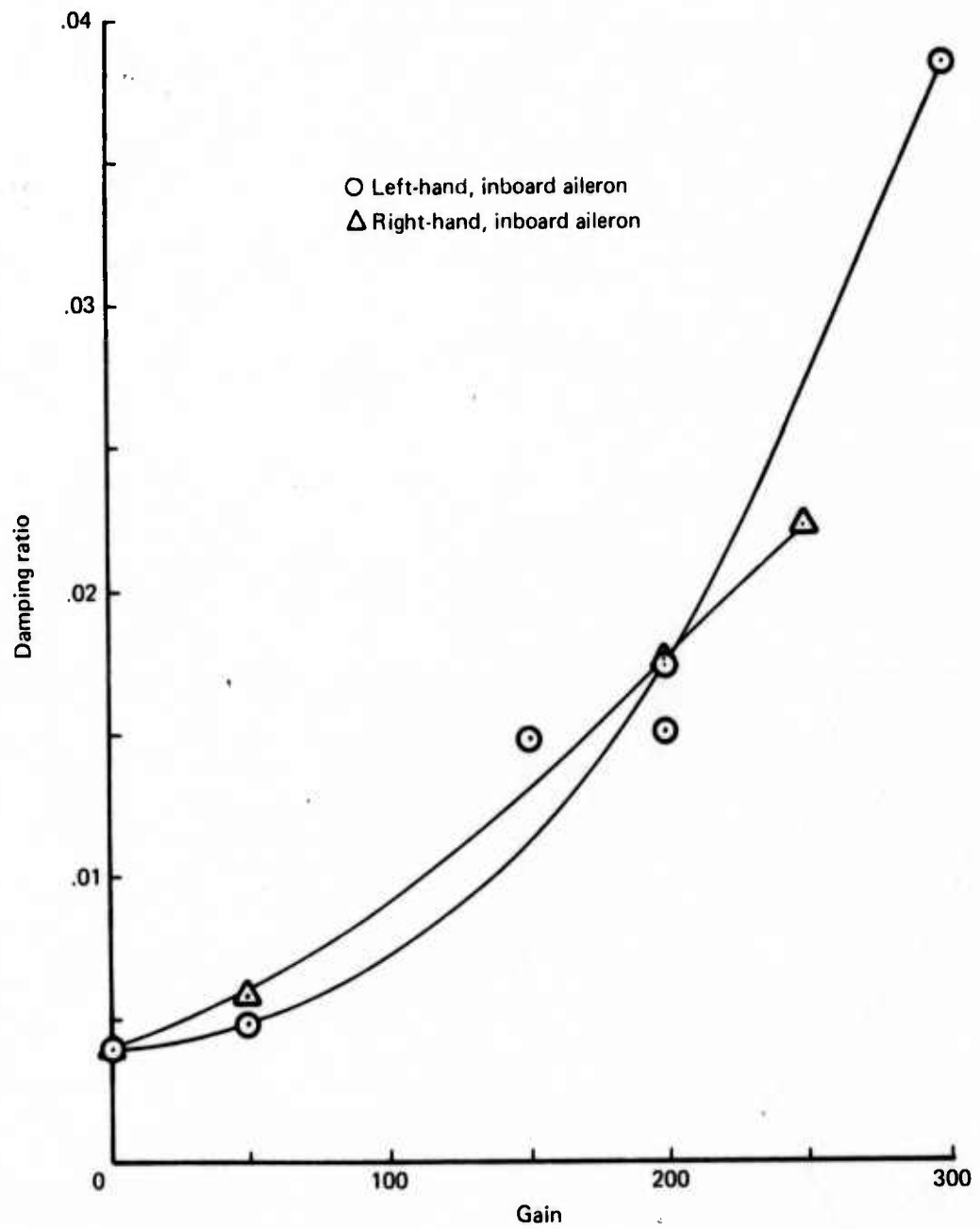


FIGURE 76.—EFFECT OF ACTIVE INBOARD AILERON ON 15 Hz MODE AT 130 KN

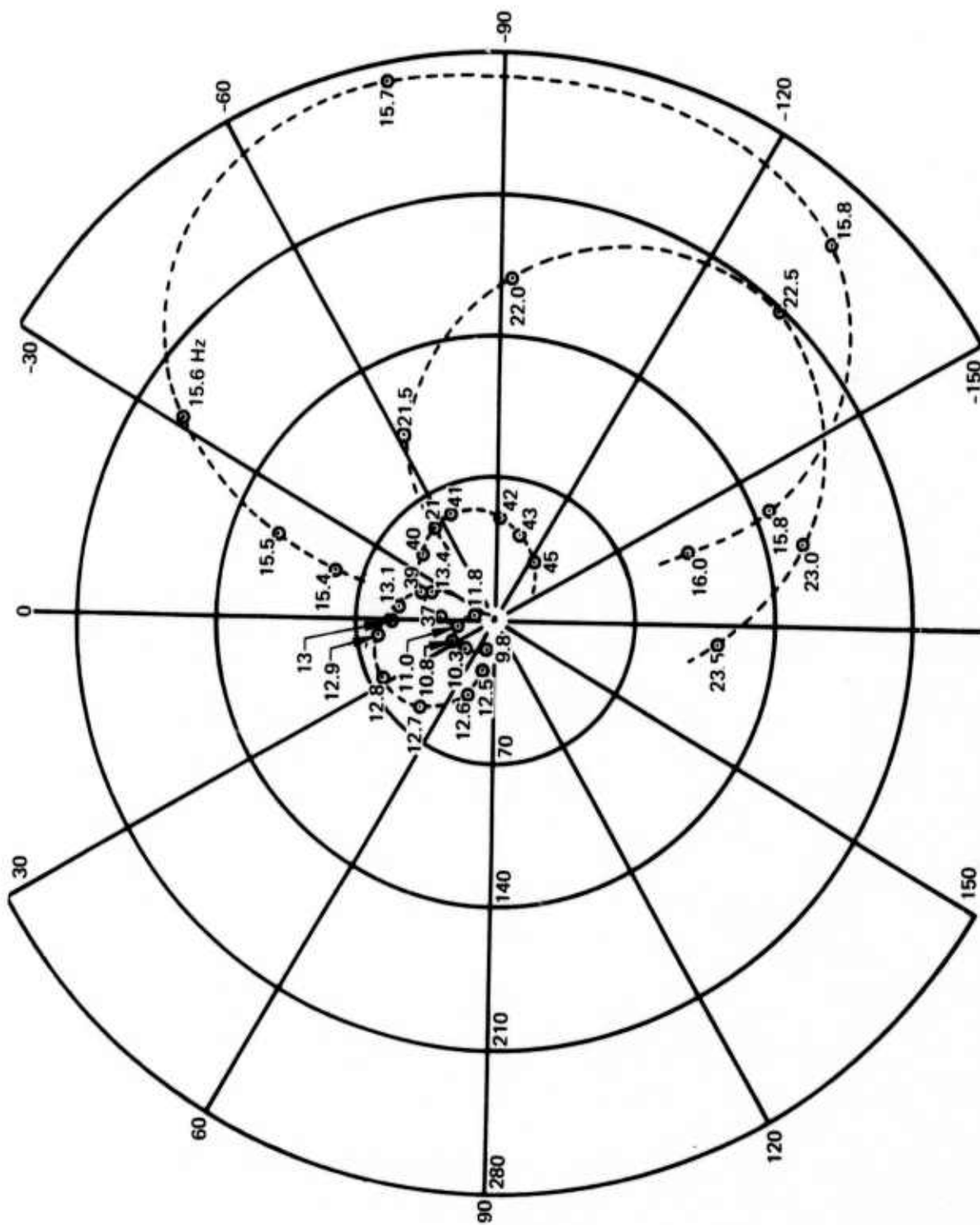


FIGURE 77.—STRAIN GAGE 30 RESPONSE TO OUTBOARD AILERON EXCITATION—130 KN

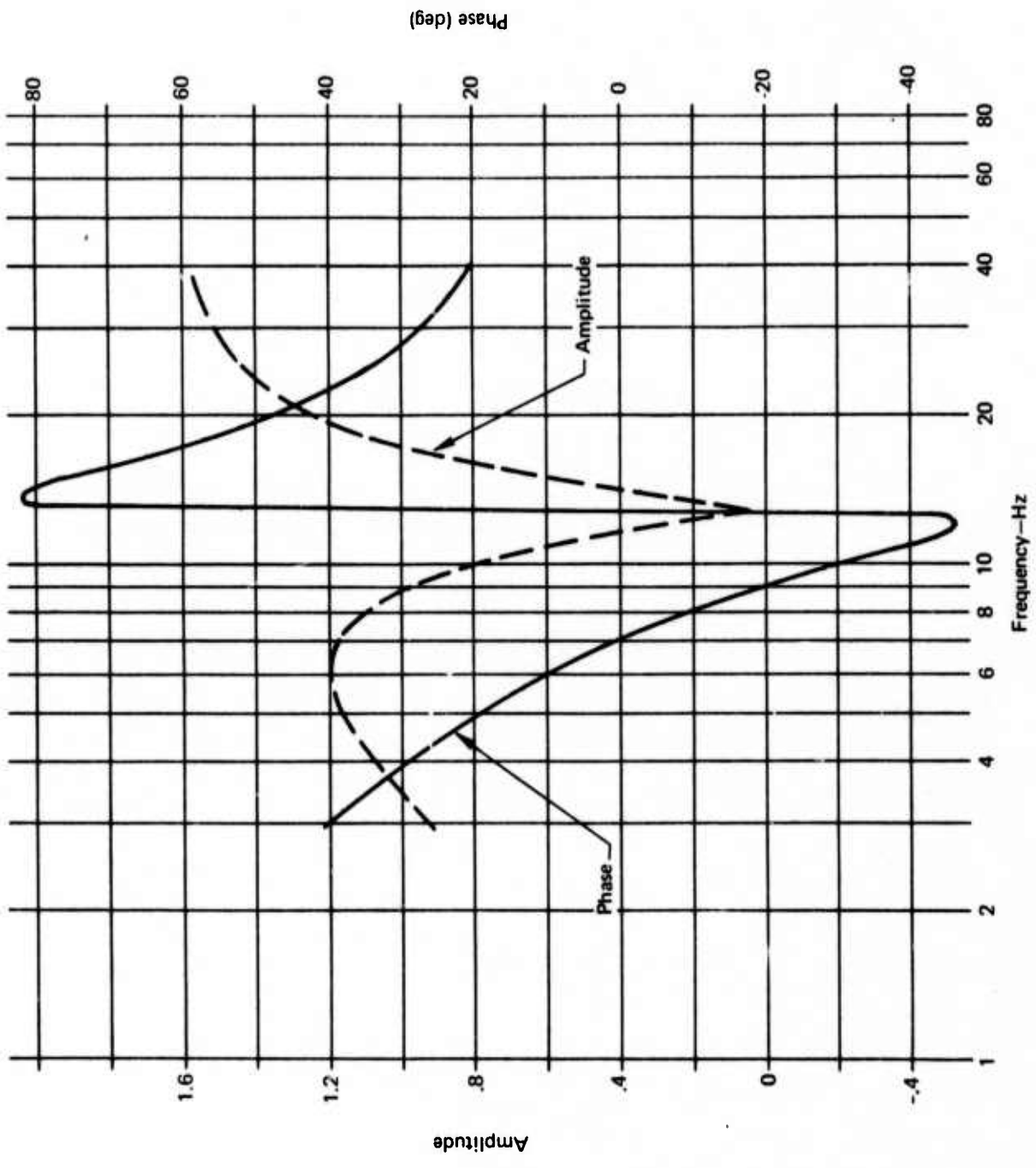


FIGURE 78—12.8 Hz NOTCH FILTER TRANSFER FUNCTION

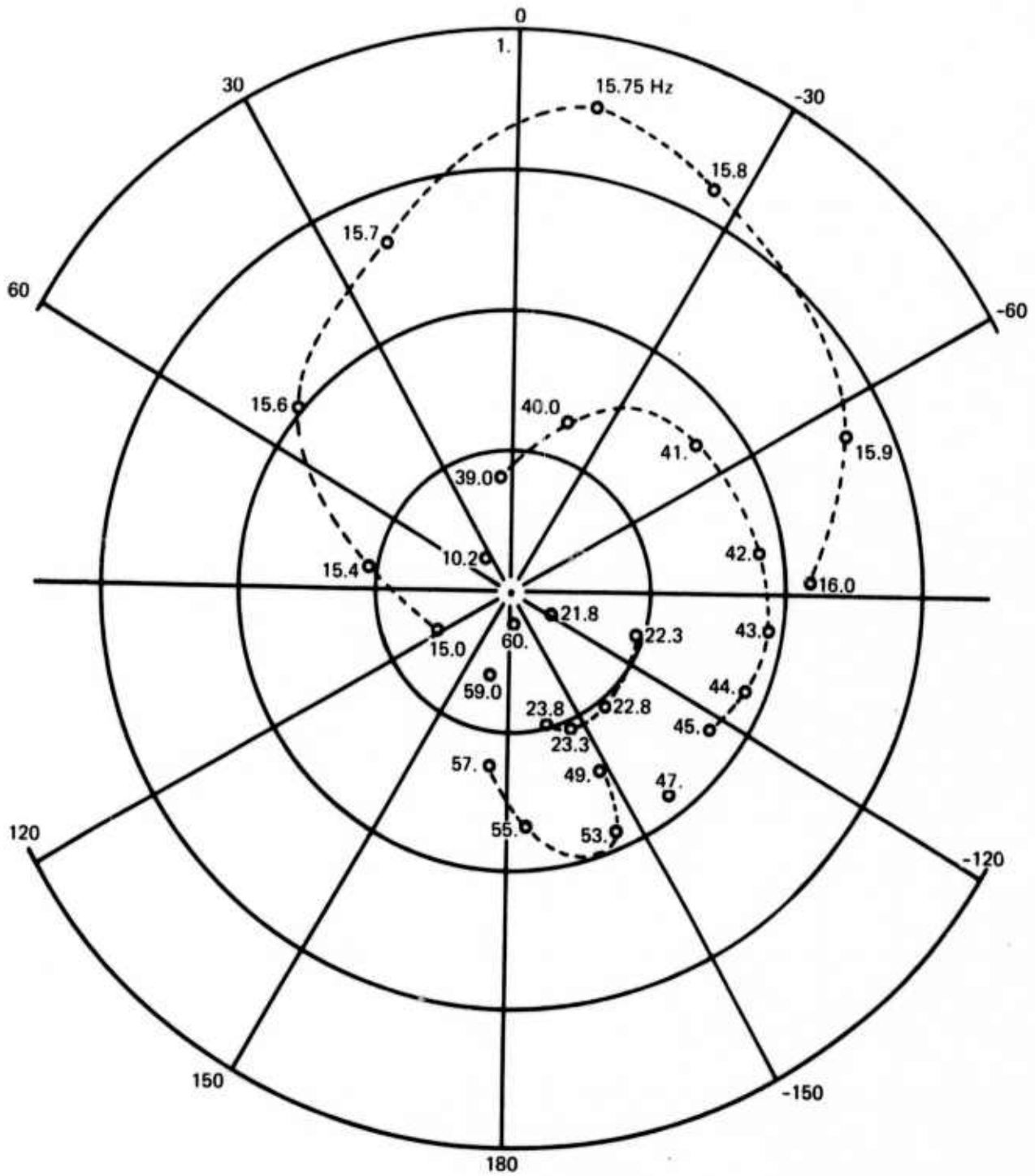


FIGURE 79—CLOSED LOOP FREQUENCY RESPONSE OF OUTBOARD AILERON SYSTEM—GAIN OF 500 AT 130 KN

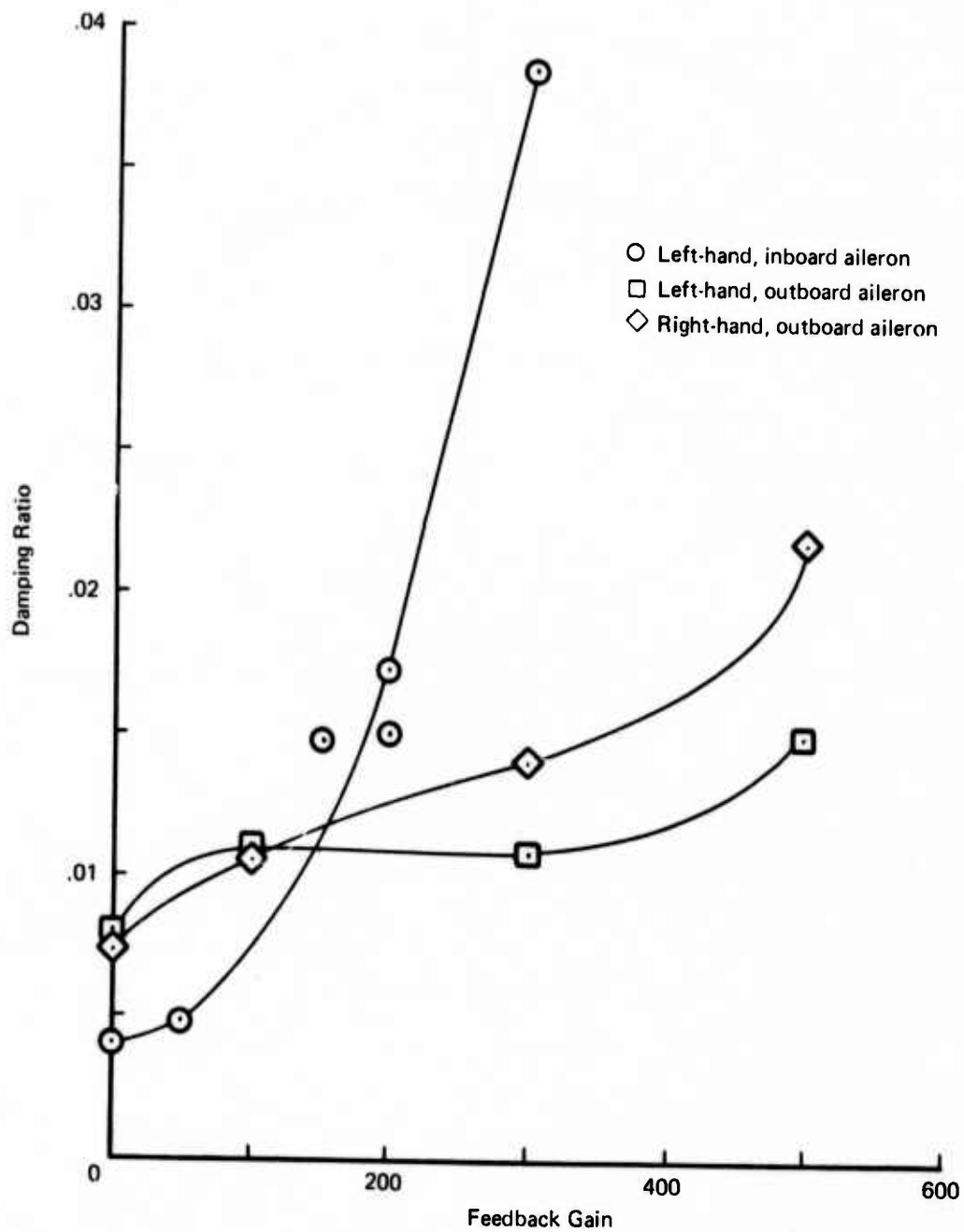


FIGURE 80.—EFFECT OF ACTIVE OUTBOARD AILERON ON 15 Hz MODE AT 130 KN

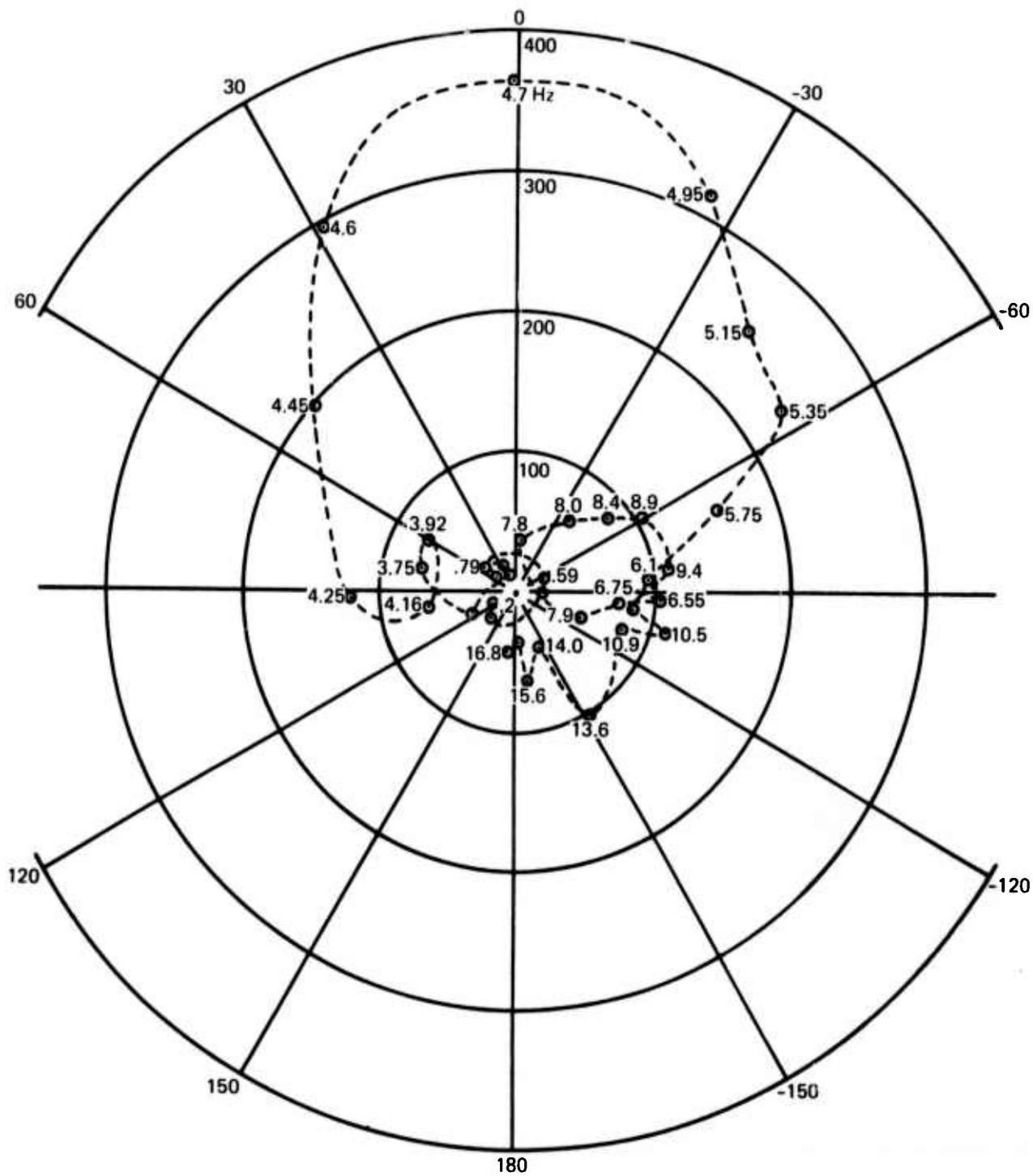


FIGURE 81.—OPEN-LOOP TRANSFER FUNCTION OF STABILIZER/ELEVATOR SYSTEM—130 KN

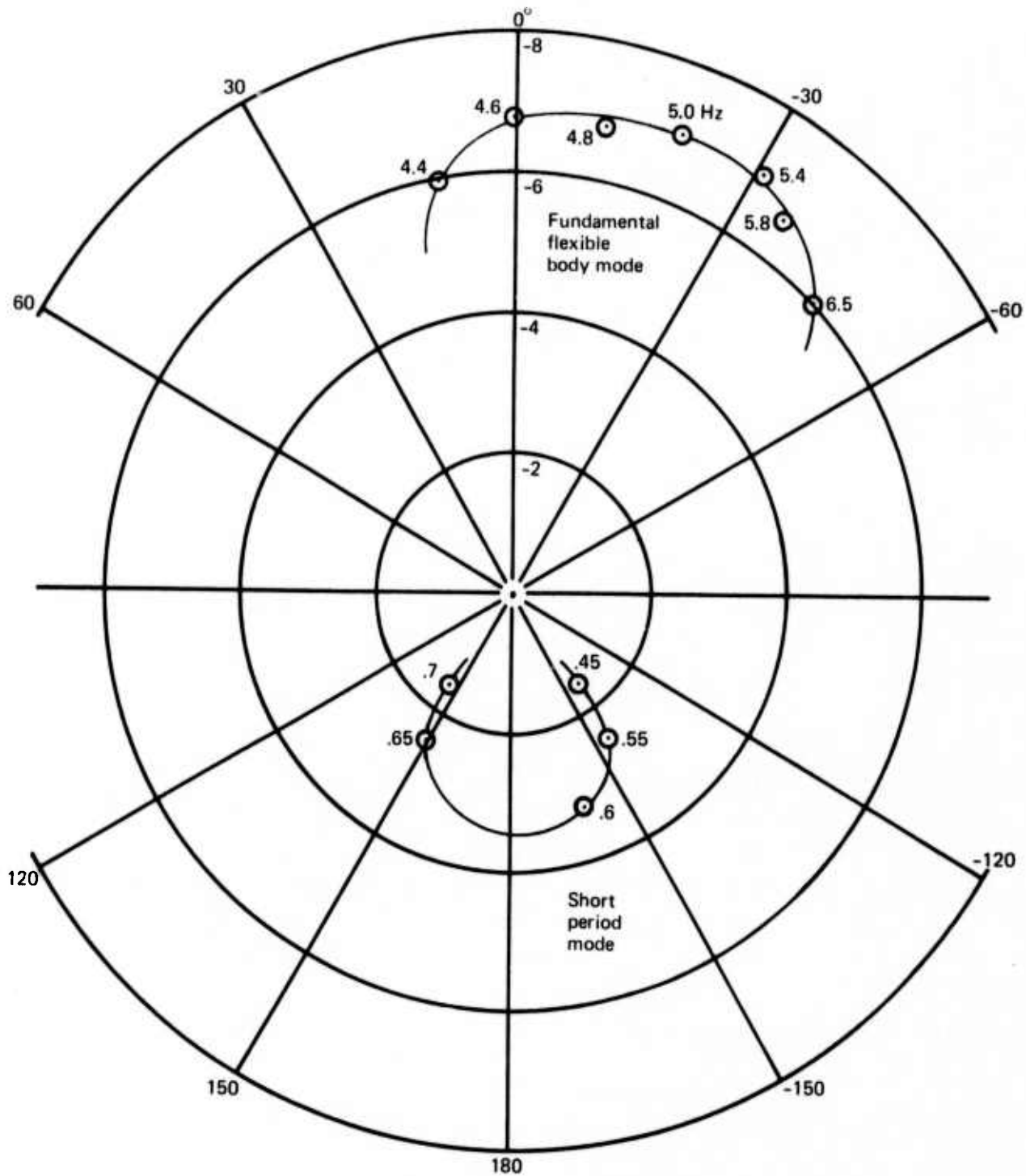


FIGURE 82.—CLOSED LOOP TRANSFER FUNCTION OF STABILIZER/ELEVATOR SYSTEM—130 KN

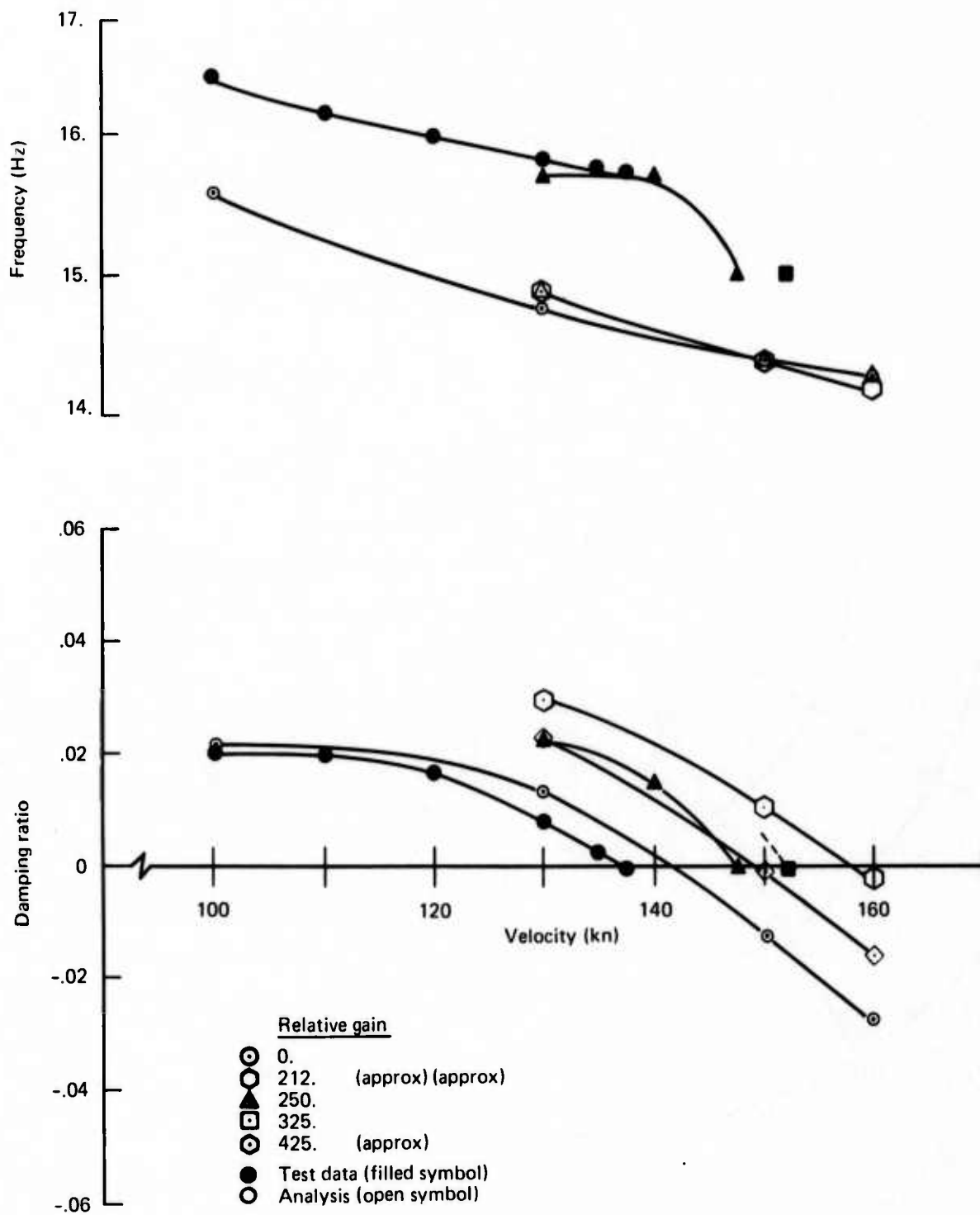


FIGURE 83.—COMPARISON OF RESULTS OF INBOARD AILERON ON WING FLUTTER

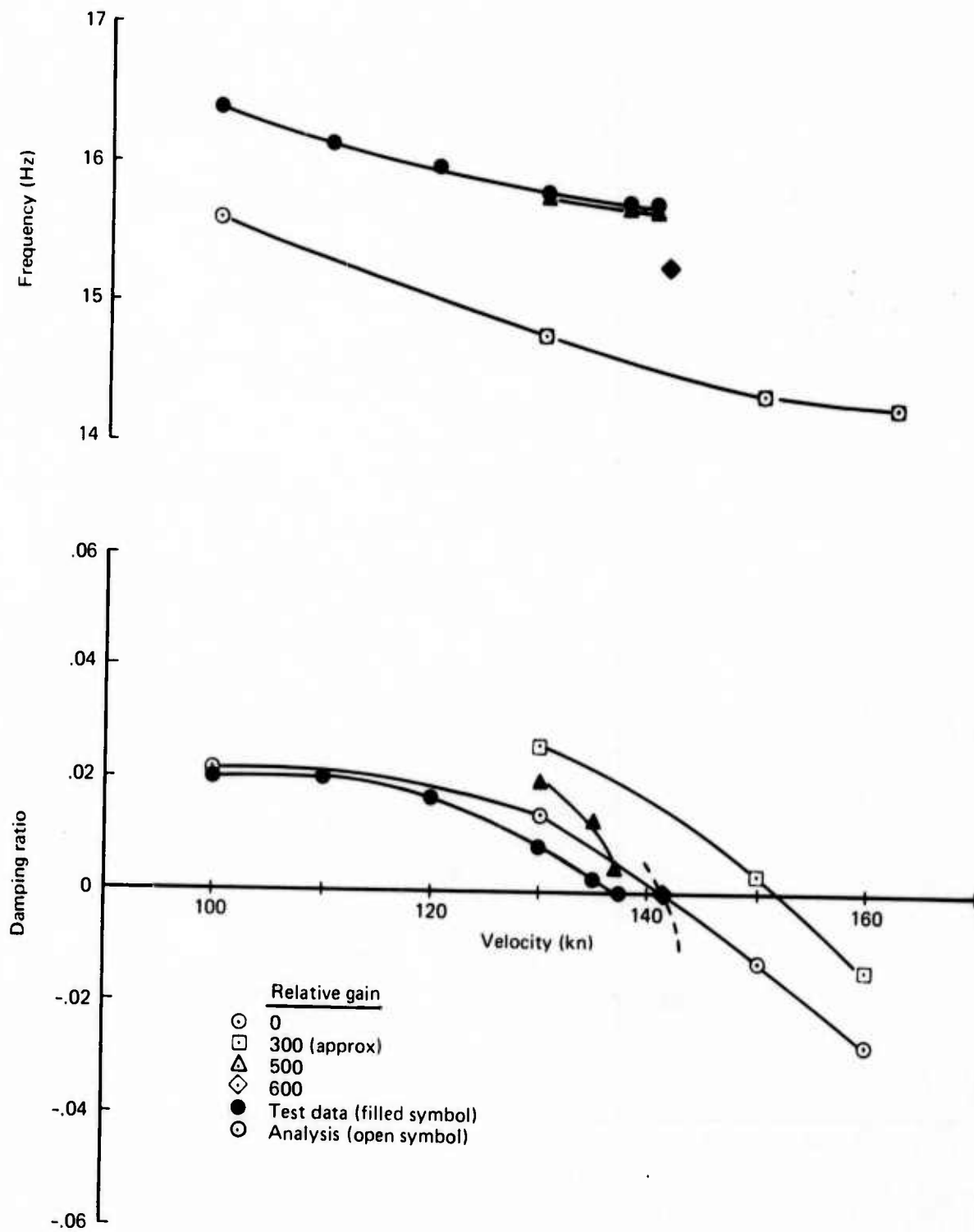


FIGURE 84.—COMPARISON OF RESULTS OF OUTBOARD AILERON ON WING FLUTTER

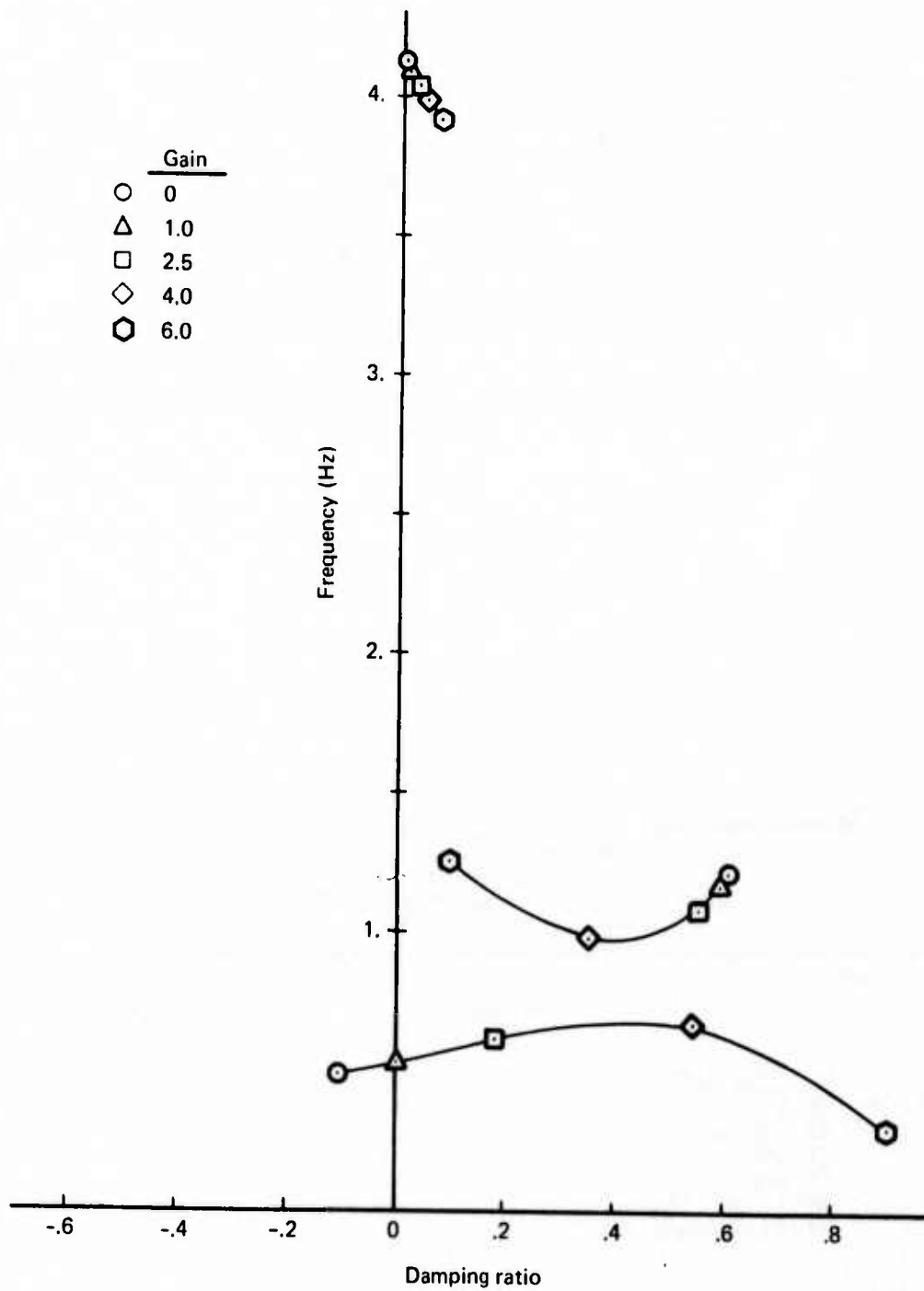


FIGURE 85.—PITCH FEEDBACK CONTROL OF LOW FREQUENCY MODES

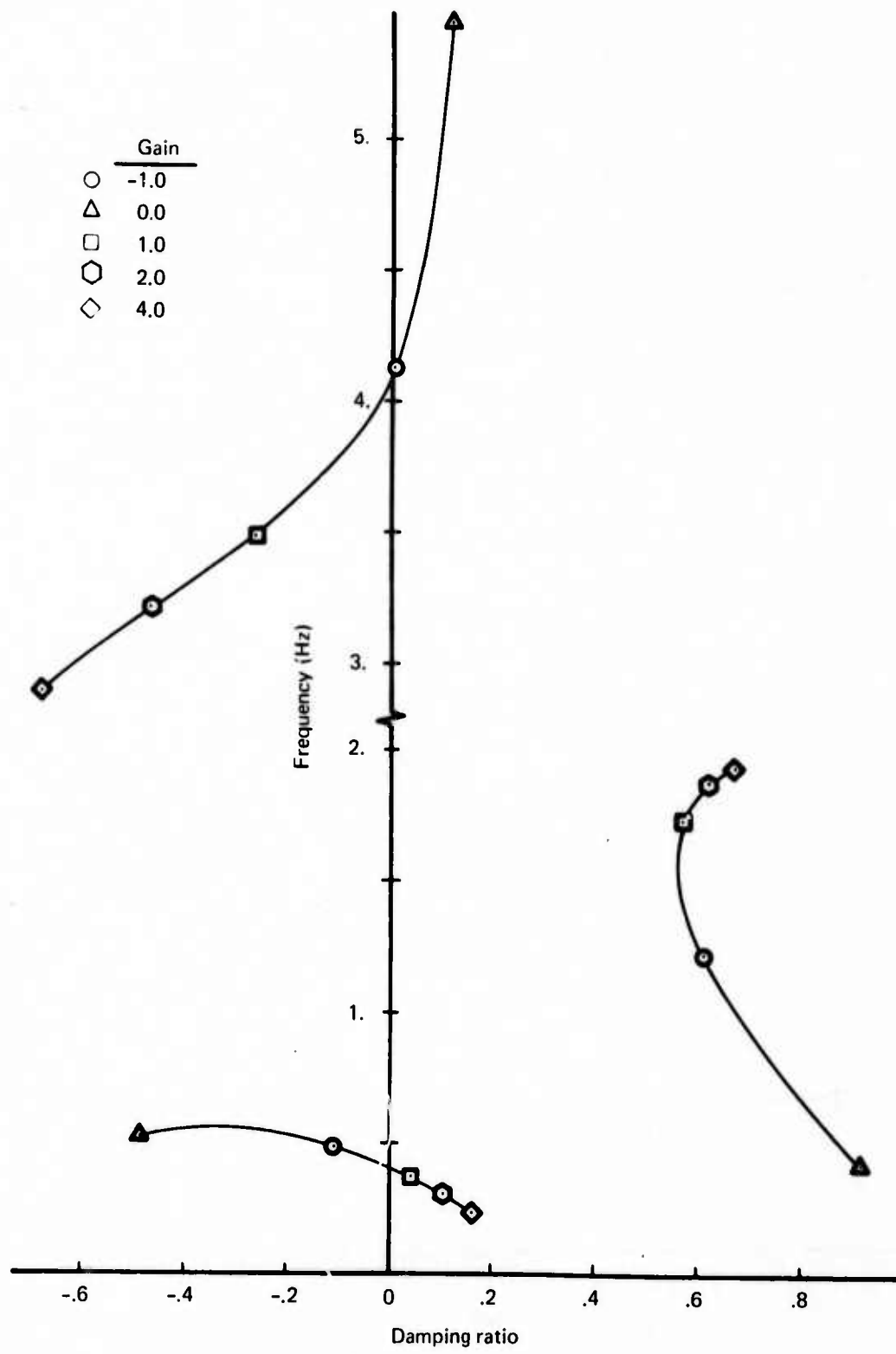


FIGURE 86.—PITCH RATE CONTROL OF LOW FREQUENCY MODES

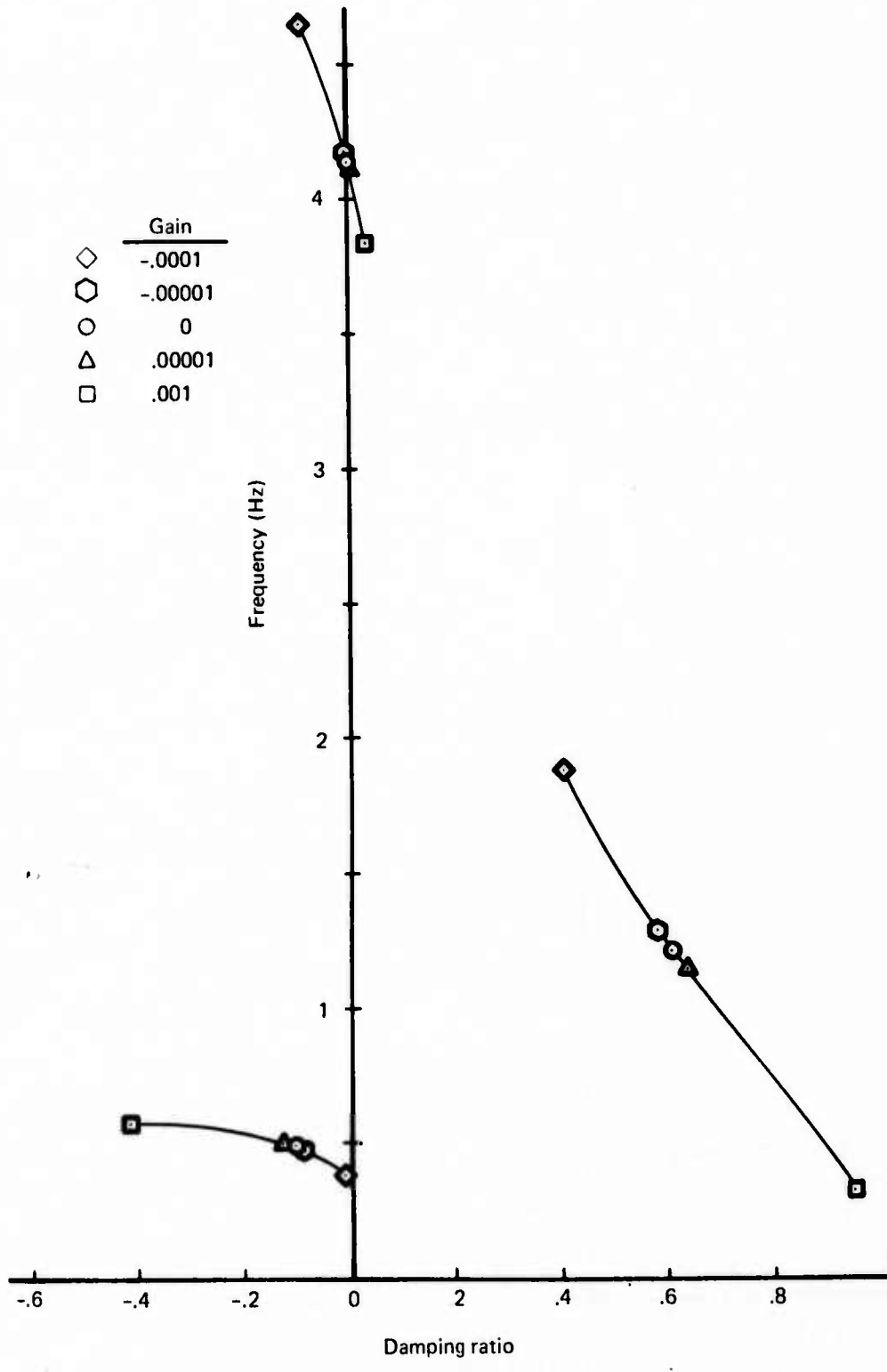


FIGURE 87.—ACCELERATION FEEDBACK CONTROL OF LOW FREQUENCY MODES

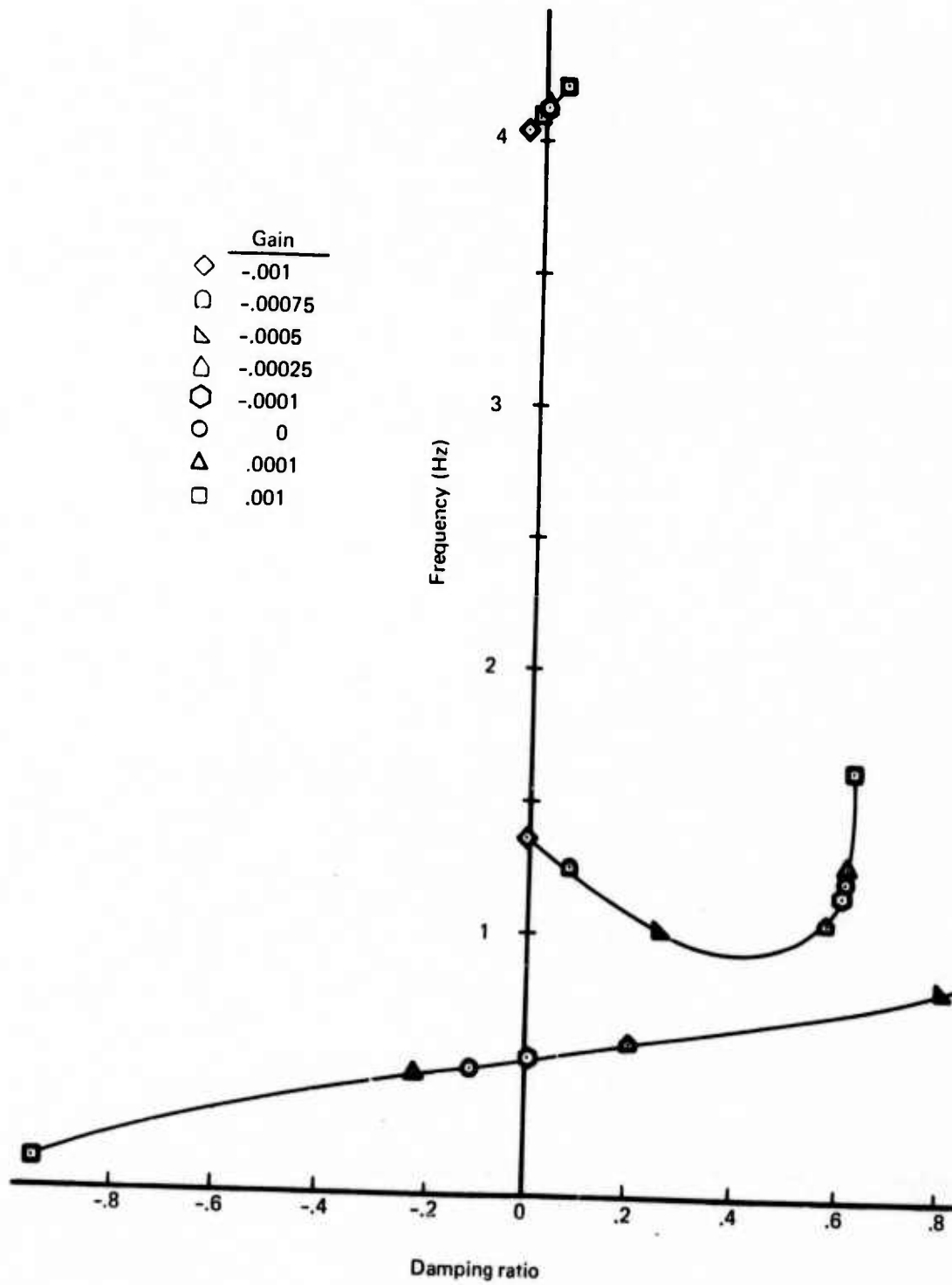


FIGURE 88.—VELOCITY FEEDBACK CONTROL OF LOW FREQUENCY MODES

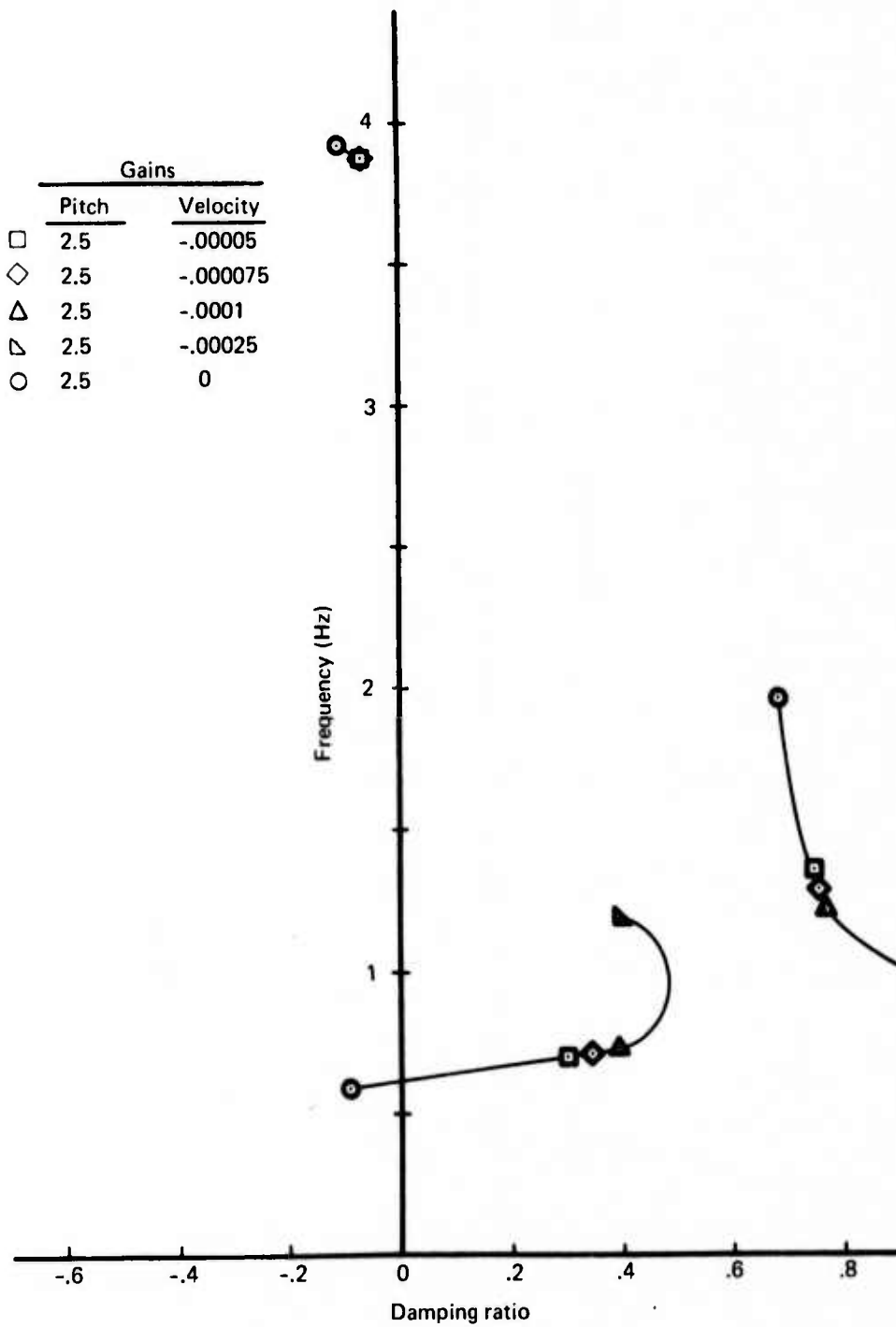


FIGURE 89.—COMBINED PITCH AND VELOCITY FEEDBACK CONTROL OF LOW FREQUENCY MODES

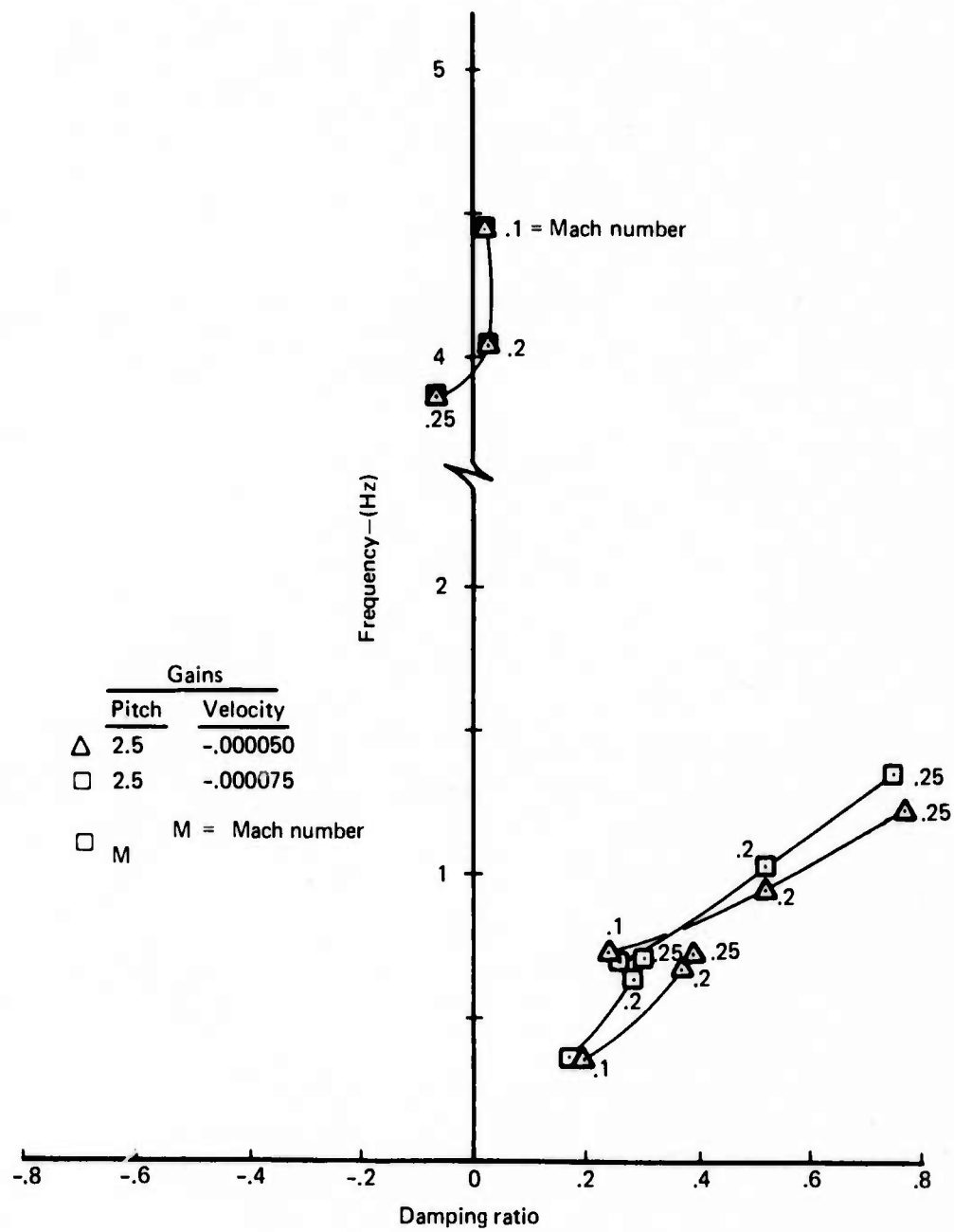


FIGURE 90.—EFFECT OF TUNNEL VELOCITY ON COMBINED PITCH AND VELOCITY CONTROL

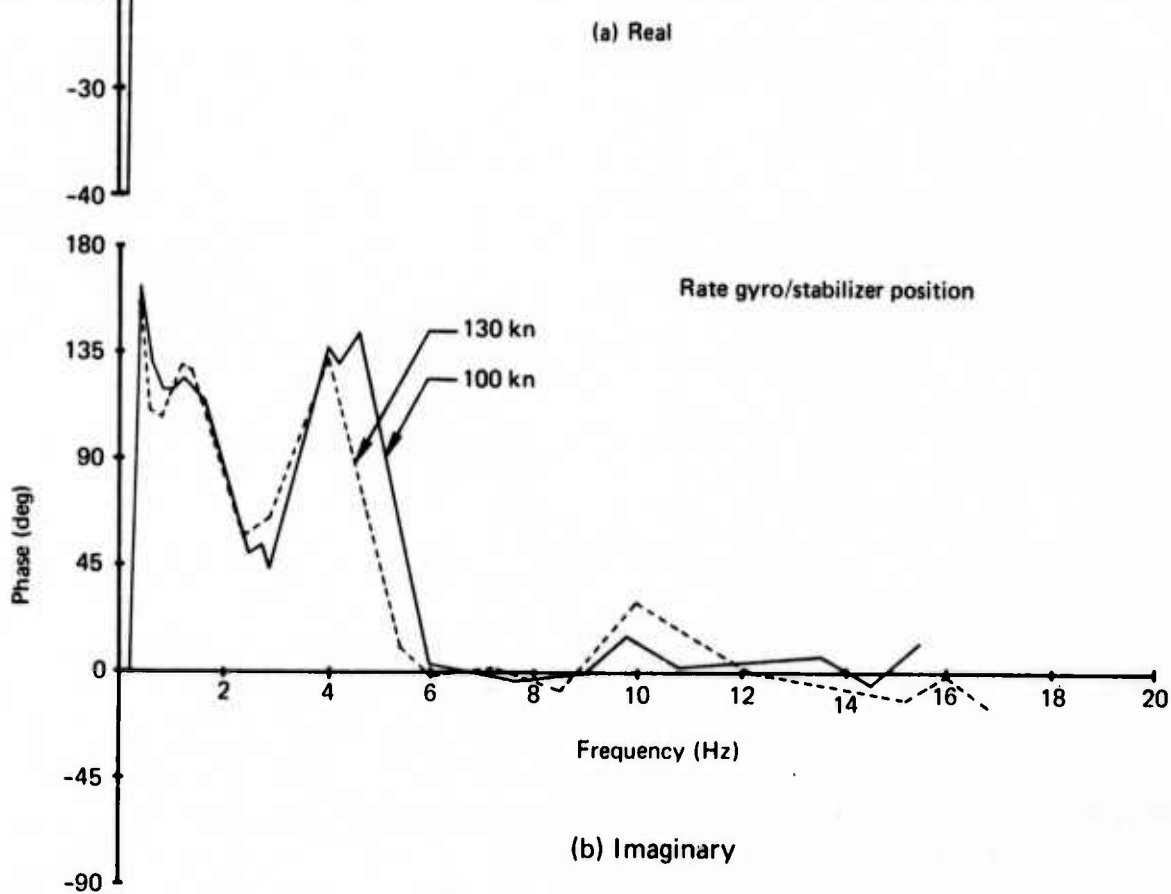
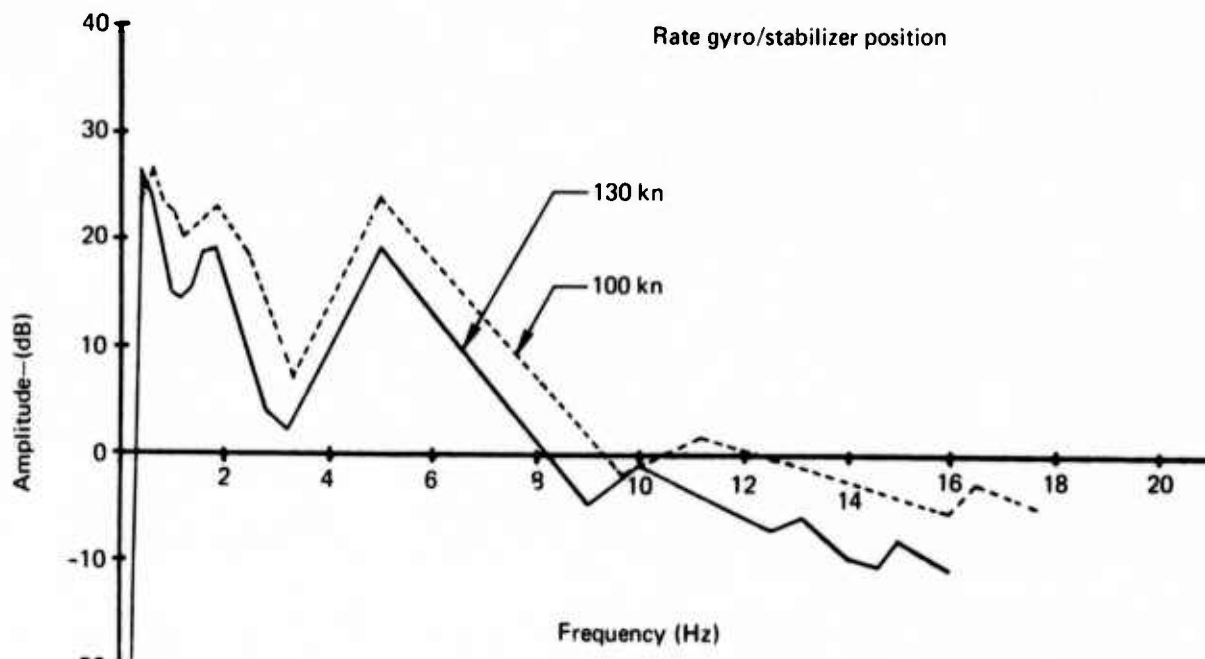
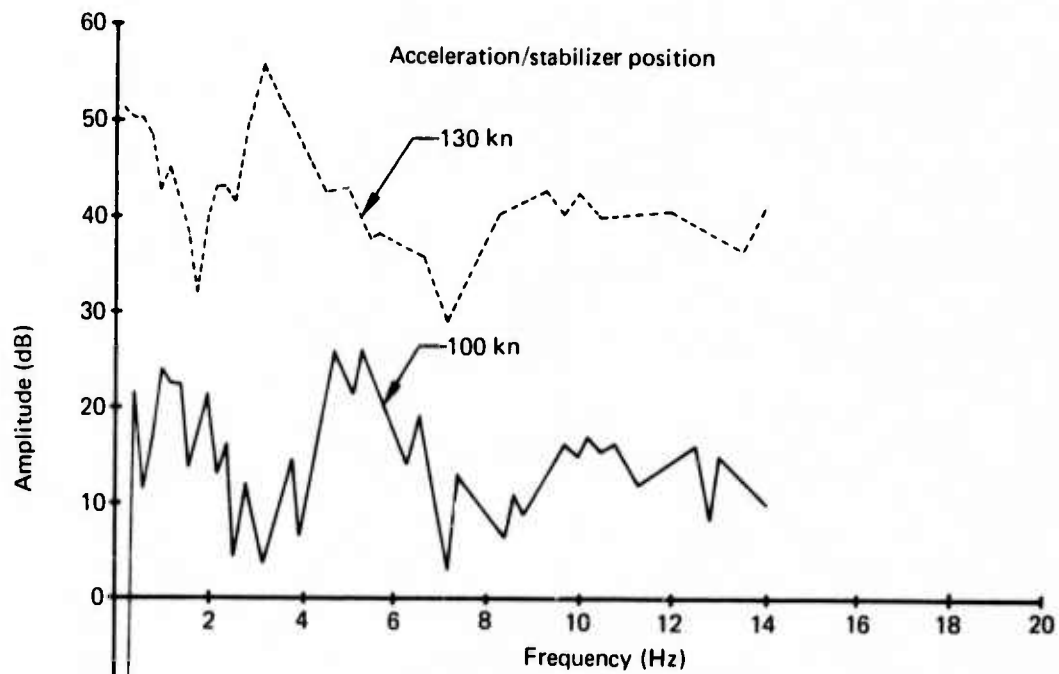
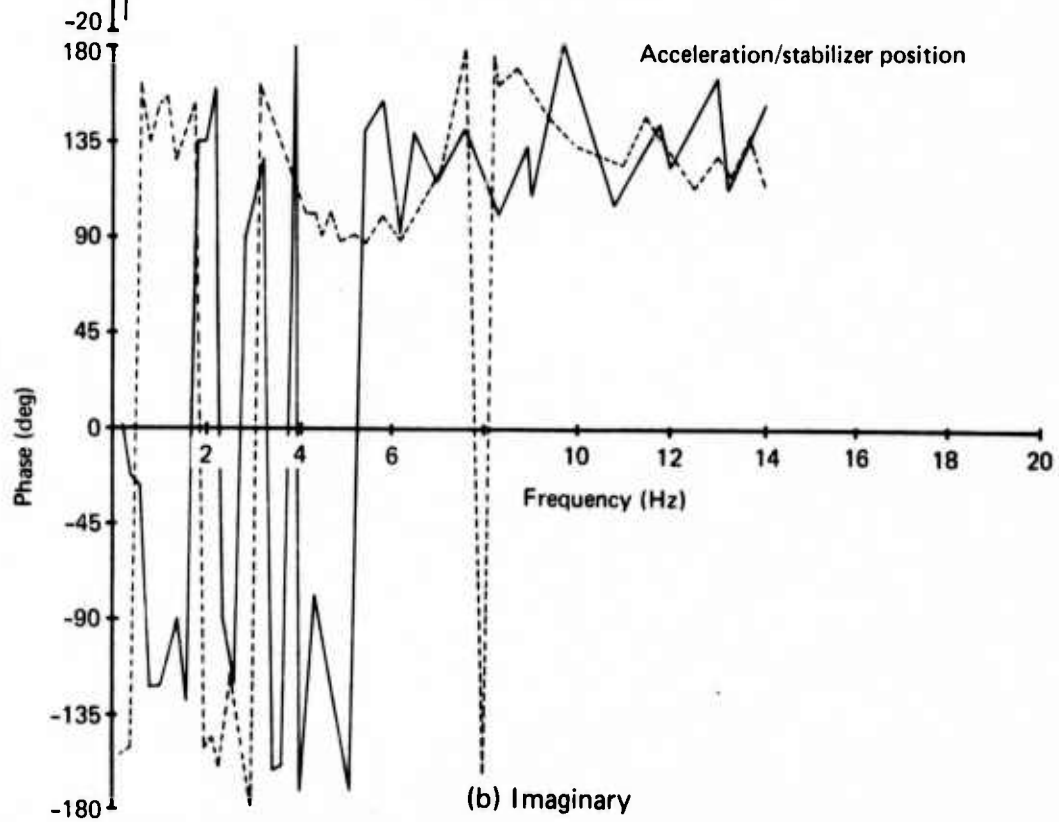


FIGURE 91.—VARIATION OF PITCH RATE TRANSFER FUNCTION WITH TUNNEL SPEED



(a) Real



(b) Imaginary

FIGURE 92.—VARIATION OF ACCELERATION TRANSFER FUNCTION WITH WIND TUNNEL SPEED

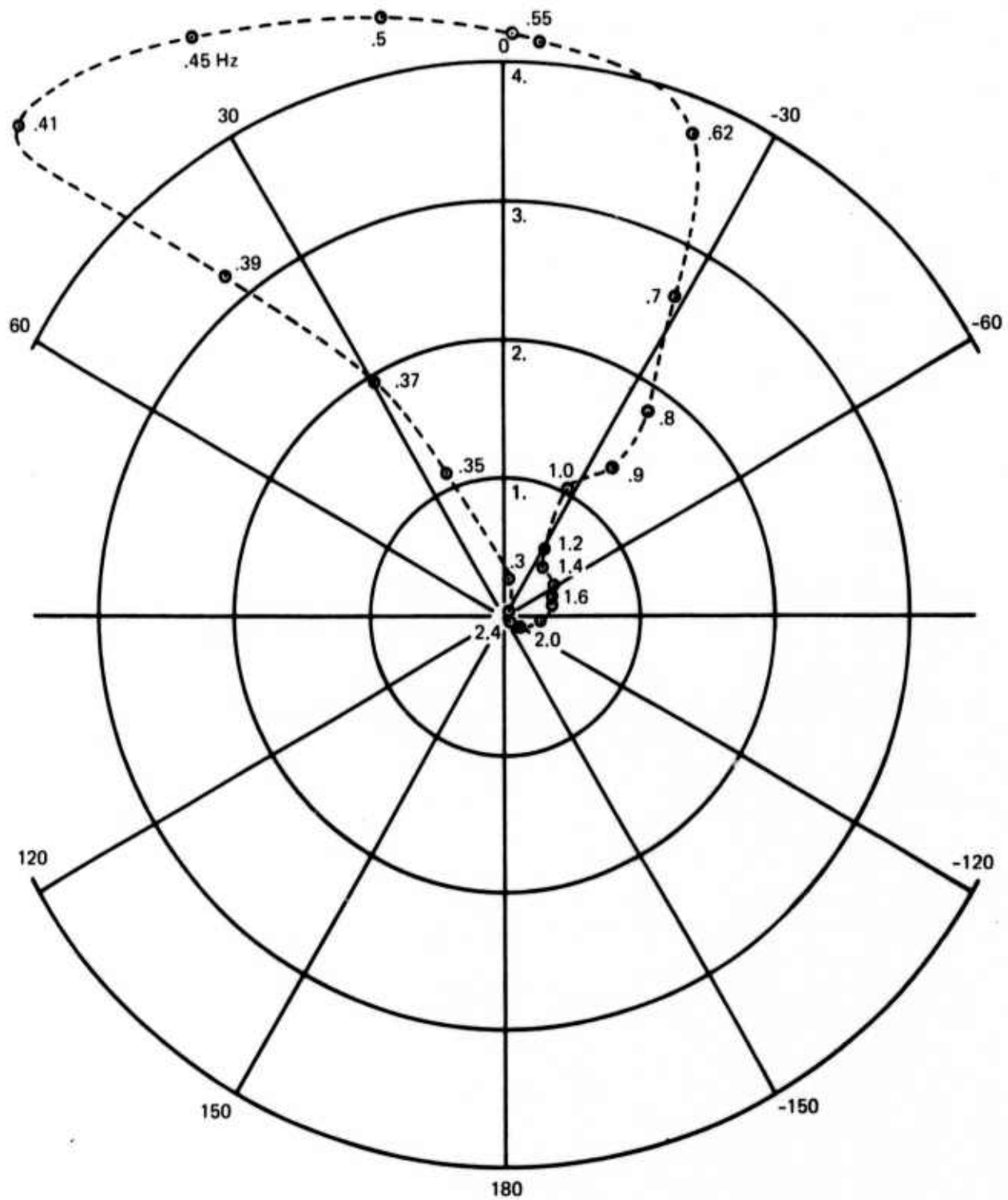


FIGURE 93.—PITCH RATE OPEN LOOP TRANSFER FUNCTION FOR PITCH MODE

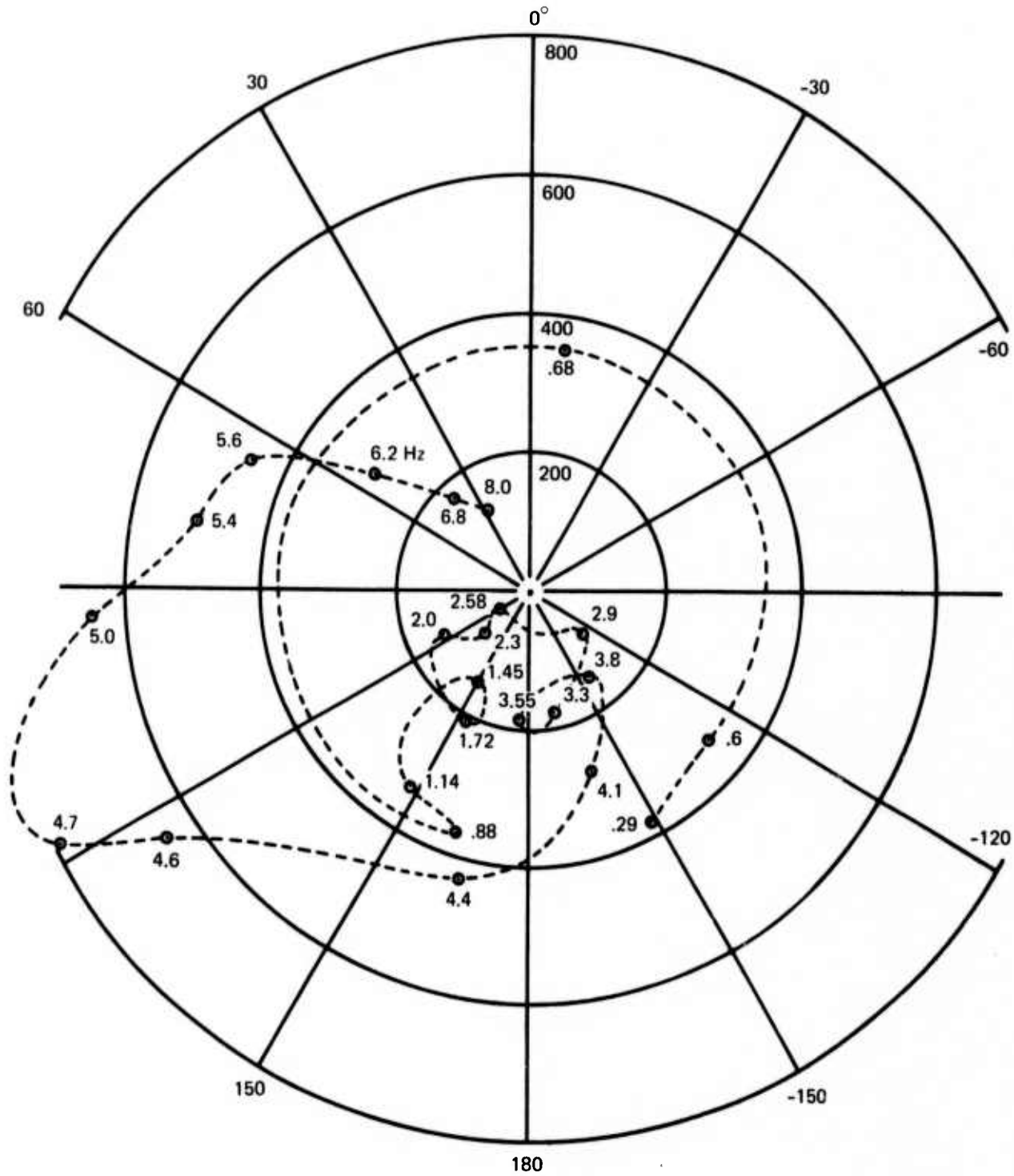


FIGURE 94.—ACCELERATION OPEN LOOP TRANSFER FUNCTION FOR PITCH MODE

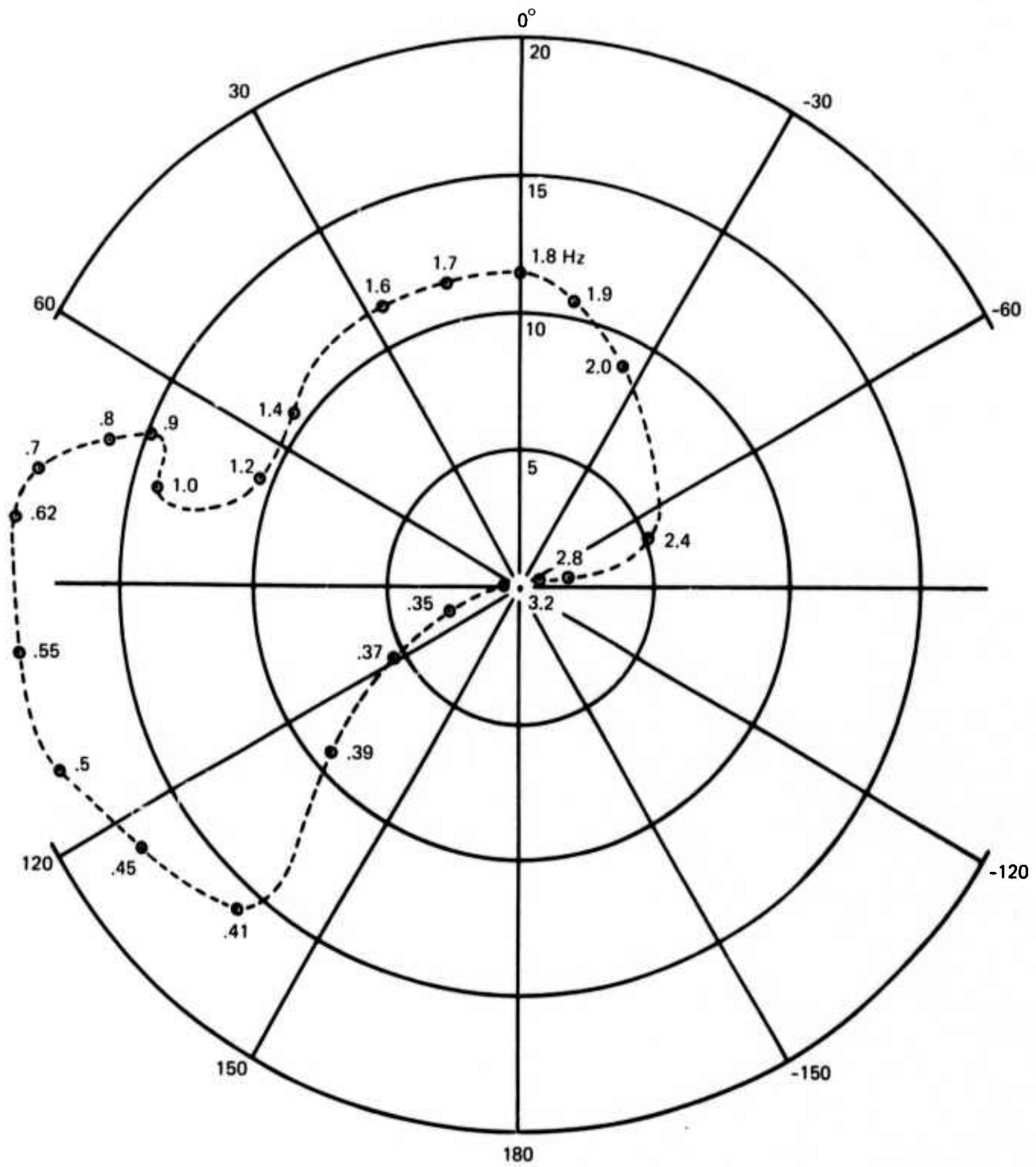


FIGURE 95.—PITCH RATE OPEN LOOP TRANSFER FUNCTION FOR PLUNGE MODE

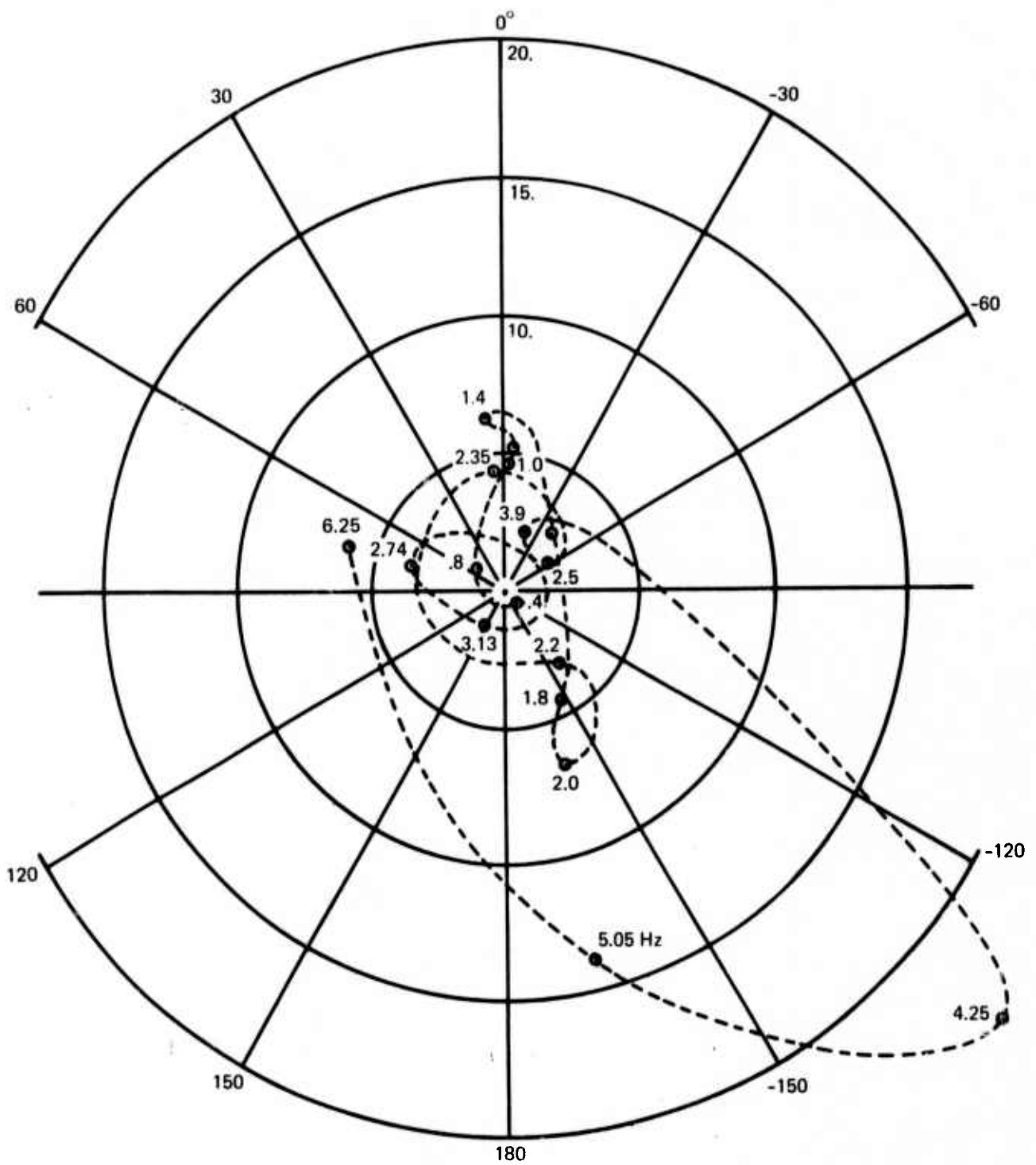


FIGURE 96.—ACCELERATION OPEN LOOP TRANSFER FUNCTION FOR PLUNGE MODE

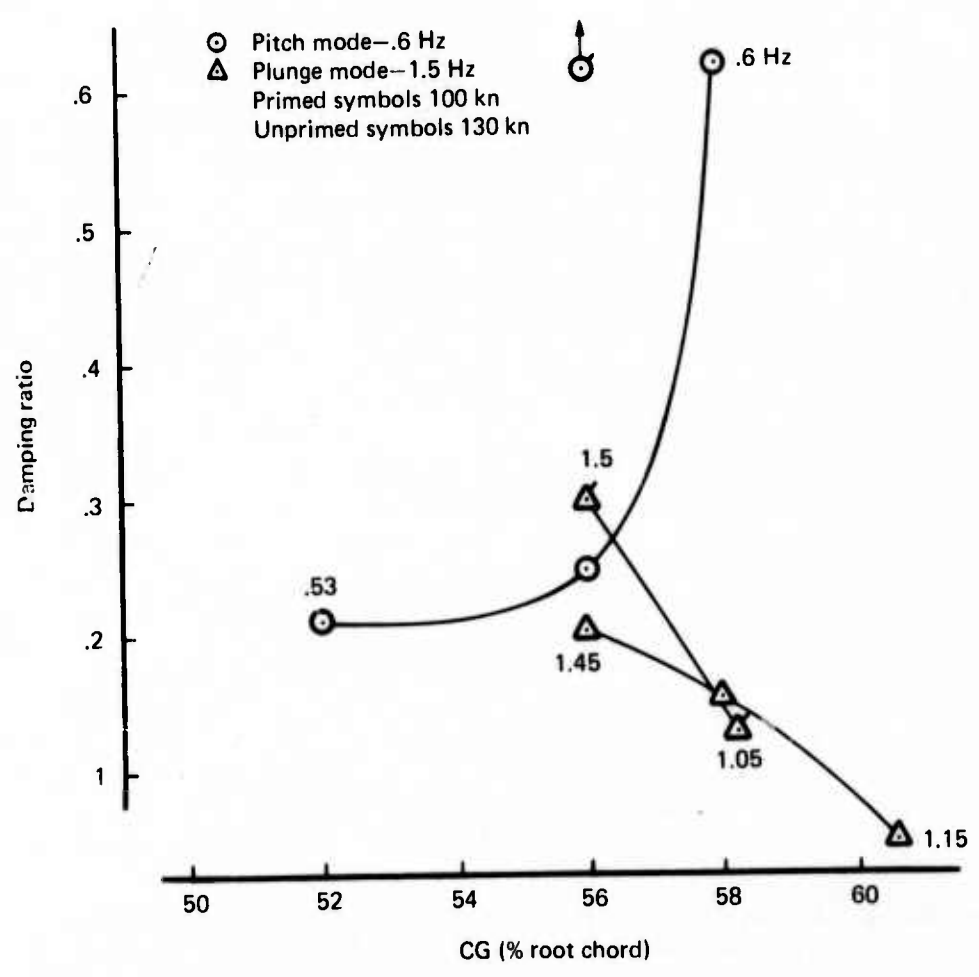
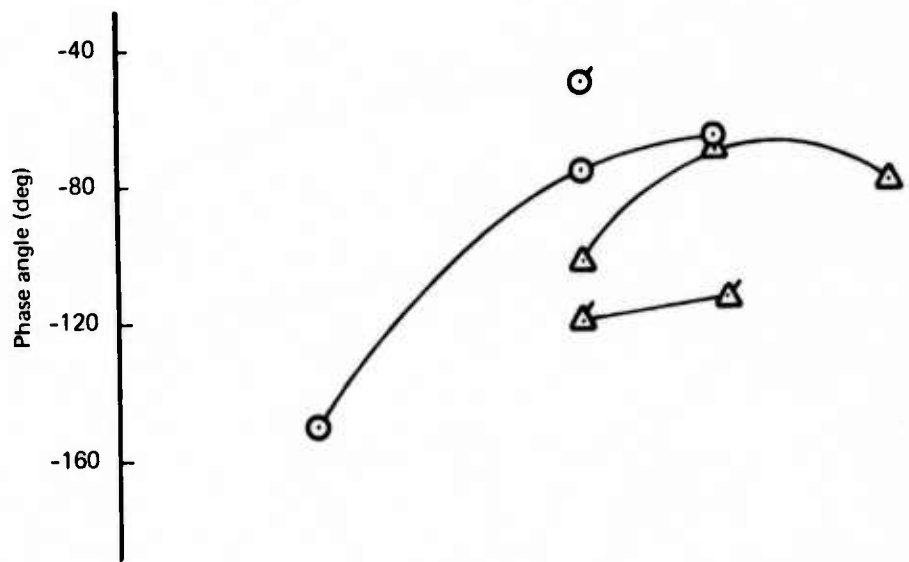


FIGURE 97.—EFFECT OF CG POSITION ON RIGID STABILITY

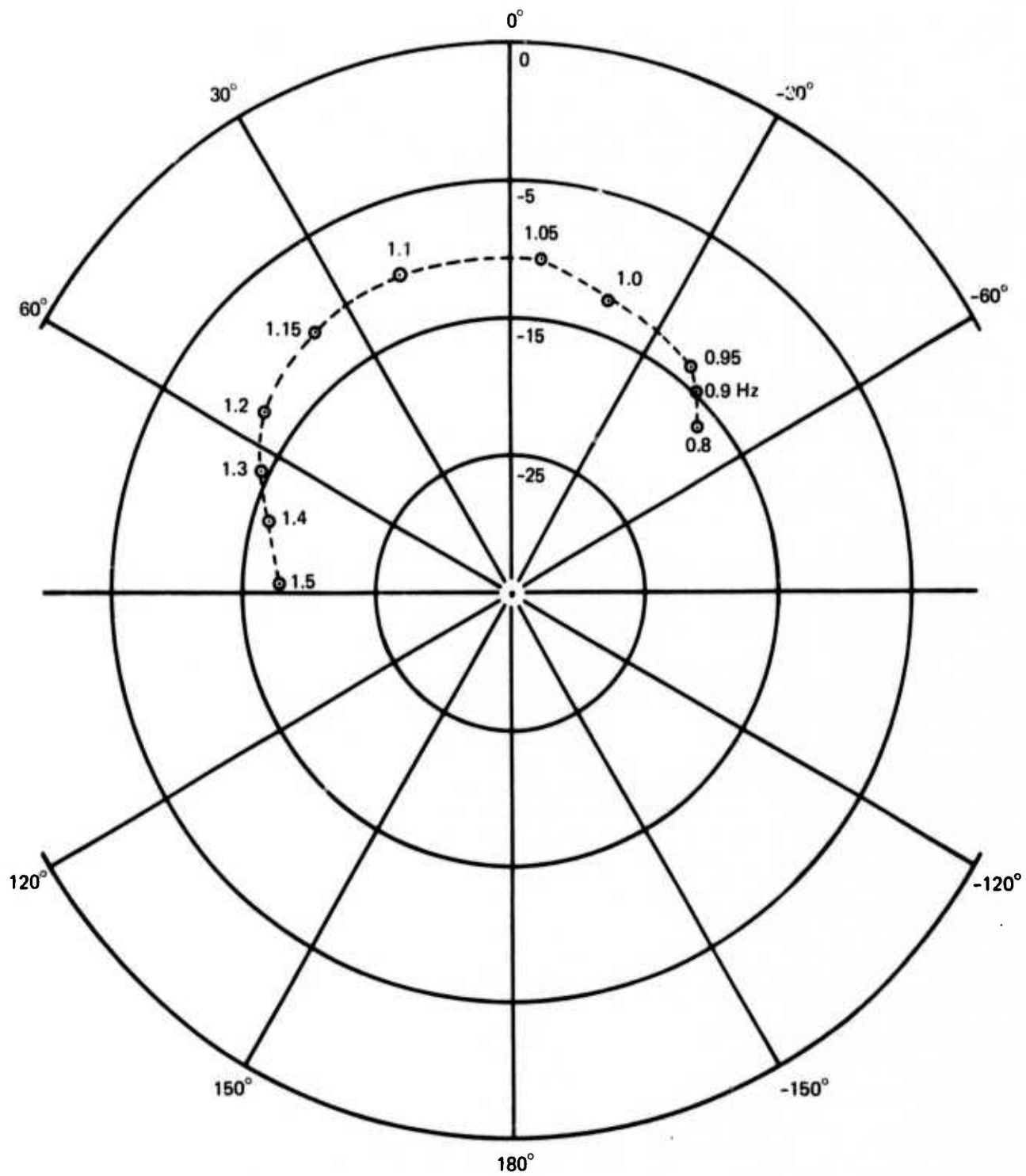


FIGURE 98.—COMPENSATION FILTER CALIBRATION FOR PLUNGE MODE

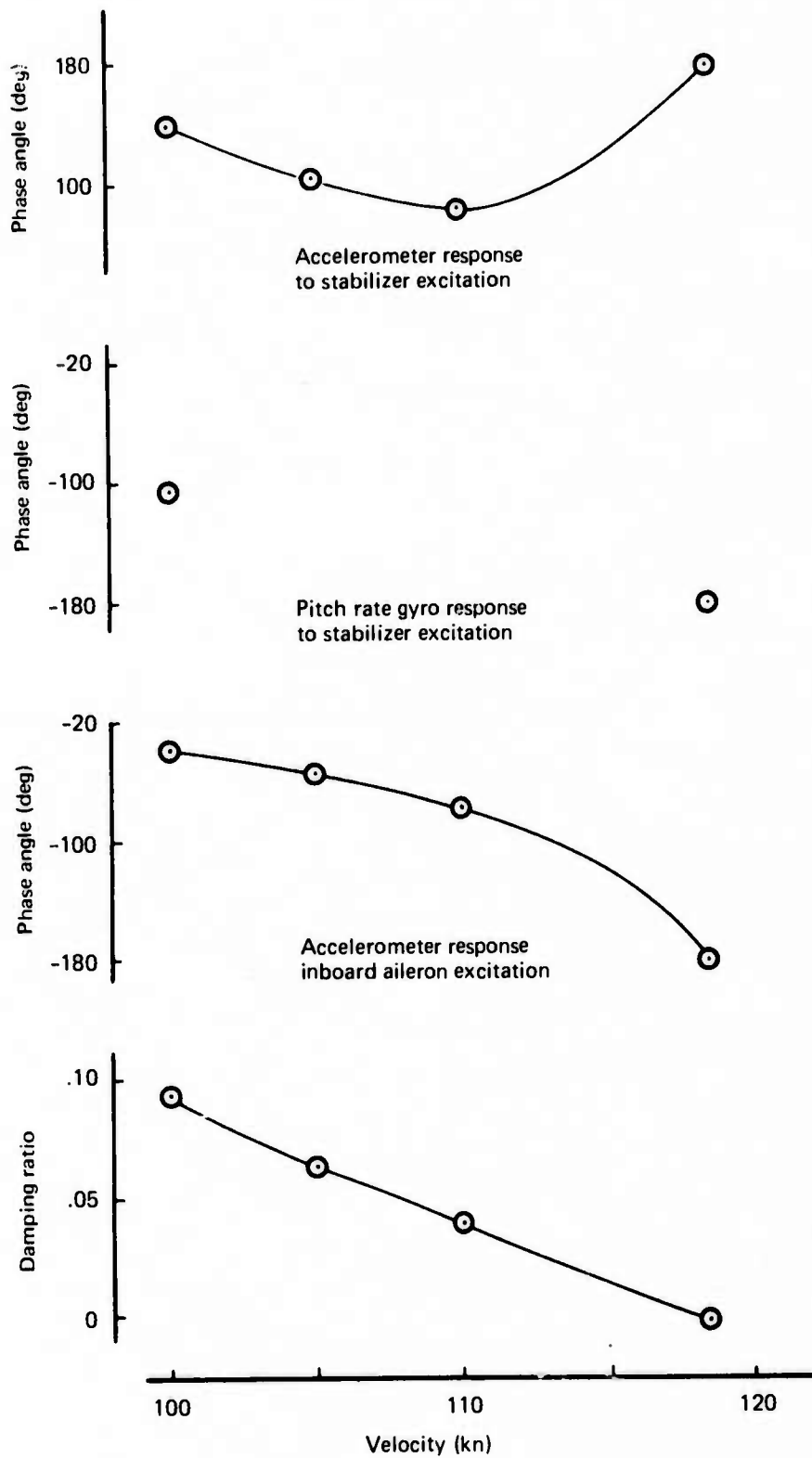


FIGURE 99.—EFFECT OF TUNNEL VELOCITY ON PLUNGE MODE

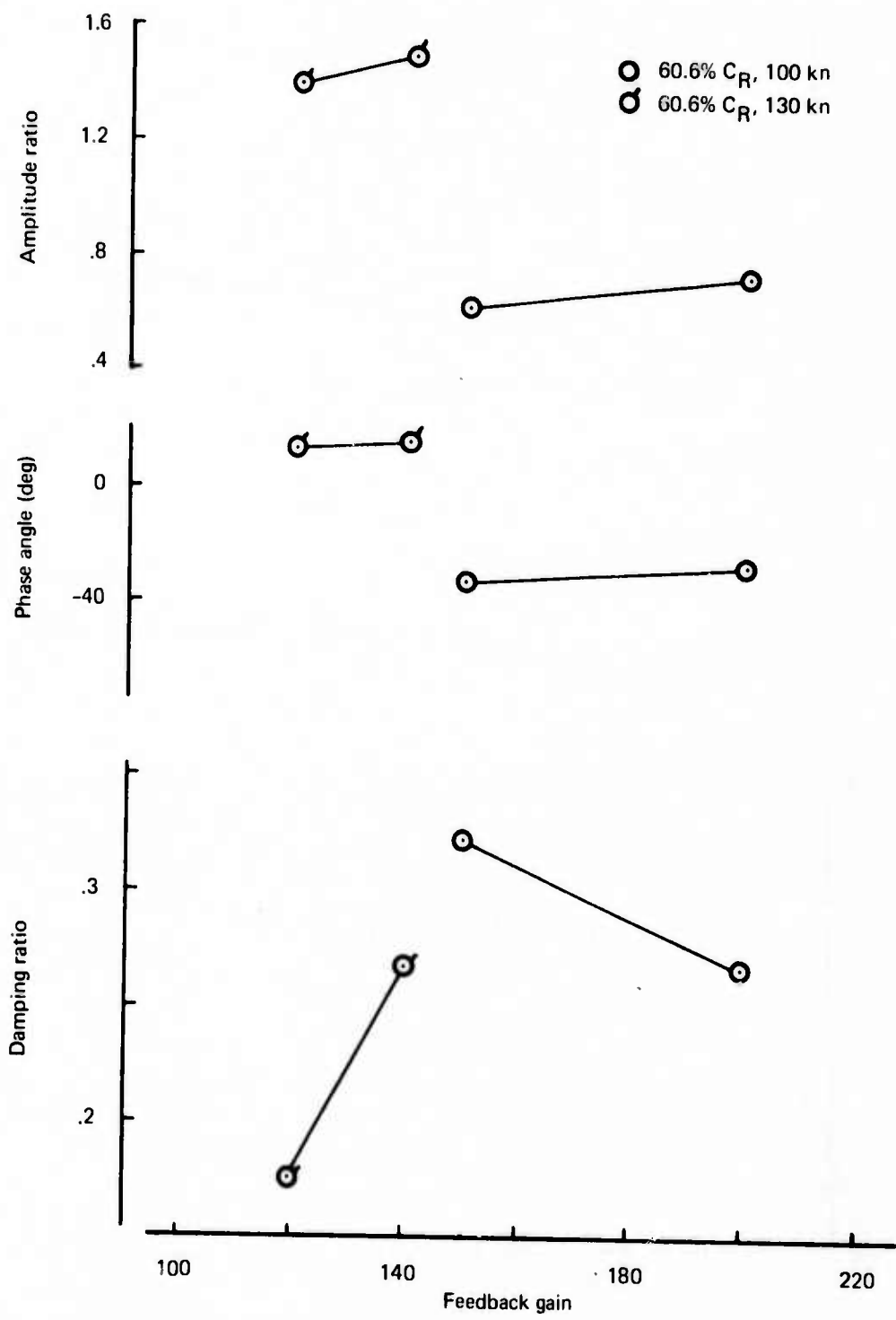


FIGURE 100.—EFFECT OF ACTIVE HORIZONTAL STABILIZER WITH PITCH RATE FEEDBACK ON PLUNGE MODE

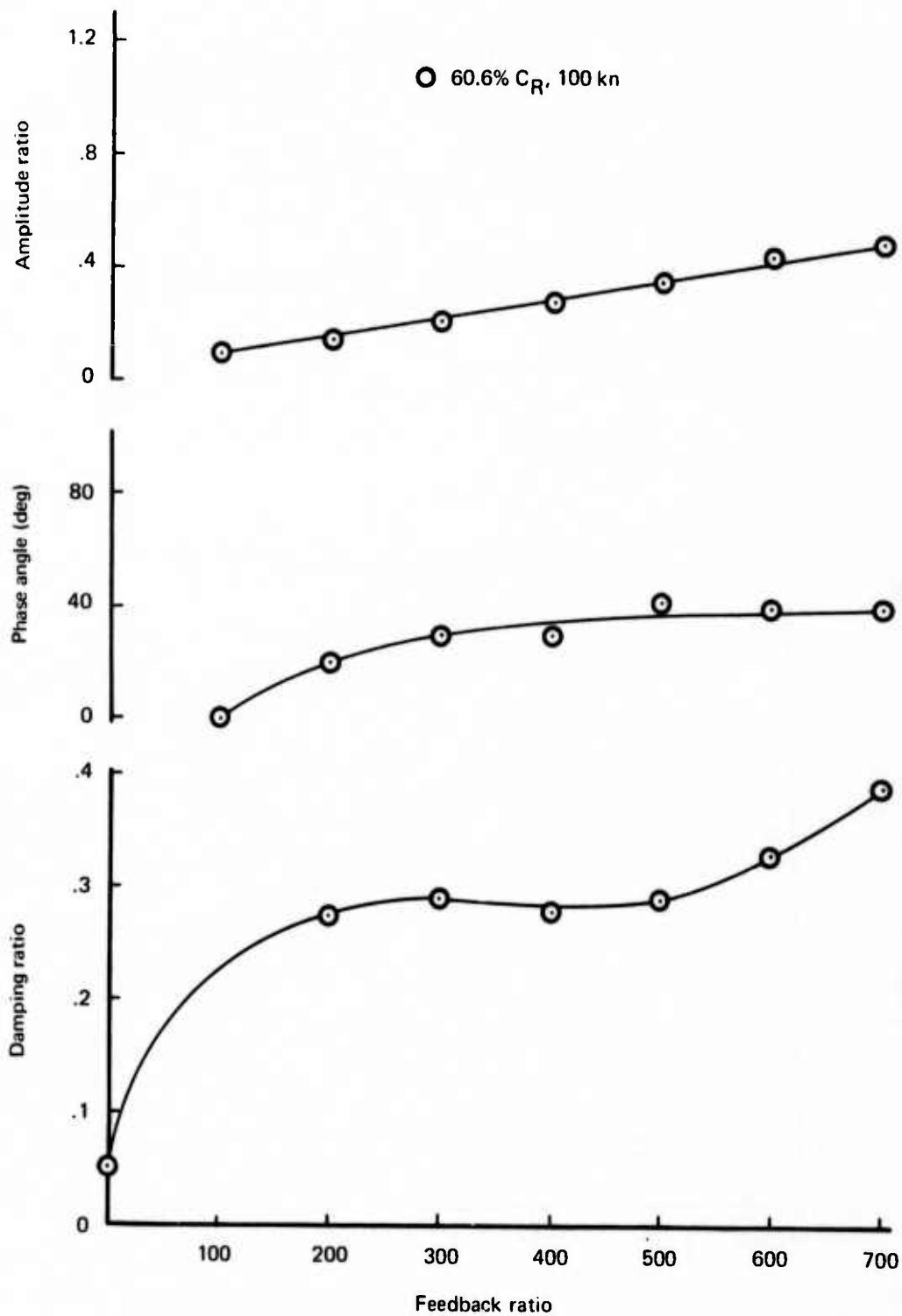


FIGURE 101.—EFFECT OF ACTIVE HORIZONTAL STABILIZER WITH VERTICAL VELOCITY FEEDBACK ON PLUNGE MODE—SENSOR AT 36% OF BODY LENGTH

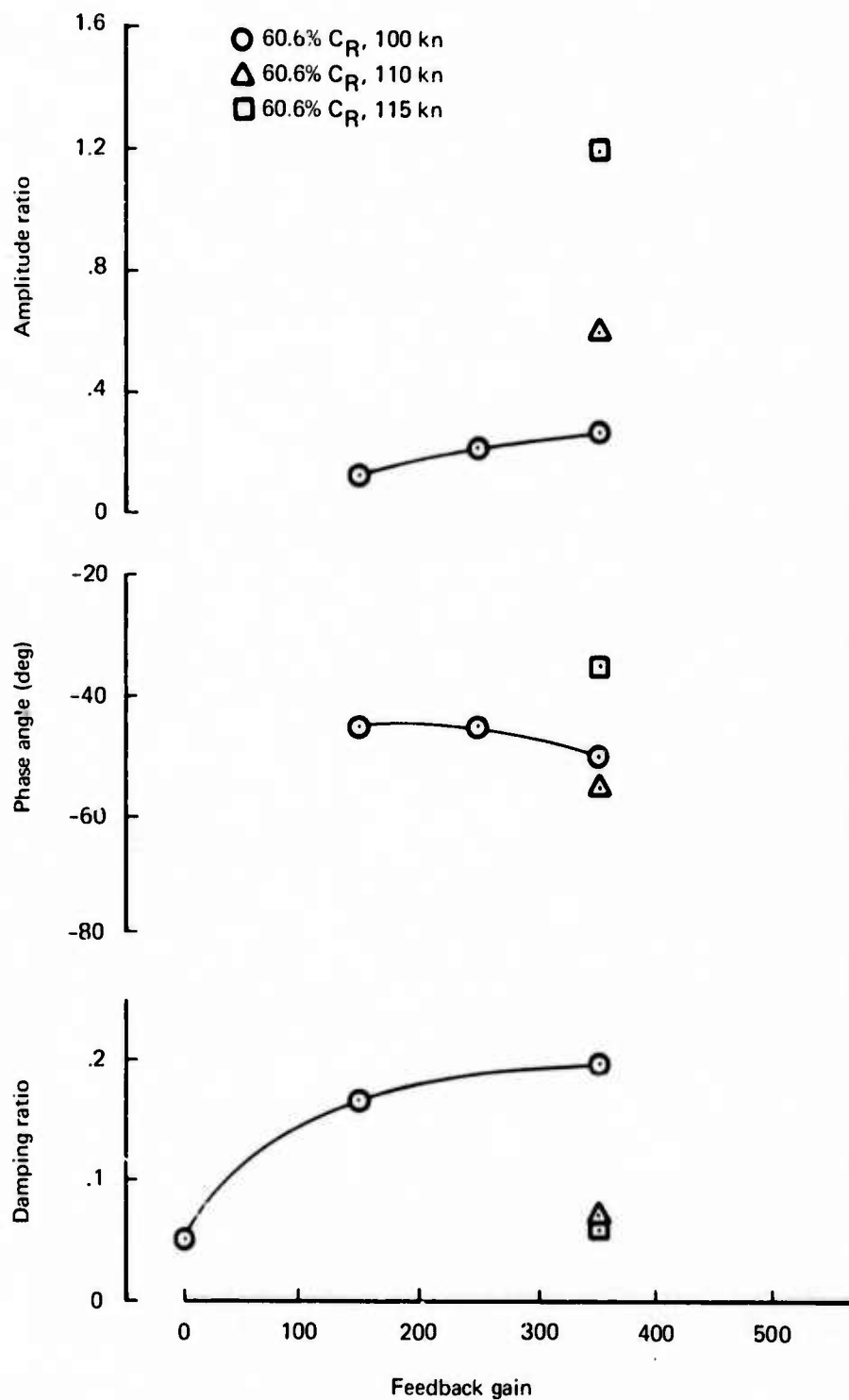


FIGURE 102.—EFFECT OF ACTIVE HORIZONTAL STABILIZER WITH VERTICAL VELOCITY FEEDBACK ON PLUNGE MODE—SENSOR AT 90% BODY LENGTH

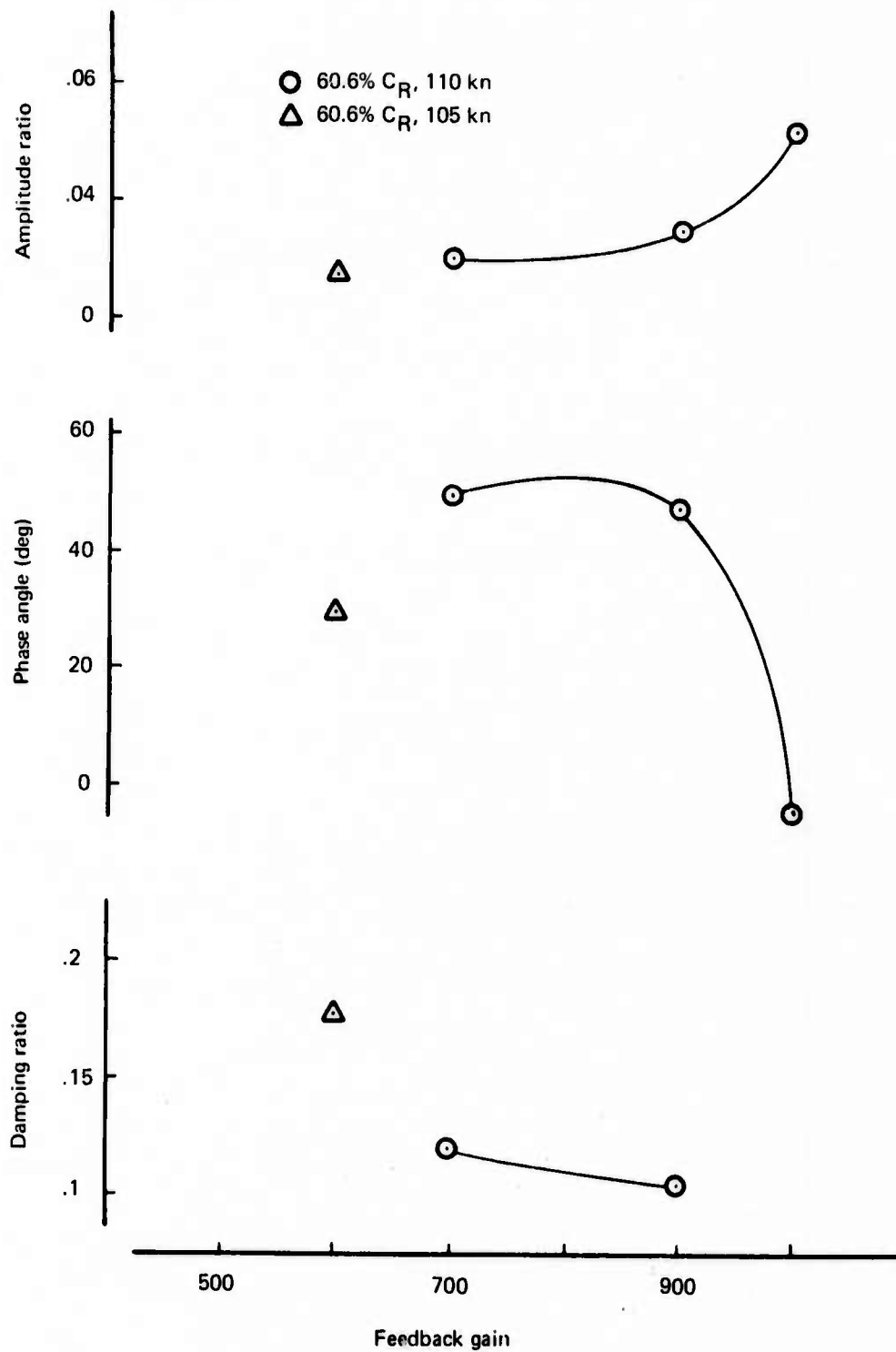


FIGURE 103.—EFFECT OF ACTIVE INBOARD AILERONS WITH VERTICAL VELOCITY FEEDBACK ON PLUNGE MODE SENSOR AT 36% OF BODY LENGTH

APPENDIX A

DESIGN DETAILS OF THE TX1129D MODEL

The model used in this program was a 1/20-scale low speed model of the Boeing 2707-300 airplane. Modifications were made to incorporate hydraulically powered control surfaces on the model. This appendix covers details on how the modification was accomplished.

Parts of the partially complete 1/17-scale full-span transonic model of the 2707-300 airplane were utilized in the pitch control system. The geared stabilizer and linkage, a small commercial piston actuator (Oil Dyne A1/2 x 1), and the three-servo valve manifold were fitted into the low speed model. The stabilizer pivot was positioned to scale location and the above elements were attached to the aft-body spar with appropriate machined parts.

The aft two body sections were rebuilt to accommodate the new geared motion stabilizer and to enclose the position transducer package. These two sections were covered with clear vinyl sheet to allow visual warning if leaks were to appear and to allow continual visual inspection of this primary installation.

The model had a full body fuel and payload simulation. The various horizontal stabilizer control elements such as machined parts, servovalves, actuator, and position potentiometers were positioned in the model to substitute for scale weights. These elements were found to be well within allowable weight. The three-servo valve manifold was rigidly mounted to the aft spar, and 3/16-dia thin-wall steel-coiled tubing was used to connect the manifold fluid supply to the actuator and to the supply manifold. The tubing was coiled to eliminate body stiffness contributions by the hydraulic lines. To minimize flexing of the tubing, the actuator was pivot-mounted midway between its two tube connections. The actuator pivot and all connections to the stabilizer crankarm contained adjustable journal bearings since several hundred hours of operation involving frequencies and amplitudes ranging up to 50-Hz and $\pm 12^\circ$ were anticipated. In order to minimize wear due to misalignment in the position transducers, the three housings were accurately and firmly positioned. The three moving cores were connected to the stabilizer actuator shaft by means of a rigid frame and three piano wire flexures 1.0-in. long by 0.03-in. dia. Figure A1 illustrates the design detail. The potentiometers used were manufactured by the Computer Instrument Corporation and were CIC linear motion potentiometer type 118. No wear problems were detected despite the large number of cycles to which they were subjected.

All of the hydraulic supply and the return passed through a distribution manifold located at body station 101. See general configuration sketch, figure 6. The distribution manifold was attached to the upper surface of the wing root. From this manifold two 1/4-in. supply lines and one return line were routed and coiled around the body spar aft to the three servovalve manifold for the stabilizer. One supply line was connected directly to the stabilizer servomanifold as shown in figure A2.

From this distribution manifold a third 1/4-in. steel supply line and a second 1/4-in. return line were coiled and routed to the four servovalve aileron manifold that was mounted

on the body centerline near the wing rear spar. No difficulties were encountered in the manifold installations or the routing of the stainless steel hydraulic lines up to the point of routing lines from the four servovalve manifold along the rear spar of the wing, figure 7. Aileron actuators were in design and development early in the active control model program and all of the hydraulic work was done concurrently with detail actuator design.

The aileron actuators were modified versions of rotary actuators designed for wing mounted trim of the 1/17-scale transonic model. Some simple design changes were incorporated in the rotary actuators to improve their frequency characteristics. Subsequent breadboard testing demonstrated the suitability of the modified actuators for use in the active controls model. A key link in the control system loop was the position feedback torsion blade which was mounted on each actuator. The natural frequency of this feedback installation was high enough so that no unwanted resonance of the torsion blade was experienced through the operational frequency range of 0-50 Hz. The mounting of the aileron actuators to the wing structures was the most difficult task. The problems encountered in this area were (1) routing four of the 3/16-in. steel tubes within wing contour (2) mounting the actuators to provide high torsional stiffness to react the aileron loads without stiffening the wing significantly. The inboard actuator was attached to the wing with aluminum beams that were rigid in vertical bending but soft in torsion thus allowing the wing to flex in span bending through this area. The outboard installation was similar. This installation is illustrated by figures 7 and A3.

Further details of the design modification of the control system model are found in reference 12.

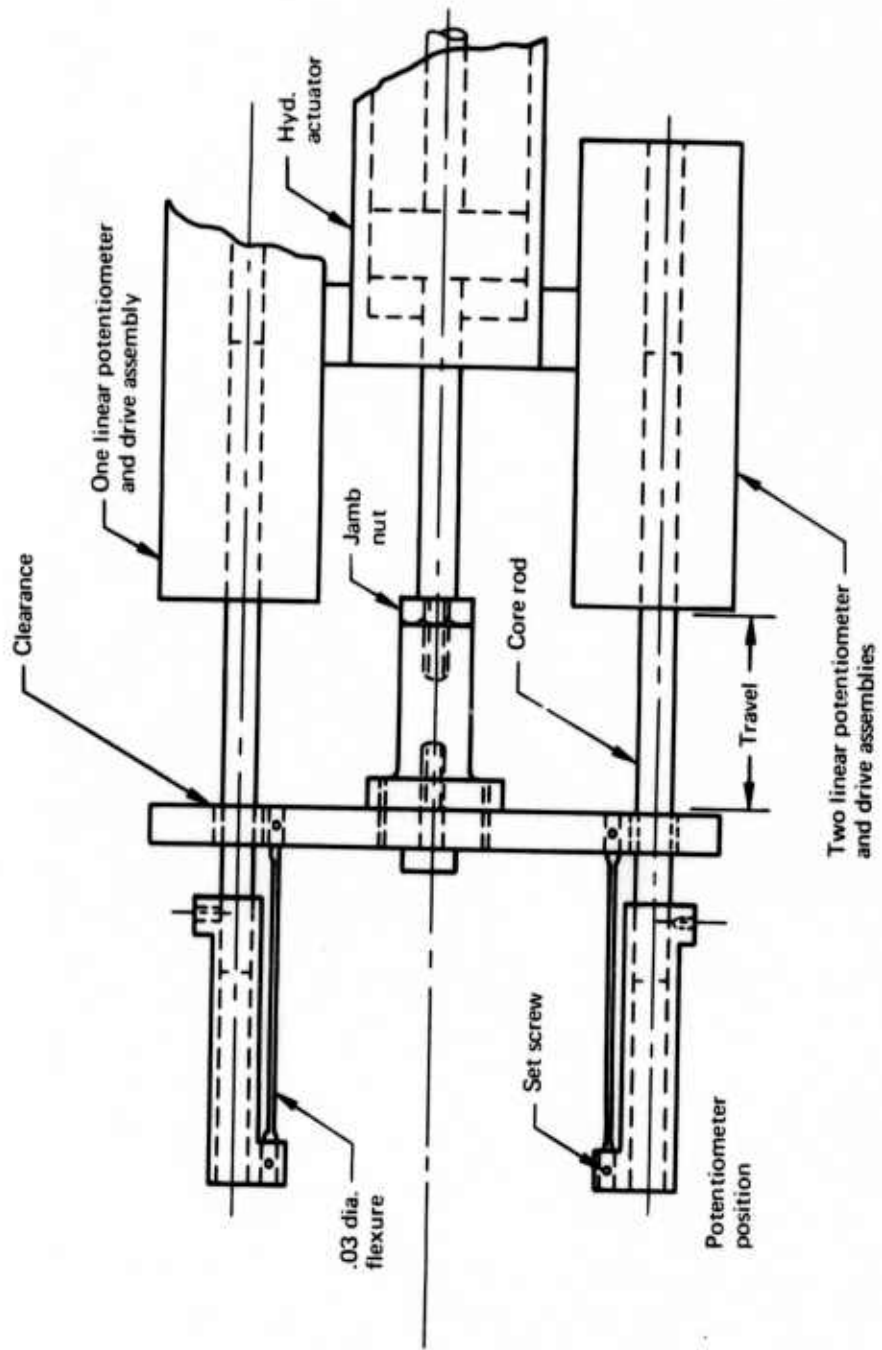


FIGURE A1.—STABILIZER ACTUATOR POSITION SENSORS

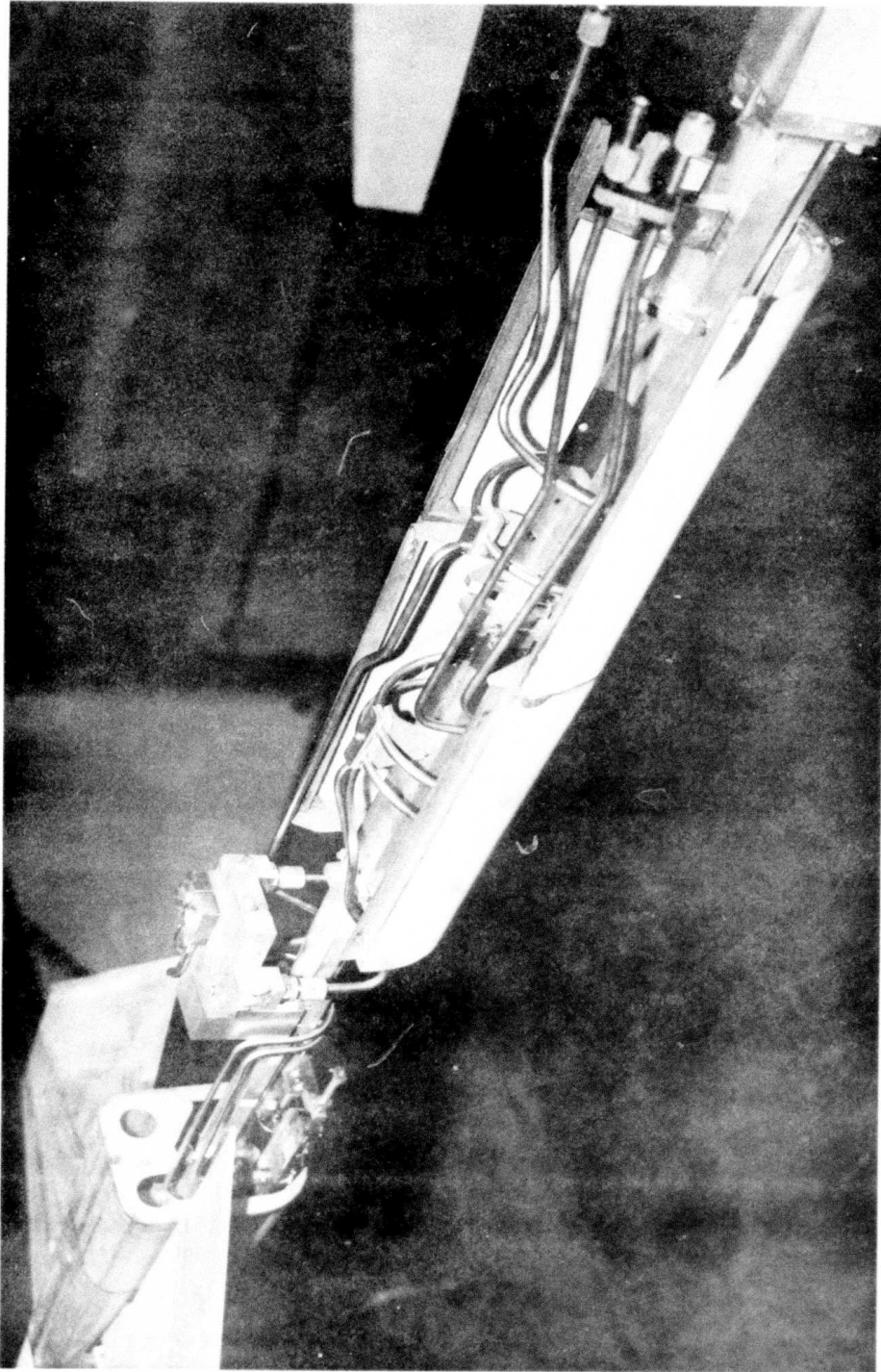


FIGURE A2.—STABILIZER HYDRAULIC LINES INSTALLATION

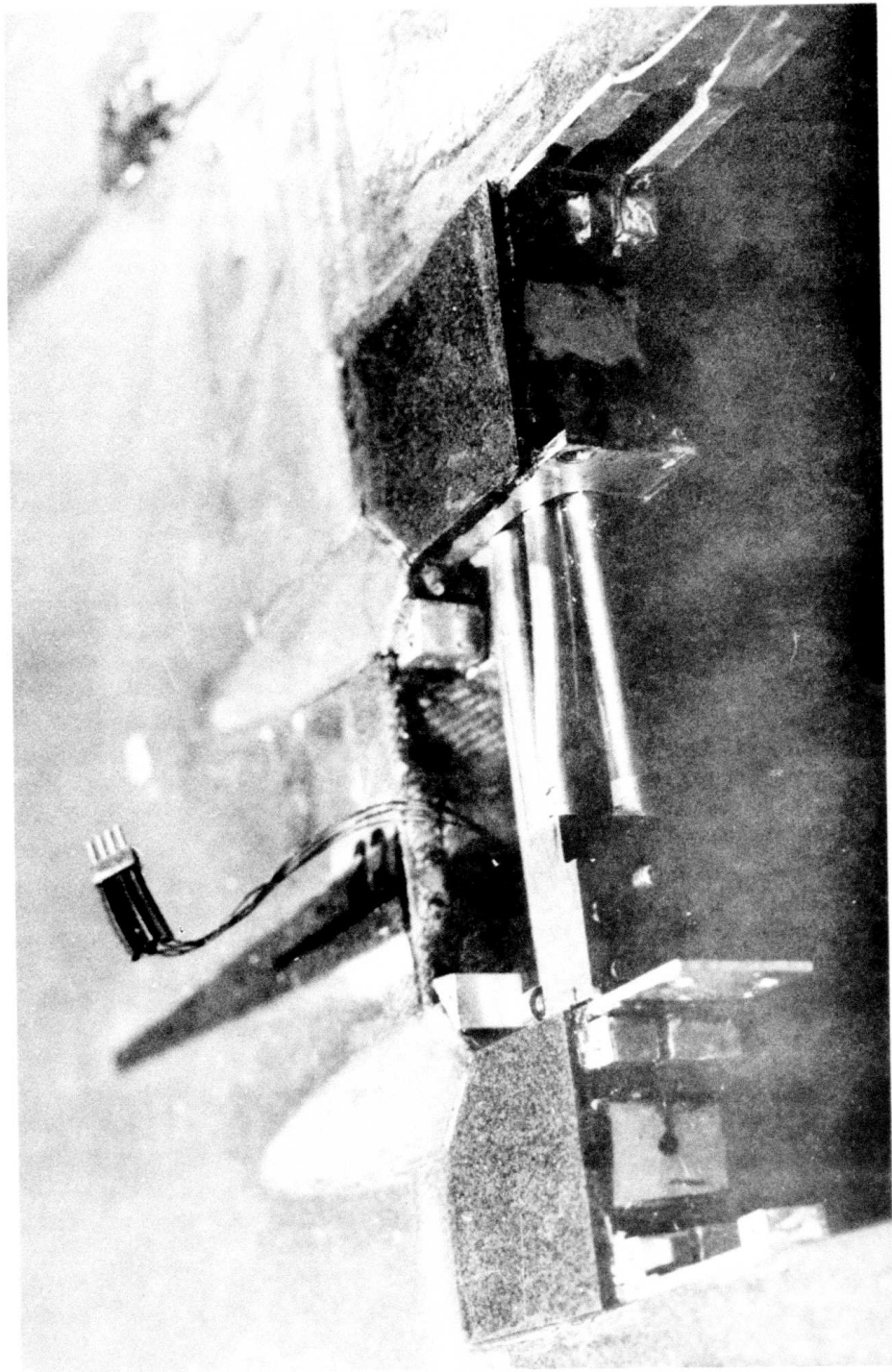


FIGURE A3.—AILERON ATTACHMENT

APPENDIX B

AUXILIARY TEST EQUIPMENT

Several major items of equipment, exclusive of the electronics, were needed to operate the model as installed in the tunnel. They were:

- a) Boeing model suspension and snubber assembly.
- b) "q" reducer, a Convair installation.
- c) Two 3-gal/min, 3,000-psi hydraulic pumps, three 90-ft lengths of hydraulic hose, two accumulators, two filters of 10-micron size, and fluid supply.
- d) Ballast control and measuring chamber with vacuum pump and gage.
- e) Model trim control box.
- f) Communication headsets.

Prior to model installation, this auxiliary equipment was positioned according to function.

The model was suspended in the tunnel by a system of 1/8-in. dia braided aircraft-type cable and pulleys, as shown in figure B1. Tension was applied to the system by a manually controlled hydraulic jack operating through a 20-lb/in. coil spring attached to one end of the rear cable. This support system allowed excursions in both lateral and vertical directions; therefore, a snubber (restraint) system was required.

The snubber mechanism was installed above the test section ceiling as shown in figure B2. Two snubber cables from above and one from below were attached to the model in a "Y" configuration at body station 95.5. A hydraulic cylinder controlled by the test director was used to take up the snubber cable slack thus capturing the model and drawing it to a predetermined location in the test section. A bungee and a shock absorber in each cable system eased and fixed the force applied to the model. A sketch of the tunnel cross section illustrates the arrangement in figure B3.

The "q" reducer, shown in figure B4, was designed to reduce the test section dynamic pressure by 20% within 0.2 sec after activation. Two 10-ft x 1-1/2-ft doors hinged at the aft end of the false floor and ceiling were solenoid-actuated; a single button permitted the test director to simultaneously activate the doors and cut tunnel power.

The noisy hydraulic pumps were operated well away (60 ft) from the model test control area. The accumulators and filters were coupled together downstream of the pumps. A schematic of the hydraulic power supply system is shown in figure B3.

The amount of water aboard the model was controlled from outside the tunnel. The total water supply was weighed by a calibrated load cell mounted within a pressure

chamber. A pressure or a vacuum inside the chamber moved water from or into the supply and to or from the model. A calibration chart was used to determine the cg station in percent of root chord resulting from the transfer of water ballast into or from the model. The amount of water in the model was indicated by a digital voltmeter. (See sketch, fig. B5.)

The model manual trim control box contained two 10-turn rotary potentiometers: one for aileron control, the other for the stabilizer control.

- Note:
1. All dimensions are in inches.
 2. All cables are 1/8 in stainless steel.
 3. All cable angles and lengths are approx.

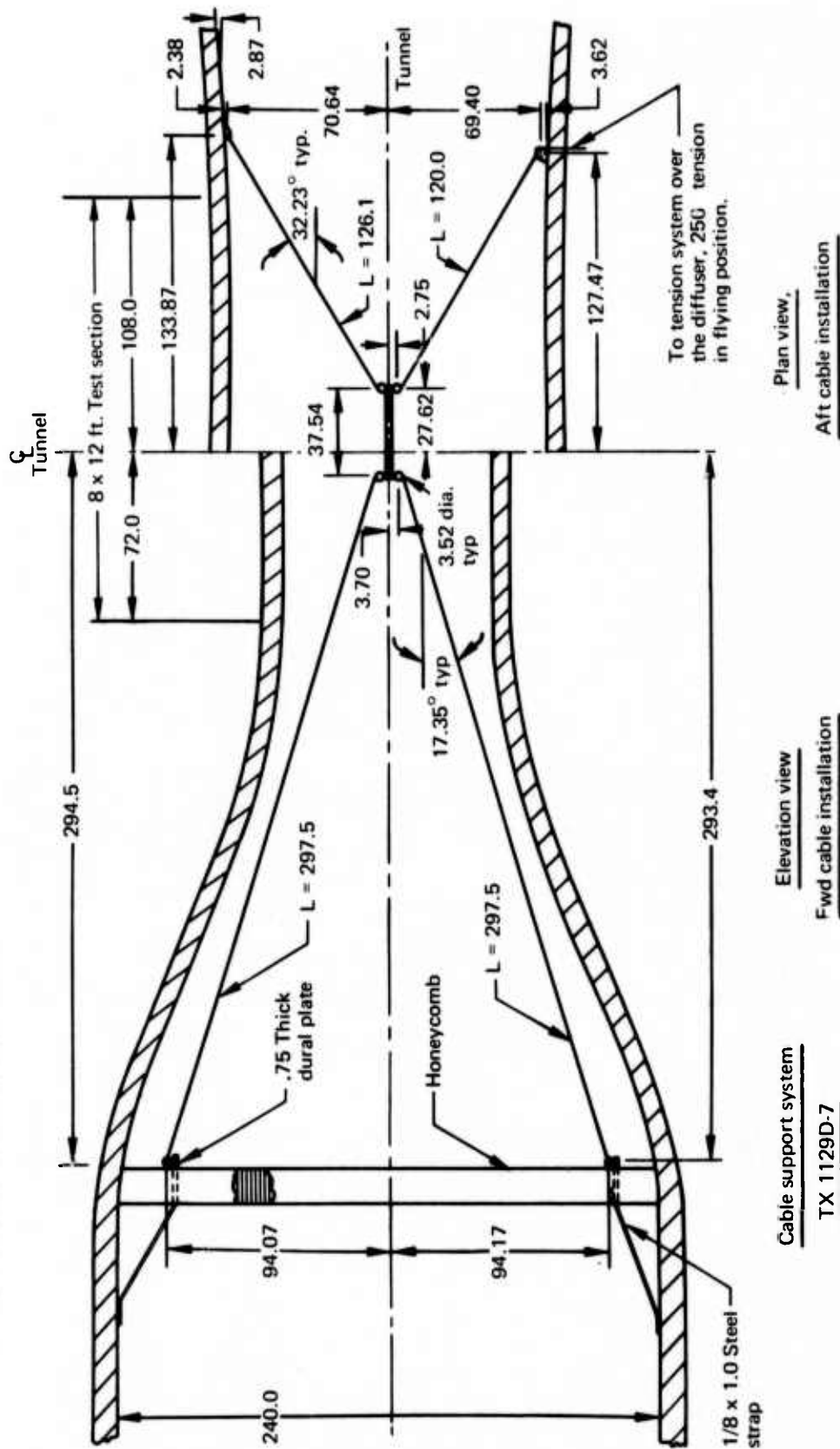


FIGURE B1.—CABLE SUPPORT SYSTEM—PLAN AND SIDE VIEWS

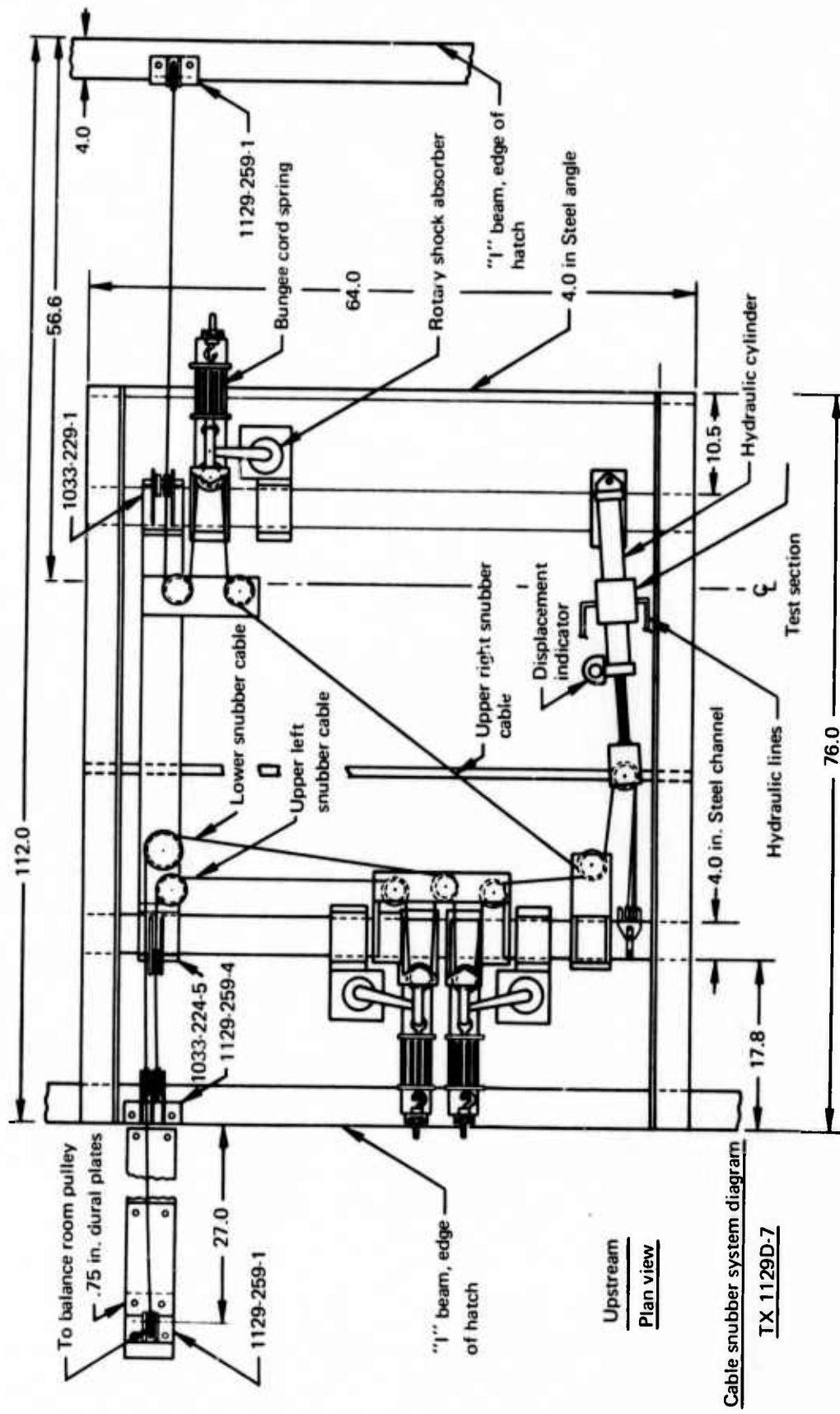


FIGURE B2.-CABLE SNUBBER SYSTEM

- 1 - Snubber cables
- 2 - Support cables
- 3 - Hydraulic lines

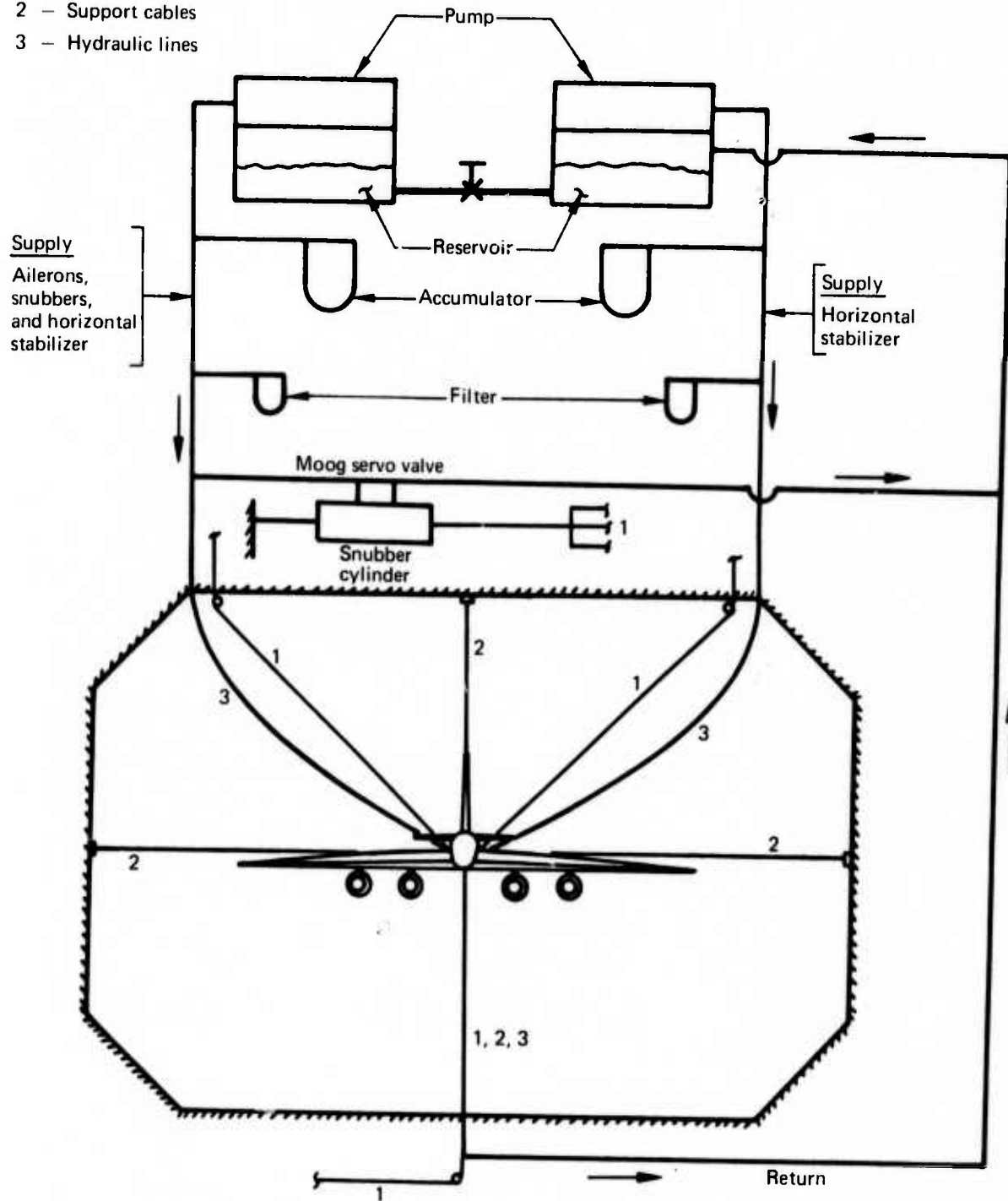


FIGURE B3.—HYDRAULIC POWER SUPPLY SYSTEM SCHEMATIC

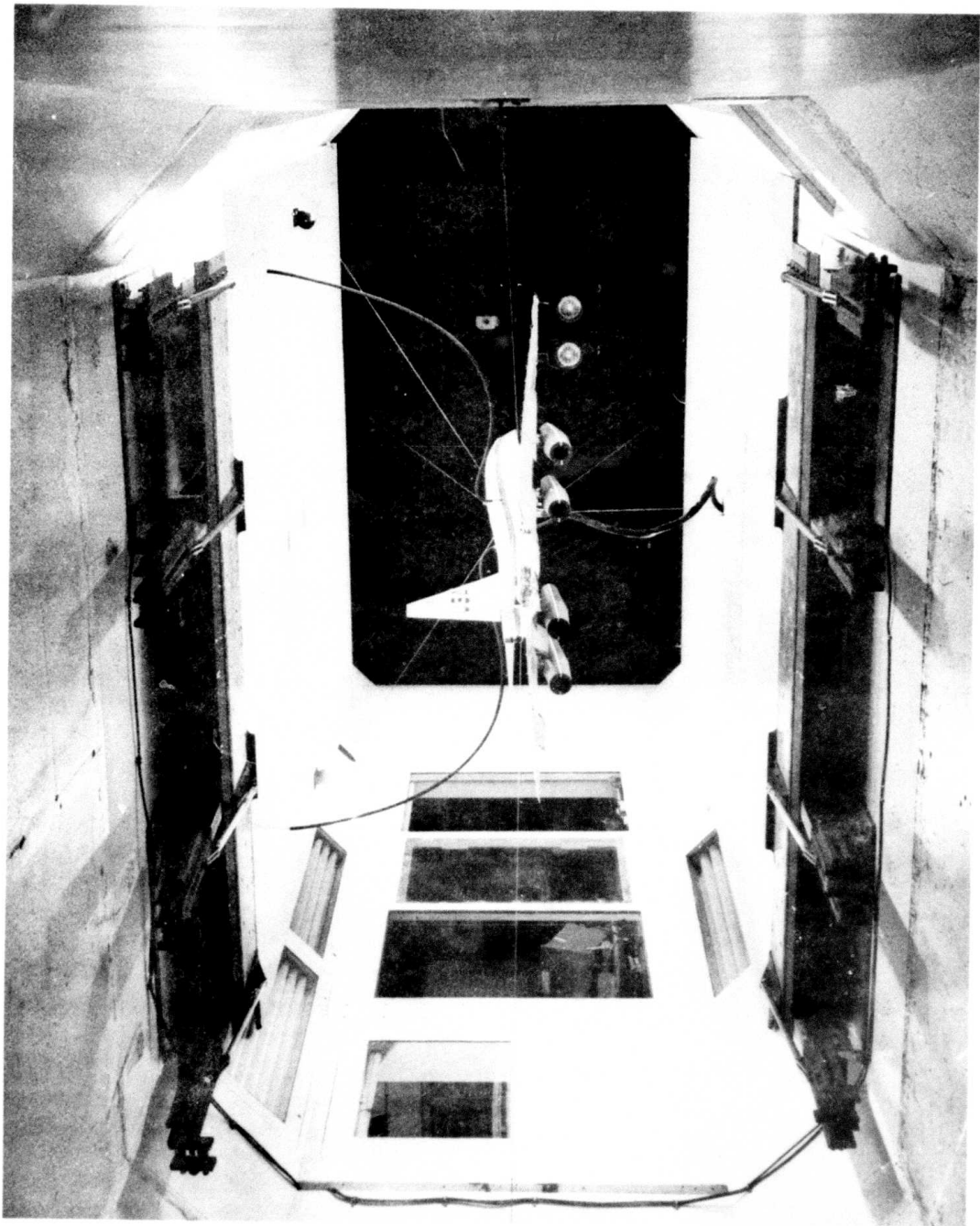


FIGURE B4.—DYNAMIC PRESSURE REDUCER

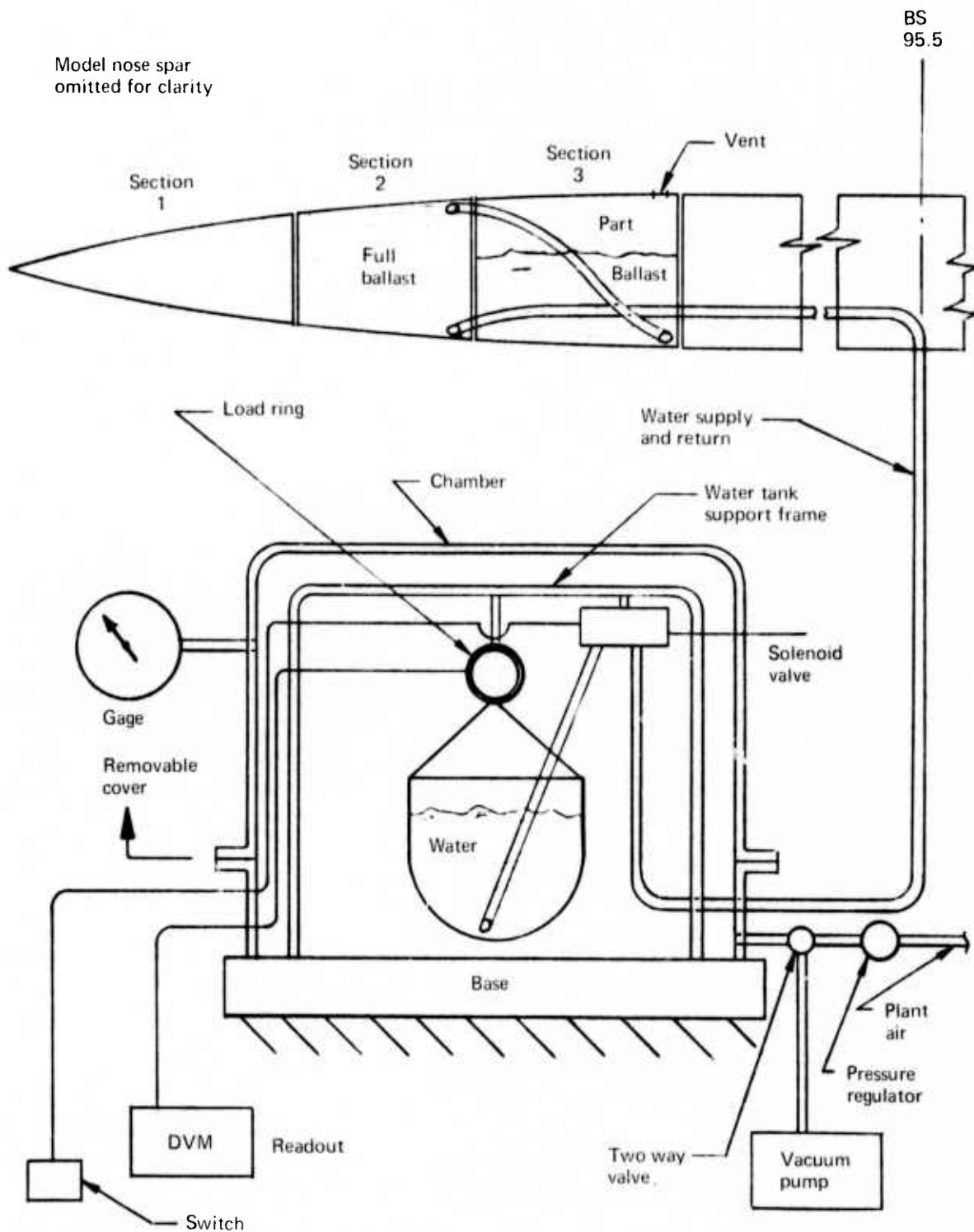


FIGURE B5.—WATER BALLAST CONTROL SCHEMATIC

APPENDIX C

INSTRUMENTATION AND ELECTRONIC EQUIPMENT

This section describes the instrumentation and electronic equipment used for the automatic flight control system (AFCS) and the flutter stability augmentation system (FSAS). A system block diagram is shown in figure C1 and an overall view of the equipment installation is shown in figures C2 and C3. Wiring connections to the model were made through an umbilical cord.

SERVOCONTROLLER

The Boeing Company model 64-30900 servocontroller provided the necessary circuitry for the internal position feedback loop (sec. 4.3.1). Modules provided positive and negative feedback gain changes, lead-lag compensation, servovalve current limiting, position feedback transducer excitation, and actuator position monitor signal conditioning and calibration. Test points were located within the loop to monitor the circuit operation.

SERVOVALVES

The servovalves installed in the model were Moog, Inc. model 30S020 rated at 3.8 in.³/sec flow with 1000-psi supply pressure.

SERVOVALVE CUTOFF UNIT

A switch panel allowed the instrumentation engineer to readily open the servovalve electrical circuit. This was a convenience during checkout. Switch covers prevented inadvertent switch operation during tunnel testing.

POSITION FEEDBACK TRANSDUCER

A typical torsion blade position sensor is shown together with a disassembled aileron actuator in figure 8. Adequate service life was obtained with normal, high quality gage installations using typical gage installation procedures. The 120 ohm gages were connected in a 4-arm bridge configuration with 5-V excitation.

PROGRAM INPUT UNIT

The program input unit provided each servosystem with switched access to four different signal sources. Random noise, discrete and sweep frequency sine, and square wave input were available. Impulses were obtained by applying a low frequency (0.1 Hz) square wave through a normally open spring return push-button switch. The pulse direction was controlled manually. The selected signal could be applied to a single servosystem or any combination of servosystems. An attenuator in the output circuit individually controlled the amplitude of the signal applied to each system. The unit contributed to the flexibility of the test procedures and was used extensively throughout the test.

EXTERNAL LOOP SENSORS

Strain gages and accelerometers were employed in the external loop of the FSAS servosystems. Kulite model GY-5-125-50 subminiature piezoelectric accelerometers were installed as primary sensors for the FSAS. The transducers, measuring 0.125 in. x 0.145 in. x 0.30 in., were attached to rigid hangers on the lower surface of the wing at locations shown in figure C4. The 5-V excitation, balance, and monitor circuits were provided by Sigma model SC610-S4 units. The accelerometers had a natural frequency in the range of 1 kHz and a damping ratio of about 0.02.

The strain gages, installed for secondary sensing, were wired in four-arm bridge networks configured to sense wing bending deflection, spanwise and chordwise. The bridge employed 350-ohm gages with 4-V excitation. The excitation, balance, and monitor circuits were provided with Sigma model SC610-S4 units. The distribution of bridges on the wing is shown in figure C4.

PATCH PANEL AND SUMMATION PANEL

All external loop control signals for the FSAS and all data signals were wired to the patch panel. The panel provided convenient access to these signals and was employed extensively throughout the test.

The summation panel provided two summing junctions, each with five input channels. Each input channel was provided with individual buffer, compensation, and attenuation circuitry. The 10-unit input terminals were located on the patch panel to provide access to all sensors on the model. The two output channels were routed directly to the compensation unit.

COMPENSATION UNIT

The compensation unit provided an individual card for each feedback sensor in the external loop. Each card had four hardwired amplifiers and one attenuator. Figure C5 shows a typical card with field-wired components installed on the terminal posts. Single and double pole high-pass and low-pass filters, tuned notch, and high-Q band pass filters were utilized during the test. The card configuration provided for installation of a series of filters in the signal path as required by an onsite evaluation of the test data. It was necessary to jumper two cards in series to provide room for the five filters ultimately incorporated in the external loop of the outboard aileron system. The attenuation on the compensation card and the amplifiers in the external loop provided continuous loop gain adjustment from zero to the maximum safe level.

SUMMATION AND Q-DIVISION UNIT

The summation and q-division unit provided a summing junction for the external loop and the excitation signal from the program unit. Each servosystem incorporated one card shown in figure C6. Test points were located to monitor individual signal inputs, the sum of all external loop signals, and the sum of the drive signal and the external loop signals. A bias adjustment was available to null the total signal.

A provision was made to compensate for the change in control surface effectiveness with tunnel airspeed by dividing the total signal with a voltage proportional to the tunnel dynamic pressure (q). The minimum q signal level was provided with an adjustable limit to prevent system saturation at low tunnel speeds.

MONITOR UNIT

The two-channel monitor unit provided switchable access to 56 instrumentation test points. In addition, two input terminals on the patch panel gave access to the 36 strain gage and accelerometer data channels.

AEROELASTIC MODAL ANALYSIS SYSTEM (AMAS)

The analog system analyzed two steady-state sine waves. The magnitude A/B and phase angle of channel A relative to channel B were plotted on-line in polar form. The incoming signals were conditioned with tuned 2-Hz-bandwidth crystal filters. The output was rc time-averaged as required to reduce the effect of nonstationary signal inputs.

DIGITAL ANALYZER

The Hewlett-Packard HP5451 equipment consisted of a Fourier analyzer, a signal generator, an oscilloscope for data display, a teleprinter, X-Y plotter, and a paper tape reader and punch for data storage. The memory storage and software programs permitted a wide variety of data processing methods and presentations. The equipment was used to generate random noise and fast sine sweep signals to the model control systems for modal analysis. The model response was analyzed by the HP5451 and presented in Bode or Nyquist plot form or in tabular frequency/amplitude/phase form. The frequency range of analysis was arbitrary, but normally for flexible mode analysis the spectrum was chosen from 0-Hz to 25-Hz.

POSITION FEEDBACK TRANSDUCERS

Linear conductive film potentiometers, type 118, manufactured by Consolidated Instrument Co., were used for position feedback transducers on the stabilizer actuator. They operated at 5 V and resistance was 1 k Ω .

STABILIZER TRIM

A thumb wheel on the manual control box, appendix B, adjusted the static position of the stabilizer to provide manual pitch trim on the model. A sensitivity control provided a manual adjustment to compensate for changes in stabilizer effectiveness with tunnel speed and cg location.

EXTERNAL LOOP SENSORS

Kistler model 303B servoaccelerometers (2 g, 5 V), mounted in the fuselage, were used to sense the vertical acceleration of the model. Hamilton Standard subminiature rate gyros (30°/sec, 5 V) were used to sense the pitch rate of the model.

DATA ACQUISITION SYSTEM

The data acquisition system block diagram is shown in figure C7. All test data transducer signals and pertinent servosystem signals were routed to the group switch and patch panel. Each 14-channel tape recorder had one channel assigned to voice and one to IRIG time code. The remaining 12 channels on recorder A were connected to the output of the 12-channel group switch to provide switchable access to all data inputs in preassigned combinations. The 12 channels on recorder B were connected to the patch panel to provide patched access to all signals.

The dynamic response actuated switch (DRAS) monitored the signal from one data transducer on the model. It tripped when the signal level exceeded a calibrated amplitude more than a preselected number of times in a set time frame interval. Therefore, it would not be tripped by a transient signal of less than the set number of cycles nor by a signal below the calibrated amplitude. A trip of the DRAS turned on the tunnel motion picture cameras and high-intensity lights, turned off the tunnel drive unit, and imposed a 400-Hz signal of 0.5 sec on the voice track on recorder A and B.

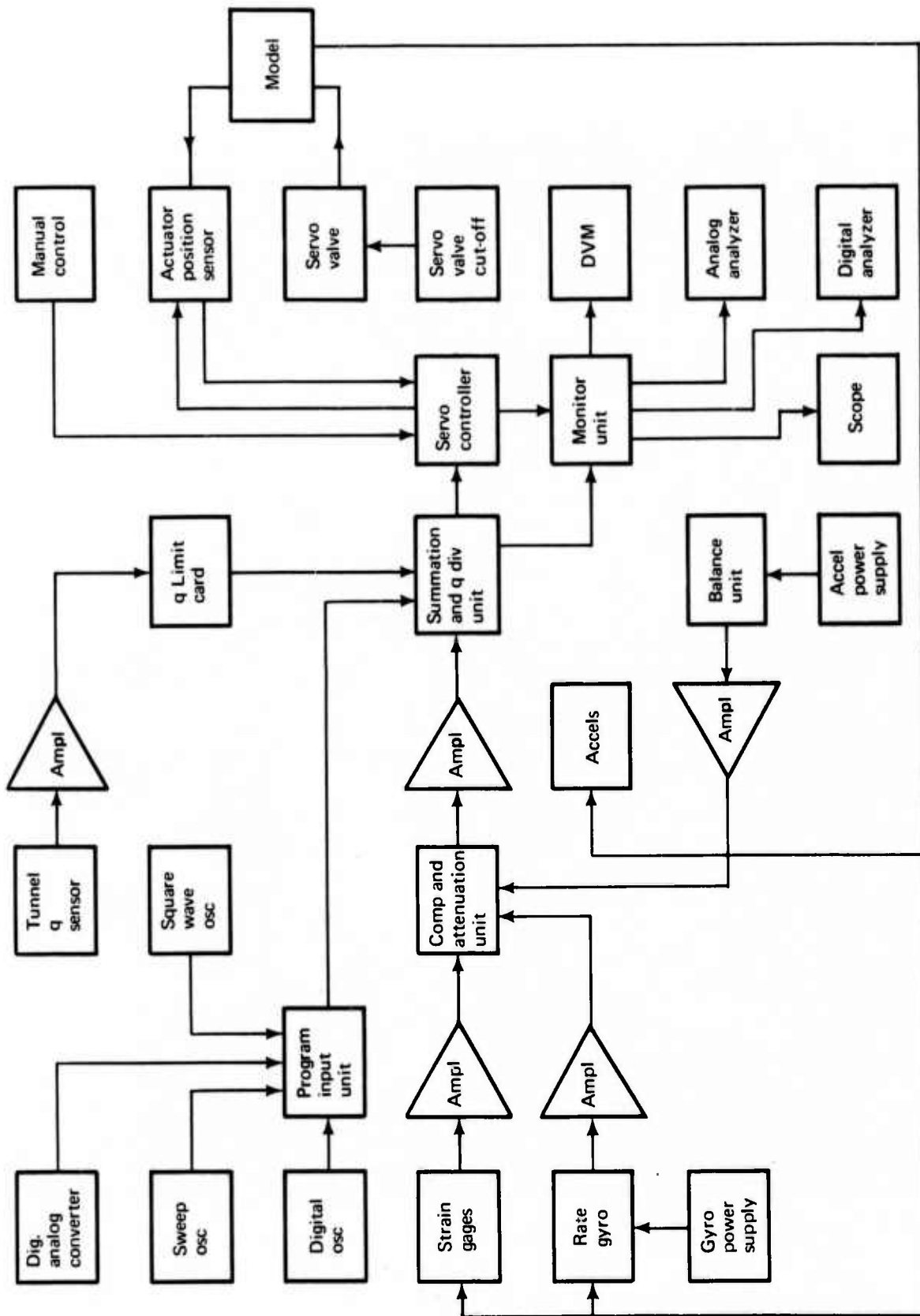


FIGURE C1.—CONTROL SYSTEM BLOCK DIAGRAM

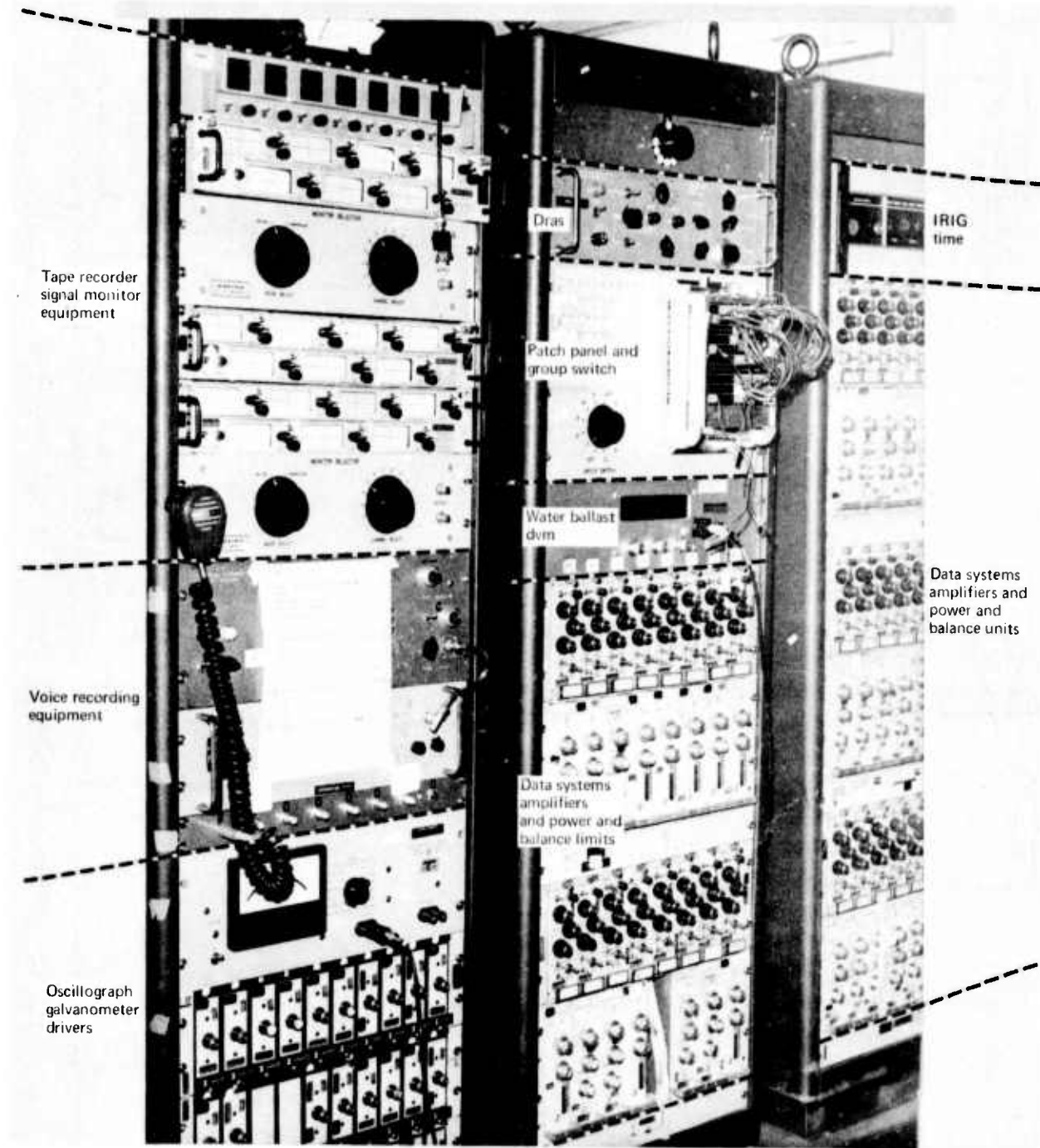


FIGURE C2.—TEST ELECTRONICS—DATA ACQUISITION RACKS

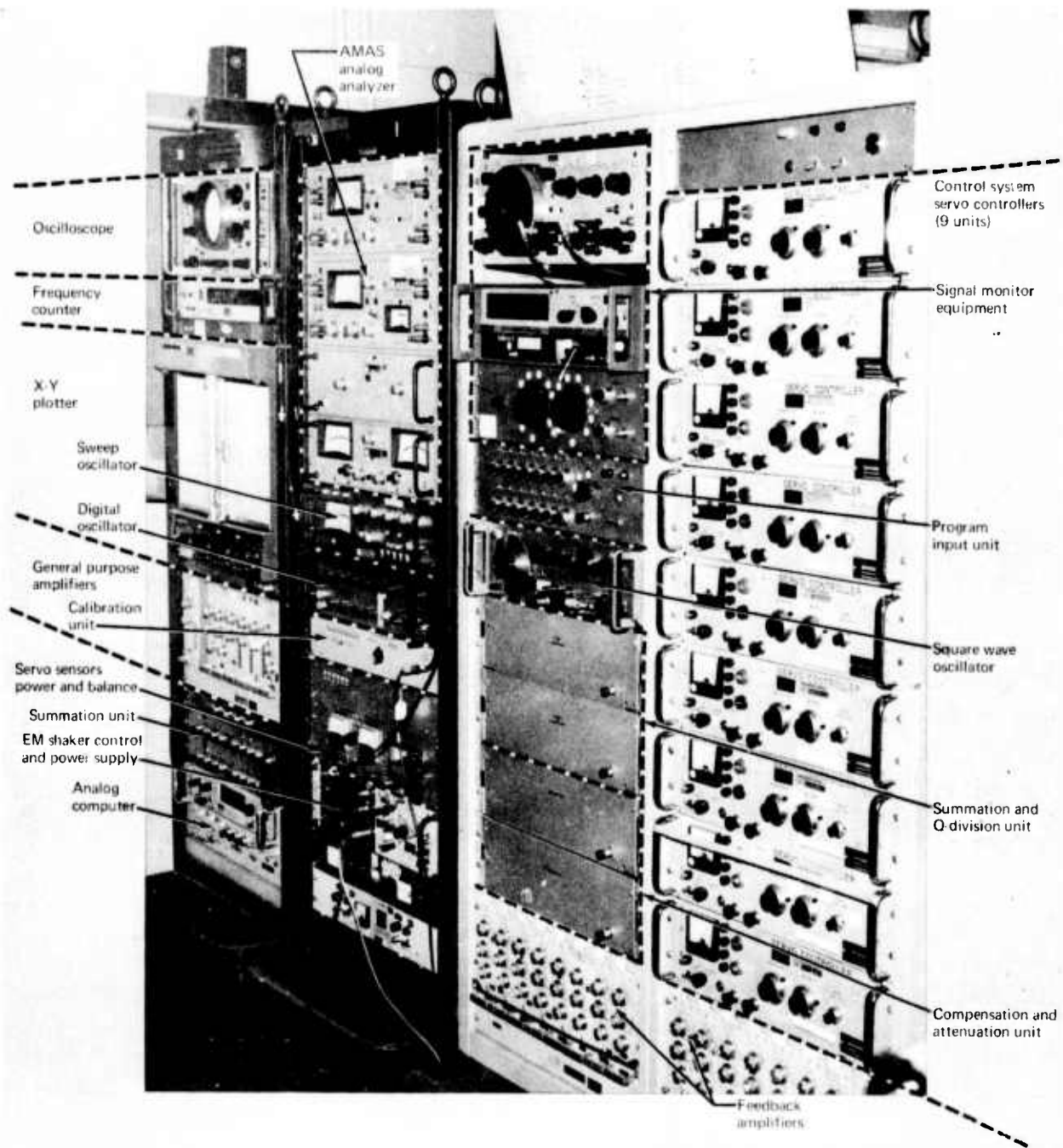


FIGURE C3.—TEST ELECTRONICS—SYSTEM CONTROL RACKS

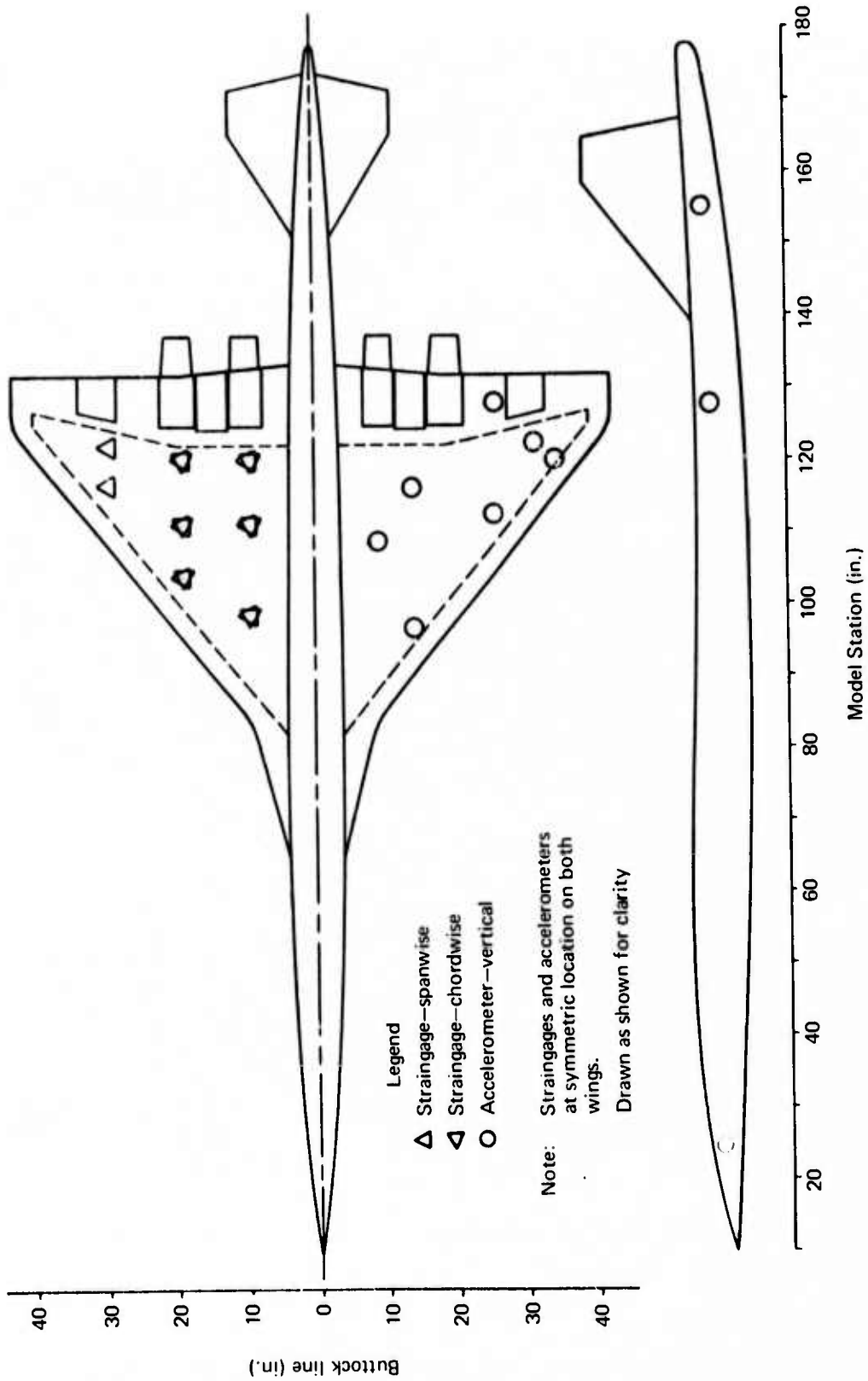


FIGURE C4.—MODEL INSTRUMENTATION

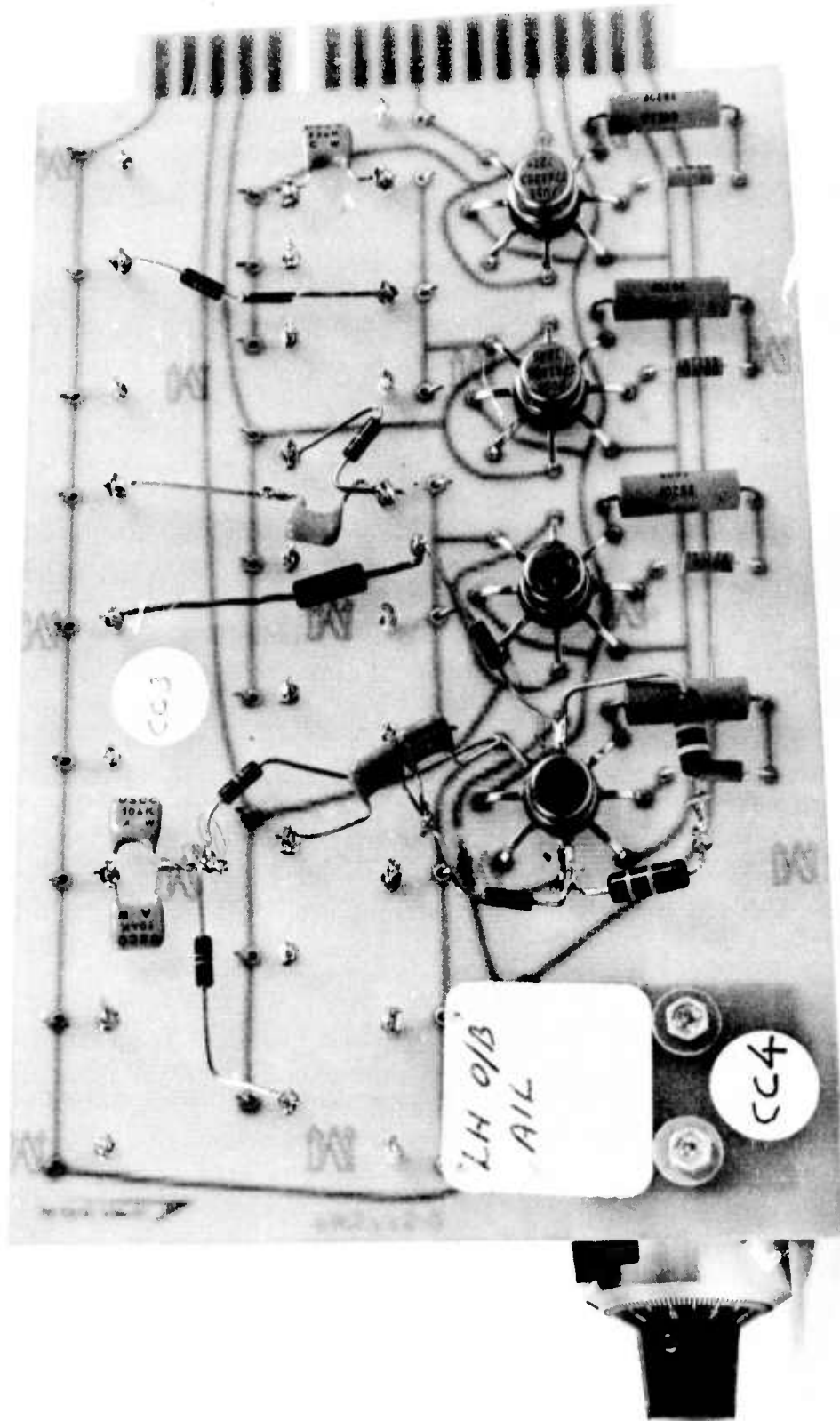


FIGURE C5.—COMPENSATION CARD

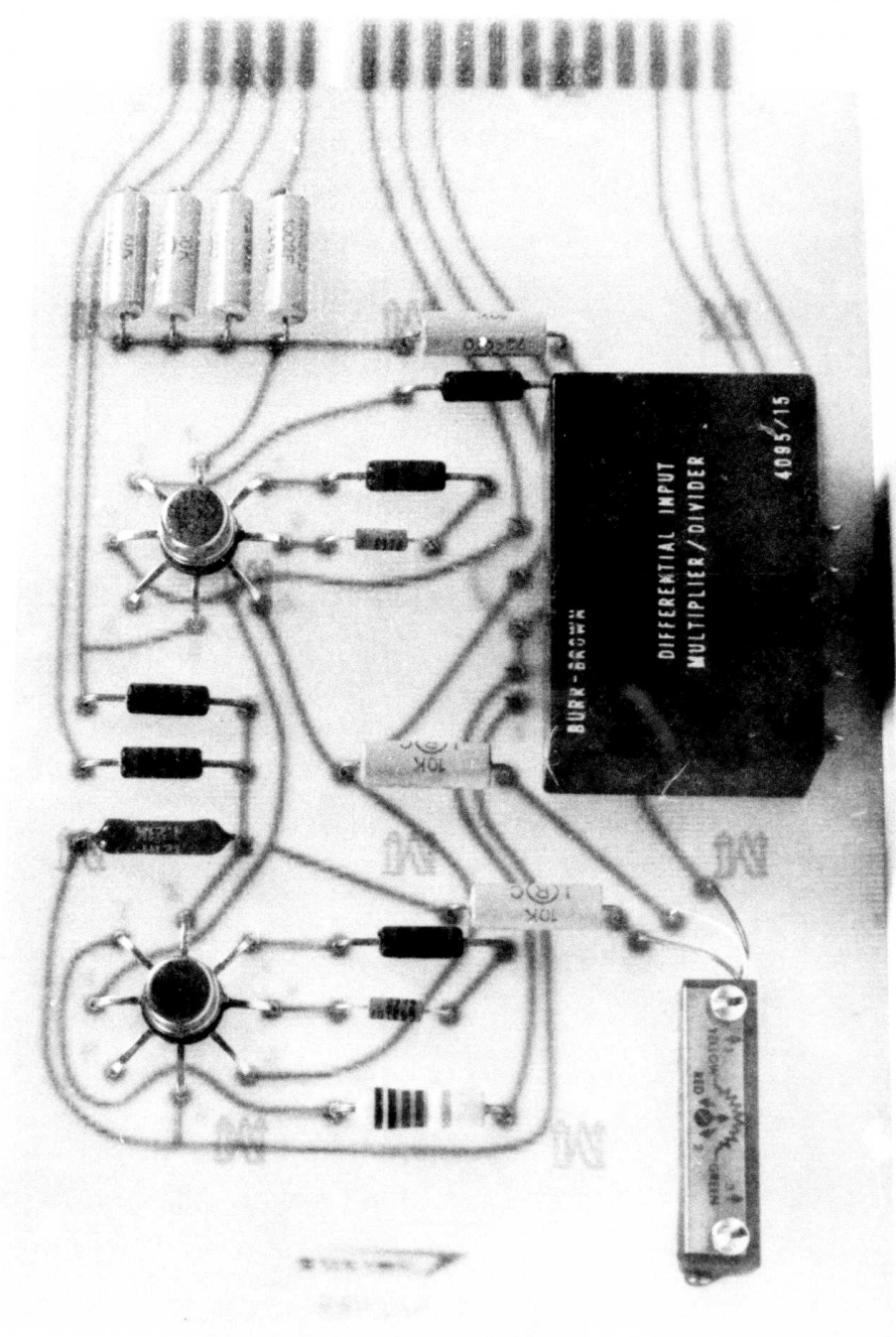


FIGURE C6.—SUMMATION AND q DIVISION CARD

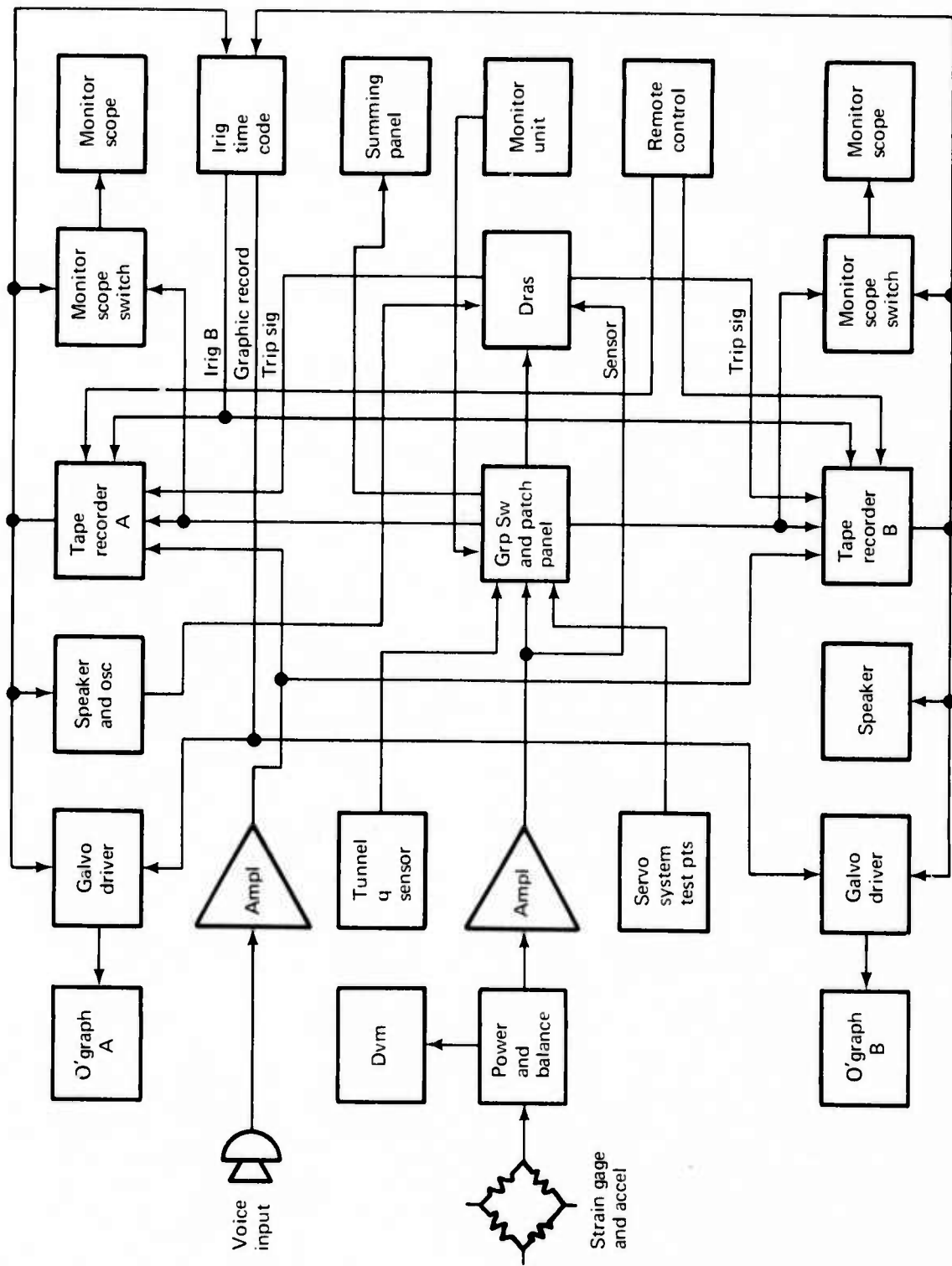


FIGURE C7.—DATA ACQUISITION SYSTEM BLOCK DIAGRAM

APPENDIX D

ANALYTICAL DETAILS

Analytical studies determined the configuration of the model and the types of sensor/control surface combinations that were tested. This section describes the requirements that the analyses had to meet, discusses the analytical methods that were available to satisfy those requirements, and gives a description of the formulation of equations of motion.

ANALYTICAL REQUIREMENTS

The model program was comprised of two distinct tasks: (1) the automatic flight control system (AFCS) which was to control the model rigid-body stability for the aft cg configurations and (2) the flutter stability augmentation system (FSAS) which was to suppress wing flutter. The analyses performed on each system were carried on separately and concurrently. Where the two tasks overlapped, the analyses were integrated.

The model analyses used existing tools since it was impossible to design and develop new computer programs and meet the program schedule. This led to some data handling and setup time problems but basically proved to be satisfactory. The discussion below presents the analytical requirements as they apply to the AFCS and FSAS systems.

Requirements for AFCS System

The analyses for the AFCS system were required to:

- a) Generate a representative mathematical model of the structure of the 1129D flutter model and of the 2-cable model support system.
- b) Calculate the rigid-body and flexible natural modes of vibration of the model on the cable support system.
- c) Generate unsteady aerodynamics over a representative speed range.
- d) Generate a mathematical model of the body-mounted sensors and the horizontal tail actuator system as installed in the model.
- e) Calculate the model stability as a function of tunnel speed and model cg location without the stability augmentation system.
- f) Calculate the model flutter speed.
- g) Investigate the effect of sensor type and location on model stability (closed loop system).

- h) Investigate the effect of the closed loop AFCS system on the model stability as a function of tunnel speed and model cg location.
- i) Investigate the effect of the closed loop AFCS system on model flutter speed.
- j) Investigate suitable compensation networks for the closed loop AFCS to improve system performance and/or to preclude interference with the FSAS system.

Requirements for FSAS System

- a) Same as for a, b, and c above.
- b) Generate a mathematical model of wing mounted sensors and the aileron actuator system as installed on the model.
- c) Calculate the model flutter speed with the open-loop FSAS system.
- d) Investigate the performance of the closed-loop FSAS system as a function of tunnel speed and model cg location.
- e) Investigate the effect of sensor type and location on the FSAS system.
- f) Investigate suitable filters for the closed-loop FSAS system to improve system performance.

ANALYTICAL METHODS

The problems of flutter stability augmentation analysis have been described in the literature (refs. 13, 14, 15). Basic analytical approaches are well known. Automatic flight control analysis methods are equally familiar. However, for completeness, the basic methods of analysis used for the AFCS and FSAS design are discussed below, together with a brief appraisal of the advantages and disadvantages of each.

Structural Analysis

The choice of balsa wood and sandwich fiberglass construction for the 1129D model precluded the use of an elastic axis-type structural analysis. The built-up model wing structure did not possess a clearly defined elastic axis, and the orthotropic nature of the structural materials led to further complications. Current finite element methods, where the geometry and stiffness of the actual structure are modeled, were employed.

Cable Support System

To approximate the free flight condition, the two-cable support system was used. The desirable characteristics of this support system are described in section 3, but it presented some analytical challenges. The stability of the model, represented as a rigid body, restrained by the flexible cable system can be calculated using several computer programs (refs. 16, 17), but the interaction of a flexible cable system and a flexible model significantly complicates the solution. Furthermore, the results obtained from the

rigid-model approximations are not always totally satisfactory due to recognized shortcomings in the description of the aerodynamic coefficients as well as the nonlinear characteristics of the pulley/cable system. For this program, the model was analyzed both as a rigid body and as a flexible structure supported by a flexible cable system.

Vibration Analysis

The first major correlation between test and analysis results was obtained by comparison of the natural modes and frequencies of vibration. Further, the vibration analysis results were the basis for all subsequent analyses and hence had to be of high quality. The method used was a standard eigenvalue/eigenvector solution of a symmetric dynamic matrix based on three distinct numerical procedures to achieve the solution: (1) tridiagonalization of the dynamic matrix by the Householder-Givens technique, (2) eigenvalue extraction of the tridiagonal matrix by either the symmetric QR or Sturm algorithms, and (3) eigenvector calculation by the Weilandt inverse method. A computer program based on these solution techniques (ref. 18) was available. The results of the structural analysis and a mass matrix served as input to this program to yield analytical modes and frequencies of vibration.

Unsteady Aerodynamics

The area which presented the greatest number of problems in the AFCS and FSAS analyses was that of unsteady aerodynamics. Fortunately, the speeds at which the 1129D model was flown were relatively low ($M = 0.2$), and thus compressibility effects were minimal. However, because the SST wing and horizontal tail planforms have low aspect ratios, unsteady aerodynamics based on strip theory were ruled out. The aerodynamics available which were suitable for low aspect ratio surfaces were of two types and are generally classified as: (1) oscillatory unsteady aerodynamics and (2) indicial unsteady aerodynamics.

The oscillatory unsteady aerodynamics systems which were available at the start of the program and which were capable of handling the effects of partial span control surface were: (1) three-dimensional compressible unsteady generalized air forces based on a kernel function formulation (ref. 11) and (2) three-dimensional compressible unsteady generalized air forces based on the doublet-lattice method (ref. 19).

The nonplanar kernel function method formulates relationships between the pressure distribution over the lifting surface and the normal wash and assumes the loading to be a series of preselected loading functions with unknown coefficients. The integration of these functions is time consuming and thus costly. On the other hand, the doublet lattice method requires no loading functions nor prior knowledge of the solution and is thus more adaptable to complex configurations. However, to achieve a valid description of the unsteady aerodynamics over a complex surface, a large number of boxes must be used. The final deciding factor for the use of the kernel formulation was the fact that the doublet lattice-based computer program proved to be limited in size capability and difficult to integrate into the expected data flow.

Indicial unsteady aerodynamics are generally based on modified lifting line theory. The lift growth parameters are modified by the use of either the Wagner or the Kussner lift growth functions. To switch from the time domain to the frequency domain, the aerodynamics must be Fourier transformed. This procedure is made more difficult by the need to set initial conditions for the lift growth function to zero and results in a discrepancy in the flutter speeds calculated using the two types of unsteady aerodynamics. The major use for indicial aerodynamics is thus for time domain studies.

Sensors and Actuator Systems

Model instrumentation which could be used for control loop sensors included strain gages, accelerometers, and rate gyros. The physical characteristics of each were investigated so that their response characteristics could be included in the analyses.

The strain gages presented an analytical problem that precluded their use in analytical studies. On the model, the various modes of vibration were sensed by the strain gages as local stresses which cycled at the response frequency. To correctly model such stress fields analytically, a complete dynamic stress analysis would have been required. The complexity of such an investigation was prohibitive in cost and flow time. Thus, strain gages as sensors were deleted from the analysis except where this effect could be included indirectly, such as in the inner feedback loop of the actuators where the position of the actuator was sensed by a torsion blade.

The accelerometers presented no particular analytical problems. Their response bandwidth was significantly larger than the range of frequencies at which the critical modes of the model were found, and accelerometer measurement accuracy was entirely satisfactory for the analyses.

The physical characteristics of the rate gyros were determined from the manufacturer's specifications as well as by tests performed in the laboratory. The transfer function for the rate gyros was thus established and included in all analyses using rate feedback control. The derivation of the gyro transfer function is included later in this section.

The response characteristics of the hydraulic actuators also had to be determined in the laboratory in order to correctly include their effect in the analysis. Their transfer functions were derived from experimental data.

Model Stability Analysis

The low frequency cable mode model stability analysis was performed using three different approaches. None proved to be entirely satisfactory, and the limited correlation between analyses and test indicates an obvious area for future work. The three approaches used were: (1) model as a rigid body on a flexible cable system in a steady-state air flow, (2) flexible model on a flexible cable system subject to unsteady aerodynamics, and (3) flexible model on a flexible cable system subject to unsteady aerodynamics and a forcing input.

Previous test experience with the 1129D model had shown it to be unstable for conditions with the cg aft of 50% root chord. Since the major purpose of the AFCS system was to control this instability, it was important to investigate the sensitivity of this phenomenon to various geometric and aerodynamic parameters as well as the preload tension capability of the cable support. Although the model had been modified, it was assumed that its rigid-body stability characteristics were not excessively changed.

The analysis of the model as a rigid body on a flexible cable system in a steady-state airflow employed a computer program (ref. 16) based on the theory in reference 8 and modified by Boeing to include such effects as pulley friction damping. Estimates of the aerodynamic stability coefficients were obtained from SST airplane data; all other information such as weights and geometry were measured. The stability in each of the six degrees of freedom as a function of cg location, airspeed, and cable tension was investigated.

The low frequency stability (0-2 Hz) of the flexible model on a flexible cable system subject to unsteady aerodynamics was investigated for the symmetric case only. The model was assumed to be rigidly restrained in the fore-aft direction leaving only vertical translation (plunge) and pitch degrees of freedom.

Cable tension was set at twice the model weight and the effects of the cable system were represented as linear springs at the pulley locations. The stability of the model, using unsteady aerodynamics (ref. 6), was investigated for 3 cg configurations (48%, 58%, and 60.6% C_R) and a range of airspeeds from 100 kn to 160 kn. Using a frequency domain-based computer program, (ref. 20), the open-loop response of the model for both the AFCS and FSAS analysis was determined.

Additional analysis was required to determine the forced subcritical response of the flexible model on a flexible cable system and subjected to unsteady aerodynamics. Since the model was used for the investigation of transient excitation techniques (see ref. 7), it was important to determine where the stability boundary lay. Further, to determine the effectiveness of both the AFCS and FSAS closed-loop systems, the model was subjected to various force inputs at speeds well below the flutter speed. A frequency domain forced-response analysis computer program (ref. 21) established the open-loop response of the model for 3 cg configurations and a range of airspeeds from 100 kn to 160 kn.

Flutter Analysis

The inclusion of an active control system in the equations of motion precludes the use of the standard V-g flutter solution. The V-g approach assumes steady harmonic oscillation and solves for the value of damping, which is required to maintain steady oscillatory response. Thus, the only points in the V-g plane which represent physical reality occur at $g = 0$.

An active control system introduces damping into the system, and the real object of a flutter analysis, which includes active controls, is to determine the velocity at which the negative aerodynamic damping is equal to the structural and control system damping. This equilibrium represents the flutter point.

The solution technique selected was similar to the standard British flutter solution method. The choice was a decay-rate type of flutter solution which uses the matched frequency parameter of the oscillatory air forces. This procedure yields a more plausible behavior of damping at subcritical and supercritical speeds. Only the fact that the aerodynamic forces are assumed oscillatory causes the solution to be not totally consistent. However, in the region of low subcritical and supercritical damping (≈ 0.05) this shortcoming was not considered a problem.

The flutter behavior was obtained for the symmetric case with the control surface loops closed separately and collectively. The effects of feedback gain on individual control loops were also investigated. Flutter speeds were obtained for all configurations which were flown.

Control System Analyses

Control system analyses can be performed in the frequency domain or in the time domain. Although Fourier transformation may be used to go from one form of analysis to the other, the problems encountered in the transformation often make it more expedient to view each domain separately. Experience has shown that the classical frequency domain analysis is suitable for active flutter stability evaluation. The advantages of frequency domain analysis are:

- a) Clearly defined dynamic stability criteria.
- b) Ease of incorporating sensor characteristics.
- c) Ease of incorporating compensation networks.
- d) Only domain in which unsteady aerodynamics were readily available.
- e) Lower cost in computing for the relatively high frequency systems encountered in model flutter.
- f) Ability to assess both low frequency effects (cable mode stability) and flutter control system stability simultaneously.
- g) Facility to understand which modes (mechanism) contribute to problem.
- h) Availability of a wide range of classical tools for control system design.

The analytical advantages of the frequency domain were attractive, but the disadvantages of such analyses could not be ignored. The major disadvantages were:

- a) Inability to correlate with physical system requirements of rate and displacement limits and power demand.
- b) Inability to easily include nonlinear effects.

Time domain analysis yields results that are not available any other way. Where these results are considered necessary, the additional effort to obtain a valid time domain representation of the control system is accepted. The advantages of time domain analyses are:

- a) Ability to include rate and displacement limits as well as power demands to represent a physical system.
- b) Ability to include nonlinear effects with relative ease.
- c) Ability to calculate quantitative values such as local accelerations and displacements and control surface angles of rotation.
- d) Ability to display results in a form familiar to nonspecialists in control theory, e.g., time histories.

Although there is no inherent reason to preclude performing a time domain analysis on a digital computer, the advantages of time domain analysis are greatest when used on an analog or hybrid computer. Using the analog, some additional advantages are obtained:

- a) Sensor characteristics may be included directly.
- b) Compensation networks may be included directly.

However, there are also some severe disadvantages associated with time domain analysis:

- a) Three-dimensional unsteady aerodynamics in the time domain have not been developed. While there are quasi-steady ($f \leq 1.0$ Hz) aerodynamics available for use, representative aerodynamics for the model flutter problem ($f = 16.0$ Hz) were unavailable.
- b) The amount of computer time (analog or digital) required to perform a time domain analysis for the higher frequencies is very large. Consequently, the cost rapidly becomes prohibitive.

EQUATIONS OF MOTION

The equations of motion used in the symmetric case automatic flight control system and flutter stability augmentation system analyses are listed below. The problem size varied according to the extent of the control system included.

Freedom Number	Description
1-20	Natural modes of vibration selected to represent the model with ailerons and stabilizer/elevator
21	Deflection-inboard aileron
22	Deflection-outboard aileron
23	Deflection-stabilizer/elevator
24-25	Actuator equation-inboard aileron
26-27	Actuator equation-outboard aileron
28-29	Actuator equation-stabilizer/elevator
30	Input signal-inboard aileron
31	Input signal-outboard aileron
32	Input Signal-stabilizer/elevator
33	Summation of sensor motion
34-40	Compensation networks

Basic Flutter Equations

Starting with the familiar Lagrange equation for a forced system:

$$\frac{d}{dt} \frac{\partial T}{\partial \dot{q}_m} - \frac{\partial T}{\partial q_m} + \frac{\partial F}{\partial \dot{q}_m} + \frac{\partial U}{\partial q_m} = Q_{A_m} + Q_m \quad (1)$$

where

- $T = \int m_{ij} \dot{z}_j d\dot{z}_i^*$ (inertial energy)
- $F = \int c_{ij} \dot{z}_j d\dot{z}_i$ (damping energy)
- $U = \int k_{ij} z_j dz_i$ (strain energy)
- $Q_{A_i} = -1/2 \rho V^2 b_o S a_{ij} \alpha_j$ (generalized aerodynamic force)
- $Q =$ generalized external force
- $m =$ inertia
- $c =$ damping coefficient
- $k =$ stiffness
- $\rho =$ air density
- $V =$ air speed
- $z =$ vertical displacement
- $q =$ generalized displacement

* Indicial notation is used here with repeated indices implying summation

- α = angle of attack
 b_o = reference chord length
 S = span
 a = aerodynamic coefficient

and

$$z_i = \phi_{ij} q_j \quad (\text{generalized coordinate}) \quad (2)$$

where ϕ_{ij} is defined as the mode shape scalar obtained by the solution of the undamped system dynamic equation:

$$k_{ij} \phi_{jk} - \omega_k^2 m_{ij} \phi_{jk} = 0$$

Also

$$\alpha_i = \dot{z}_i/V + \left(\frac{\partial z}{\partial x}\right)_i \quad (3)$$

expressed the generalized velocity and slope at the generalized coordinates. Substituting (2) into (3):

$$\begin{aligned} \alpha_i &= \phi_{ij} \dot{q}_j/V + \left(\frac{\partial \phi}{\partial x}\right)_{ij} q_j \\ &= \phi_{ij} \dot{q}_j/V + \phi'_{ij} q_j \end{aligned}$$

The forcing function is given by:

$$Q_m = \phi_{im} F_i \quad (4)$$

Substituting equations (2) and (3) into (1):

$$T = \int \phi_{im} m_{ij} \phi_{jn} \dot{q}_n d\dot{q}_m$$

$$F = \int \phi_{im} c_{ij} \phi_{jn} \dot{q}_n dq_m$$

$$U = \int \phi_{im} k_{ij} \phi_{jn} q_n dq_m$$

$$Q_{A_m} = -1/2 \rho V^2 b_o S \phi_{im} a_{ij} (\phi_{jn} \dot{q}_n/V + \phi'_{jn} q_n)$$

Calculating the terms for the Lagrange equation:

$$\frac{d}{dt} \left(\frac{\partial T}{\partial \dot{q}_m} \right) = \phi_{im} m_{ij} \phi_{jn} \ddot{q}_n \quad (5)$$

$$\frac{\partial T}{\partial q_m} = 0$$

$$\frac{\partial F}{\partial \dot{q}_m} = \phi_{im} c_{ij} \phi_{jn} \dot{q}_n$$

$$\frac{\partial U}{\partial q_m} = \phi_{im} k_{ij} \phi_{jn} q_n$$

Substituting and collecting terms leads to:

$$\begin{aligned} & \phi_{im} m_{ij} \phi_{jn} \ddot{q}_n + (\phi_{im} c_{ij} \phi_{jn} + 1/2 \rho V b_o S \phi_{im} a_{ij} \phi_{jn}) \dot{q}_n \\ & + (\phi_{im} k_{ij} \phi_{jn} + 1/2 \rho V^2 b_o S \phi_{im} a_{ij} \phi_{jn}') q_n \\ & = \phi_{im} F_i \end{aligned}$$

Now let

$$M_{mn} = \phi_{im} m_{ij} \phi_{jn}$$

$$C_{mn} = \phi_{im} c_{ij} \phi_{jn}$$

$$K_{mn} = \phi_{im} k_{ij} \phi_{jn}$$

$$A_{mn} = \phi_{im} a_{ij} \phi_{jn}$$

$$B_{mn} = \phi_{im} a_{ij} \phi_{jn}'$$

and the condition $Q_m = 0$ which reduces the Lagrange equation to the basic flutter equation:

$$M_{mn} \ddot{q}_n + (C_{mn} + 1/2 \rho V b_o S A_{mn}) \dot{q}_n + (K_{mn} + 1/2 \rho V^2 b_o S B_{mn}) q_n = 0 \quad (6)$$

Control System Equations

Inclusion of control system equations in the flutter formulation requires some modifications to isolate control surface motions from the flexible airplane modes. The assumption that the control system actuator provides the restoring hinge moment for a given control surface deflection requires that:

$$\text{or } z_i = \phi_{ij} q_j \quad (3)$$

$$z_i = \phi_{im}^e q_m + \phi_{in}^{CS} q_n$$

or

$$\phi_{im}^e q_m = \phi_{ij} q_j - \phi_{in}^{CS} q_n \quad (7)$$

The elastic strain energy for a system with control surface then becomes:

$$U = \int \phi_{im}^e k_{ij} \phi_{jn}^e q_n d_{qm} + \dots$$

so that

$$\frac{\partial U}{\partial q_m} = \phi_{im}^e k_{ij} \phi_{jn}^e q_n + \dots$$

The effect is to increase the order of the flutter problem by the number of control surfaces included in the flutter problem.

To assure that all structural hinge moment comes from the actuator equation, the matrix $\phi_{im}^e k_{ij} \phi_{jn}^e$ must be singular. This condition is true only if ϕ_{ij} is the same order as k_{ij} .

For the analyses in this report, a Choleski triangular decomposition of $\phi_{im}^e k_{ij} \phi_{jn}^e$ was performed so that:

$$\phi_{im}^e k_{ij} \phi_{jn}^e = D_{mi} D_{in} \quad (8)$$

Using an identity matrix, modified to set the terms corresponding to control surface rotations to zero, the generalized stiffness matrix becomes:

$$D_{mi}^* I_{ij} D_{jn}^* = K_{mn}^* \quad (9)$$

Actuators driving the control surfaces were assumed to have an equation of motion of the form:

$$\delta_A + H(s) F_A + G(s) \epsilon = 0 \quad (10)$$

δ_A = actuator displacement

ϵ = input signal

F_A = actuator force

s = Laplace transform variable

G, H = transfer functions defined by experimental test

The derivation of specific actuator equations is treated later.

Sensor equations were assumed to have the forms given below:

1) accelerometers:

$$\ddot{z}_i - \phi_{ij} \ddot{q}_j = 0 \quad (11)$$

and

2) the pitch rate gyro:

$$(s^2 + 2 \xi \omega_n s + \omega_n^2) \theta_i - K \phi_{ij}' \dot{q}_j = 0 \quad (12)$$

where

ξ = damping ratio

ω_n = natural circular frequency

θ_i = pitch angle

K = gain factor

Compensation networks (filters) were also included in the control system equation of motion. Their general form was assumed to be:

$$\epsilon + G_\theta(s) \theta_i + G_z(s) z_i = 0 \quad (13)$$

where

G_θ, G_z = transfer functions defined by experimental test or analysis design.

In summary, the complete set of equations of motion for an active flutter stability augmentation control system are:

a) $\delta_A + H(s)_A F + G(s) \epsilon = 0$

$$b) \ddot{z}_i - \phi_{ij} \ddot{q}_j = 0 \quad (11)$$

$$c) (s^2 + 2\xi\omega_n s + \omega_n^2) \theta_i - K \phi'_{ij} q_j = 0 \quad (12)$$

$$d) \epsilon + G_\theta(s) \theta_i + G_z(s) z_i = 0 \quad (13)$$

$$e) M_{mn} q_n + (C_{mn} + 1/2 \rho V b_o S A_{mn}) \dot{q}_n \\ \pm (K_{mn}^* + 1/2 \rho V^2 b_o S B_{mn}) q_n = 0 \quad (14)$$

Actuator Equations

The actuator equations were derived from experimental data obtained by laboratory testing of each actuator before it was installed in the model. These tests established the basic inner loop gains for subsequent test and analysis. All actuators were also tested after installation in the model. Although the initial response characteristics were used in the early stages of analysis, the transfer functions reflecting "as installed" are derived here.

Horizontal Stabilizer Actuator

Assuming the actuator has the form of equation 10, for a zero error signal condition, one would obtain:

$$\frac{F_A}{\delta_A} = \frac{1}{H(s)} \quad (15)$$

Consider now the actuator experimental stiffness curves, figure D1, to establish the corner break frequency and the static and dynamic stiffness levels. From figure D1 the corner break frequency is $\omega_1 = 14.5$ Hz, the static stiffness level is 13.2 kips/in., the dynamic stiffness level is 20.4 kips/in. By assuming:

$$\frac{1}{H(s)} = \frac{1}{H_\infty} \left(\frac{s + \omega_1}{s + \omega_2} \right) \quad (16)$$

so that for static condition ($s = 0$):

$$\frac{1}{H_\infty} \left(\frac{14.5}{\omega_2} \right) = 13.2 \text{ kips/in.}$$

and

$$\frac{1}{H_\infty} = \left(\frac{\omega_2}{14.5} \right) 13.2 = 20.4 \text{ kips/in.}$$

then

$$\omega_2 = 22.4 \text{ Hz}$$

Now

$$\omega_1 = 2\pi(14.5) = 91.1 \text{ rps}$$

$$\omega_2 = 2\pi(22.4) = 140.7 \text{ rps}$$

thus

$$H(s) = 4.9 \times 10^{-5} \left(\frac{s + 140.7}{s + 91.1} \right) \quad (17)$$

Now consider the total response curve, figure D2. For $F = 0$ the output becomes

$$\delta_A/\epsilon = G(s) \quad (18)$$

Assuming

$$G(s) = \frac{G_\infty}{(s + \omega_G)[s^2 + (\zeta - 1)\omega_G s + \omega_G^2]} \quad (19)$$

Let

$$\zeta = 2.1, \omega_G = 15 \text{ Hz} = 94.3 \text{ rps}$$

then

$$G(s) = \frac{G_\infty}{(s + 94.3)(s^2 + 103.7s + 8883)}$$

Also let $G(0) = 1 \text{ in./V} = G_\infty/\omega_G^3$; then $G = (94.3)^3 = 8.37 \times 10^5$.

Substituting equations (17) and (19) into (10) one obtains:

$$\delta_A + 4.9 \times 10^{-5} \left(\frac{s + 140.7}{s + 91.1} \right) F_A + \frac{8.37 \times 10^5 \epsilon}{(s + 94.3)(s^2 + 103.7s + 8883)} = 0 \quad (20)$$

To relate actuator displacement to control surface motion some additional information must be considered:

$$\delta_A = \frac{1}{K_\delta} F_A + l_\delta \delta_H \quad (21)$$

where

K_δ = actuator linkage stiffness

l_δ = length of arm between actuator and surface

δ_H = angular rotation of horizontal slab about its pivot

Measured value for $K_{\delta} = 7.1 \times 10^5$ and $l_{\delta} = 2.33$ in., thus:

$$\delta_A = 1.405 \times 10^{-6} F_A + 2.33 \delta_H \quad (22)$$

Substituting (22) into (20):

$$\begin{aligned} & [(1.405 \times 10^{-6} F_A + 2.33 \delta_H)(s + 91.1) + 4.90 \times 10^{-5} (s + 140.7) F_A] \\ & \times [(s + 94.3)(s^2 + 103.7s + 8883)] + 8.37 \times 10^5 (s + 91) \epsilon = 0 \end{aligned} \quad (23)$$

Finally, to make the equation compatible with the modal coordinates, the angle δ_H has to be converted to a normalized displacement of the horizontal tail surface, or:

$$\delta_H = \frac{.6738}{12.65} q_H = 0.05326 q_H \quad (24)$$

Also, since the analysis applies to half the model:

$$F_{A/2} = 0.5 F_A \quad (25)$$

Substituting (24) and (25) into the equation (23) for the horizontal stabilizer actuator as used in the analysis reduces to:

$$\begin{aligned} & [(1.01 \times 10^{-5} s^2 + 2.33 \times 10^{-4} s + 1.29 \times 10^{-2}) F_{A/2} \\ & + (.124s^2 + 22.7s + 10.38) q_H] (s^2 + 103.7s + 8883) \\ & + (8.37 \times 10^5 s + 7.63 \times 10^7) \epsilon = 0 \end{aligned} \quad (26)$$

Aileron Actuators

While there were small performance differences between the four actuators used for the aileron control surfaces, for analytical simplicity they were assumed identical.

Starting with equation 10 and assuming the zero error signal condition to arrive at equation 15:

$$\frac{F_A}{\delta_A} = \frac{1}{H(s)} \quad (15)$$

Inspection of curves, figure D3, yield the corner frequencies:

$$\omega_1 = 20 \text{ Hz} = 126 \text{ rps}, \omega_2 = 125 \text{ Hz} = 785 \text{ rps}$$

and the static stiffness level as 4.4 in.-lb/deg.

The dynamic stiffness level is found by using equation 16 so that:

$$\frac{1}{H_{\infty}} \left(\frac{20}{125} \right) = 4.4 \text{ in.-lb/deg}$$

then

$$\frac{1}{H_{\infty}} = 4.4 \left(\frac{125}{20} \right) = 27.5 \text{ in.-lb/deg}$$

and

$$H(s) = 3.64 \times 10^{-2} \left(\frac{s + 785}{s + 126} \right). \quad (27)$$

Considering the response curve, figure D4, for $F_A = 0$;

$$\delta_A / \epsilon = G(s)$$

Assuming $G(s)$ is described by equation 18, and that $\omega_G = 48 \text{ Hz} = 302 \text{ rad/sec}$; for $\zeta = 1.65$:

$$G(s) = \frac{G_{\infty}}{(s + 302)(s^2 + 196s + 90960)} \quad (28)$$

Let

$$\begin{aligned} G(0) &= 1.0 \text{ deg/v} \\ &= \frac{G_{\infty}}{2.743 \times 10^7} \end{aligned}$$

then

$$G_{\infty} = 2.743 \times 10^7 \text{ deg/v}$$

Substituting equations 27 and 28 into 10, one obtains:

$$\delta_A + 3.64 \times 10^{-3} \left(\frac{s + 785}{s + 126} \right) F_A + \frac{2.743 \times 10^7 \epsilon}{(s + 302)(s^2 + 196s + 90960)} = 0 \quad (29)$$

To relate actuator rotation to control surface displacement

$$\delta_A = q_A / 10.35 \text{ (rad)}$$

or

$$\delta_A = 5.536 q_A \text{ (deg)}$$

Including this conversion factor in equation 29, one obtains the equation for the aileron actuator as used in the analysis:

$$\begin{aligned} & [(5.54s^2 + 2.36 \times 10^3s + 2.10 \times 10^5) q_A \\ & + (3.64 \times 10^{-2}s^2 + 39.5s + 8.61 \times 10^3) F_A] \\ & \times [s^2 + 196s + 9.10 \times 10^4] + (2.743 \times 10^7s + 3.448 \times 10^9) \epsilon = 0 \end{aligned} \quad (30)$$

Sensor Equations

The sensors used in the analyses were accelerometers and pitch rate gyro accelerometers. Acceleration feedback and/or its integrated response signal, velocity, were assumed ideal (eq. 11). Experimental verification justified this assumption. The pitch rate gyro accelerometer transfer function was derived from experimental data and follows below.

Pitch Rate Gyro Accelerometer

Assuming the transfer function of the gyro accelerometer may be described by:

$$\frac{\theta_G}{\theta_i} = \frac{1}{(s^2 + 2\zeta\omega_n s + \omega_n^2)}$$

and manufacturer specifications show that

$$\zeta = 0.4 \text{ to } 1.0, \omega_n = 30 \text{ Hz} = 188.5 \text{ rps}$$

then for

$$\zeta = 0.6: \quad \frac{\theta_G}{\theta_i} = \frac{K_G}{(s^2 + 226.2s + 35530)}$$

the static stiffness is given by:

$$\left. \frac{\theta_G}{\theta_i} \right|_{s=0} = \frac{K_G}{35530}$$

the sensitivity of the gyro was found to be 0.1 v/deg/sec

thus,

$$K_G = 0.1 \frac{180}{\pi} 35530 = 203575.$$

Now

$$\theta_i = \phi_{ij}' q_j$$

Thus the gyro transfer function reduces to:

$$(s^2 + 226.2s + 35530) \theta_G - 203575 \phi_{ij}' q_j = 0$$

Compensation Networks

The compensation networks listed below are identified by their "as flown" designations. The alterations made to suit the analyses are described.

Filter F-1

As flown, this filter was:
$$\frac{1}{1 + 6.31 \times 10^{-3}s}$$

No reason to alter this transfer function for the analysis.

Filter 10 Hz N

As flown, this filter was:
$$\frac{s^2 + 64^2}{s^2 + 38s + 64^2}$$

The analytical mode occurred at 9.36 Hz. Thus the filter was altered to:

$$\frac{s^2 + 59^2}{s^2 + 35s + 59^2}$$

Filter FG 90

As flown, this filter was:
$$\frac{1}{1.021 \times 10^{-4}s^2 + 3.03 \times 10^{-2}s + 1.0}$$

The purpose of the filter was to compensate the open-loop response with F-1 and 10 Hz N active. To achieve this analytically required:

$$\frac{1}{1.12 \times 10^{-4}s^2 + 3.18 \times 10^{-2}s + 1.0}$$

Filter HP 2

As flown, this filter was:
$$\frac{5.6 \times 10^{-2}s}{1 + 5.6 \times 10^{-2}s}$$

This filter was used to remove D. C. components; no reason to change for analysis.

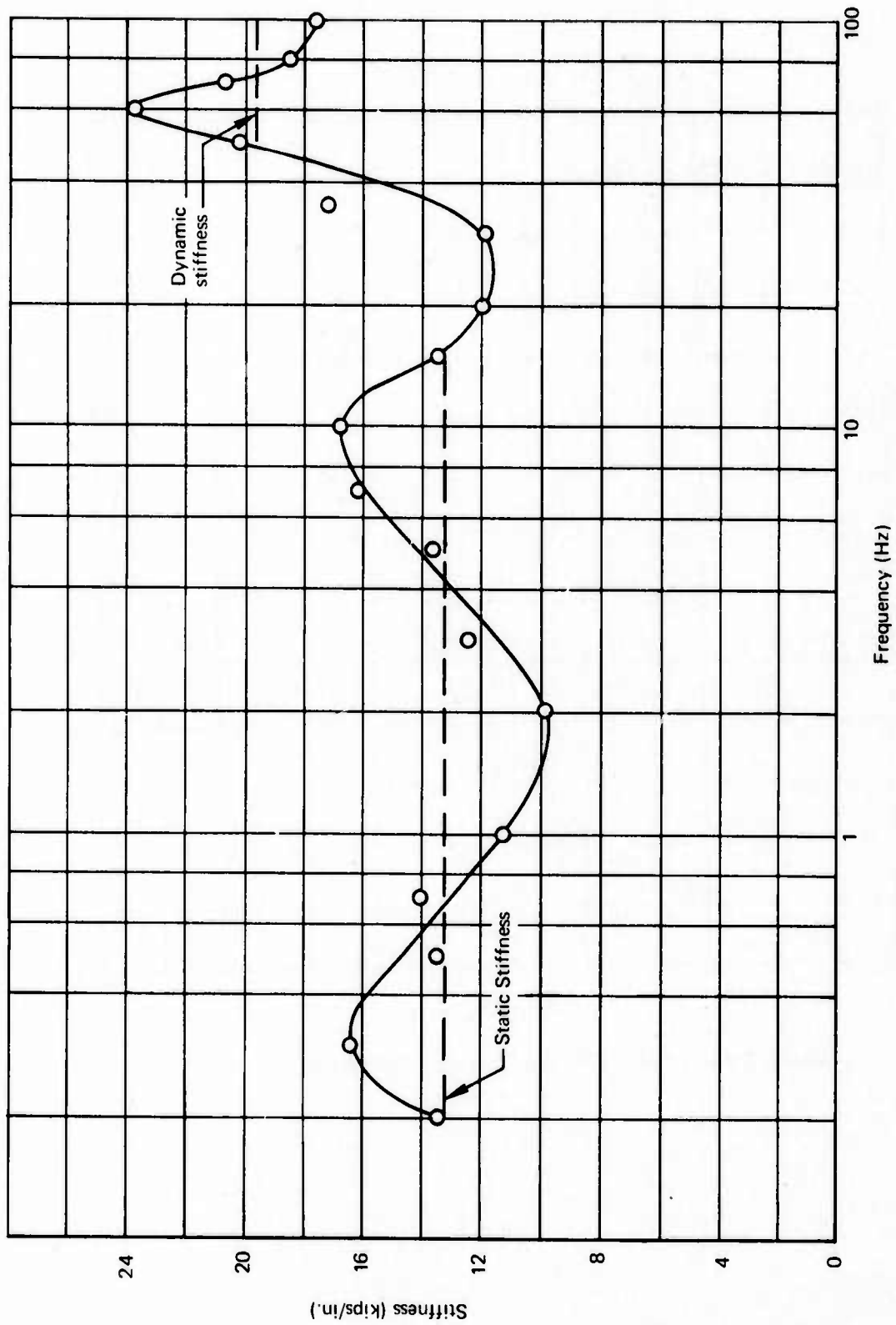


FIGURE D1.—STABILIZER ACTUATOR STIFFNESS

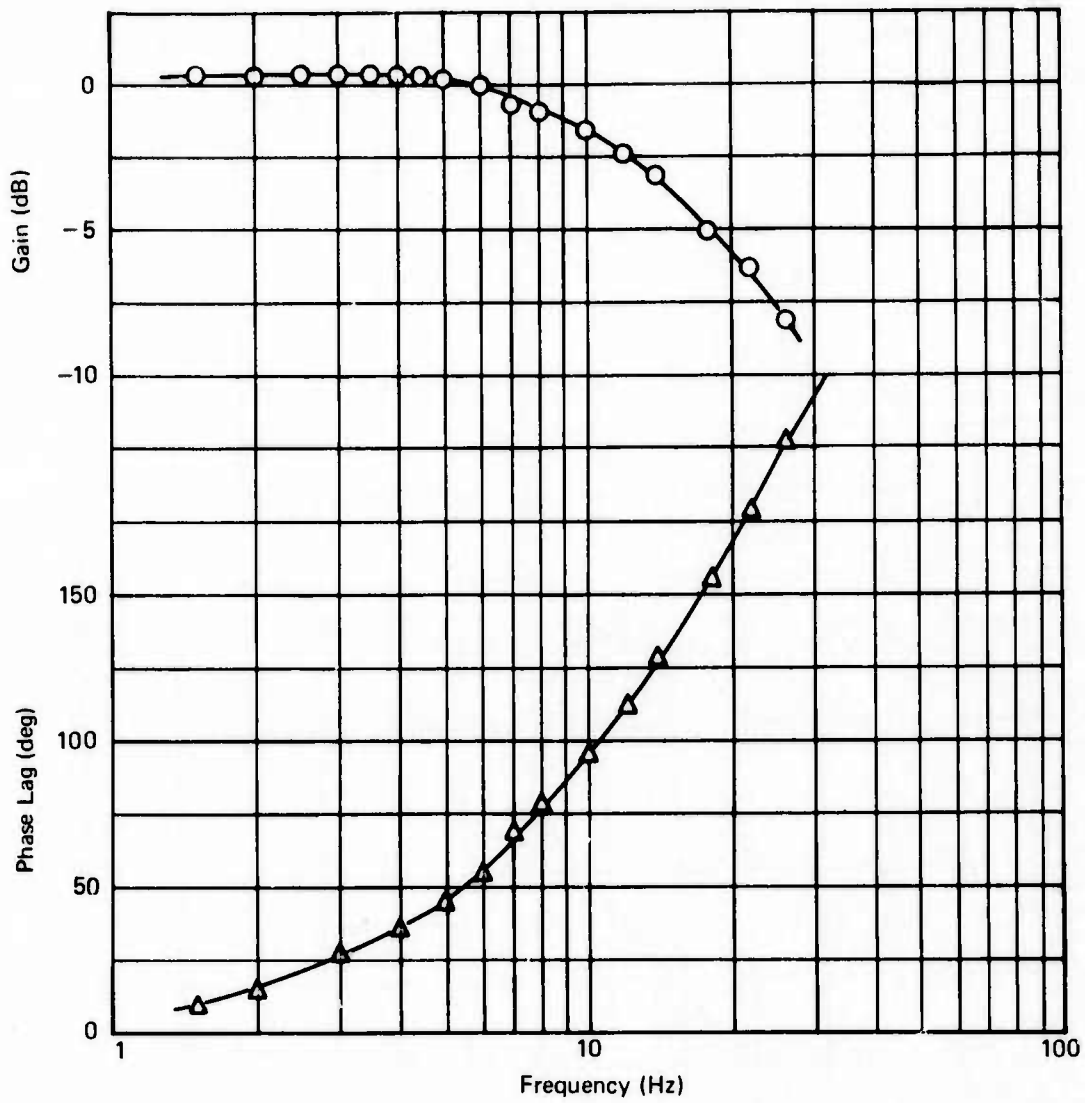


FIGURE D2.—STABILIZER ACTUATOR RESPONSE

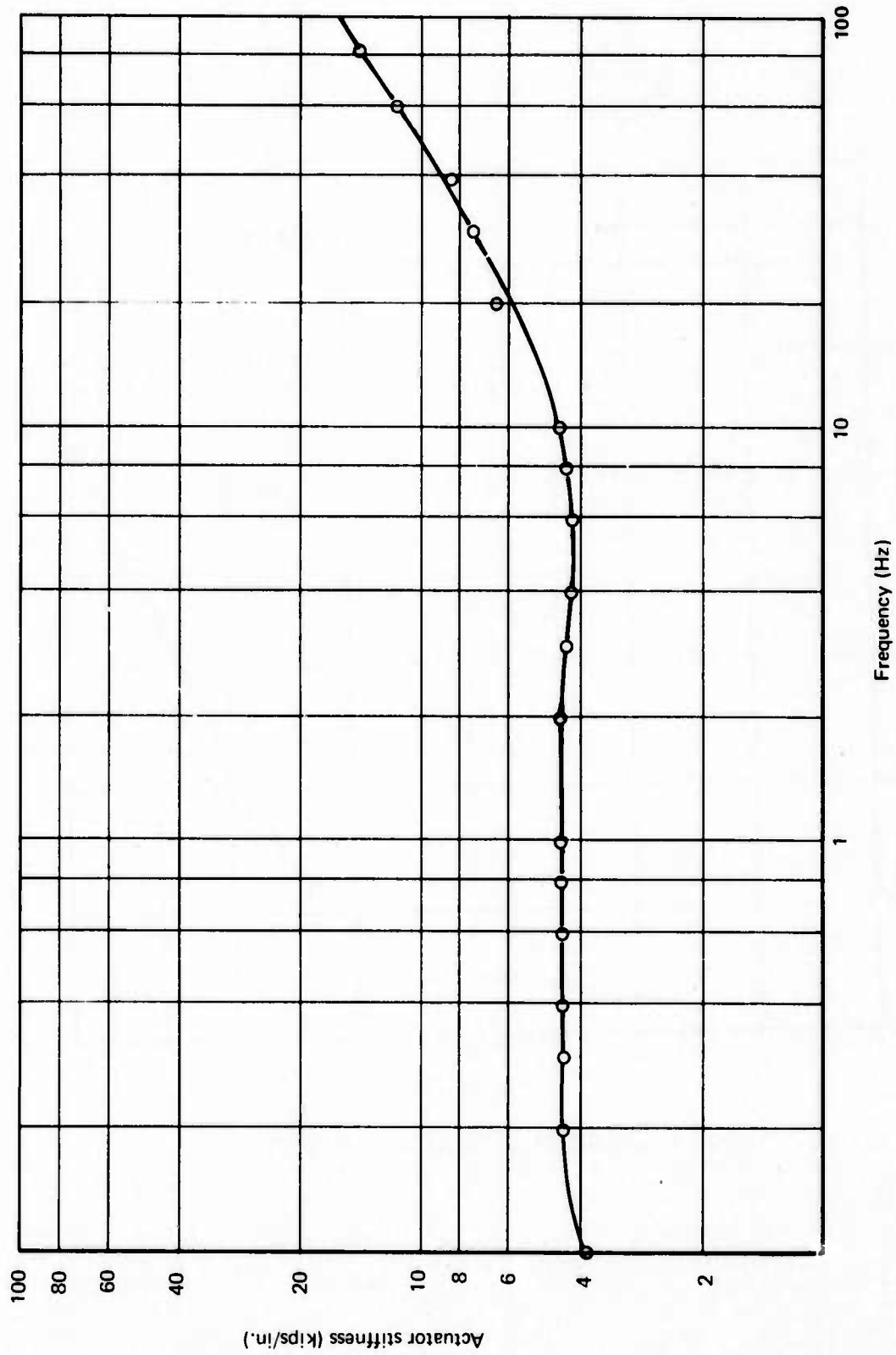


FIGURE D3. --AILERON ACTUATOR STIFFNESS

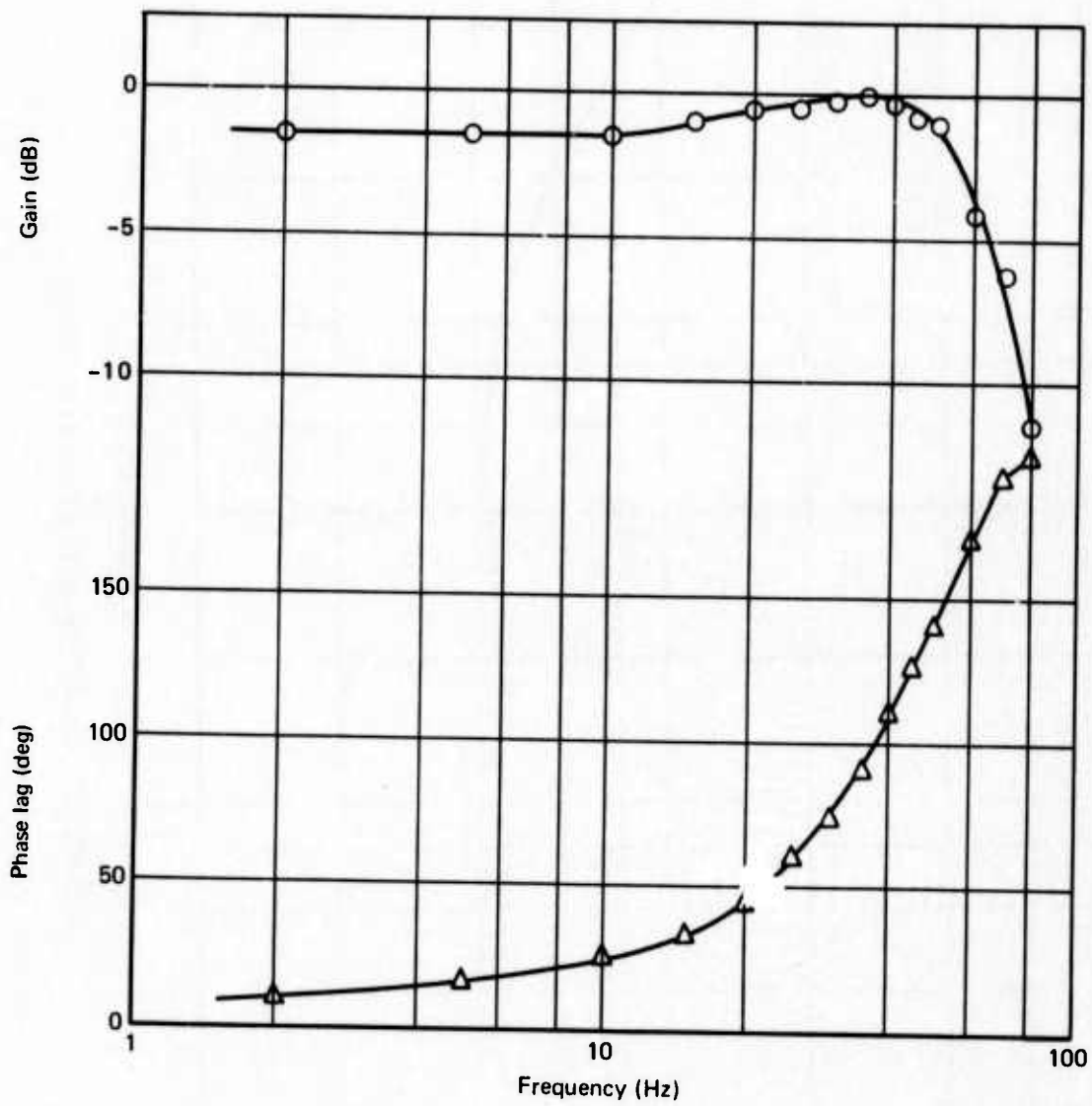


FIGURE D4.—AILERON ACTUATOR RESPONSE

APPENDIX E

PROBLEM AREAS

The discussion that follows is designed to stimulate thought by researchers of similar purpose to reevaluate their designs or applications to avoid similar difficulties.

ANALYTICAL PROBLEMS

The problem areas encountered during the subject analyses were quite well known at the start of the program. Consequently, an effort was made to avoid these known difficulties as much as possible or to at least limit their influence. The following compilation identifies specific problem areas and examines their impact on the results obtained.

Structural Analysis

The main problems relating to structural analysis were: (1) material stiffness modulus, (2) hydraulic tubing, and (3) cable support. While all three problem areas influenced the structural analysis, the cable support presented the greatest challenge and undoubtedly accounted for the lack of correlation between some of the analysis and test results.

Previous experience and testing had shown that considerable variation in material properties could be expected for composite structural materials. Excellent production quality control minimized overall variation in material properties, but it did not preclude the possibility of variation in stiffness moduli up to 50%. Finite element analysis facilitated the inclusion of a wide range of stiffness properties and thus helped to average the deviation. However, in order to take advantage of this analytical capability, samples of each type of construction had to be built and tested to establish its typical material stiffness modulus values.

The hydraulic tubing was built into the model structure to power the various control surfaces. Its diameter was kept to a minimum to decrease its effect on the structural stiffness, but flow requirements and hydraulic stiffness clearly governed the sizing. Placement of the tubing areas as near to the wing neutral plane as possible helped to control the contribution to torsional stiffness. However, at each point where the tubing touched or was attached to the model structure, the tubing affected the local stiffness. During the structural analysis, special attention was given to the structure/tubing interface points, but the success of this approach could have been evaluated only by a careful comparison of the analysis with a stiffness calibration. A stiffness calibration of the modified model was not conducted.

The cable support system introduced several effects which were difficult to account for analytically. Although the 2-cable method was a "soft" suspension, it changed the model rigid-body modes to low frequency cable modes. Rigid-body modes may be treated analytically fairly readily, but the cable modes required a good description of the interaction between the cable system and the flexible model.

The inertia model was constructed to help differentiate those effects due to the cable system from those of the model structure. The results of this investigation are reported in section 6.2, but some of the measurements made proved to be inconsistent with the actual 1129D model. Lacking better data, the model analysis used the inertia model results to synthesize the cable system.

Adding to the difficulty of determining cable system stiffness levels is the tendency for nonlinear behavior. For small amplitudes, the motions of the model on the cable support could be adequately described by linear theory, providing there was no deviation angle in the plane of the cables. However, at larger amplitudes and very near neutral stability, the system is nonlinear. At large amplitudes, the degree of translation/pitch and translation/yaw coupling changes nonlinearly as the pulleys traverse the cables. These motions are usually greater than those a prudent test engineer would wish to allow and thus are not normally encountered. Nevertheless, if the analysis were able to predict correctly the stability of the model at such large excursions, the safety of the test might be improved. The analysis did not account for large amplitudes.

Near the neutral point another nonlinear effect is introduced. Depending on the cable tension used, a "dead-zone" does occur at the neutral point. Also known as the small angle problem, the effect is to change the model altitude nonlinearly due to small changes in the angle between the pulleys and the cable. The analysis was not capable of including this effect.

Aerodynamics

For the subject investigation, the low frequency, rigid-body stability problem was most affected by the apparent shortcoming of the analytical aerodynamic forces. The problem, in fact, covers the whole frequency spectrum, and for clarity will be discussed as: (1) rigid-body aerodynamics, (2) low frequency (quasi-steady) aerodynamics, and (3) unsteady aerodynamics.

Rigid-body aerodynamics have been calculated without question for many years. The parameters which affect the stability derivatives are well documented. Representing the 2707-300 airplane, the 1129D model could be expected to respond like the full-scale vehicle. Consequently, the rigid-body aerodynamic coefficient data released for the airplane were adapted for the model by suitable corrections made for different cg configurations.

It appears that this procedure may have had its shortcomings. Besides the scale effects (Reynolds and Froude numbers), the differences in the wing aerodynamic sections were ignored. The question of how close flutter model stability derivatives may be approximated by airplane data remains open to further investigation.

Aerodynamics for low-frequency aeroelastic analyses also represented a problem area. For long flexible bodies such as the SST, the effect of aerodynamics on the body may be significant. Studies during the SST program and work in progress (ref. 22) indicated that accurate low frequency stability derivatives could be calculated for these configurations, but at considerable cost. For the subject analyses, only the aerodynamics of the wing and horizontal tail/elevator were calculated.

Unsteady aerodynamics for the flutter analyses represent an area which probably is open to the greatest improvement. As discussed in appendix D, the choice of indicial or circulatory aerodynamics had to be made. The present discussion is limited to circulatory aerodynamics.

A major problem with circulatory aerodynamic formulation is the fact that the assumption of uniform sinusoidal motion automatically leads to approximations for damped motion. As the response becomes less sinusoidal, the aerodynamics calculated become less accurate. Clearly, work in this area is necessary to improve subcritical response analysis.

Computer program calculations of unsteady aerodynamic forces for part span control surfaces are a rather recent development. The accuracy of the programs had been evaluated for a limited number of cases. The lack of good experimental data hampered such checks, but it was fairly clear that both the kernel function and the doublet lattice formulations yielded higher-than-measured hinge moments.

The capability to analyze both leading and trailing edge control surfaces is also desirable. The doublet lattice program was designed to have such capability, but its limited capability did not fit the problem size for the model with leading and trailing edge controls. Development of the kernel function program (ref. 6) to include leading edge control is well under way and should be applied to a problem of this type when available.

Solution Methodology

Investigation of all available solution packages capable of handling flutter stability augmentation problems led to the selection of the program described previously (ref. 14). One consequence of this choice was that the aerodynamic virtual inertia could not be included in the formulation. In general, it would have been desirable to isolate virtual inertia effects, especially for control surface flutter. Another consequence of the solution package was the restriction of maximum order of "s." The second order value was the maximum allowed; third order equations were treated in the subject analyses by transformation. For more complex systems, this restriction would cause severe difficulties.

While there are no theoretical limitations on the use of strain gages as feedback sensors, present solution packages are not suitable. Dynamic stress analyses are complex and costly to the extent of presently being prohibitive for consideration in a flutter stability augmentation analysis.

EXPERIMENTAL PROBLEMS

Sensing

One of the more formidable problems in active control system work is the problem of separating modes of closely spaced frequencies. This problem was recognized before the flutter suppression system was designed for the model. A sensing system was devised that employed multiple accelerometers to collectively sense selected in-flight modes instead of total local accelerations. This system assumed that an in-flight mode could be synthesized

by combining accelerometer signals according to the formula:

$$a_{ij} x_{jk} = \delta_{ik}$$

where

a_{ij} is the coefficient for the i^{th} in-flight mode and j^{th} sensor.

x_{jk} is the complex response of the j^{th} sensor and k^{th} in-flight mode.

δ_{ik} is the Kroniker Delta.

Among the advantages were: (1) ease in selecting mode to be controlled, (2) the multiple sensor grid eliminates the need for a thorough analysis of transducer placement as undesirable signals are canceled out in the summation process, and (3) the ability to use the measured transfer functions directly in the development of a flutter suppression system with any type of sensor. This system of mode sensing was tested, but results were not as expected due to problems with accelerometers and inability to model coefficients with simple analog filters.

The Kulite GY-5-125-50 accelerometers that were installed on the model wing surface were selected for their small size and response range. However, the damping characteristics of the transducers were unsatisfactory for the application because of high-frequency "ringing." Attempts to filter the transducer output improved the signal-to-noise ratio, but the quality of the signal remained too poor for closed-loop application.

The manner selected for transducer signal combination led to insufficient signal separation between modes. A single pole filter was used to model the coefficient in the summation equation. The filter characteristics of the single pole filter were not the same as the coefficients. A more attractive approach might be to sum the signals directly using complex algebra. This approach may better be handled in a digital system.

Servo Valve Magnetic Coupling

The servocontrol valves for the control surfaces of the model were installed in two groups, a group of four for the ailerons, and three for the three-channel stabilizer. Each group of servo valves were closely spaced over a hydraulic distribution block which ducted fluid to the proper control surface actuator from a common supply source.

During the initial checkout of the powered systems of the model, a high-frequency, low-amplitude instability was encountered. The frequency of oscillation was approximately 500 Hz in both the stabilizer and aileron systems. Initial attempts to eliminate the instability were unsuccessful. By accident, the cause of the instability was determined when a metallic instrument was passed over the cluster of the valve transformers. The problem was found to be the result of electrical interference between the transformers and was cured by placing a metallic band around the valve control transformers, which were integral with the valves.

Critical Electric Wiring

There are many critical electrical and electronic circuits in the demonstration of a closed-loop control system; a failure of the most obscure component can result in disaster. One of the critical areas is electrical wiring in the feedback circuits. Few electrical failures were experienced during the experimental demonstration, but those which occurred illustrated the hazard. The most hazardous failure is illustrated in figure E1. The figure is a top view of one of the three-stabilizer linear position feedback transducers. The electrical cable on the left failed from fatigue after approximately 500 hr of vibration testing, even though the cables were supported every few inches. The conclusion to be drawn is that all critical wiring connections should be designed for a severe vibration environment.

Since the model was 15 ft long, the electrical cables as well as the structure were designed to be disassembled for shipment and storage. All instrumentation and electrical wiring were coupled to quick-disconnect connectors. Some difficulties were experienced with corroded contacts in the plugs. Unfortunately, there was no visible indication of corrosion, but when the contacts were cleaned with a commercial solvent, the malfunction disappeared. Consequently, the source of the intermittent contact was difficult and time consuming to locate. There probably is no permanent solution to this problem. The ultimate solution is to permanently wire all circuits, but for most applications, it is impossible to achieve.

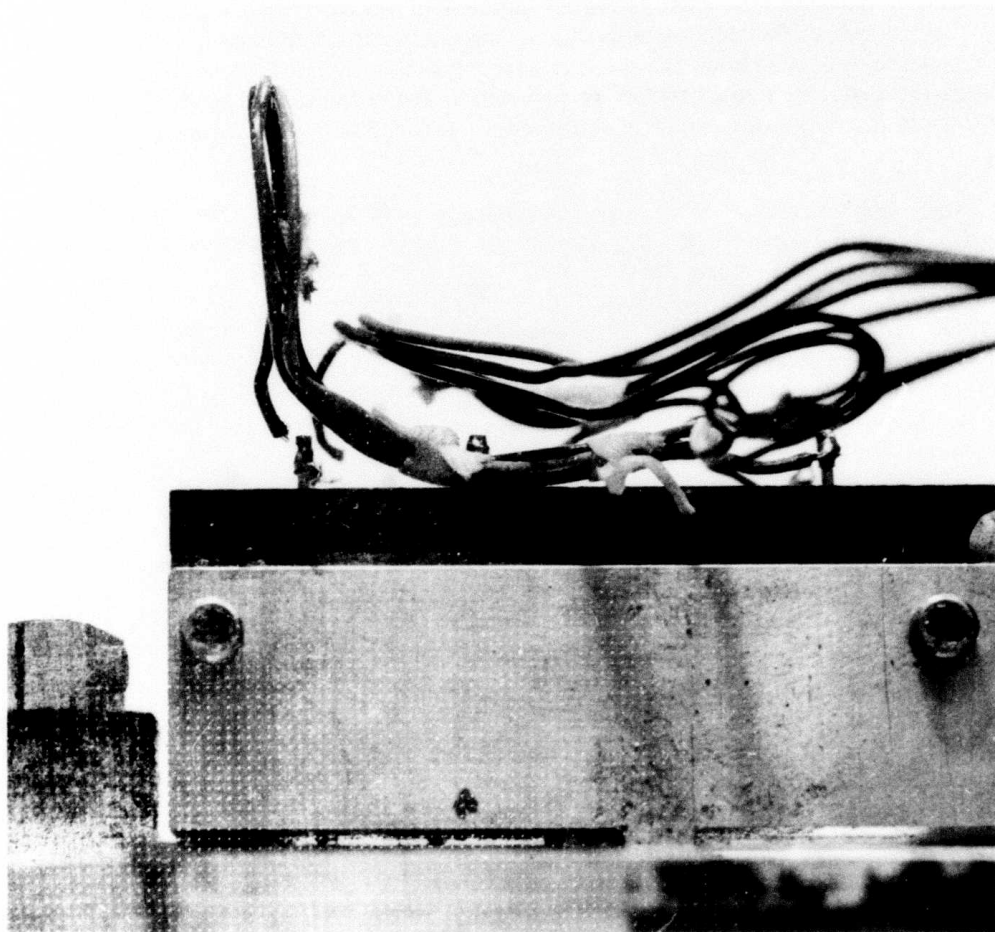


FIGURE E1.—STABILIZER ACTUATOR SYSTEM FAILURE

REFERENCES

1. J. B. Bartley and M. J. Turner, *Advanced Flutter Design Techniques*, S.A.E. Paper No. 730935, National Aerospace Engineering and Manufacturing Meeting, Los Angeles, California, October 1973.
2. A. D. Ryneveld, *Correlation of Flutter Analysis and Test Results for Half-Span SST Wing Models in Subsonic and Supersonic Flow*, SST Technology Follow-On Program—Phase II Report No. FAA-SS-73-3-17, 1973.
3. *Technical Proposal-Flutter Development Program*, DOT/SST Technology Follow-On, Phase II Boeing Document D6-26041-9, 1971.
4. E. Nissim, *Flutter Suppression Using Active Controls Based on the Concept of Aerodynamic Energy*, NASA TND-6199, 1971.
5. I. Abel and M. C. Sanford, *Status of Two Studies on Active Control of Aeroelastic Response*, NASA TMX-2909, 1973.
6. W. S. Rowe, B. A. Winther, and M. C. Redman, *Prediction of Unsteady Aerodynamic Loadings Caused by Trailing Edge Control Surface Motion in Subsonic Compressible Flow*, NASA CR-2003, 1972.
7. A. D. Ryneveld, *Transient Excitation Techniques for Wind Tunnel and Flight Flutter Testing of SST Configurations*, SST Technology Follow-On Program—Phase II Report No. FAA-SS-73-14, 1974.
8. W. H. Reed, III and F. T. Abbott, Jr., *A New "Free-Flight" Mount System for High Speed Wind-Tunnel Flutter Models*, Proceedings of the Symposium on Aeroelastic Dynamic Modeling Technology, U.S. Air Force Systems Command, RTD-TDR-63-4197, Part I, 1964.
9. C. C. Kennedy and D. D. P. Pancu, *Use of Vectors in Vibration Measurement and Analysis*, J. Aero. Sciences, Vol. 14, No. 11, 1947.
10. J. Hill, *Mass Properties of Flutter Research Model TX1129D-3*, Boeing Document D6-41178TN, 1973.
11. T. R. Anderson, *Residual Stiffness Effects in Truncated Modal Analysis of SST*, Boeing Document D6A-11560-ITN, 1969.
12. P. C. Foster, *TX1129D-3 Active Control Model Design and Installation*, Boeing Document D6-43032, 1974.
13. W. E. Triplett, H. P. F. Kappus, and R. J. Landy, *Active Flutter Suppression Systems for Military Aircraft—A Feasibility Study*, Technical Report AFFDL-TR-72-116, Air Force Flight Dynamics Laboratory, Wright-Patterson Air Force Base, Ohio, 1973.

14. J. I. Arnold and W. J. Wattman, *Supersonic Transport Flutter SAS Conceptual Study Results*, Boeing Document D3-7600-9, 1969.
15. F. D. Severt, S. M. Patel, and W. J. Wattman, *Analysis and Testing of Stability Augmentation Systems—Final Report*, Boeing Document D3-8884, 1972.
16. A. D. Ryneveld, *Stability Analysis of a Cable Mounted Model*, Boeing Coordination Sheet FRG-72 43, January 12, 1972.
17. A. G. Rainey and I. Abel, *Wind-Tunnel Techniques for the Study of Aeroelastic Effects on Aircraft Stability, Control, and Loads*, AGARD Flight Mechanics Panel Meeting, Marseilles, France, 1969.
18. L. Coven and C. F. Durbin, *A Comprehensive Eigensolution Program for Structural Vibration Analysis—TEV 142*, Boeing Document D6-40289, 1972.
19. J. M. Ii and D. F. Tankersley, *Unsteady Aerodynamic Interaction for Advanced Aircraft Configurations in Subsonic Flow (Improved Doublet Lattice TEV 155)*, Boeing Document D6-41258, 1973.
20. J. R. Billings and W. P. Jennings, *A Rational Quadratic Flutter Solution Procedure*, Programs CASBAII/COIR, Boeing Document D6-24812TN, 1971.
21. W. P. Jennings, *Transfer Function Calculation From Flexible Airplane Dynamic Equations of Motion*, Boeing Coordination Sheet YC-14-Struct-55, November 15, 1973.
22. A. R. Dusto, et al., *A Method for Predicting the Stability Characteristics of an Elastic Airplane*, Boeing Document D6-41064-1, Vol. 1, 1974.